Università degli Studi di Milano
Facoltà di Scienze e Tecnologie

Dipartimento di Chimica

Corso di Dottorato di Ricerca in Chimica Industriale
XXXIV Ciclo

Design and synthesis of photoluminescent Pt(II) and Ir(III) complexes for life science and OLEDs application

Giulia De Soricellis
R12348

Tutor: Prof.ssa Alessia Colombo
Co-Tutor: Prof.ssa Claudia Dragonetti

A.A. 2020/2021

Aim of the thesis 8

Chapter I - Photoluminescent properties of Pt(II) and Ir(III) complexes..................... 14

1. Introduction to photoluminescence 14

1.1 Theoretical basis of photoluminescent phenomena 14

1.2 Photoluminescent properties of organometallic complexes 20

2. Photoluminescent organometallic complexes: overview and state of the art 21

2.1 Photoluminescent Pt(II) complexes: an overview 21

2.1.1 Cyclometalated Pt(II) complexes based on the 1,3-di(2-pyridyl)benzene moiety ... 28

2.2 Photoluminescent cationic cyclometalated Ir(III) complexes: an overview 30

2.2.1 Photoluminescent cationic cyclometalated Ir(III) complexes: finely tuning the photophysical properties 32

3. Photoluminescent cyclometalated complexes for biomedical applications 36

3.1 Organometallic photoluminescent complexes as bioimaging probes: an introduction . 36

3.1.1 Pt(II) cyclometalated bioimaging probes: state of the art 39

3.1.2 Synthesis and characterization of an innovative series of cyclometalated Pt(II) complexes bearing sterically hindered substituents 44

3.1.2.1 Synthesis of Pt(II) emitters functionalized with bulky aryl substituents 44

3.1.2.2 Photophysical properties of Pt(II) emitters functionalized with bulky aryl substituents 49

3.1.2.3 Singlet fission: an overview 53

3.1.2.4 Singlet fission kinetics: an insight 58

3.1.2.5 Singlet fission: cases of study 63

3.1.2.6 Conclusion 66

3.1.3 Ir(III) cyclometalated complexes for bioimaging: state of the art 68

3.2 Targeting cancer metabolism to selectively address emitters in the biological environment 73

3.2.1 Targeting cancer cells through L-tryptophan transporters 74

3.2.1.1 Binding L-tryptophan to Ir(III) complexes: state of the art 78

3.2.2 The role of glucose in tumorigenesis: an overview 81

3.2.3 Synthesis and characterization of bioconjugated Pt(II) and Ir(III) complexes 84
3.2.3.1 Synthesis of a tryptophan conjugated Pt(II) cyclometalated complex 84
3.2.3.2 Synthesis of a glucose conjugated cyclometalated Pt(II) complex 85
3.2.3.3 Synthesis of a Pt complex for bioconjugation through exchange of the ancillary ligand 87
3.2.3.4 Synthesis of a cyclometalated Pt(II) complex for bioconjugation 88
3.2.3.5 Synthesis of a series tryptophan-conjugated cyclometalated Ir(III) complexes 89
3.2.3.6 Synthesis attempt of a glucose-conjugated cyclometalated Ir(III) complex..... 92
3.2.3.7 Synthesis of phenanthrolinine-based Ir(III) complexes for bioconjugation..... 94
3.2.3.7.1 Photophysical properties 95
3.2.3.7 Conclusion 100
3.3 Photodynamic therapy: introduction 102
3.3.1 Pt(II) complexes as anticancer agents: an overview 105
3.3.1.1 Pt(II) complexes as photosensitizers for photodynamic therapy 108
3.3.2 Cyclometalated Ir(III) complexes for photodynamic therapy 112
3.3.2.1 Ir(III) complexes as singlet oxygen sensitizers: introduction and state of the art 112
3.3.2.1.1 Bis-cyclometalated Ir(III) complexes 112
3.3.2.1.2 Ir(III) complexes bearing imidazolyl modified phenanthroline ligands .. 116
3.3.2.1.3 Imidazolyl modified phenanthroline Ir(III) complex functionalized with a biological vector 119
Chapter II- Phosphorescent organometallic complexes for OLEDs 121
1. OLEDs: introduction and principles 121
2. Cyclometalated Pt(II) complexes for OLEDs: introduction and state of the art............. 127
2.1 Pt(II) emitters for OLEDs fabrication displaying outstanding quantum yield 132
2.2 Fluorinated cyclometalated Pt(II) phosphors bearing highly hindered substituents. 135
2.2.1 Synthesis and characterization of the developed sterically hindered Pt(II) emitters 138
2.2.1.1 Synthesis of the fluorinated highly hindered Pt(II) complexes 138

2.2.1.2 Photoluminescent properties in solution 138

2.2.1.3 Highly hindered Pt(II) complexes: OLEDs fabrication 139

2.2.1.3.1 OLEDs fabrication: Pt-1 140

2.2.1.3.2 OLEDs fabrication: Pt-5 144

2.2.1.3.3 Conclusions 147

Chapter III- Experimental section 151

1. General comments 151

2. Synthesis of cyclometalated Pt(II) and Ir(III) complexes 152

2.1 Synthesis of the fluorinated Pt(II) complexes bearing highly hindered substituents 152

2.1.1 Synthesis of Pt-1 to P-4 153

2.1.1.1 Synthesis of 2,2'-(4,6-difluoro-1,3-phenylene)bis(4,4,5,5-tetramethyl-1,3,2-dioxaborolane) 154

2.1.1.2 Synthesis of Pt-1 155

2.1.1.3 Synthesis of Pt-2 158

2.1.1.4 Synthesis of Pt-3 160

2.1.1.5 Synthesis of Pt-4 162

2.1.2 Synthesis of Pt-5 to P-8 164

2.1.2.1 Synthesis of Pt-5 165

2.1.2.2 Synthesis of Pt-6 167

2.1.2.3 Synthesis of Pt-7 169

2.1.2.4 Synthesis of Pt-8 172

2.2 Synthesis of cationic tryptophan-conjugated Ir(III) complexes 175

2.2.1 Synthesis of the tryptophan-conjugated phenanthroline-based ligand 177

2.2.2 Synthesis of the Ir-dimers 179

2.2.3 Synthesis of the tryptophan-conjugated Ir(III) complexes 181

2.3 Synthesis of cationic phenanthroline-based Ir(III) complexes for bioconjugation...... 183

2.3.1 Synthesis of Ir-4 183

2.3.2 Synthesis of Ir-5 185

2.4 Synthesis of a Pt complex for bioconjugation through exchange of the ancillary ligand 187

2.5 Synthesis of the tryptophan-conjugated Pt(II) complex 189

2.6 Synthesis of a Pt complex for bioconjugation through modification of the N^C^N pincer 191

2.7 Synthesis of the glucose conjugated Pt(II) complex 193

2.7.1 Preparation of the glucose moiety 194

2.7.2 Synthesis of the cyclometalated Pt(II) pincer 195

2.7.3 Glucose appendage 196

2.7.4 Synthesis of the Pt(II) complex 197

3. X- Ray analysis 200

3.1 X-ray analysis of Pt-1 200

4. Thin film preparation 204

4.1 Pt-1 204

4.2 Pt-5 209

Chapter IV – Conclusion 213

Chapter V – Bibliography 216

Aim of the thesis

The photoluminescent properties of cyclometalated complexes have been widely investigated, due to their optimal features and applicability to a large variety of fields. In particular, the introduction of a metal center provides an enhancement in the photophysical properties of the organometallic chromophores with respect to highly conjugated organic molecules. Indeed, the metal center allows to imprint a specific geometry to the structure of the complex: the number of ligands bound to the metal center and their three-dimensional arrangement in the coordination sphere determines the molecular orbital energies of the complex. The electronic structure of the molecule constitutes the basis of the observed luminescent properties. In addition, the nature of the ligands surrounding the metal center allows to tune the electronic properties of the compound, thus making organometallic complexes versatile and attractive for many purposes.

In my PhD thesis two main topics will be extensively discussed:

a) The application of the developed luminescent metal complexes as luminescent labels for bioimaging and as photosensitizers for photodynamic therapy (PDT);
b) The synthesis and analysis of cyclometalated complexes bearing highly hindered aryl substituents for OLEDs application.

The first part of the thesis focuses on the synthesis and characterization of luminescent Pt(II) and Ir(III) complexes functionalized with a vector able to selectively target cancer cells. The mechanism of action underlying the tumor treatment is based on the cytotoxicity induced within the biological tissues by the singlet oxygen produced through light activation of the metal complex, which serves as a photosensitizer. The generation of reactive oxygen species (ROS) *in loco* using a photoluminescent complex is at the basis of a non-invasive and innovative procedure known as photodynamic therapy (PDT).

In order to control the localization of the photosensitizer inside the cell, the Pt(II) and Ir(III) complexes were designed bearing targeting fragments that could lead them inside specific biological structures. In this context, glucose and L-tryptophan were selected due to the observed upregulation arising as a consequence of cancer cells proliferation.

Specifically, the glucose moiety provides an optimal targeting group since the overexpression of glucose transporters GLUT-1, discovered in many cancer cell lines, could be exploited.[1] Indeed, the proliferation of tumorous cells requires significant amount of energy, which results in the storage of larger quantities of glucose, a phenomenon known as Warburg effect.[2]

Furthermore, glucose increases the water solubility of the metal complexes, thus making their elimination easier and faster. This aspect is crucial since heavy metal ions such as Pt(II) and Ir(III) could induce toxicity among the biological tissues, thus leading to significant side effects.[3]

L-tryptophan represents another promising targeting vector due to its involvement in many biosynthetic pathways, being the precursor of biologically relevant substrates, namely serotonin and L-kynurenine.[4]

Similarly to the Warburg effect, the up-regulation of the L-amino acid transporter LAT1, responsible for the uptake of large neutral aromatic amino acids as L-tryptophan, was observed in malignant cancers.[5]

The overexpression of LAT1 transporters provides a potential approach to increase the biological selectivity and thus, to enhance the influx of the tryptophan-conjugated emitters inside tumorous cells, preventing cytotoxicity to be induced in healthy cells.

The photosensitizers were designed so that the light activation could be carried out through the two-photon absorption (TPA) mechanism. Indeed, the longer-wavelength light of the near IR could give rise to a higher yield of the singlet oxygen formation since it penetrates deeper inside the biological tissues with respect to the visible light.[6]

Given these premises, the synthesis of a series of cationic tryptophan conjugated Ir(III) complexes bearing different cyclometalated ligands in the coordination sphere and the synthesis of a tryptophan conjugated Pt(II) emitter were achieved. The molecular structure of the designed compounds is reported in **Figure 1.**

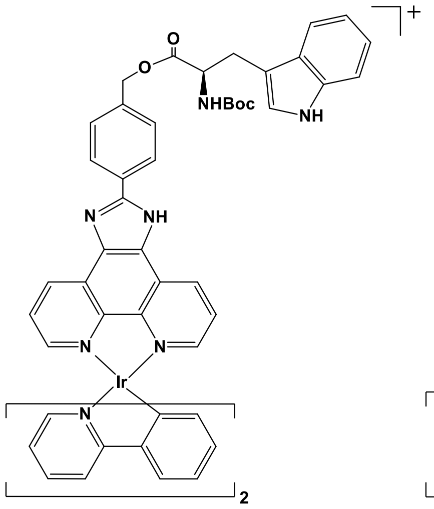

Ir-1

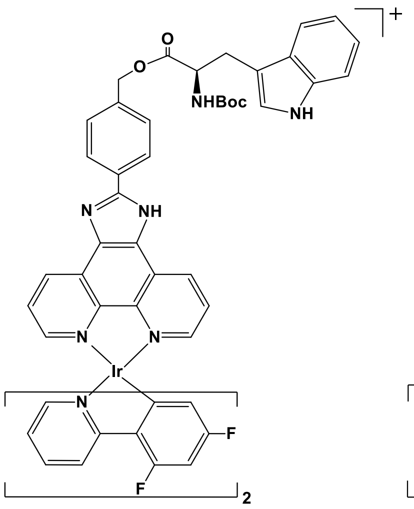

Ir-2

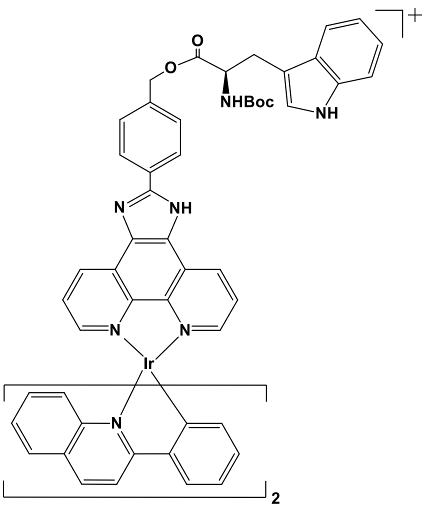

Ir-3

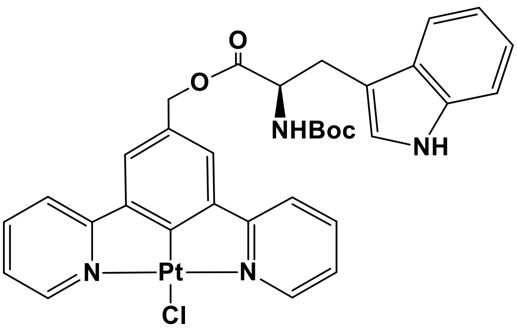

Pt-10

Figure 1. Molecular representation of the tryptophan conjugated cyclometalated Ir(III) and Pt(II) complexes.

In the context of bioconjugated luminophores, the appendage of glucose to the cyclometalated backbone meant for Pt(II) and Ir(III) complexation was attempted, introducing the sugar moiety through the hydroxymethyl group (**Figure 2**).

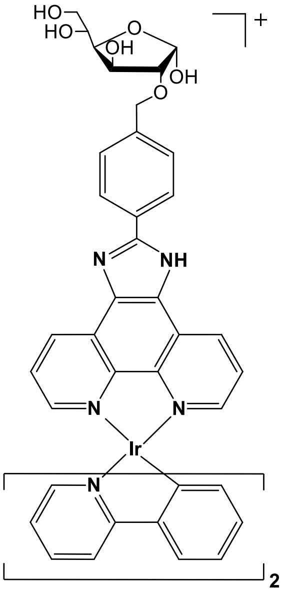

Ir-6

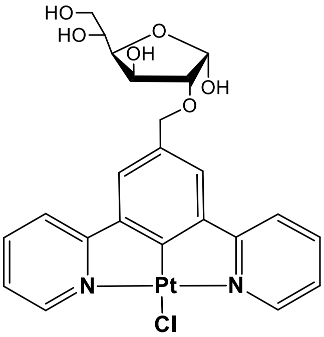

Pt-11

Figure 2. Molecular representation of the targeted glucose-appended emitters.

In parallel, Pt(II) and Ir(III) complexes bearing anchoring groups on the scaffold to enable the subsequent introduction of a biologically relevant substrate were synthesized. Specifically, **Ir-4** and **Ir-5** display the key functional group on the cyclometalated pincher, whilst for **Pt-9** the anchoring hydroxymethyl was inserted through the ancillary ligand exchange. The developed emitters are represented in **Figure 3.**

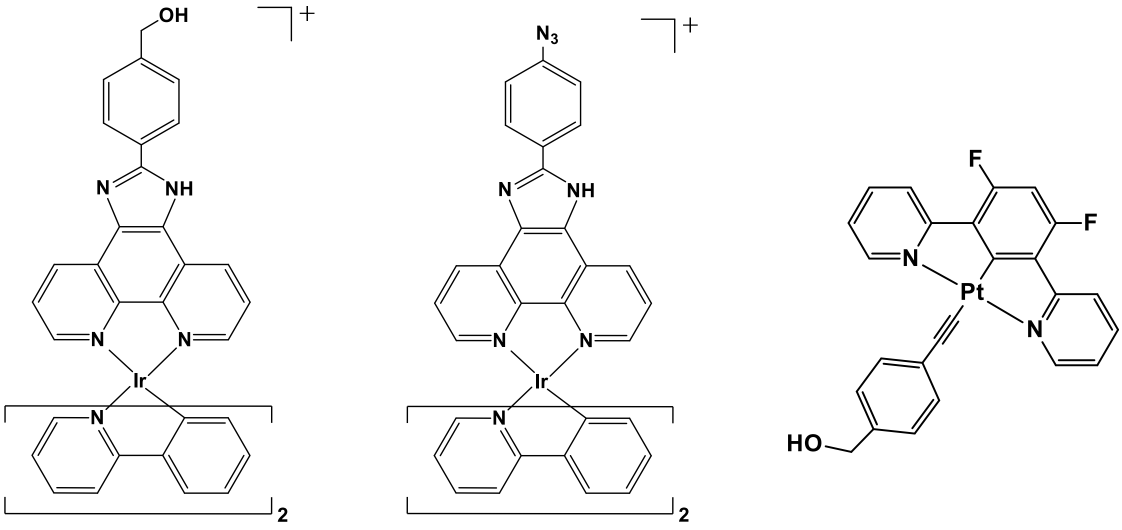

Ir-4 **Ir-5** **Pt-9**

Figure 3. Molecular structure of the emitters designed for further bioconjugation.

The investigation over the efficacy of the bio-conjugated complexes within the biological environment were performed testing the emitters inside the brain tissues *in vitro*.

The biological assays were carried out at the University of Curtin, Perth, Australia, by the research group of Prof. Massimiliano Massi, in the context of a collaboration.

The second section of the thesis describes the properties of cyclometalated Pt(II) complexes bearing fluorinated ligands functionalized with a variety of highly hindered aryl substituents for the development of efficient OLEDs devices.

The introduction of bulky functional groups was carried out in order to enhance the efficiency of the metal-organic emitters, thus investigating the role played by steric hindrance on the photophysical properties:

- λ emission;
- Excited state life-time;
- Quantum yield.

In addition, the developed Pt(II) complexes were designed aiming to control aggregation in the emitting layer of the OLEDs devices arising from the π-π stacking interaction occurring within neighboring square planar Pt(II) complexes, a process that could lead to excitation energy loss.[7]

The molecular structure of the synthesized sterically hindered emitters is reported in **Figure 4**.

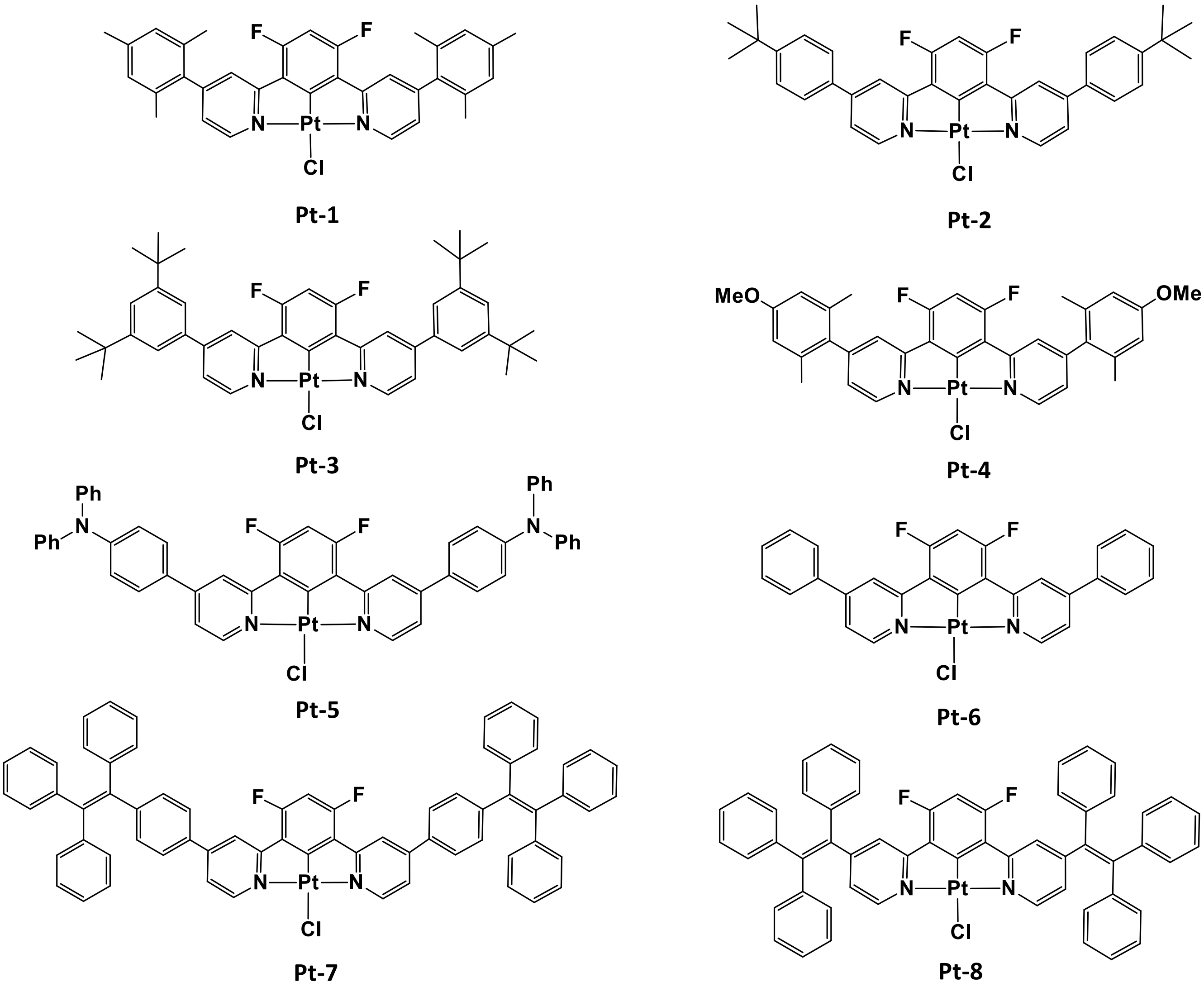

Pt-1 Pt-2 Pt-3 Pt-4 Pt-5 Pt-6 Pt-7 Pt-8

Figure 4. Molecular structure of the sterically hindered Pt(II) complexes.

The project was carried out in collaboration with the research groups of Dr. Bertrand Carboni and Dr. Veronique Guerchais, during my stay at Université de Rennes 1, France.

Chapter I - Photoluminescent properties of Pt(II) and Ir(III) complexes

1. Introduction to photoluminescence

1.1 Theoretical basis of photoluminescent phenomena

According to quantum mechanics,[8] an electromagnetic radiation is described as a stream of photons, particles that transport discrete amounts of energy. The energy associated with a single photon is defined by the Planck's equation: E = hν, where h corresponds to the Planck's constant (h = 6.626 x 10^{-34} J s) and ν represents the frequency of the radiation.

In 1924, De Broglie introduced the wave-particle duality theory which stated that photons exhibited the properties of both particles and waves. Given these premises, a mathematical representation of a photon can be assigned through the wave function Ψ.

The wave function Ψ can be estimated solving the time (t) dependent Schrödinger equation: as a function of the position *x* (Eq. (1)):

$$\widehat{H}\Psi(x,t) = i\hbar\frac{\partial\Psi(x,t)}{\partial t} \qquad \widehat{H} = \left[-\frac{\hbar^2}{2m}\frac{\partial^2}{\partial x^2} + V(x,t)\right] \qquad \text{Eq. (1)}$$

$$\hbar = \frac{h}{2\pi}$$

Where *m* represents the mass of the particle moving along the x-axis and V(x,t) the potential energy as a function of the time along the x-axis.

Anyway, the equation is unsolvable for most of the systems, so it is possible to simplify it considering steady state functions, (Eq. (2)) where the potential energy V doesn't change over the time and so V(x)=V:

$$\widehat{H}\Psi(x) = i\hbar\partial\Psi(x) \qquad \widehat{H} = \left[-\frac{\hbar^2}{2m}\frac{\partial^2}{\partial x^2} + V\right] \qquad \text{Eq. (2)}$$

In this way, the time dependence of the wave function is removed and as a result the equation contains the spatial coordinate x as the only parameter.

The time-independent Schrödinger equation is particularly useful when it comes to describing the molecular systems, which are stationary state systems, and the luminescence phenomena theory.

When matter is exposed to electromagnetic radiations, they interact with atoms and molecules, giving rise to multiple phenomena, such as the absorption of photons.

Talking about a molecular system, when a photon is absorbed, an energy transfer occurs and this results in an electron distribution variation in the molecule. In particular, the energy allows the promotion of electrons to higher energy molecular orbitals and the system switches from the ground state to the excited state.

However, the excited molecule is not stable and so tends to rearrange its electronic density in order to release the excess of energy and return to the lowest energy state.

Three main pathways allow the loss of the exceeding energy:

- Non-radiative decay;
- Fluorescence;
- Phosphorescence.

Whilst the non-radiative decay consists in a slow heat dissipation in the surrounding environment and so it is not interesting from a photophysical point of view, fluorescence and phosphorescence form the basis of photoluminescence. Indeed, fluorescence and phosphorescence give rise to a spontaneous emission of photons, which is attractive for many applications.

However, there's a key difference between fluorescence and phosphorescence which resides in the life-time of the excited state. Thus, an insight concerning the theoretical basis of the two phenomena will be provided in detail in the following paragraph.

The promotion of electrons to higher energy levels will be discussed applying the Born-Oppenheimer[9] approximation: since atoms' nuclei have a greater mass then electrons, it's reasonable to consider that during the excitation process the nuclei remain steady. This represents a strong simplification of the mathematical discussion. Indeed, the molecular wave function $\Psi(q_e, q_n)$ includes the information about all the nuclei and all the electrons in the molecule (Eq. (3)):

$$\Psi(q_e, q_n) = \Psi_e\,(q_e)\,\Psi_n\,(q_n) \qquad \text{Eq. (3)}$$

Where $\Psi_e\,(q_e)$ describes the electronic states of the molecule and $\Psi_n\,(q_n)$ the vibrational and rotational states.

Considering that the nuclei are steady, the coordinates q_n can be treated as parameters and the electronic, vibrational and rotational components can be written separately (Eq. (4)):

$$\Psi = \Psi_e \Psi_v \Psi_r \qquad \text{Eq. (4)}$$

Solving the Schrödinger equation for each wavefunction's component, the electronic, vibrational and rotational energy levels of the molecule are obtained.[8] The schematic representation of the electronic levels and the corresponding vibrational and rotational states of a generic molecule, through the potential energy curve diagram, is reported in **Figure 5**.

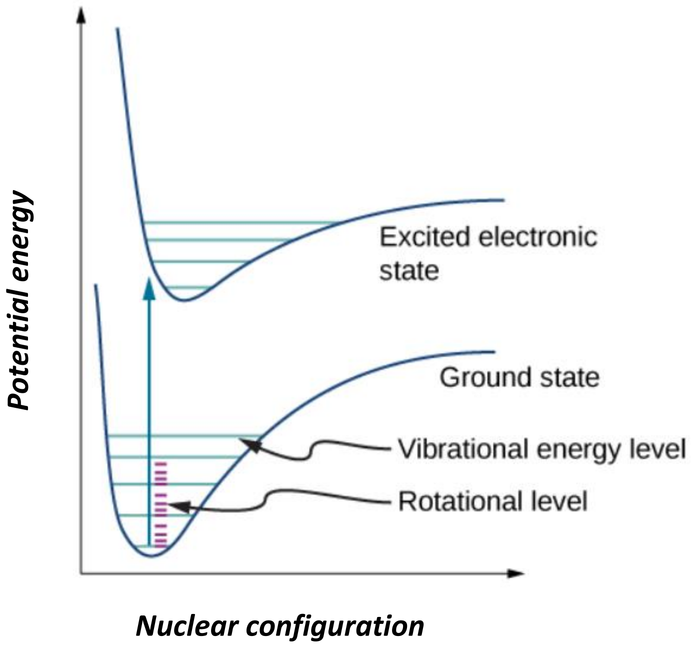

Figure 5. Potential energy curves diagram depicting the electronic, vibrational and rotational levels involved in the vertical transition of a generic molecule.

The discussion of the florescence and phosphorescence phenomena will be carried out referring to the Jablonski diagram reported below (**Figure 6**), where the electronic energy levels and the corresponding vibrational substructure are represented.

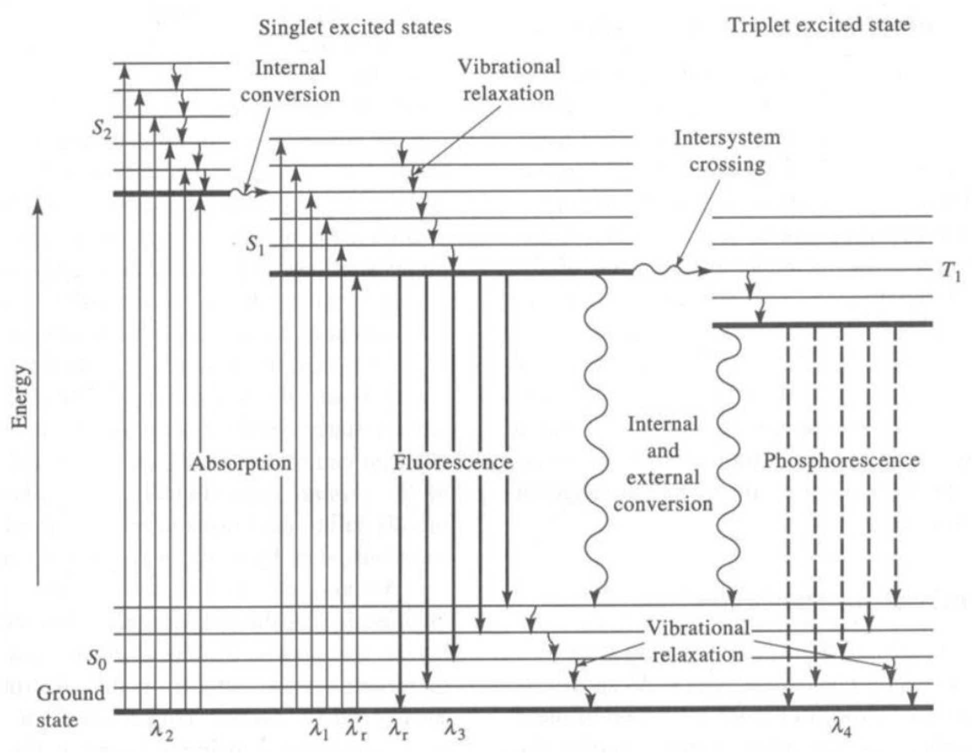

Figure 6. Jablonski diagram representing the photophysical processes occurring upon excitation of a generic molecule.

When a molecule is irradiated with a photon beam, the absorption of its energy can occur only if the Planck's equation is fulfilled. If this condition is satisfied, the molecule passes from the lowest vibrational state within the ground electronic state S_0 to one of the excited vibrational states of the excited electronic state S_1. The excited molecule tends to relax via non-radiative releases of exceeding energy to the ground vibrational state of S_1, through vibrational relaxation and internal conversion. This process is in accordance with the Kasha's rule, which states that the emission always involves the lowest vibrational state of the lowest energy excited electronic level. At this point the molecule can completely relax to the ground state S_0 by two main radiative pathways: fluorescence of phosphorescence.[10]

Fluorescence occurs when the molecule directly relaxes to S_0 through a spontaneous emission of photons within 10^{-7} and 10^{-9} s. It is very quick and as soon as the excitation source is removed, the emission stops.

On the other hand, from S_1 the molecule can undergo an intersystem crossing, which is a non-radiative process in which the electron reverses its spin and the molecule lands in the triplet excited state T_1. At this point, the molecule goes through a vibrational relaxation to the vibrational ground state of T_1 and lastly, the exceeding energy is gradually released via phosphorescence. This phenomenon takes place in a time span of 10^{-3}-10^{2} s and so can be observed even when the excitation source is removed.

Phosphorescence relies on a spin forbidden transition because the radiative decay involves a triplet excited state T_1 and the singlet ground state S_0. However, the selection rule can be partially circumvented due to the spin-orbit coupling and so these transitions can still occur. In particular, it is observable in heavy metal organometallic complexes.

Nowadays many devices and technologies rely on photoluminescence and so it's crucial to maximize the efficiency of the phenomenon. For this purpose, it is necessary to consider the conditions to be fulfilled.[8]

In the first place, the selection rules have to be taken into account:

- The interaction between an electromagnetic radiation and a molecule induces an electric dipole moment variation. Its entity is strictly related to the overlapping between the molecular wavefunction describing the ground state and the molecular wavefunction of the excited state involved in the transition. Indeed, the wavefunction Ψ doesn't have a direct physical meaning, but its square multiplied by the length of the infinitesimal region, $|\Psi|^2 dx$, represents the probability density function that gives information about the probability to find the particle in a specific region in a one-dimensional system. A schematic representation of the vibrational wavefunctions associated with the vibrational sublevels of the electronic states is reported in **Figure 7.**

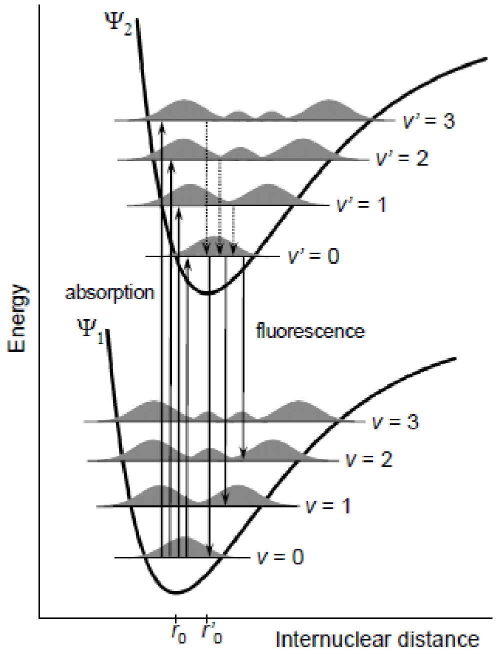

Figure 7. Potential energy curve diagram representing the vibrational wavefunctions and the related transitions.

- In the case of centrosymmetric chromophores, the molecular wavefunctions are labelled as gerade (g) and ungerade (u) and the Laporte's rule states that allowed transitions occur within wavefunctions of opposite parity only (g → u and u → g).

- Transitions in which the spin of the molecule is reversed are forbidden.

Given these premises, it’s essential to clarify that these rules aren’t always strictly observed. In particular, the symmetric selection rules are easily violated since the vibrational motion of the molecule tends to suppress the center of symmetry and so the Laporte’s rule falls.

Spin-forbidden transitions are more difficult to circumvent, but spin-orbit coupling enables it. Indeed, the spin-orbit coupling mixes singlet and triplet states, so that the rule becomes less strict. The interaction between the magnetic moment of the electronic spin and the magnetic field deriving from its orbital angular momentum around the nucleus, relies on the nuclear charge (Z). The greater is the nuclear charge, the greater is the coupling. Indeed, the spin-orbit coupling shows a dependence from the atomic number proportional to Z^4.[11]

In addition to the selection rules, the molecular structure must be taken into account in order to favor the radiative decay mechanism over the heat dissipation. Indeed, the variation of the electronic density related to the excitation process results in the population of the antibonding molecular orbitals, which provokes the decrease of the bonds strength. Overall, this leads to a distortion of the molecular structure in the excited state, well represented by shifted potential energy curves in the energetic diagram, that tend to cross each other. When the excited state potential energy curve crosses the potential energy curve of a lower energy electronic state, the non-radiative decay is spontaneous. For that reason, rigid ligands are preferred.

However, a loss of excitation energy occurs through non-radiative relaxation pathways and this results in longer wavelength of emission associated to fluorescence and phosphorescence, with respect to absorption. As a consequence, the absorption and emission spectra are not superimposed and indeed the emission spectra is shifted towards longer wavelengths. In **Figure 8** the absorption and emission spectra of anthracene is reported as a model.[12]

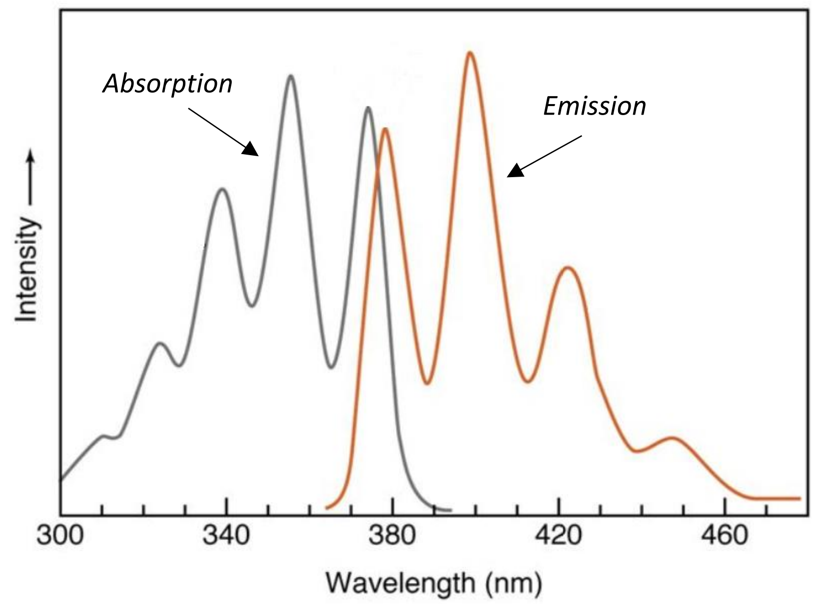

Figure 8. Absorption and emission spectra of anthracene.

1.2 Photoluminescent properties of organometallic complexes

Organometallic compounds represent a class of molecules characterized by metal-carbon bond. The development of photoluminescent organometallic complexes gained increasing interest since they show promising photophysical properties exploitable in many fields.

In the context of luminescence, phosphorescence is considered the most attractive radiative phenomenon, mainly due to the long life-time of the excited state.[13] In order to obtain phosphorescence, the excited complex has to be prone to undergo the intersystem crossing to switch to the triplet state, thus allowing a forbidden triplet-singlet transition to occur. These phenomena are more likely to happen in systems that show a strong spin-orbit coupling.

In this context, the transition metals of the 2nd and 3rd row provide promising metal centers to design highly luminescent organometallic complexes. Furthermore, by selecting the proper coordination sphere, it's possible to tune and optimize their photoluminescent properties such as the wavelength of emission, the life-time of the excited state and the quantum yield.

In this first chapter, a detailed description concerning the design of luminescent Pt(II) and Ir(III) complexes will be provided.

2. Photoluminescent organometallic complexes: overview and state of the art

2.1 Photoluminescent Pt(II) complexes: an overview

Phosphorescent Pt(II) complexes have attracted great interest over the years due to their promising properties for bioimaging,[14] anticancer activity[15] and OLEDs applications16. In order to fully exploit the potential of Pt(II) complexes, it's essential to investigate their molecular orbital structure and the key role played by the ligands forming the coordination sphere.

Pt(II) is a d^8 metal ion and so it contains eight electrons in the d atomic orbitals, which are degenerate when the ion is isolated. When a d^8 ion is complexed with ligands, it tends to display a square planar geometry.[17] The reason behind the great stability of d^8 square planar complexes relies on the molecular orbitals occupancy.

In the energetic diagrams reported below, the orbital splitting of the d-metal orbitals in a square planar field (**Figure 9, A**) and the molecular orbitals of a square planar complex bearing generic ligands (**Figure 9, B**) are represented.

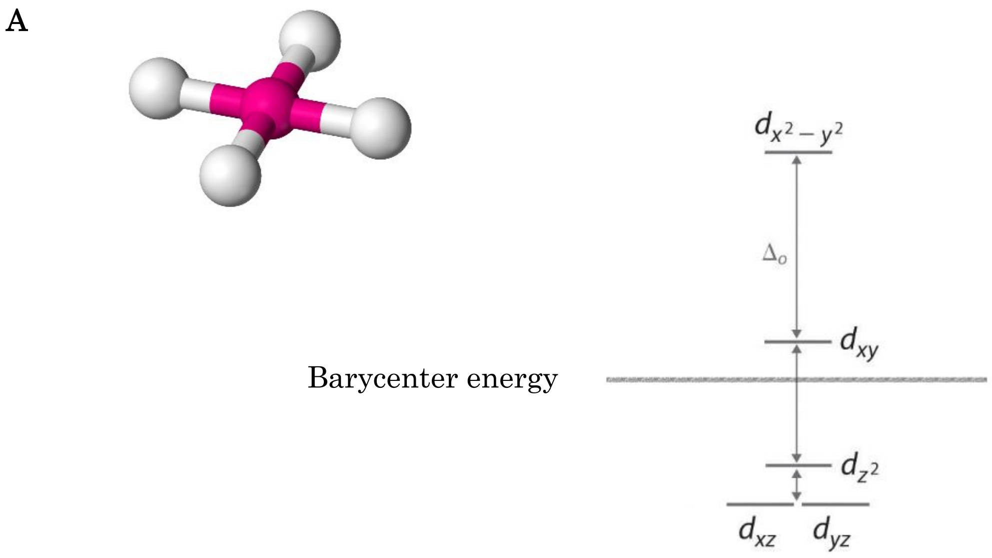

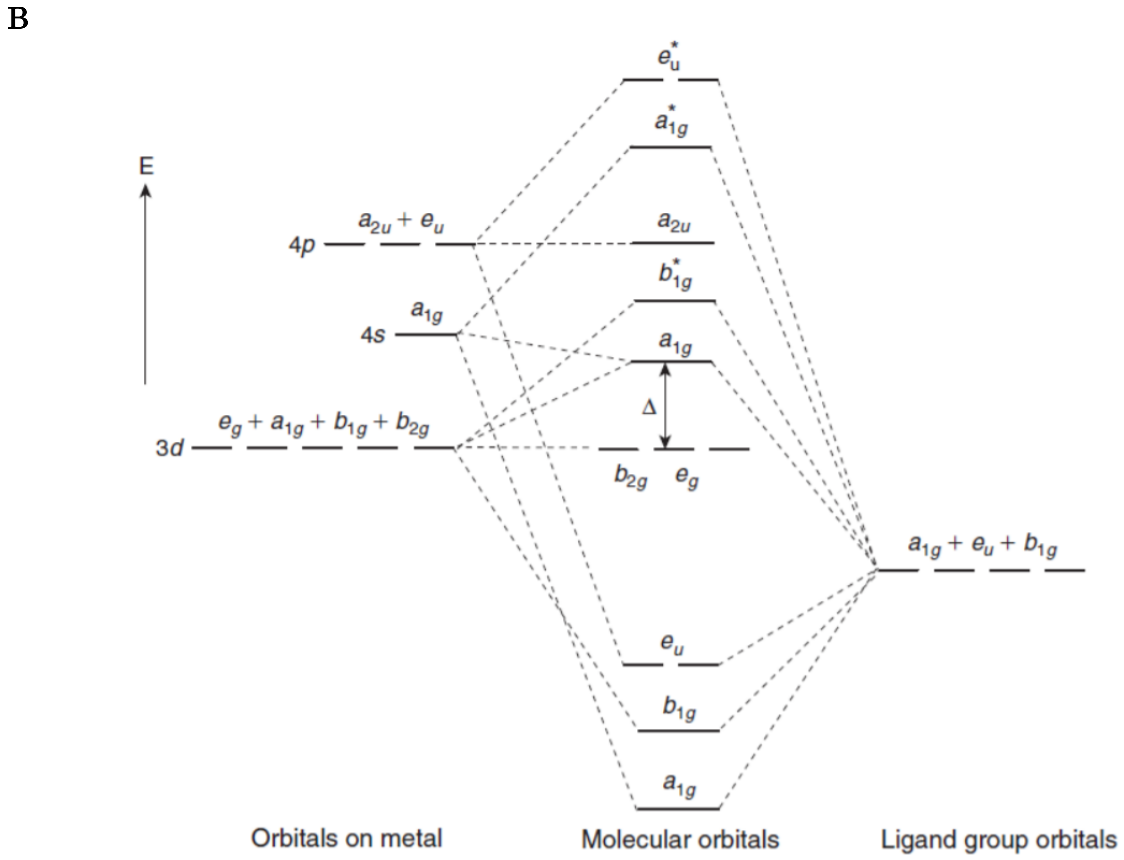

Figure 9. (A) Schematic representation of the d-metal orbitals' splitting in a square planar field. (B) Detailed scheme of the 3d orbitals splitting arising from the complexation with generic ligands.

The eight electrons given by the metal are placed in the molecular orbitals where the main contribution derives from the four metal atomic orbitals d_{xz}, d_{yz}, d_{xy} and d_{z^2}. These four molecular orbitals are characterized by slightly bonding, non-bonding and antibonding features. If the complex had more than eight electrons, they would occupy the higher energy anti-bonding molecular orbital resulting from the overlapping of the metal $d_{x^2-y^2}$ atomic orbital with the σ-donor orbitals of the ligands. Since the three-dimensional orientation of $d_{x^2-y^2}$ in space is such that it lies on the x and y axes, its lobes point directly towards the ligands and so the anti-bonding character is strong. As a consequence, the occupancy of this molecular orbital would provoke the destabilization of the complex.

Given these premises, the promotion of an electron to higher energy molecular orbitals through irradiation leads to the occupation of the anti-bonding level. When the electronic density increases within a region with one or more nodes, it affects the strength of chemical bonds. In particular, molecular bonds become weaker, and the overall structure undergoes distortion. The geometry of the excited molecule defines the inclination of the complex to relax through a radiative decay. Representing the potential curve energy diagram, two main cases can be outlined considering the distortion of the excited state (**Figure 10**).[18]

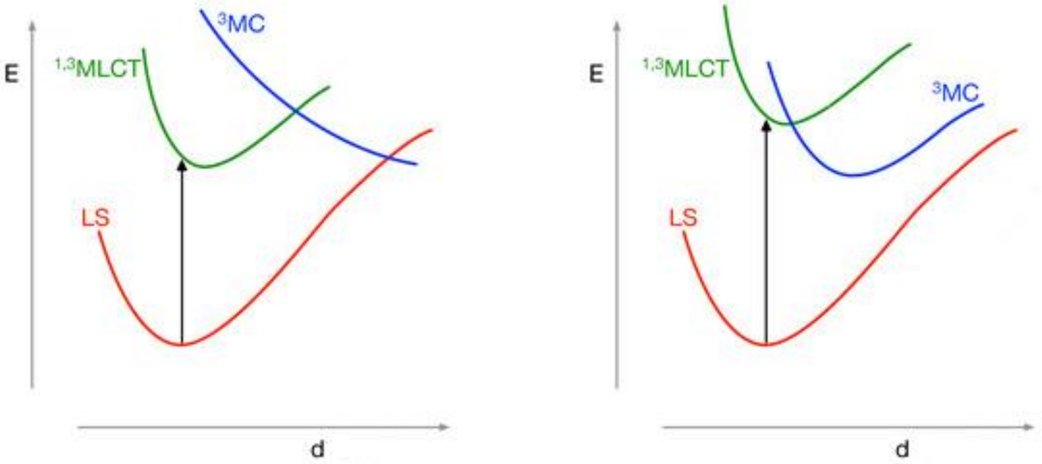

Figure 10. Representation of the potential energy curves diagram given by highly distorted excited states (left) and in case of slightly distorted excited states (right).

Case I. If the excited state is highly distorted, its potential energy curve can cross the potential energy curve of the fundamental state (**Figure 10, left**). This configuration suggests that a non-radiative decay will occur, since the vibrational levels of the two electronic states involved are superimposed. Thus, the molecule would spontaneously move from a vibrational level to the following via internal conversion and then through vibrational relaxation until the complete relaxation is achieved.

Case II. If the excited state is slightly distorted, its potential curve doesn't intersect the potential curve of the ground state (**Figure 10, right**). In this case, the only way for the molecule to release the exceeding energy is through radiative decay.

With the objective to design Pt(II) complexes with optimal photoluminescent properties, it's essential to avoid the heavy distortion of the structure and thus to obtain a system that falls under the case II. In this context, the square planar geometry typical of Pt(II) complexes are highly affected by the nature of the ligands coordinated to the metal ion. Indeed, the two vacant axial coordination sites favor the spatial rearrangement of the coordination sphere in the excited state to relieve the molecular strain, leading to non-radiative deactivation. For instance, the molecular representation of the ground state (S_0) and triplet excited state (T_1) structure of a terdentate cyclometalated Pt(C^N^N)Cl (C^N^N: 6- phenyl-2,2'-bipyridyl) complex, obtained through X-ray characterization and theoretical calculations, was reported by Che and co-worker.[19] **Figure 11** shows the inclination of the planar ground state complex to undergo distortion upon excitation, resulting in poor photoluminescent properties.

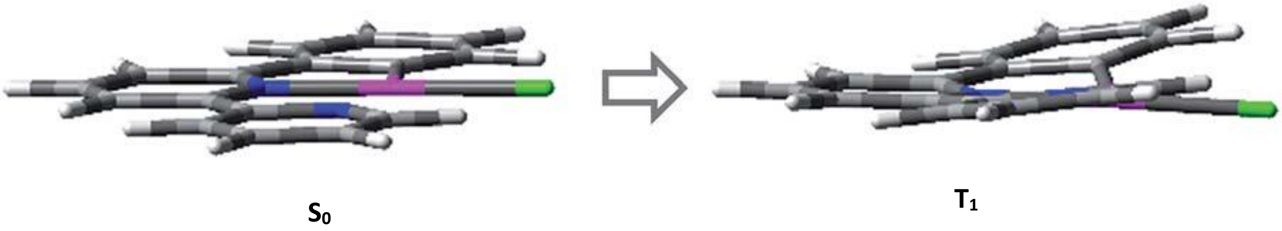

Figure 11. Molecular representation of distortion caused by the excitation process.

Thus, proper rigid strong σ-donor multidentate ligands should be preferred to prevent structural reorganization and non-radiative decay pathways.

Indeed, the photophysical properties rely on the electronic structure of the complex thus, its molecular geometry and the different electronic transitions expected have to be taken into account.

For the purpose, the molecular structure of the complex and the different electronic transitions expected have to be discussed. By way of illustration, the diagram reported below (**Figure 12**) represents the molecular orbitals of an octahedral complex. Basically, four types of electronic transitions can be outlined:

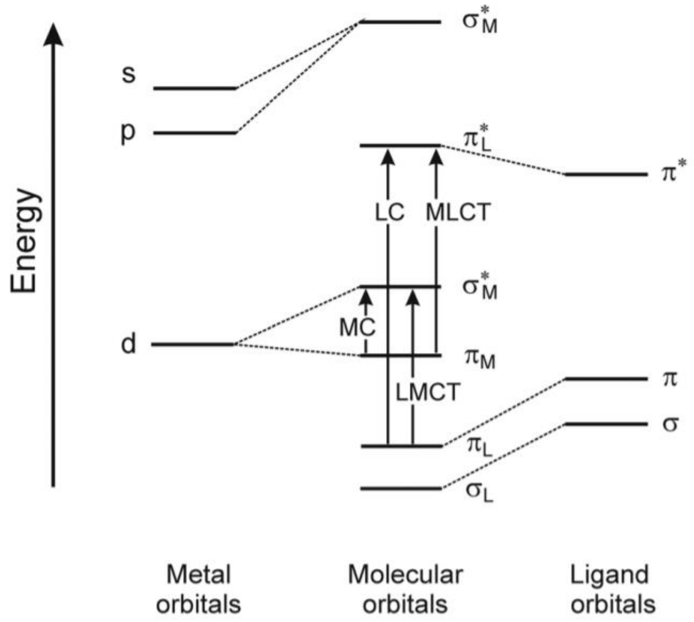

Figure 12. Schematic representation of d-orbitals splitting in an octahedral field.

- Metal-centered transitions (MC) in which a charge transfer between a non-bonding and an anti-bonding d metal orbital occurs;
- Ligand-centered transitions (LC) in which the electron is promoted from a π-bonding to a π-antibonding orbital localized on the ligand;
- Ligand to metal charge transfer (LMCT) and metal to ligand charge transfer (MLCT), characterized by a charge transfer between an orbital centered on the ligand/metal to an orbital localized on the metal/ligand.

The electronic transition observed mainly depends on the ligands constituting the coordination sphere. In this regard, the spectrochemical series lists the strong and weak ligand field ligands. In principle, monodentate ligands should be avoided due to their poor stabilizing effect on the complex. In particular, if monodentate ligands can't create π interactions with the metal, the charge is transferred from π_M to σ^*_M and thus strong distortions are induced on the molecular structure of the excited state. The MC excited state potential curve intersects the ground state paraboloid and a quick non-radiative decay results.[20]

Anyway, a wide variety of monodentate ligands can give rise to π interactions with the metal center:

- π-donor ligands: fall under this category all the ligands that have p orbitals full of electrons (Cl^-, F^-) that can overlap with the t_{2g} orbitals of the metal. In this case the LMCT transition $\pi_L \rightarrow \pi^*_M$ is observed. Even though this doesn't give rise to a conspicuous distortion, there is the possibility that the excited state deriving from the $\pi_L \rightarrow \sigma^*_M$ transition has a similar energy if the ligand is electronegative and the σ interaction is weak. If so, the potential energy curve of the $\pi_L \rightarrow \sigma^*_M$ transition crosses both the $\pi_L \rightarrow \pi^*_M$ and ground state paraboloid, resulting in a thermal release of the exceeding energy. To avoid this case, it's necessary to destabilize the σ_M^* orbital.

- π-acceptor ligands: some ligands possess empty π^* orbitals that are particularly advantageous for the complex stability. Indeed, in this case the metal can donate electrons to the ligand through a MLCT transition, giving rise to a backdonation. The overall effect is synergistic: a π-acceptor ligand can share its electronic density with the metal through a σ orbital, conversely the metal transfers the electrons to the π^* orbitals of the π-acceptor ligand. The charge transfer from the metal center to the ligands relieves the metal from the negative charge excess, which strengthens the bonds in the complex and the energy gap in the ligand field splitting increases. Thus, the σ^*_M orbital has a high energy and is less likely that the potential energy curve deriving from the MC transition crosses the paraboloid of the ground state. The radiative decay is favored.

Given these premises, the π interactions occurring between the metal center and the ligands play a key role in the stabilization of the organometallic complex. For that reason, rigid π-conjugated ligands are desirable since electronic transitions involve π orbitals which don't provoke a heavy distortion of the molecular backbone.

Terdentate cyclometalated complexes provide an example of promising photoluminescent systems: the deprotonated carbon atoms represent strong σ-donor atoms, leading to high stabilization of the complex and to the consequent formation of a short and strong ligand-metal bond.

Multidentate cyclometalated ligands coordinate the metal ion through a thermodynamically favored process, which results in the formation of a chelate ring.[21] Furthermore, the main advantage of cyclometalated ligands resides in the possibility to tune the wavelength of emission through two strategies:

- Introduction of a proper electron-withdrawing or electron-donating functional group on the cyclometalated ligand. This leads to alteration of the energy gap between the molecular orbitals involved in the electronic transition. Consequently, the position of the paraboloids representing the excited states changes, affecting the efficiency of the radiative decay.

- Introduction of specific ancillary ligands that completes the coordination sphere of the metal transition ion. The ancillary ligand affects the electronic density distribution and the complex molecular orbitals distribution. For instance, the cyanide (CN^-)[22] ion represents an optimal ancillary ligand since it's π-acceptor and contributes to strongly stabilize the complex.

Another aspect that has to be taken into account with respect to the photophysical properties of the Pt(II) complexes, is the inclination of square planar geometry complexes to favor the interaction between Pt ions. The d_{z^2} atomic orbitals are oriented in a way that the toroid lies on the molecular plane (*xy*), whilst the two lobes lie on the z axis. The Pt-Pt interaction occurring within neighboring Pt complexes is responsible for the resulting overlap of the d_{z^2} orbitals, leading to the formation of new molecular orbitals. As a consequence, the photophysical properties are affected by the occurring intermolecular interactions. The representation of the molecular orbital diagram arising from the stacking interaction is represented in **Figure 13**.

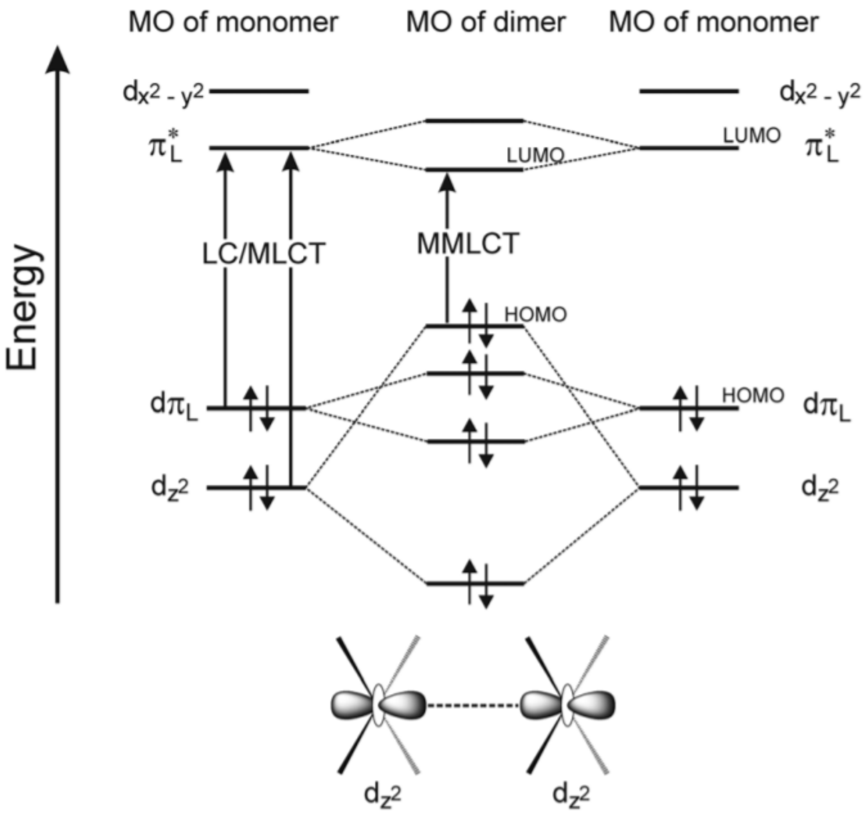

Figure 13. Molecular orbital diagram arising from d_{z^2} overlapping in stacked complexes.

The metal-metal bond length is highly variable and depends on electrostatic and steric factors.[23] In particular, the nature of the ligands in the coordination sphere plays a central role in the stacking process: π-acceptor ligands displace electronic density from the metal center, thus reducing the electrostatic repulsion occurring between metal ions. Overall, the Pt-Pt bond becomes stronger and thus shorter. On the other hand, π-donor ligands such as chloride cause an increase in the electronic density on the metal center, giving rise to higher electronic repulsion and longer Pt-Pt distance.

2.1.1 Cyclometalated Pt(II) complexes based on the 1,3-di(2-pyridyl)benzene moiety

Phosphorescent Pt(II) complexes raised increasing interest over the years due to their promising photoluminescent properties, exploitable in many fields of application.[20, 24, 25] Third row transition metal ions provide suitable metal centers for the design of highly photoluminescent complexes, due to the strong spin-orbit coupling interaction induced. In order to favor a bright emission, strong-field ligands have to be selected. 1,3-di(2-pyridyl)benzene represents a convenient terdentate cyclometalated neutral ligand to achieve an efficient radiative decay of the excited state. The first 1,3-di(2-pyridyl)benzene Pt(II) complex was synthesized in 1999 by Càrdenas *et al.*.[26] The research of Càrdenas *et al.* investigated the activation of the C-H bond of the ligand in the reaction with Pd(II) and Pt(II). The results highlighted the formation of different species: whilst Pd(II) tends to create multinuclear complexes, Pt(II) leads to the activation of the C-H bond and the cycloplatination at C-2 of the benzene ring occurs. **Figure 14** represents the products of the reaction.

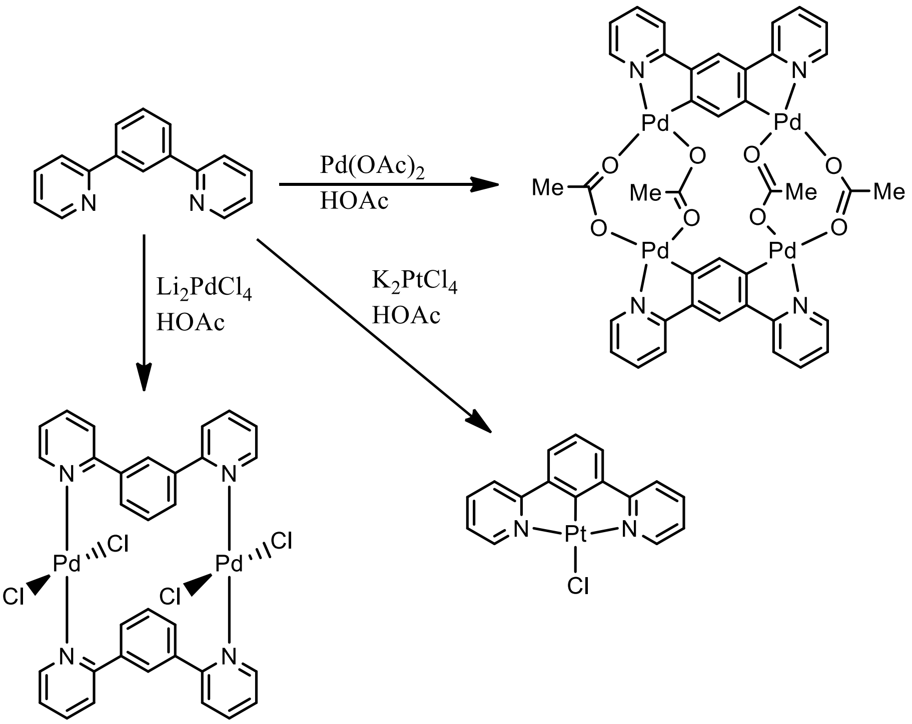

Figure 14. Representation of Pd(II) and Pt(II) complexes investigated by Càrdenas *et al.*.

In the following years, the photophysical properties of the Pt(II) complex built with the terdentate 1,3-di(2-pyridyl)benzene have been investigated.[27] In this context, high resolution spectroscopy at cryogenic temperatures was performed, in order to narrow the bands width and to provide more clear spectra.

Practically, a low concentration solution of the complex in *n*-octane was prepared and cooled down to liquid helium temperature. The nature of the emissive state was thus characterized: it can be mainly described as a ligand centered (^{3}LC) excited state mixed with a component of metal-to-ligand charge transfer. The high ligand field of the 1,3-di(2-pyridyl)benzene ligand raises the energy of the d-d state discouraging the non-radiative decay. Furthermore, the rigidity of the cyclometalated ligand prevents a strong distortion of the molecular backbone during the excitation and thus contributes to favor phosphorescence.

The photophysical analysis performed in degassed dichloromethane solution at room temperature (298 K) evidenced the potential of the 1,3-di(2-pyridyl)benzene Pt(II) complex as a promising emitter, displaying a quantum yield of Φ_{PL} = 0,60 associated to a life time of the excited state of τ = 7,2 µs.[27] As a consequence, many other Pt(II) complexes bearing a modified 1,3-di(2-pyridyl)benzene ligand were synthesized and analyzed. The main effect of the introduction of various substituents on the 5-position of the ligand resides in the perturbation of the energy levels. For instance, the introduction of an electron-donating methyl group on the benzene ring increases the HOMO energy, resulting in a red shifted emission. On the other hand, an electron-withdrawing ester group leads to a decrease in the HOMO energy.[25]

The tuning of the photophysical properties of the complex and the maximization of the radiative decay can be accomplished selecting the proper ancillary ligand. The Pt(II) complexes described so far were synthesized using the anionic π-donor Cl^- ligand to complete the coordination sphere. π-acceptor ligands are more desirable, since they contribute to strengthen the σ interactions in the complex through backdonation of electron density from the metal center to the ligand. Various Pt(II) complexes bearing derivatives of 1,3-di(2-pyridyl)benzene as ligands have already been modified substituting the Cl^-. For instance, phenylacetylene[28] and NCS^- [29] were introduced in the coordination sphere.

2.2 Photoluminescent cationic cyclometalated Ir(III) complexes: an overview

In addition to Pt, another transition metal belonging to the same group in the periodic table that finds application in a broad variety of fields is Ir. Over the years, Ir(III), which displays a d^6 electronic configuration, was widely investigated due to its potential use in the design of highly luminescent emitters.[30] In particular, cationic bis-cyclometalated Ir(III) complexes represent the archetype, due to their outstanding photophysical properties and excellent capability to be finely tuned through minor modifications of the molecular structure.

In this context, the first-ever bis-cyclometalated cationic Ir(III) emitter synthesized was $[Ir(ppy)_2bpy]^+$,[31] an octahedral complex made of two cyclometalated 2-phenylpyridine and a 2,2'-bipyridine in the coordination sphere **Figure 15**.

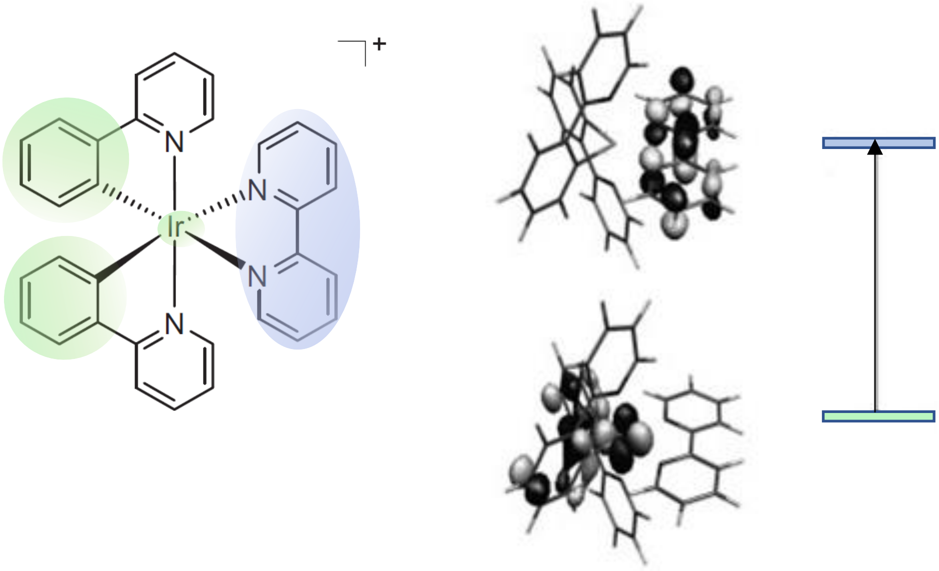

Figure 15. Schematic representation of the frontier orbitals and of the electronic density of $[Ir(ppy)_2(bpy)]^+$.

Cyclometalated ligands serve as promising chelating agents, given their strong σ-donating nature and the consequent ability to favor a d^6 low spin configuration, which confers high stability to the complex, thus decreasing the cytotoxicity induced by the heavy metal ion. The complexation through the aryl ring provides to increase the energy of the orbitals localized on the metal ion, giving a larger contribution to the excited state and favoring the intersystem crossing.

Furthermore, the HOMO and the LUMO are positioned on distinct parts of the complex: whilst the HOMO is centered on the Ir(III) ion and on the aryl rings (**Figure 15, green**), the LUMO is localized on the pyridines (**Figure 15, blue**).[32]

Hence, the electronic structure of the molecule can be finely tuned through conscientious introduction of specific atoms or functional groups on the backbone. This represents a great advantage, making it possible to optimize the photophysical properties, ranging from the UV-visible to the NIR. The insertion of an electron-donating or electron-withdrawing group on the ligands represents a strategy for the purpose. Precisely, the modification of the bipyridine moiety with an electron-donating function leads to the destabilization of the LUMO, giving rise to an increase of the energy gap between the orbitals involved in the transition and thus, to a blue shift.[33]

In addition, a variety of alternative cyclometalated and N^N ligands can be selected besides bipyridine, even choosing chelating molecules containing a different heterocycle in the place of the pyridine rings.[34] Another possibility is provided by the enhancement of the N^N ligand conjugation.[35]

Güdel et al.[36] characterized $[Ir(ppy)_2(bpy)]PF_6$ (**Figure 16**), investigating its photophysical properties at room temperature in dichloromethane.

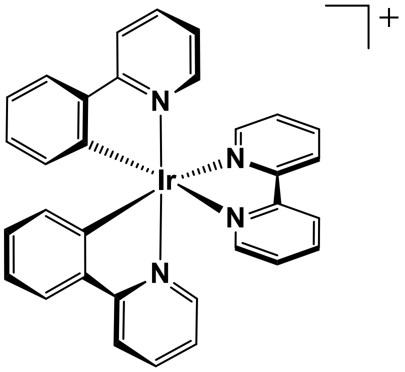

Figure 16. Molecular structure of $[Ir(ppy)_2(bpy)]^+$.

Photoluminescence analysis were performed in a solution of dichloromethane at room temperature, exciting at λ = 458 nm. The emission spectrum evidenced the presence of a broad band centered at 585 nm. Given the shape of the structureless band, it was attributed to a ^{3}MLCT transition, in which the Ir center displaces electronic density towards the cyclometalated 2-phenylpyridine ligands (Ir $\longrightarrow$ ppy), displaying a quantum yield equal to Φ_{PL}: 0.14.[37]

Further investigations carried out in a crystalline media ($[Ir(ppy)_2bpy]PF_6$ doped into $Rh(ppy)_2bpy]PF_6$) at 10 K,[36] highlighted the change in the nature of the transition at low temperature. Indeed, the photophysical phenomenon responsible for the principal emission is given by a ligand centered transition (^{3}LC). Thus, in a crystalline host, the electronic levels are reversed, and the typology of the observed transitions is affected by the environment surrounding the emitter, making this class of complexes very appealing under a photophysical point of view.

Given the collected photophysical data and electronic structure of the complex, it is possible to associate the triplet emitting state to a metal to ligand charge transfer (^{3}MLCT) mixed with a ligand-to-ligand charge transfer (^{3}LLCT) state.

Subsequently, a study concerning a family of Ir(III) complexes obtained replacing the 2,2'-bipyridine ligand with an imidazolyl-phenanthroline ligand was reported by Mandal *et al.,*[38] highlighting their great potential as photosensitizes for photodynamic therapy and as biological probes for cellular imaging. The details of the assays performed are described in paragraph 2.2.1.

2.2.1 Photoluminescent cationic cyclometalated Ir(III) complexes: finely tuning the photophysical properties

Bis-cyclometalated heteroleptic Ir(III) complexes represent a promising class of emitters, due to their optimal stability, excellent photophysical properties and versatility, making them highly appealing for the application as photoactive species.

A valid strategy to design robust and bright emitters involves the coordination of the metal ion with π-conjugated ligands. In this context, a wide variety of options were already investigated and reported in literature.[38, 39]

Y. You *et al.*[40] characterized a series of Ir(III) complexes made of a 1,10-phenanthroline as the N^N ligand, and a range of cyclometalated N^C pincers assessing the effect of the substitution on the photophysical properties of the system. The molecular structure of the investigated Ir(III) complexes is provided in **Figure 17**.

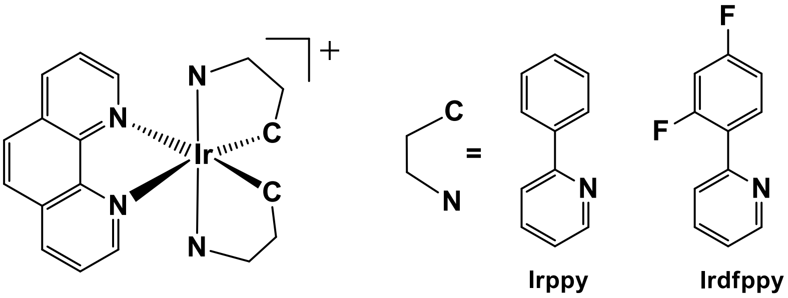

Figure 17. Molecular representation of the 1,10-phenanthroline-based Ir(III) complexes.

The complexes were characterized in degassed acetonitrile solutions at room temperature, exciting at the MLCT transition wavelength.

The most basic structure of the series is displayed by Irppy, which was built replacing the 2,2'-bipyridine encountered in the archetype complex in paragraph 2.2 with 1,10-phenanthroline. The precise comparison of the wavelengths of emission is prevented due to the different solvents in which the photophysical analysis were performed. Nevertheless, upon excitation at λ = 409 nm, the introduction of the π-conjugated N^N ligand results in a strong emission at λ = 584 nm. Most remarkably, the quantum yield (Φ_{PL}: 0.49) was reported to be significantly increased with respect to the analogous complex bearing the 2,2'-bipyridine fragment.[41]

On the other hand, the insertion of two fluorine atoms on the aryl ring of the 2-phenylpyridine moiety, as represented in Irdfppy (**Figure 17**), provoked a shift towards the blue, underlining an increase of the HOMO-LUMO energy gap. The photoexcitation at λ = 388 nm gave rise to the emission at λ = 518 nm.

Overall, the investigated photoluminescent properties of $[Ir(C^\wedge N)_2phen]^+$ complexes are governed by the low energy MLCT transition, underlining the central role played by the electron density associated to the N^C ligands. Specifically, the introduction of electron withdrawing atoms, such as fluorine atoms, leads to HOMO stabilization, consequently resulting in a blue-shift.

Conversely, LUMO stabilization through enhancement of the N^N ligand π-conjugation, provokes an overall red-shift of the emission.[42]

Hence, the analysis performed on Irppy and Irdfppy highlight how much a minor modification introduced on the complex backbone affects the photoactivation process, providing a powerful mean to suitably tune the phosphorescence phenomenon.

The design of a more complex, π-conjugated imidazolyl-modified phenanthroline ligand[38] provides a promising strategy not only to enhance the photoluminescent properties of the emitter, but also to create a more sophisticated backbone for further functionalization. In this context, S. Mandal *et al.*[38] reported the synthesis of a family of imidazolyl modified phenanthroline based Ir(III) complexes. In particular, the photophysical analysis performed dissolving IrImppy (**Figure 18**) in dichloromethane, revealed that the introduction of an elaborated N^N scaffold has an impact on the quantum yield, leading to a significant increase to ϕ: 0.41 with respect to the phenanthroline based complex Irppy, whilst the wavelength of emission is not affected (λ = 575 nm).

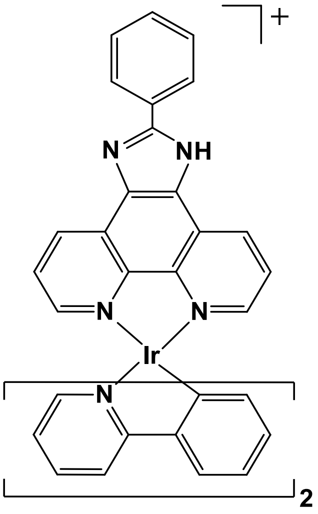

IrImppy

Figure 18. Molecular structure of IrImppy.

The discussion concerning the class of phenanthroline based Ir(III) complexes developed by Mandal *et al.* is thoroughly reported in paragraph 3.3.2.1.2.

Given the promising results highlighted in literature, a series of cationic imidazolyl-modified phenanthroline based Ir(III) complexes bearing a variety of N^C ligands were designed, synthesized and characterized, aiming to provide an insight concerning the role played by the structure on the electronic arrangement, thus outlining the main features for the development of efficient Ir(III) based emitters. The molecular structure of the designed imidazolyl-modified Ir(III) emitters is given in **Figure 19**.

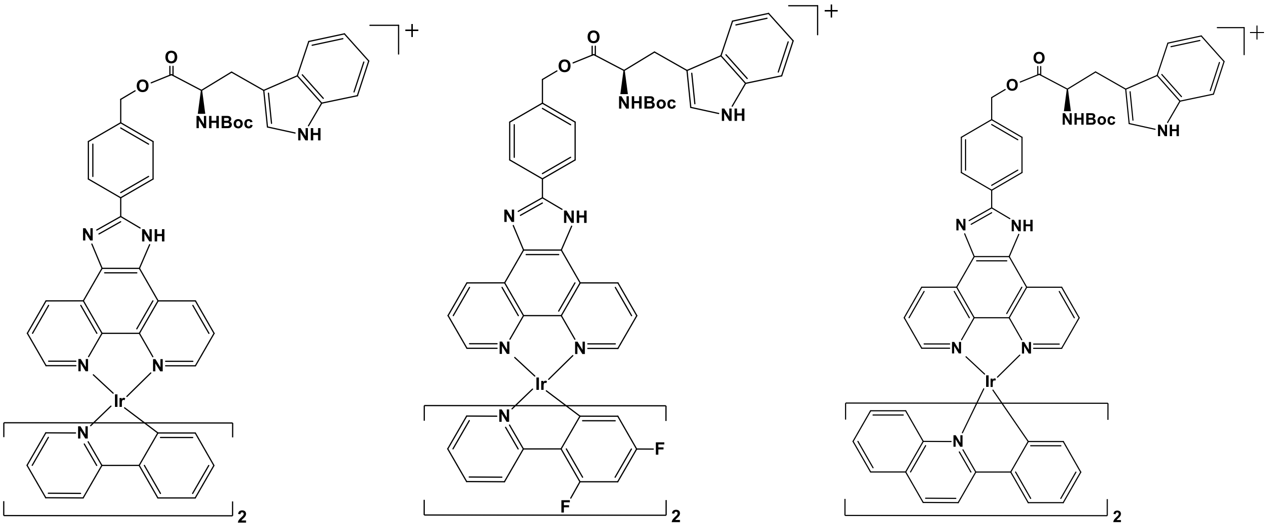

Ir-1 **Ir-2** **Ir-3**

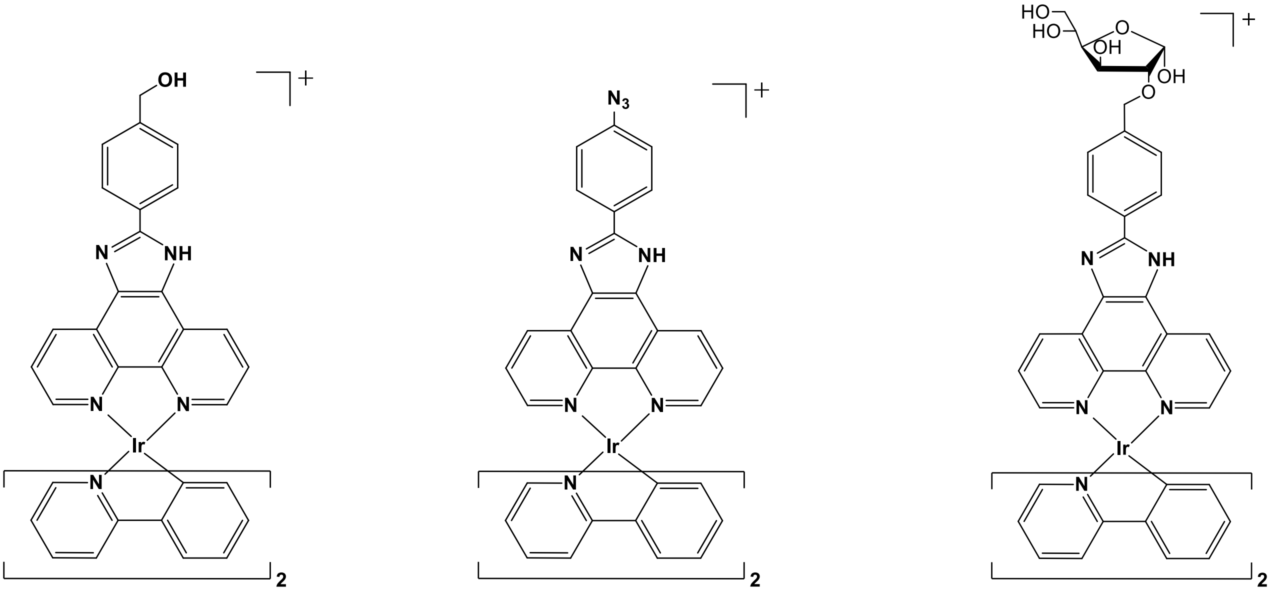

Ir-4

Ir-5

Ir-6

Figure 19. Molecular structure of the developed phenanthroline-based Ir(III) emitters.

3. Photoluminescent cyclometalated complexes for biomedical applications

3.1 Organometallic photoluminescent complexes as bioimaging probes: an introduction

The optimal photoluminescent properties displayed by metal complexes gained increasing attention over the years for a wide range of applications, in particular as bioimaging probes.[24, 43]

The possibility to exploit the radiative deactivation of an excited molecule to obtain high resolution images of living cells, biological tissues and cellular substructures raised much interest. The combination of visible light fluorescence with simple optical microscopies, enables a spatial resolution of 1 µm, that can be further enhanced using confocal microscopy.[44] The high sensitivity achieved with modern revelators makes it possible to detect the emission of a single molecule.

The design of heavy metal organometallic complexes as bioimaging probes provides a promising strategy for the purpose. Indeed, the population of the more easily accessible triplet excited state though intersystem crossing gives rise to a long radiative decay, namely phosphorescence. A long lifetime of the excited state represents a major advantage in bioimaging, since it allows to remove the background contribution of the fluorescent chromophores inserted in the biological tissues.[45] The use of a pulsed source offers the possibility to detect the emission signal from the probe with a delay of few nanoseconds with respect to the excitation pulse. In the range of nanoseconds, the quick fluorescence decay deriving from the biological molecules in the surrounding tissues is over, or so weak to be negligible, and thus the acquisition can be performed detecting the phosphorescent probe only. In this manner the quality of the obtained image is significantly improved. A schematic representation of the time-resolved acquisition is given in **Figure 20**.[32]

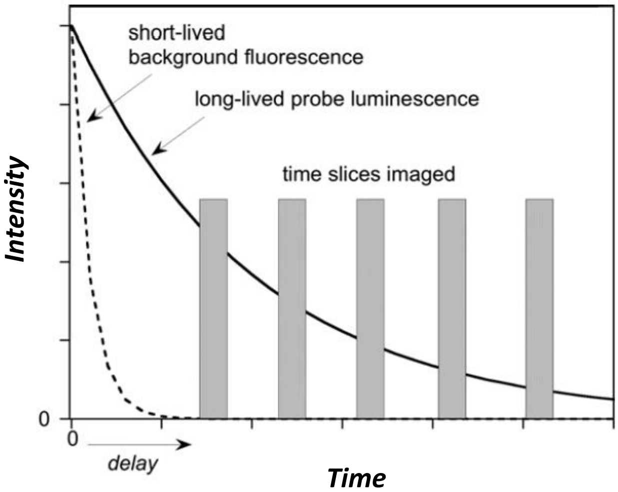

Figure 20. Simplified scheme representing the concept of time-resolved acquisition, with background fluorescence removal.

Phosphorescent decay represents an advantageous radiative phenomenon in terms of self-absorption. Indeed, the excitation of a fluorescent probe could lead to a radiative decay characterized by a wavelength of emission close to the wavelength of absorption due to the stabilization of the excited state exerted by the reorganization of the surrounding solvent molecules. The slight difference between the excitation and emission wavelength leads to a little Stokes shift. Thus, when the absorption and the emission spectra of the fluorophore are almost superimposable, the photons released by the probe could be absorbed back by the probe itself. To prevent self-absorption, phosphorescent organometallic complexes should be exploited, since intersystem crossing ensures a large Stokes shift. In this context, upon excitation, the metal complex releases part of the exceeding energy through non-radiative pathways as it passes from the singlet excited state to the triplet excited state. Also, vibrational relaxation contributes to the non-radiative energy loss.

The quantity of energy released before the phosphorescent deactivation, gives rise to a large difference between the wavelength of excitation and the wavelength of emission, making the self-absorption highly unlikely.

However, the use of organometallic complexes for bioimaging has to take into account the possible occurrence of unwanted side processes, such as the phosphoresce quenching. Indeed, the excited state energy could be transferred to a close triplet oxygen molecule in the biological tissues, giving rise to the activation of the reactive singlet oxygen species which results in cytotoxicity. The singlet oxygen generation through photoactivation forms the basis of photodynamic therapy, discussed in paragraph 3.3. Nevertheless, the phosphorescence quenching by triplet oxygen is not so relevant due to the oxygen molecules diffusion rate and because the collision with the metal complex isn’t that likely, especially when the organometallic probe is bound to a highly sterically hindered biomolecule.

Photoluminescent organometallic complexes have to display certain features in order to provide optimal bioimaging probes:

- The complexes have to be water soluble;
- The probes have to permeate cell membranes easily;
- The cytotoxicity has to be negligible;
- The molar extinction coefficients have to be high to ensure an efficient visible light absorption process.
- The near-infrared light to which biological tissues are transparent should be exploited for the excitation process. In this context, organometallic complexes with a large cross section for two photon absorption should be designed.
- The radiative decay has to display a high quantum yield;
- Have a good stability in the media and upon irradiation, in order to prevent photobleaching.

- The binding of the probe to a cellular structure doesn't have to cause any alteration within its photophysical properties.

The organometallic complexes made up of 2nd and 3rd transition metal centers are considered promising, due to the efficient phosphorescent decay and the possibility to tune the photophysical properties by selecting the proper coordination sphere. In this context, cyclometalated Pt(II) and Ir(III) complexes have been widely investigated.[18,46]

Cyclometalated ligands for the complexation of both Pt(II) and Ir(III) have been studied: the benzene ring provides a strong σ-donor, which contributes to highly destabilize the metal centered excited state thus favoring the intersystem crossing and the radiative deactivation. Furthermore, cyclometalated ligands shield the metal charge giving rise to a complex with a lower net charge with respect to non-cyclometalated complexes. This represents a major advantage in the biological environment, since low charged species are more likely to spontaneously cross the lipophilic cell membrane *via* passive diffusion.[32]

2-phenylpyridine was investigated for the coordination of Ir(III), whilst either bidentate and tridentate cyclometalated ligands have been designed for the complexation of Pt(II) metal centers for their photophysical characterization. Pt(II) ions display a square planar geometry upon coordination, in contrast to the distorted octahedral coordination favored by d^6 Ir(III) ions. To stabilize the square planar geometry, 1,3-di(2-pyridyl)benzene and its derivatives were investigated. Indeed, the electronic structure of Pt(II) complexes suggests the importance to select rigid strong field splitting ligands, in order to raise the energy of the metal centered excited state which is highly distorted and gives rise to thermal deactivation.[32]

The molecular representation of the most significant Ir(III) and Pt(II) complexes designed and characterized are reported in **Figure 21.**

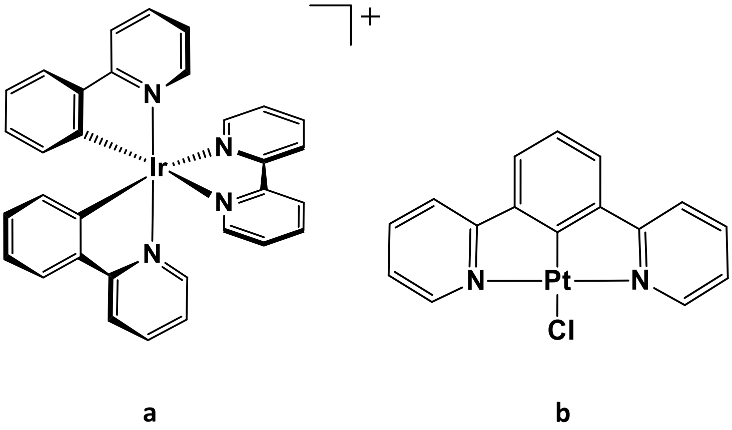

Figure 21. Molecular structure of $[Ir(ppy)_2(bpy)]^+$ (a) and of the Pt(II) complex built with the 1,3-di(2-pyridyl)benzene pincer (b).

A major advantage in the use of cyclometalated ligands is the possibility to finely tune the efficiency of the radiative decay and the photophysical properties of the complex by proper functionalization of the ligand.

Indeed, investigations conducted over complex **b** reported in **Figure 21** revealed the details concerning the electronic structure of the emitter and the localization of the frontier molecular orbitals. Specifically, it was assessed that the major contribution to the HOMO is given by the aryl rings of the cyclometalated ligands, whilst pyridine rings are responsible for the modifications induced within the LUMO.

Thus, the introduction of either electron-withdrawing groups in the central benzene ring or electron-donating groups in the pyridine rings results in a blue shift, whereas reversing the nature of the introduced groups leads to red shift. Hence, cyclometalated ligands allows to adjust the HOMO and the LUMO energy separately.

Furthermore, the modification can be performed with the purpose to bind a specific vector fragment to the complex backbone. The introduction of a proper functional group favors the interaction with a selective targeted intracellular structure thus allowing to selectively localize the probe in a specific region of the cell. In this context, the conjugation with biomolecules provides an effective approach.

Additionally, bioimaging requires a little amount of emitter to obtain a successful image. Thus, even though Pt and Ir are relatively rare in nature and thus expensive, the costs concerning the purchase of the metal ion results overall compensated.[32]

3.1.1 Pt(II) cyclometalated bioimaging probes: state of the art

N^C^N cyclometalated Pt(II) complexes represent a class of bright emitters, suitable for many applications.[20, 27, 47]

Càrdenas *et al.*[26] reported the synthesis of the first terdentate cyclometalated Pt(II) complex, bearing the strong filed splitting 1,3-di(2-pyridyl)benzene in the coordination sphere. The molecular representation of the investigated complex is given in **Figure 22**.

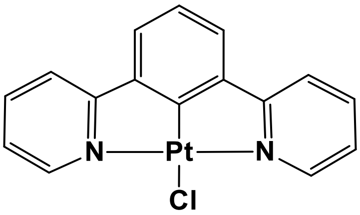

Pt(dpyb)Cl

Figure 22. Molecular structure of Pt(dpyb)Cl.

The photophysical characterization, reported by Williams *et al.*[48] highlighted its optimal properties as emitter in a deoxygenated dichloromethane solution at room temperature. The overall photoluminescent phenomenon revealed to be very efficient, displaying emission in the visible range λ_{max} = 491 nm with a long lifetime of the excited state τ = 7.2 µs and a quantum yield of Φ = 0.60. The nature of the observed band arising from the radiative decay has been attributed to a combination of the intraligand ($^3\pi$-π^*) excited state and a component of MLCT state.

The first bioimaging assays reported with regard to Pt(dpyb)Cl were carried out by Botchway *et al.*.[24] *In vitro* studies were performed inserting the Pt(dpyb)Cl in the cell cultures in a variable concentration between the range of 1-100 µM, incubating for a time span within 5 min and 24h. The complex displayed poor cytotoxicity in the cells, in contrast to the data obtained in the organic solvents where a slight singlet oxygen generation activity was observed. This partial phosphorescence quenching suggested that in the biological media the Pt(II) complex interacts with hydrophobic regions of biomolecules that protect the probe, preventing the contact with triplet oxygen molecules.

The high stability of the complex upon prolonged irradiation with either UV light, λ = 390 nm, and near infrared light, λ = 780 nm, in the cells media was also assessed.

Over the years, a wide variety of Pt(II) complexes bearing the 1,3-di(2-pyridyl)benzene moiety functionalized with both electron-withdrawing and electron-donating groups were synthesized and characterized.[32] The molecular representation of the investigated complexes' series is reported in **Figure 23**.

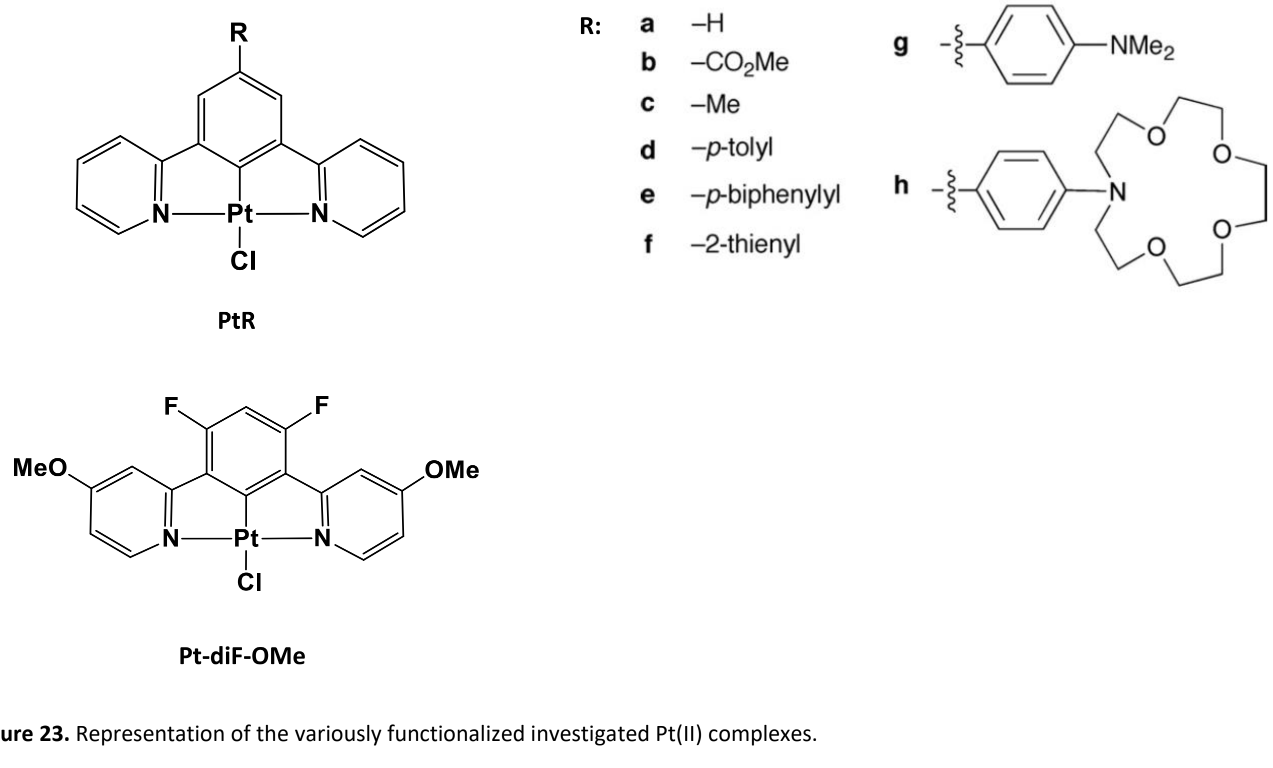

Figure 23. Representation of the variously functionalized investigated Pt(II) complexes.

Pt(dpyb)Cl (**Figure 22**) showed a tendency to quickly accumulate in the cells: the limited dimension of the complex and the neutral charge provided by the cyclometalated ligand together with the chlorine anion, favor the spontaneous cell membrane crossing. Furthermore, the selective localization in the nucleoli was observed.

The efficiency displayed by Pt(dpyb)Cl as a bioimaging probe is due to the protecting activity against triplet oxygen supplied by the interaction with the hydrophobic regions among nucleic acids. This hypothesis is further supported by the 1,3-di(2-pyridyl)benzene similarity to the terpyridine moiety which is an acknowledged DNA intercalator.

The introduction of functional groups on the para position of the central aryl ring allowed a fine tuning of the wavelength of emission towards red or blue, depending on the nature of the substituent, and a variation of the life-time of the excited state as well as of the quantum yield. The photophysical properties of the investigated Pt(II) emitters were assessed in dichloromethane solution at room temperature.

In this context, the most promising quantum yield was provided by complex Pt-diF-OMe[49] whilst the longest emitting excited state was observed for PtR-f (τ = 20.5 μs).[50]

The detailed photophysical data collected has been reported in **Table 1**.

Table 1. Photophysical data collected analyzing PtR-a to PtR-h and Pt-diF-OMe in degassed dichloromethane solution at room temperature.

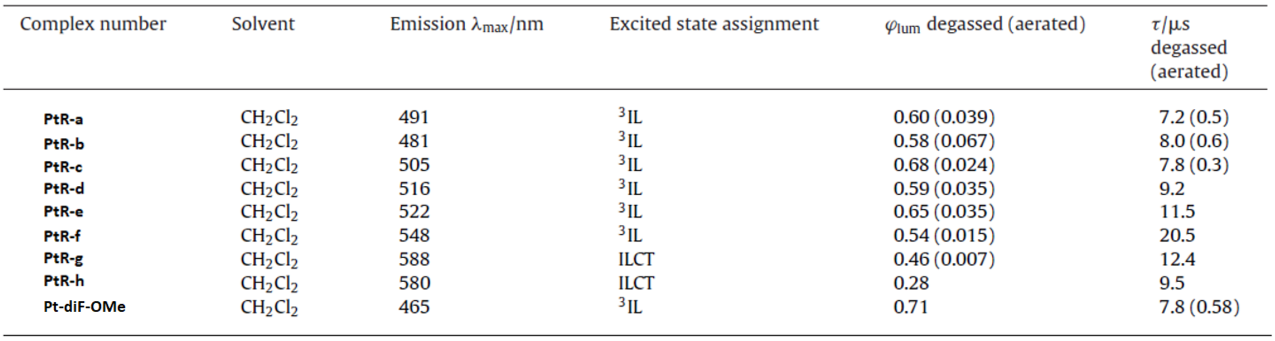

Complex number	Solvent	Emission λ_{max}/nm	Excited state assignment	φ_{lum} degassed (aerated)	τ/μs degassed (aerated)
PtR-a	CH_2Cl_2	491	^{3}IL	0.60 (0.039)	7.2 (0.5)
PtR-b	CH_2Cl_2	481	^{3}IL	0.58 (0.067)	8.0 (0.6)
PtR-c	CH_2Cl_2	505	^{3}IL	0.68 (0.024)	7.8 (0.3)
PtR-d	CH_2Cl_2	516	^{3}IL	0.59 (0.035)	9.2
PtR-e	CH_2Cl_2	522	^{3}IL	0.65 (0.035)	11.5
PtR-f	CH_2Cl_2	548	^{3}IL	0.54 (0.015)	20.5
PtR-g	CH_2Cl_2	588	ILCT	0.46 (0.007)	12.4
PtR-h	CH_2Cl_2	580	ILCT	0.28	9.5
Pt-diF-OMe	CH_2Cl_2	465	^{3}IL	0.71	7.8 (0.58)

The study concerning the modulation of the photophysical properties through the introduction of substituents at the central position of the benzene ring, confirmed the aformentioned effects. In particular, taking as the reference Pt(dpyb)Cl (black line, **Figure 24**), a shift towards longer wavelenghts was assessed as a consequence of the role played by electron-donating aryl or alkyl substituents (PtR-c to PtR-f). Conversely, PtR-b (light blue line, **Figure 24**) results in a blue shift, owed to the electron-withdrawing ester group. The maximum blue shift was obtained with Pt-diF-OMe through functionalization of the 4-position of the pyridyl rings with electron donating groups together with the insertion of two fluorine atoms on the central aryl ring.

The synergistic effect overall results in a blue shifted emission λ_{max} = 465 nm. The emission spectra progression achieved with the modification of the substituents inserted on the cyclometalated moiety is depicted in **Figure 24**.[32]

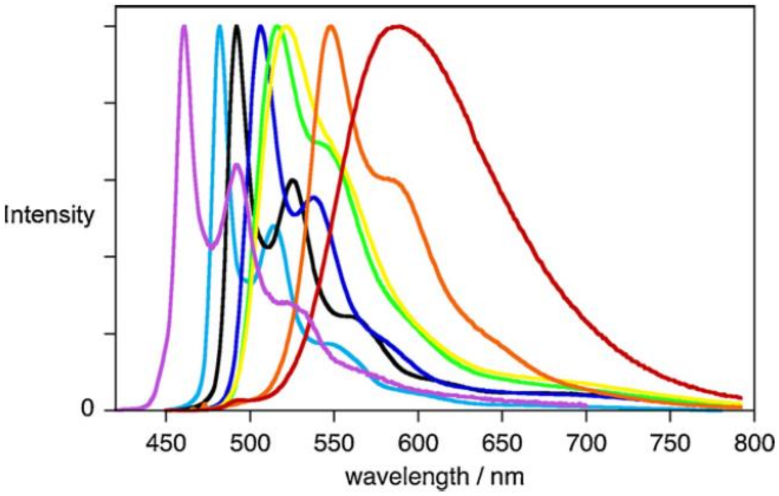

Figure 24. Emission spectra obtained through introduction of various functional groups on the N^C^N pincer. Specifically, the wavelength of emission can be red-shifted with respect to the basic PtR-a complex (black line) with electron-donating groups on the central benzene ring of the ligand (PtR-c to PtR-f). Conversely, a blue-shift arises introducing an electron-withdrawing ester group (PtR-b, blue line). The maximum blue-shift can be induced through modification of the para-position of the pyridine rings (Pt-diF-OMe, purple line).

Given these premises, a series of cyclometalated Pt(II) based emitters bearing the 1,3-di(2-pyridyl)benzene moiety functionalized with highly hindered substituents were designed, synthesized and characterized. To my knowledge, no Pt(II) complexes modified with bulky aromatic substituents on the 4-position of the pyridyl rings haven't been investigated as bioimaging probes yet.

The molecular representation of the developed luminophores is given in **Figure 25.**

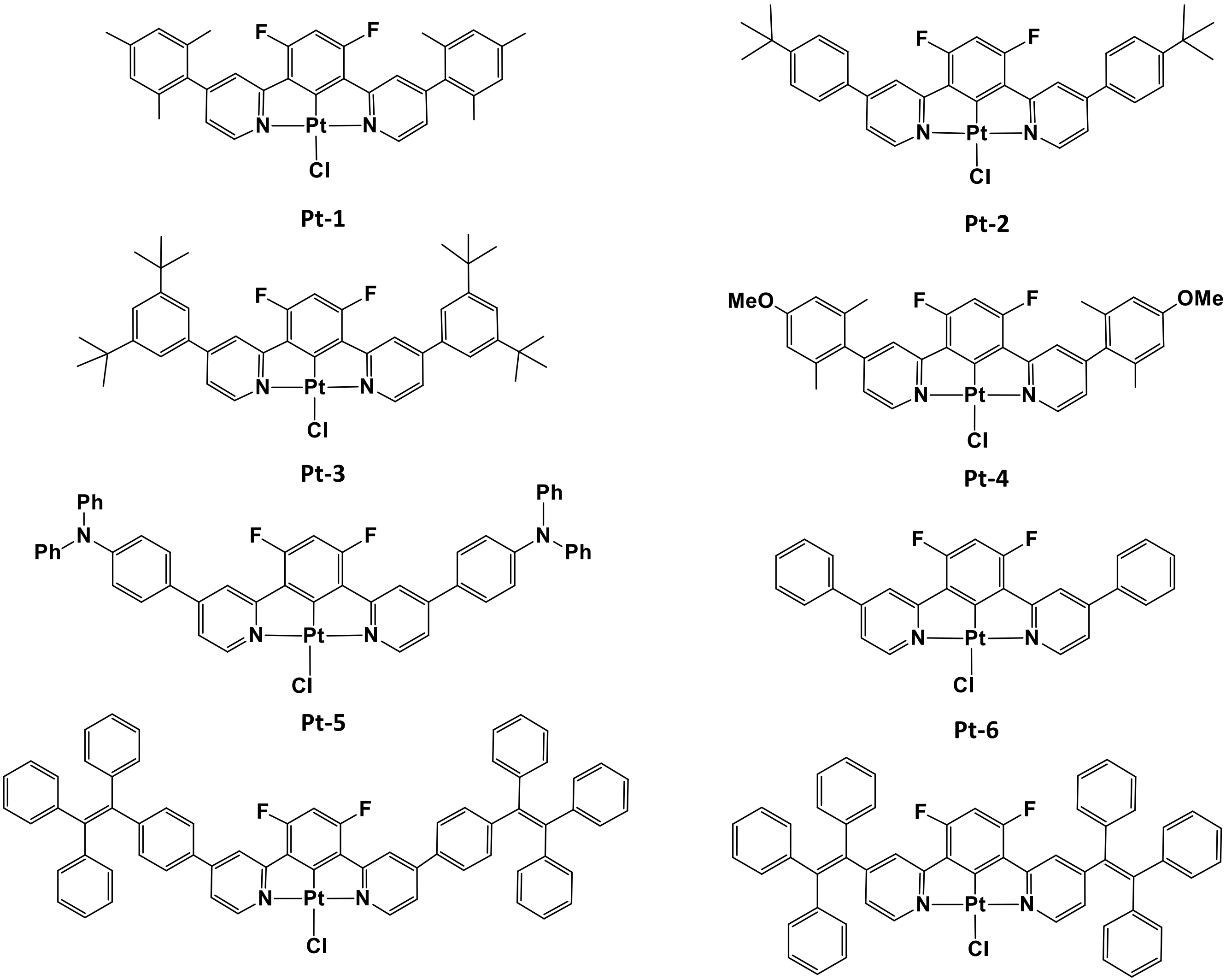

Figure 25. Molecular representation of the designed sterically hindered Pt(II) emitters Pt-1 to Pt-8.

The particular focus of the present thesis concerned the impact of the spatial arrangement of the sterically hindered groups introduced in the Pt(II) based emitters on the intermolecular interactions and their consequent effect on the photophysical properties. In particular, a special interest addressed the evaluation of the developed Pt(II) luminophores efficiency as luminescent labels for bioimaging in brain cells cultures. The biological assays are still in progress.

3.1.2 Synthesis and characterization of an innovative series of cyclometalated Pt(II) complexes bearing sterically hindered substituents

3.1.2.1 Synthesis of Pt(II) emitters functionalized with bulky aryl substituents

Given the outstanding results presented in the previous paragraphs, a series of cyclometalated fluorinated Pt(II) complexes functionalized with sterically hindered aryl substituents introduced on the para position of the pyridine rings were synthesized and investigated (**Figure 26**).

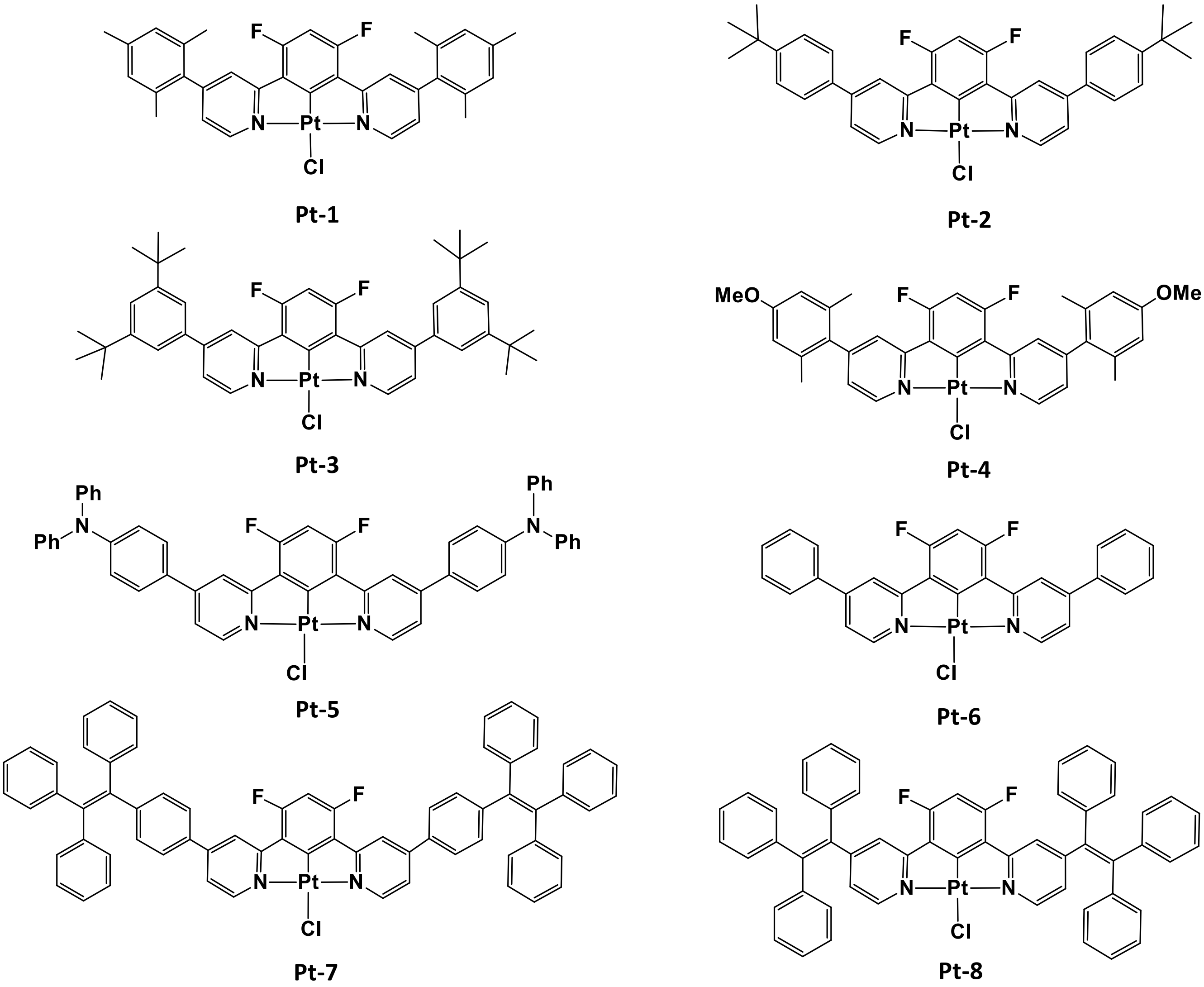

Figure 26. Molecular representation of the designed sterically hindered Pt(II) emitters Pt-1 to Pt-8.

The detailed synthetic pathway for each compound is reported in the Experimental Section (Chapter III).

The synthesis of all the designed complexes was performed starting from the construction of the functionalized 3,5-difluoro-2,6-di(2-pyridinyl)phenyl ligand , which involved the use of two subsequent Suzuki couplings, followed by the complexation reaction with K_2PtCl_4 as the Pt(II) source.

The key substrate was obtained performing a bromination reaction of the 1-bromo-2,4-difluorobenzene, to produce the intermediate 1,3-dibromo-4,6-difluorobenzene which was purified via distillation. Subsequently, the two bromine atoms were displaced through reaction with bis(pinacolato)diboron, achieving the crystalline final product.

The synthesis of the sterically hindered cyclometalated ligands was accomplished through the Suzuki coupling performed between the properly substituted pyridine and the bispinacol ester of the benzene-1,3-difluoro-4,6-diboronic acid.

In the context of pyridine functionalization, two possible routes are available for the sequential Suzuki couplings: the highly hindered moiety can be introduced on the pyridine, mixing the boronic acid of the aryl substituent and 2-chloro-4-iodopyridine.[51] Then, the obtained intermediate undergoes the second Suzuki coupling with the pinacol ester of benzene-1,3-difluoro-4,6-diboronic acid to give the N^C^N ligand.[7]

The steps of the route a) are depicted in **Figure 27**.

Route a)

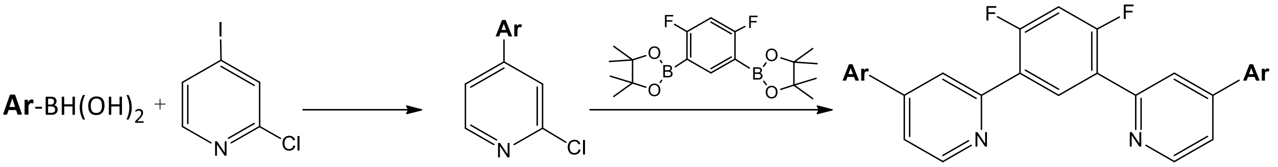

Route b)

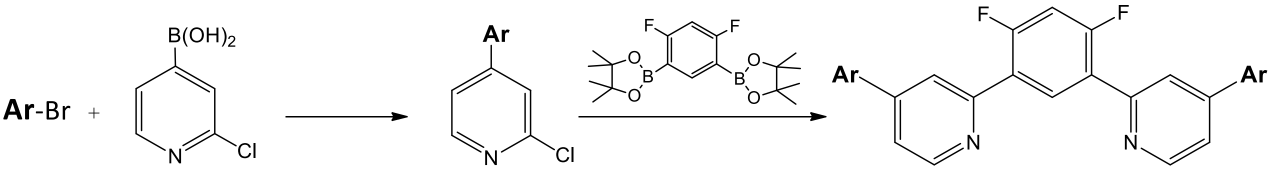

Figure 27. Schematic illustration of the synthetic route a), involving the combination of the boronic acid of the aryl substituent and 2-chloro-4-iodopyridine. Representation of synthetic route b), performed combining the bromine derivative of the bulky substituent and the boronic acid of 2-chloropyridine.

As an alternative, route b) (**Figure 27**) could be used, where the functionalization of pyridine can be carried out combining the bromine derivative of the highly hindered aryl substituent with the boronic acid of 2-chloropyridine to obtain the first intermediate,[52] which is then used to build the cyclometalated ligand through reaction with the pinacol ester of the benzene-1,3-difluoro-4,6-diboronic acid.[7]

In this regard, **Pt-1**, **Pt-2**, **Pt-3** and **Pt-4** were synthesized through route a), using 2-chloro-4-iodopyridine and the boronic acid of the aryl substituent. Specifically, in case of **Pt-1** purification issues arose, since 2-chloro-4-iodopyridine displayed the same polarity of the desired product and the isolation of the mesityl-functionalized pyridine couldn't be achieved through chromatography. Thus, the displacement of the iodine atom to convert 2-chloro-4-iodopyridine into 2-chloropyridine with *n*-butyllithium was attempted. The reaction brought to full consumption of 2-chloro-4-iodopyridine, allowing to isolate the mesityl-functionalized pyridine as a pure intermediate, since 2-chloropyridine displayed a significantly different polarity with respect to the desired product.

Conversely, **Pt-5**, **Pt-6**, **Pt-7** and **Pt-8** were successfully synthesized through route b) and the desired ligands were isolated after purification by flash chromatography.

Pt-1 to **Pt-8** were then obtained through complexation of the ligand with K_2PtCl_4 in an acetonitrile:water mixture (9/1, v/v) . In particular, the desired cyclometalated backbone was dissolved in acetonitrile whilst K_2PtCl_4 was completely solubilized in water *via* sonication and placed in a Schlenk tube under inert atmosphere. The reaction was let run for 72h heating at 110°C, until the formation of a yellow or orange suspension was assessed (**Figure 28**).

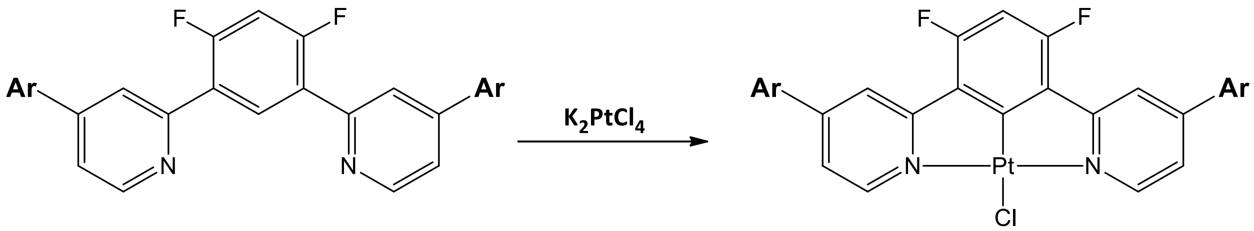

Figure 28. Illustration of the platination step, carried out using K_2PtCl_4 as the Pt(II) source.

The final formation of the desired Pt(II) complexes was evaluated recording the ^{1}H-NMR spectra, since characteristic signals and significant differences from the ligands pattern can be discerned.

By way of illustration, the ^{1}H-NMR of **Pt-1** and of its related ligand **L^1** is represented in **Figure 29**.

Specifically, the insertion of the Pt(II) ion gives rise to a shift downfields of the signal arising from the resonance of the H in the α position of the pyridine rings. Additionally, the signal displays two satellite peakes, resulting from the coupling with the ^{195}Pt. (**Figure 29, blue circle**)

The ^{1}H-NMR spectrum provides an additional significant hint, since the triplet aring from the resonance of the proton on the central phenyl ring on the free ligand, disappears as a consequence of the hydrogen abstraction concerning the cyclometalation process.

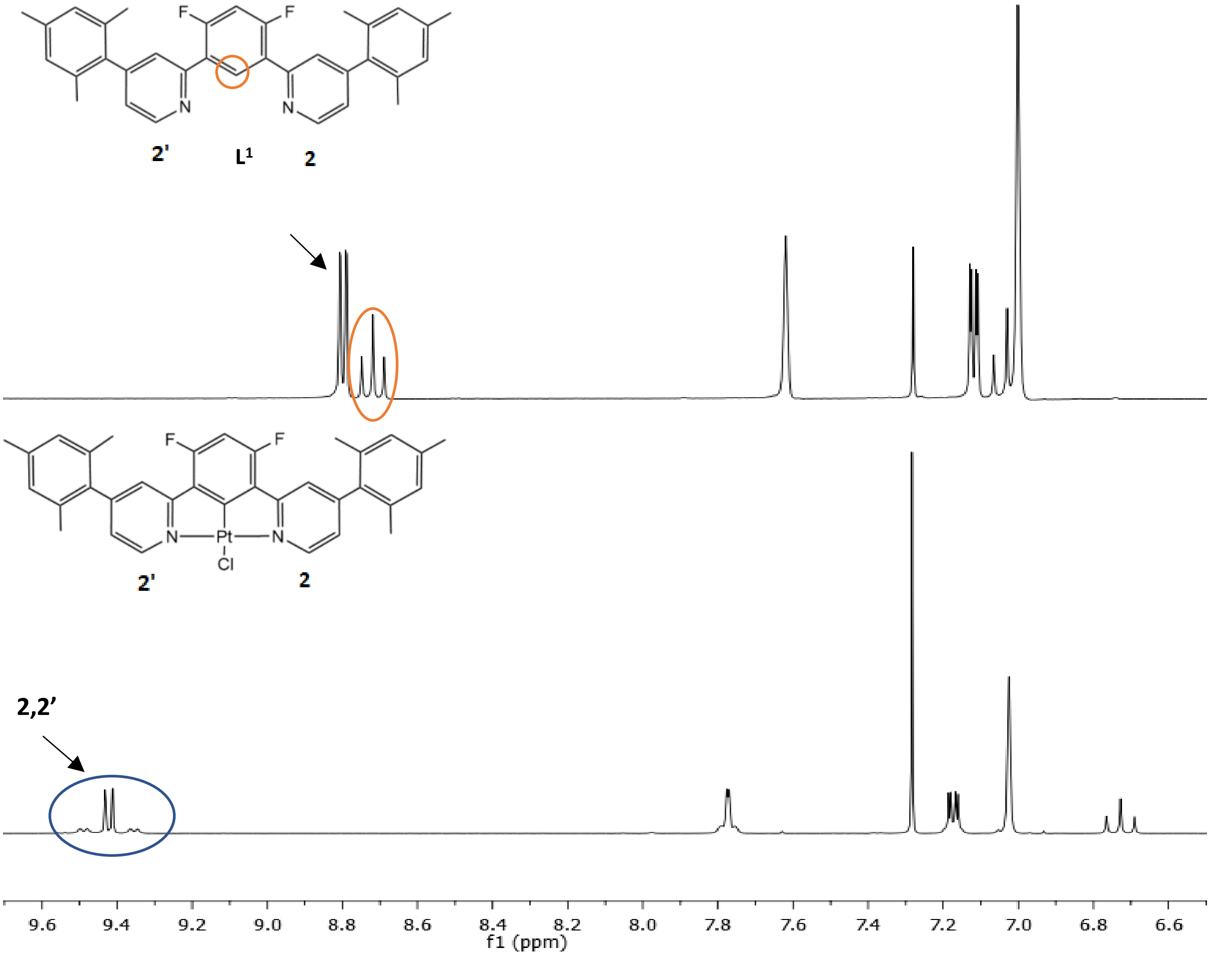

Figure 29. ^{1}H-NMR spectra of the Pt(II) pincer L^1 before (above) and after the complexation (below). Specifically, the triplet signal arising from the resonance of the H on the central benzene ring (orange circle), disappears as a consequence of abstraction within the cyclometalation mechanism.

Information about the purity of the complexes were obtained recording the ^{19}F-NMR, since the presence of a single fluorinated species can be assessed thorugh observation of an individual peak in the spectrum. Potential impurities can thus be easily identified.

Elemental analysis and mass spectrometry further confirmed the occurred complexation.

Photophysical analysis on complexes **Pt-1** to **Pt-8** were performed in degassed DCM solutions at room temperature. Biological assays are still in progress, aiming to accomplish a complete characterization of the photophysical properties. For the purpose, **Pt-1** to **Pt-8** will be tested *in vitro* in brain cells cultures to assess their efficiency as luminescent labels for bioimaging.

3.1.2.2 Photophysical properties of Pt(II) emitters functionalized with bulky aryl substituents

Pt-1 to **Pt-6** were dissolved in dichloromethane at room temperature. Solutions of gradually increased concentration were thus prepared, aiming to fully characterize the photoluminescent properties of the complexes. The photophysical analysis of **Pt-7** and **Pt-8** are still in progress.

Absorption and emission spectra were recorded at room temperature, 298 K, after freeze-pump-thaw treatment, performed to remove the oxygen, a potential phosphorescence quencher.

The photophysical parameters of the synthesized Pt(II) complexes are listed in **Table 2**.

Table 2. Photophysical parameters collected for Pt-1 to Pt-6. [a] Data obtained in 10^{-5} M CH_2Cl_2 solution at 298K. [b] Data obtained in 10^{-5} M deoxygenated CH_2Cl_2 solution at 298K (λ_{ex}= 400 nm).

Complex	λ_{abs} / nm ($\varepsilon \times 10^{3}$ / $M^{-1}cm^{-1}$)[a]	λ_{em} / nm[b]	τ/µs[b]	Φ_{lum} %[b]
Pt-1	263 (22.7), 287 (15.4), 334 (7.6), 360 (6.3), 376 (7.8)	471	4.77	200
Pt-2	280 (49.8), 312 (38.5), 341 (17.3), 383 (23.4)	480	4.09	168.7
Pt-3	278 (35.1), 311 (24.3), 340 (11.6), 382 (15.5)	479	4.06	157.1
Pt-4	238 (39.4), 264 (37.8), 335 (15.6), 377 (14.1)	471	4.56	169.0
Pt-5	293 (44.9), 373 (22.5), 423 (56.4)	562	103.94	89.9
Pt-6	277 (56.5), 308 (34.2), 340 (13.9), 382 (20.5)	480	3.27	141.2

The recorded absorption spectra of **Pt-1** to **Pt-6** are shown in **Figure 30**.

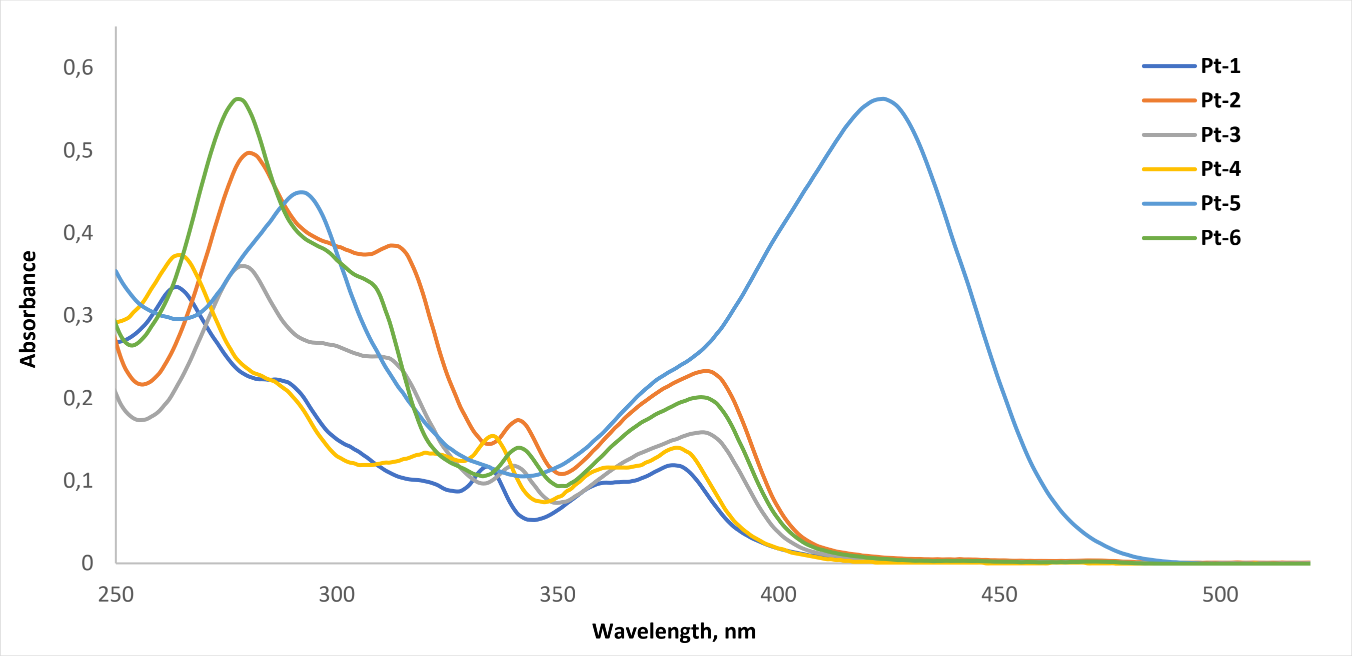

Figure 30. UV-vis absorption spectra recorded in 10^{-5}M CH_2Cl_2 solution for Pt-1 to Pt-6 at 298K.

With reference to the previous investigations carried out in the context of cyclometalated Pt(II) complexes built on the 1,3-di-(2-pyridyl)benzene pincer,[48] the strong absorbtion bands arising below λ = 300 nm, can be attributed to the ligand centered transitions ($^1\pi \longrightarrow \pi^*$). This evidence is further confimed by the presence of the aforementioned intense bands within the absorption spectrum of the free cyclometalated ligand.[53] In the range comprised between 300-420 nm, at least three absorption bands are embedded, where the lowest energy component is strongly affected by the substituent on the 4-position of the pyridine rings. Specifically, a blue shift occurs as electron-withdrawing groups are introduced. Additionally, given the hypsochromic effect assessed for the considered transition, besides the $^1\pi \longrightarrow \pi^*$ transition, a contribution is also given by a charge-transfer transition.

Overall, the investigated complexes display bright photoluminescence associated to outstanding quantum yields over 100%. The observed emission was mainly attributed to a ^{3}LC ($^3\pi \longrightarrow \pi^*$) transition, which is favoured by intersystem crossing promoted by the presence of the heavy metal Pt(II) ion. Consequently, a minor contribution is given by the metal orbitals, resulting in a mixed transition comprising a ^{3}MLCT transition.[48]

The six investigated Pt(II) complexes display a Stokes shift of 200-250 nm. **Figure 31** depicts the emission spectra obtained upon irradiation of $1 \cdot 10^{-5}$M solutions of **Pt-1** to **Pt-6**.

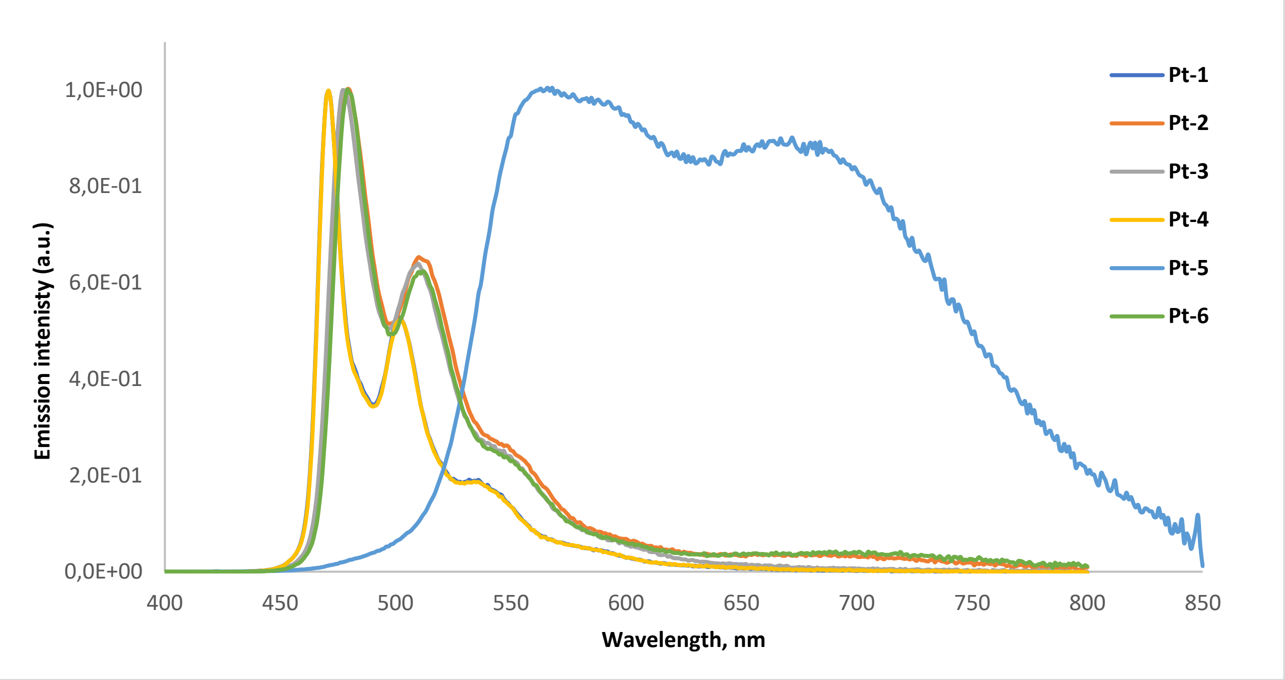

Figure 31. Emission spectra of Pt-1 to Pt-6 in degassed CH_2Cl_2 ($1 \cdot 10^{-5}$M) at 298K. Pt-1, λ_{ex} = 375 nm; Pt-2, λ_{ex} = 383 nm, Pt-3, λ_{ex} = 382 nm, Pt-4, λ_{ex} = 377 nm, Pt-5, λ_{ex} = 374 nm, Pt-6, λ_{ex} = 380 nm.

Square planar geometry of N^C^N Pt(II) complexes favours the formation of excimers, due to their tendency to undergo π-π stacking intermolecular interactions. In this context, photoluminescence analysis of increased concentration solutions of **Pt-1**, **Pt-2**, **Pt-3**, **Pt-4**, **Pt-5** and **Pt-6** highlight the formation of a red shifted broad band at ~ 700 nm, associated to a decreased lifetime of the excited state.

As a model, the emission spectra obtained analysing increased concentration solutions of **Pt-5** is reported in **Figure 32**.

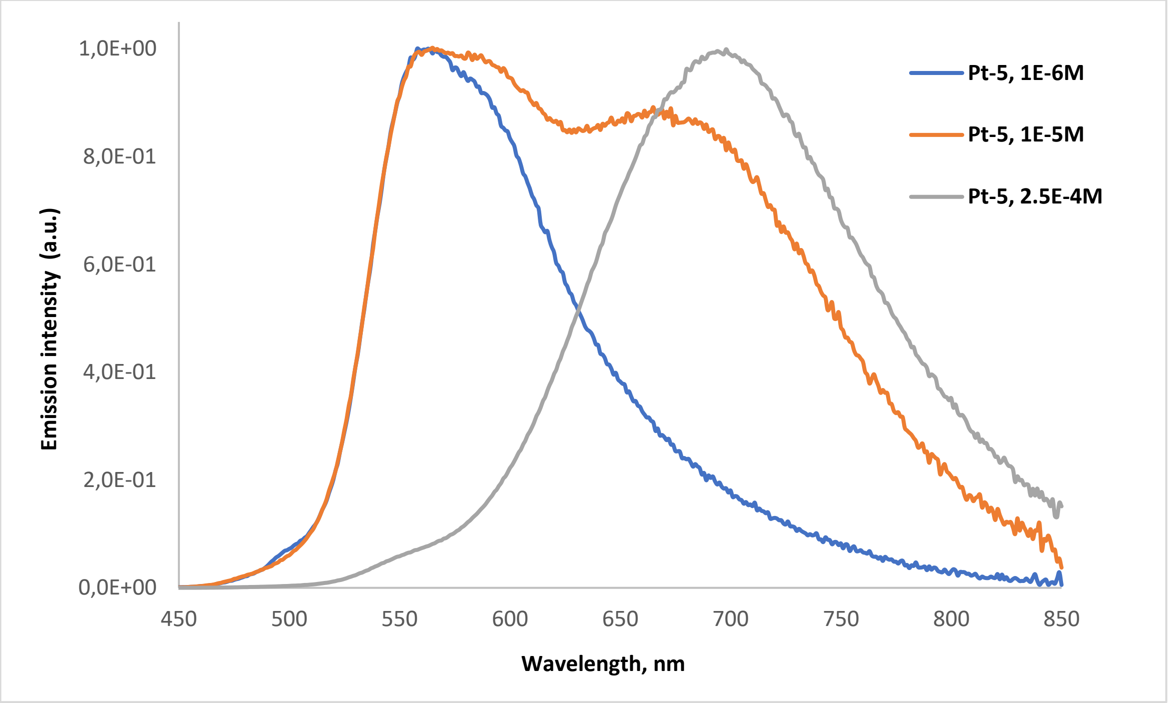

Figure 32. Emission spectra of Pt-5 recorded in degassed CH_2Cl_2 ([] = 10^{-6}M, 10^{-5}M, $2.5{\cdot}10^{-4}$M), λ_{ex} = 422 nm, at 298K.

Comparing the data collected for the sterically hindered Pt(II) emitters with the basic complexes investigated by Gareth et *al.,*[48] no significant difference in the context of aggregates formation was evidenced in solution.

The twisted orientation of the bulky substituents could indeed not influence the aggregation process in a fluid, considering that the aryl rings are free to rotate around the σ-bond that connects them to the Pt(II) pincer at room temperature.

The photophysical analysis performed over the innovative sterically hindered complexes evidenced outstanding results, especially in the context of quantum yield (**Table 2**). The remarkable values obtained, opened up towards the hypothesis that the investigated cyclometalated emitters involve the singlet fission mechanism for the radiative deactivation pathway.

3.1.2.3 Singlet fission: an overview

Singlet fission (SF) is a quantum mechanics phenomenon firstly described in 1965[54] to explain the outstanding and particularly efficient photon generation observed for anthracene crystals.

Generally, SF relies on the interaction between two neighbouring chromophores upon irradiation. In particular, a chromophore in an excited singlet state shares its excitation energy with a ground-state chromophore, leading to the formation of two triplet excited states. The mechanism could both involve molecules of the same type, homofission, or different substrates, heterofission. A schematic representation of the singlet fission is reported in **Figure 33**.

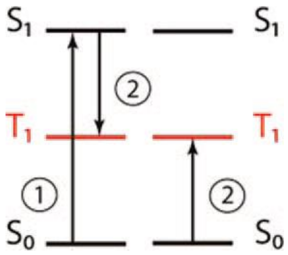

Figure 33. Schematic illustration of the singlet fission mechanism. (1) Chromophore 1 (left) is excited to the S_1 state. (2) The excited chromophore shares its energy with the chromophore on the right, creating a T_1 state on each.

Even though singlet fission mechanism has not been clearly understood, experimental evidence and theoretical calculations evidenced that the process proceeds through an intermediate state, namely a double triplet coherently coupled as an overall spin singlet, which can be outlined as a strong spin correlation.[55]

In literature, the thus formed intermediate is labelled as ^{1}(TT). The process that converts the singlet excited state into two paired-triplet occurs very rapidly since it is spin-allowed, given the overall spin conservation.

Additionally, the triplet pair could also couple into an overall triplet ^{3}(TT) or quintet ^{5}(TT) state, thus leading to the formation of nine substates. Since the triplets are always affected by some sort of interaction, the nine sublevels are not degenerate but they are mixed with each other. Thus, the pure double triplet coupled into a singlet ^{1}(TT) is not a pure singlet, but a state of mixed multiplicity. Indeed, the wavefunction of ^{1}(TT) is represented by the coherent superposition of the nine substates. Given these premises, the radiationless formation of the double triplet species could be actually addressed as a peculiar case of intersystem crossing. Interestingly, the intersystem crossing observed in the context of singlet fission and the intersystem crossing related to the spin-orbit coupling present significant differences. In particular, spin-orbit coupling is responsible for the combination of singlets with triplet states, whilst spin dipole-dipole interaction allows to mix singlets with triplets and singlets with quintets. The additional possibility to mix singlets with quintets is crucial for the singlet fission outcome. Furthermore, at short distances, the paired triplet could convert into two independent triplets through Dexter energy transfer.[56]

Conversely, when the spatial distance between the triplets is significant, the electronic coupling fades away and the intermediate double triplet state is no longer mixed to other configurations, thus being properly outlined by a pure singlet state ^{1}(TT). Given that this radiationless transition occurs between states with the same multiplicity, the phenomenon can be considered a particular case of internal conversion.

In literature, ^{1}(TT) provides an adequate label to address the detailed discussion concerning the singlet fission mechanism.

Within the last step, once the ^{1}(TT) intermediate formed, the double triplet undergoes a decoherence mechanism, leading to the formation of two separated triplets. The overall process is described by Eq. (5).

$$\mathrm{S_0 + S_1 \underset{k_2}{\overset{k_{-2}}{\rightleftarrows}} {}^1(TT) \underset{k_1}{\overset{k_{-1}}{\rightleftarrows}} T_1 + T_1} \qquad \text{Eq. (5)}$$

This last step relies on the surmounting of the binding energy implied in the formation of the ^{1}(TT) species. Specifically, when the two chromophores involved reside on two separate molecules, the binding energy is low. In this context, the triplet pair undergoes decorrelation when an alteration of the coupling is assessed: the triplets could indeed diffuse apart through a material or separate as a consequence of the structural modification of the involved dimer.[57] Particularly, decorrelation is favoured in crystalline structures, where excitons can move apart hopping from a site to another and in solution where chromophores diffusion can take place.

Conversely, in case the binding energy is significant, the double triplet coupled in a singlet provides an observable intermediate, and the pathway can be considered as split into two distinct steps.

The expanded Jablonski diagram including singlet fission is depicted in **Figure 34**.

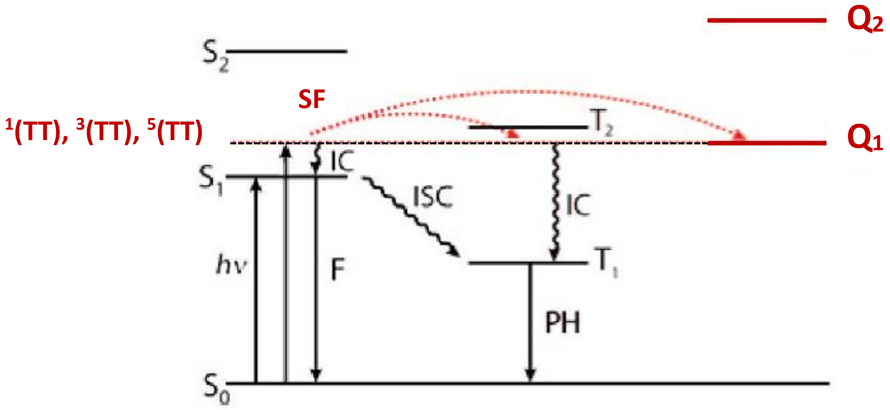

Figure 34. Schematic representation of the singlet fission mechanism.

Basic principles of singlet fission

With reference to Eq. (5), singlet fission mechanism is governed by four kinetic constants, which enable to give a detailed but oversimplified description of the process.[58] Specifically, k_{-2} and k_2 are related to the formation of the double triplet coupled into a singlet $^1(TT)$, whilst k_{-1} and k_1 outline the final decorrelation into two independent triplets T_1+T_1. Conventionally, the probability that the pathway leads to decoherence of $^1(TT)$, rather than to the singlet excited state S_1, is better defined by the branching constant $\varepsilon = k_2/k_{-1}$.

$$S_0 + S_1 \underset{k_2}{\overset{k_{-2}}{\rightleftharpoons}} {}^1(TT) \underset{k_1}{\overset{k_{-1}}{\rightleftharpoons}} T_1 + T_1 \qquad \text{Eq. (5)}$$

The quantum mechanics treatment results facilitated if the considered chromophores are infinitely distant from each other. Conversely, neighbouring chromophores undergo overlapping, complicating the definition of the involved states. For clarity, weakly coupled systems will be discussed, where the overlapping is negligible. In this context, chromophores embedded in an ordered structure such as crystals and systems made of two chromophores A and B, facilitate the singlet fission analysis. Another simplification is introduced considering solely the highest occupied molecular orbital (HOMO) and the lowest unoccupied molecular orbital (LUMO) on each chromophore.

The interaction between neighbouring chromophores A and B, can be discussed using the Hamiltonian. Specifically, in case the interplay is weak, the Hamiltonian can be split into two contributions: the part related to the single isolated chromophore, and the component relying on the interaction between the two.

The starting point for a clear analysis of the phenomenon considers S_0 and S_1 as eigenstates of the independent chromophores, forming the singlet excited state. Considering a weakly coupled system, the interaction doesn't significantly affect the energy of the initial states. Additionally, the final double excited state T_1+T_1 is obtained from the eigenstates of the single configuration of the chromophores including the interaction Hamiltonian.

In the model, the Hamiltonian is defined as $H = H_{el} + H_{spin}$ and it is thus composed by two contributions. In the context of the Born-Oppenheimer approximation, H_{el} includes the electrostatic factors implied in the process, namely, the kinetic energy of the electrons, the reciprocal repulsion between negative charges, their attraction to the nucleus and the repulsion within the nucleus, which is constant. The H_{el} term is not responsible for the mixing between states of diverse multiplicity, thus it is related to the ^{1}(TT) formation, which is theoretically spin-allowed, governed by the kinetic constants k_{-2} and k_2. This term is affected by the molecular structure.

The second contribution, H_{spin}, is spin-related and includes the interaction with an applied external magnetic field (Zeeman effect), the hyperfine interaction with the nuclear spin, the spin-orbit coupling and the spin dipole-dipole interaction. Contrary to the previously mentioned term, H_{spin} enables the mixing within states characterized by diverse multiplicity, facilitating the intersystem crossing process involved in the formation of T_1+T_1, which is governed by the rate constants k_{-1} and k_1.

Aiming to give an insight concerning the basics of singlet fission, three classes of molecules were identified to outline the dependence of the phenomenon on the structural features of the designed chromophores.[58]

- Chromophores of class I: this class includes π-conjugated substrates such as anthracene, perylene, 1,3-diphenylisobenzofuran and tetracene in which the excitation of the electron from the HOMO provokes the formation of the singlet excited state (S_1) as a consequence of the considerable energy gap between the S_1 and the S_2 state.
- Chromophore of class II: chromophores belonging to this class directly access the S_2 state through absorption of photons, subsequently undergoing fast internal conversion to reach the S_1 state, which is slightly lower in energy with respect to S_2. The generalization of the phenomenon could be outlined considering transitions that involve h-1 → l and h → l+1, where h-1 represents the first molecular orbital below the HOMO and l+1 the next molecular orbital above the LUMO.
- Chromophore of class III: similarly to the previuos case, the transition can be described as h → l, where the promotion of charge involves higher electronic states (S_2) followed by internal conversion

to occupy the slightly lower in energy S_1 state. Nevertheless, in contrast with the aforementioned process, the S_1 state is characterized by a predominant contribution given by a configuration arising from the double promotion of both the electrons (h,h $\longrightarrow$ l,l). Pentacene provides an example of class III chromophore.

Even though the process depicted in Eq. (5) is still not fully understood and a detailed description of the phenomenon for any case is not available, it's clear that the entity of the interaction between neighbouring chromophores governs the phenomenon. To date, three typologies of mechanisms were outlined:

a) Direct mechanism: the formation of the ^{1}(TT) state directly occurs from the (S_0S_1) state.
b) Mediated mechanism: the ^{1}(TT) species is obtained through an intermediate virtual charge-transfer state which lies at higher energy.
c) Non coherent singlet fission: the aforementioned mechanisms both contribute to the formation of ^{1}(TT), but the energetic and electronic factors that underlie it are not clear.

The latter case is also known as quantum coherent mechanism and it is given by the combination of the (S_0S_1) and ^{1}(TT), which sometimes implies the presence of the charge-transfer state. The fate of the triplet pair then, depends on the investigated media.

In a packed solid, where the molecules are close to each other, the triplets can move apart through the media and give rise to decoherence. On the other hand, if the triplets are located on a dimer, decorrelation can be assessed only if the two chromophores interact weakly, leading to a mixing of the ^{1}(TT) and ^{5}(TT) states, which promotes decorrelation. Conversely, when the monomers are involved in a strong coupling, ^{1}(TT) undergoes triplet-triplet annihilation coming back to the ground state.

In order to observe efficient singlet fission, the formation of the ^{1}(TT) has to be thermodynamically favourable, enhancing the yield of decorrelated triplets. Specifically, the designed chromophores should give rise to an exoergic (which involves release of energy), isoergic (occurring without change of energy) or slightly endoergic (involving absorption of energy) (S_0S_1) $\longrightarrow$ ^{1}(TT) process, preventing concurrent phenomena to occur. To fulfil the requirement, the energy of the ^{1}(TT) state should be at least twice the energy of the S_1 state, thus $2E(T_1)-E(S_1)$ should be negative.[58]

Additionally, intermolecular processes such as the excimer formation and charge separation provide the major threats concerning singlet fission efficiency. Indeed, intermolecular interactions could decrease the S_1 state energy, possibly causing the triplets formation to be endoergic. Furthermore, charge separated states and excimers tend to relax through internal conversion or intersystem crossing, leading to excitation energy loss. Nevertheless, excimers and charge separated states retain most of the energy absorbed upon excitation, thus singlet fission could still be observed but the formation of these species should be controlled and limited.

3.1.2.4 Singlet fission kinetics: an insight

As reported in the previous paragraphs, inter-chromophores interactions and electronic coupling are crucial for the development of the process. In particular, the entity of the interaction depends on the electronic coupling between the molecules involved in the formation of the dimers.

Mathematically, the extent of the electronic coupling is provided by the resonance integral V, Eq. (6), where the involved states ($V_{i\neq j}$), are correlated to each other through the H_{el} term, highlighting the predominant role of the electronic coordinates.[58]

$$V_{i\neq j} = \psi_i|H_{\mathrm{el}}|\psi_j \qquad \text{Eq. (6)}$$

In fact, the discussion is built on the Born-Oppenheimer approximation, which assumes that the nuclear configurations are frozen.

Eq. (6) represents the expression describing the coupling between the initial singlet excited state S_1S_0 and the double triple final state $^1(TT)$. Electronic coupling, together with the energetic driving force, provides a satisfactory explanation of the phenomenon.

Generally, the first step of singlet fission, involving the formation of the double triplet coupled into a singlet $^1(TT)$, can be represented and described through the potential energy surfaces diagram. Indeed, the transition within the two involved states can occur implying the conical intersection of the potential energy surfaces or through a single surface when intersection is prevented.[60]

Mainly, two cases can be outlined (**Figure 35**):

- Non-adiabatic regime: the monomers coupling is weak and the rate of singlet fission is directly proportional to the square of the coupling V, given by Eq. (6). The two electronic states involved are represented by separated states depicted by potential energy curves intersecting each other, giving rise to a sudden transition. (**Figure 35, a**)
- Adiabatic regime: when the coupling between chromophores is strong, the potential energy curve arising from the dimer formation is depicted by a continuous line, implying that the transition evolves from the S_1S_0 states to the $^1(TT)$ state smoothly as the reaction progresses. Given the high value of V, the kinetic is independent from the coupling, conversely, it relies on the nuclear rearrangement rate (τ_{ad}). (**Figure 35, b**) The rate expression for adiabatic regime includes two new parameters, namely the reorganization energy λ and the energetic driving force ΔG.

The energetic driving force ΔG is associated to the free energy involved in the process. The reorganization energy λ represents the energy required to convert the initial structural arrangement of the chromophores and their solvation sphere into the structural arrangement of the final species, with the related solvent molecules. The reorganization energy is made of two contributions: λ_{int} which describes the internal structural modification and λ_{out} which accounts for the reorientation of the solvent molecules.[59]

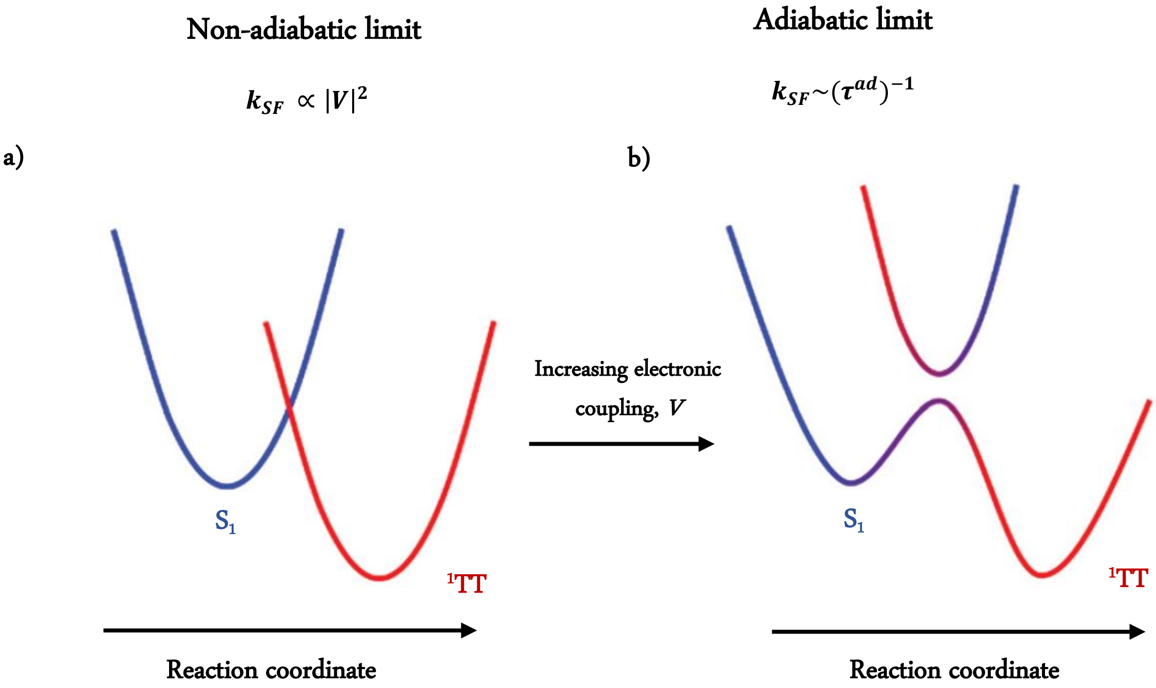

Figure 35. Schematic representation of the kinetic model for singlet fission through the potential energy curves diagram. As the coupling between the involved states S_1 and ^{1}(TT) increases, the regime switches from non-adiabatic (left) to adiabatic (right).

Thus, the occurring transition can switch from non-adiabatic to adiabatic as a function of the coupling intensity, which can be controlled synthetically tuning the properties of the involved monomers.

The energy gap between the S_0S_1, ^{1}(TT) and CT state, defines the mechanism involved.

In this context, if the electronic coupling is intense and the CT state is energetically accessible, it contributes to the formation of ^{1}(TT), giving rise to the diabatic coupling and leading to the mediated mechanism. Conversely, when the electronic coupling is negligible, the CT state results highly destabilized thus giving rise to a direct mechanism, where the CT state is not involved.[60]

Direct mechanism:

Class I chromophores bearing π-conjugated backbones tend to interact with each other giving rise to π-π stacked structures, with a contact distance of ~ 3-3.5 Å on average.[58] This configuration leads to frontier molecular orbitals overlapping. The charge densities superpositions embody the electronic interactions between the chromophore A and B and they are outlined by the integrals eh_Ah_B, eh_Al_B, el_Ah_B and el_Al_B.

In a perfectly stacked dimer, the entity of repulsion and attraction are equivalent since the charge density eh_Ah_B is negative all over the surface, whilst eh_Al_B is characterized by a negative charge on half of the surface and by a positive charge on the remaining half. Given these premises, the electron repulsion integral is zero.

Nevertheless, if chromophores undergo a shift along the transition moment direction, the charge densities don't annihilate each other and the repulsion term is no longer zero. This observation can be explained considering the role of the $<S_0S_1|H_{el}|^1TT>$ term in the Fermi golden rule (Eq. (7)), which allows to estimate the rate of the singlet fission process within the framework of the Born-Oppenheimer approximation, where FCWD is the Franck-Condon weighted density of states of the final state.

$$k_{\mathrm{SF}} = \frac{1}{h}|\langle \mathrm{S_1S_0}|H_{\mathrm{el}}|\mathrm{T_1T_1}\rangle|^2(\mathrm{FCWD}) \qquad \text{Eq. (7)}$$

According to the Fermi golden rule, the singlet fission rate displays a proportional dependence to the $<S_0S_1|H_{el}|^1T_1T_1>$ matrix element. Given that the $<S_0S_1|H_{el}|^1T_1T_1>$ term contains the contributions of the electronic repulsion integrals, its value is strongly dependent on the electronic repulsion magnitude. Consequently, it's fundamental to inhibit the perfect π-stacking, in order to prevent the cancellation of this term.

Charge-transfer mediated mechanism:

Considering the case in which either the matrix element $<S_0S_1|H_{el}|^1T_1T_1>$ has a small value or a singlet charge transfer state (^{1}CA or ^{1}AC) is readily accessible since it lies close to the S_1S_0 state, the Fermi golden rule could become unsatisfying for the intrinsic rate calculation. Indeed, the energetically close states (S_1S_0, ^{1}CA or ^{1}AC) can give rise to strong coupling, resulting in an initial state that is described by a linear combination of the three involved states. In turn, the latter can further couple with the $^1T_1T_1$ state, enabling the mediated mechanism to take place. The schematic representation of the general mechanism is provided in **Figure 36**.

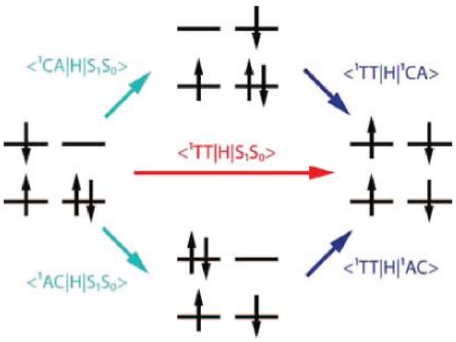

Figure 36. General scheme depicting the singlet fission pathways.

The charge transfer mediated mechanism was firstly proposed for singlet fission involving molecular crystals[61] and lately for covalent dimers.[62]

Generally, the key features needed to optimize the singlet fission efficiency involve an exoergic or isoergic process, in which the charge transfer states are energetically accessible and wherein the interacting monomers are not correlated by symmetry. In contrast to the aforementioned direct mechanism, which is maximized for slipped stacked π-conjugated chromophores, covalent dimers seem promising candidates for the charge transfer mediated mechanism. Particularly, linearly linked atoms overlap, giving rise to maximum superposition within the planar configuration, which reaches zero as the backbone twists orthogonally. Nevertheless, some drawbacks arise considering that direct conjugation binds monomer A to monomer B, converting them into a single chromophore. As a consequence, the singlet excited state S_1 is stabilized, leading it below the $E(S_1)>2E(T_1)$ limit and resulting in an endoergic process. Furthermore, some doubts concerning the capability of the linearly linked dimer to host two triplets, have arisen. Lastly, direct conjugation provokes non negligible interaction between the chromophores, making the approximated treatment hereby reported inadequate. Thus, a more detailed discussion should be provided.

Nevertheless, the charge transfer state serves as a virtual state in the case that ^1CA or ^1AC are located at higher energy with respect to S_1S_0, S_0S_1 and $^1(TT)$ states. Consequently, upon mixing within the states, the charge transfer state doesn’t contribute to the formation of a minimum in the potential energy surface of the lowest excited state and the coherent singlet fission mechanism is favored. Conversely, if chromophore A and B are strongly coupled, the excitation to S_1 produces a delocalized excited state in which the four molecular orbitals involved are equally distributed over the chromophore A and B. Nonetheless, the strong coupling leads to the aforementioned limitations.

Another possibility features the charge transfer state contributing to the formation of a minimum in the potential energy surface. In this case, the charge transfer provides a real intermediate in the transformation of the initial state S_1S_0 into $^1(TT)$, giving rise to a two-step mechanism.

The second step of the charge transfer mediated mechanism is an independent process, since it consists of a back electron transfer in an ion pair. (**Figure 36**) The formation of the final double triplet is achieved through the spin dipole-dipole interaction, which allows transitions involving quintet states.

The charge transfer mechanism is highly affected by the nature of the solvent. In this context, the processes taking place as a consequence of photoexcitation, induce a modification in the charge density. This is particularly relevant in polar solvents, which are described as dipoles.

Firstly, solvent molecules surround the individual species, undergoing a redistribution upon photoexcitation of the monomer. After the dimer formation, three additional distinct steps could be outlined: the solvent molecules rearrange to properly solvate the dimer, then they assist the charge transfer and lastly, as the final species is produced, the solvent molecules undergo another reorientation to stabilize it. A schematic representation of the process is provided in **Figure 37**.[63]

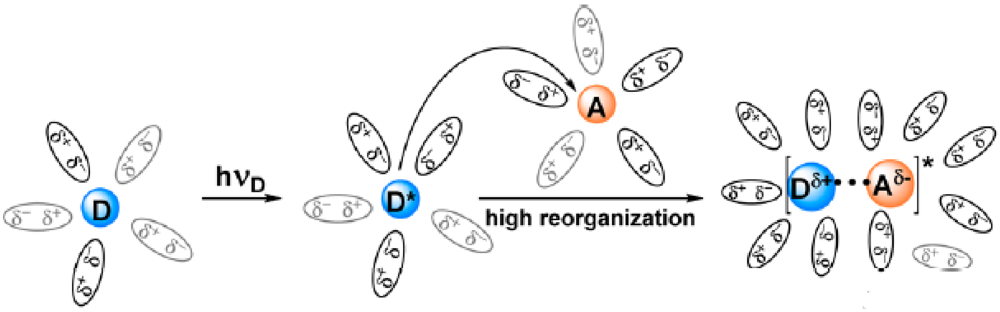

Figure 37. Schematic illustration of the solvent reorganization induced by excitation.

The interaction between solvent molecules and the emitting species, play a crucial role on the energy of the CT state, thus affecting the superposition within the involved states and the course of the process.

Confronting the investigations conducted on the direct and mediated mechanism for class I chromophores, it has been hypothesized that the more efficient approach to observe single fission relies on the development of slip stacked π- conjugated monomers that exploit the direct mechanism instead of the mediated one.[58]

3.1.2.5 Singlet fission: cases of study

Molecular crystals

In the first instance, singlet fission was observed and investigated in molecular crystals,[58] where the excitation produces an exciton, which behaves as a quasiparticle. Two types of excitons could form: singlet excitons which display a short life-time (ns) and triplet excitons, characterized by a long life-time (µs). Additionally, it was assessed that singlet excitons could delocalize over the crystal structure, whilst triplet excitons mainly reside in one site. In perfectly ordered crystals, the excitons can move through the structure hopping from a site to another. Nevertheless, due to the distinct lifetime, the diffusion length for the two typologies of excitons significantly varies. Indeed, singlet excitons can diffuse for tens of nm, whereas triplets display a diffusion length of tens of µm. Consequently, the enhanced capacity of triplet excitons to propagate further in the crystal, prevents recombination to occur, promoting singlet fission. Nonetheless, defects within the crystalline structure could provoke trapping of the excitons, leading to its localization. Excimers formation provide an example of self-induced imperfections.[58]

In literature, high density imperfection polycrystalline solid films bearing intergrain boundaries were considered as well. Significant differences were assessed within the singlet fission kinetics. Specifically, the lifetime of triplet excitons is shorter with respect to single crystal structures.

Isolated molecules

The singlet fission phenomenon in isolated molecules has not been extensively discussed and in literature few works have been published in this context.[58] As previously aforementioned, the promotion of singlet fission is favoured when two weakly interacting chromophores are able to host two triplet excitons.

Aiming to enhance the efficiency of direct or mediated mechanism, the interchromophore interaction strength can be improved. Nevertheless, two drawbacks could be encountered if the chromophores coupling becomes too strong: the $E(S_1)>2E(T_1)$ condition could not be respected and the triplet excitons could not be able to diffuse apart. Covalent dimers perfectly exemplify this condition, since the triplet excitons are localized and can't move away leading to the occurrence of competitive processes.

Thus, even though covalently linked dimers appear advantageous due to the easy tunability of the structural features, they display very low triplet yields. Conversely, investigations over slip-stacked dimers provide a promising strategy for the design of singlet fission chromophores.[58]

1,3-Diphenylisobenzofuran

Extensive studies concerning 1,3-diphenylisobenzofuran have been performed and reported in literature.[64, 65, 66, 67]

1,3-Diphenylisobenzofuran (**Figure 38**) provides the first example of molecule giving rise to efficient singlet fission, purposely designed for this application besides polyacenes.[68]

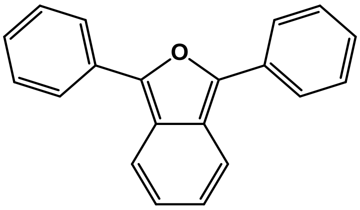

Figure 38. Molecular structure of 1,3-diphenylisobenzofuran.

The structure of the molecule with the related X-ray structure is given in **Figure 39**. The molecule is characterized by steric interaction within the backbone that prevents the coplanarity. Indeed, the oxygen lone pair interferes with the ortho hydrogens on the phenyl rings, provoking a rotation of the phenyl substituents of about 24° angle. This results in two conformers with C_2 and C_s symmetry respectively, differing in the sense of rotation. Thus, two distinct ground state conformations bearing approximately equal energies and geometries arise.

The X-ray structure of the C_2 conformation has been solved and is reported in **Figure 39**.

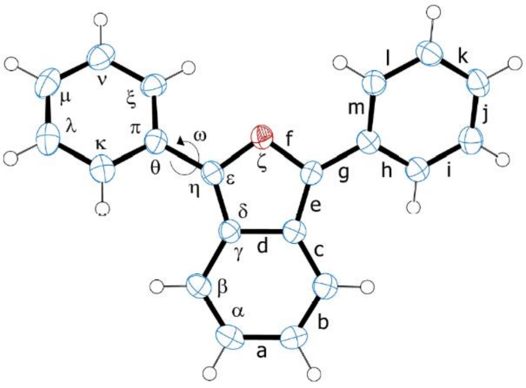

Figure 39. X-ray structure of the ground-state of the C_2 conformer obtained from a single crystal.

The study of the bond lengths in the isobenzofuran moiety evidenced the highly π-conjugated nature of the molecule, leading to the conclusion that it can be related to a π-conjugated heterocyclic polyene bearing two phenyl rings.[68]

The energy of the electronic states of the chromophore were evaluated in solution, where $E(S_1) = 2.8$ eV and $E(T_1) = 1.5$ eV, and in the crystalline structure, $E(S_1) = 2.7$ eV and $E(T_1) = 1.4$ eV. 1,3-Diphenylisobenzofuran displays intense fluorescence with a quantum yield of $\Phi_{PL} = 0.96$ in cyclohexane. The formation of the triplet excited state was not observed, leading to the conclusion that intersystem crossing induced by the spin-orbit coupling and the competitive nonradiative processes are not relevant. The singlet fission energetic condition $E(S_1)>2E(T_1)$ results thus satisfied.[58, 64]

The investigations carried out on the crystalline structure of 1,3-diphenylisobenzofuran evidenced the presence of slip stacked dimers (**Figure 40**), which facilitate the singlet fission occurrence through direct mechanism.

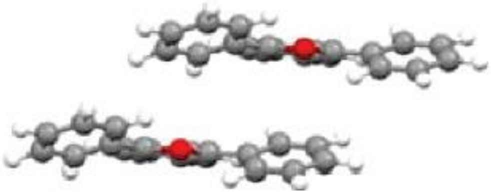

Figure 40. Slip-stacked orientation of two 1,3-diphenylisobenzofuran molecules embedded in crystal lattice.

Additionally, polycrystalline layers of 1,3-diphenylisobenzofuran grown onto sapphire were used to perform photoinduced triplet absorption and ground-state bleaching measurements aiming to determine the triplet yield.[69] The analysis were conducted in a range of temperatures comprised between 12K and ambient temperature and a yield over 100% was assessed. The determined time constant (~ 25 ps) then, is equal to the time constant of both the S_1 decay consequent to absorption and to the time constant of the S_0-S_n decrease absorption, associated to the increased ground-state bleaching. These results clarified that the triplet formation is a consequence of singlet fission.

Further investigations concerning the geometry alteration upon excitation have led to the conclusion that the π-conjugation results enhanced as a consequence of photon absorption. Such observation explains the rearrangement of the two phenyl rings, which in the S_1 and T_1 excited state display a twist angle of 9-10° with respect to the 24° of the ground state. This structural change makes the two C_2 and C_s conformers almost indistinguishable, leading to the formation of a single minimum in the potential energy surface.

In conclusion, the collected results underline the outstanding photophysical properties of 1,3-diphenylisobenzofuran, imprinted through the application of the aforementioned theoretical basics to obtain efficient singlet fission.

3.1.2.6 Conclusion

The sterically hindered cyclometalated Pt(II) based emitters (**Figure 41**). bearing various functional groups were extensively investigated, to assess their photophysical properties. The detailed collected data are reported in paragraph 3.1.2.2.

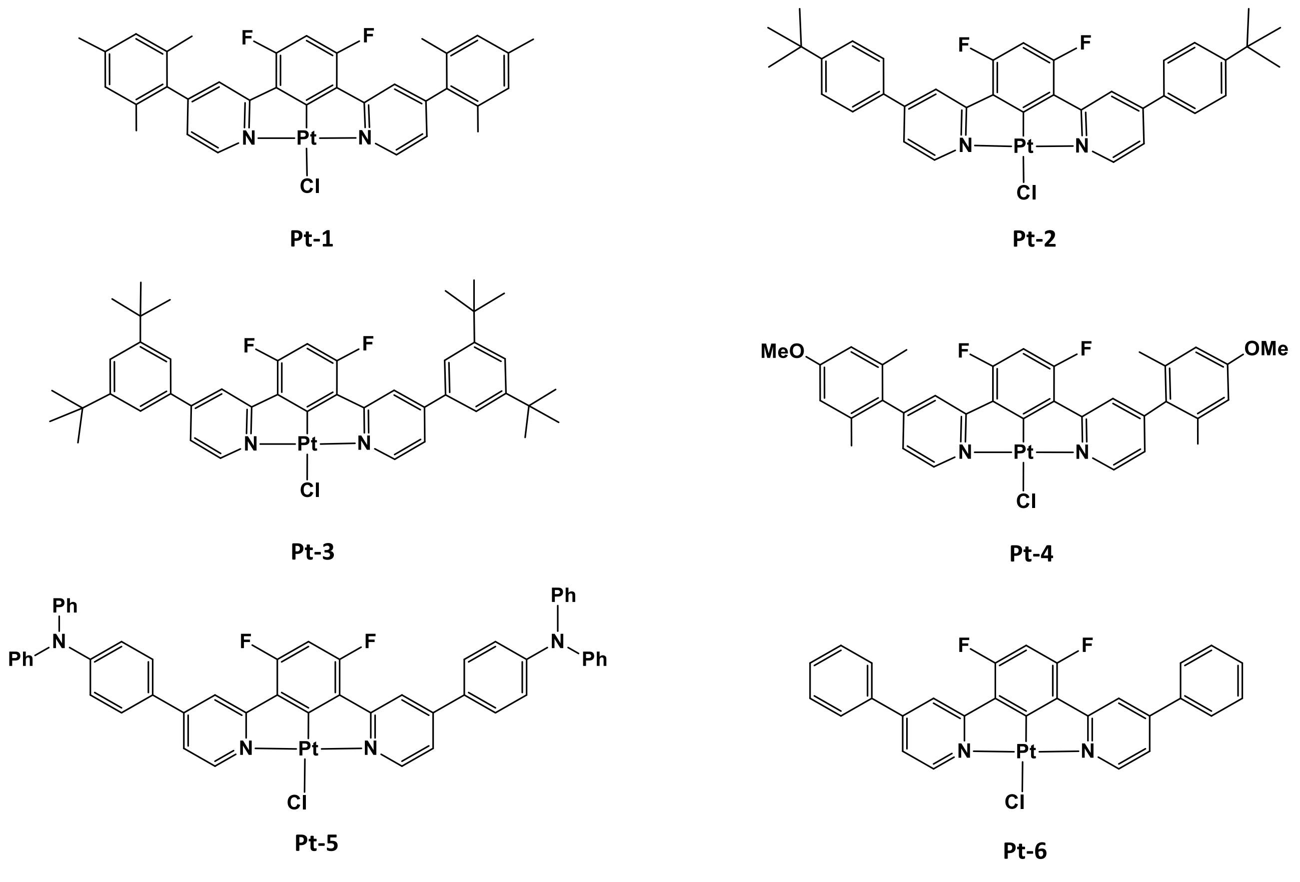

Pt-1

Pt-2

Pt-3

Pt-4

Pt-5

Pt-6

Figure 41. Molecular structure of Pt-1 to Pt-6.

The photophysical analysis conducted on **Pt-1** to **Pt-6** in dichloromethane solution, highlighted outstanding results, especially concerning the measured quantum yields. Specifically, the values exceed 100%, which is the theoretical limit imposed by the definition of quantum yield $\left(\Phi = \frac{N^\circ\, photons\ emitted}{N^\circ\, photon\ absorbed}\right)$.

Extensive investigations have led to the hypothesis that the collected data could be explained on the basis of singlet fission. Given the extremely complicated mechanism, it has not been clearly understood yet. Nevertheless, photoexcitation of the chromophore results in the formation of a singlet excited state which, as a consequence of the interaction with a neighbouring molecule, evolves in the formation of two triplet excited states coupled into a singlet.

In the specific case of the investigated complexes **Pt-1** to **Pt-6,** it was hypothesized that the species responsible for the observed fenomenon could be dimers, rather than monomers. Specifically, two neighboring monomers in the ground state interact with each other, forming the dimer. Upon excitation, the coupled chromophores are excited to the singlet excited state and the interaction with an adjacent dimer in the ground state occurs, giving rise to the energy transfer involving the multimeric species and the consequent formation of the double triplet coupled in an overall singlet.

The mentioned hypothesis relies on the photophysical data collected: the triplet monomeric emission is centred around $\lambda \sim 480$ nm, whilst the dimeric emission is centred at $\lambda \sim 680$ nm. The photon energy (eV) corresponding to $\lambda = 480$ nm can be calculated applying the equation $E\ (\mathrm{eV}) = \frac{hc}{\lambda(nm)}$, where *h* is the Planck's constant ($6.6261 \cdot 10^{-34}$ J·s) and c is the speed of light ($2.9979 \cdot 10^{8}$ m/s). Considering then that 1 eV is equal to $1.602176634\times10^{-19}$ J, the equation can be rewritten as follows: $E\ (\mathrm{eV}) = \frac{1239.8}{\lambda(nm)}$. Thus, $E\ (\mathrm{eV}) = \frac{1239.8}{480} = 2.58$ eV.

Given the $E(S_1)>2E(T_1)$ requirement, the singlet excited state energy should be at least equal to $E\ (\mathrm{eV}) = 2.58\ \mathrm{eV} \cdot 2 = 5.16$ eV, which corresponds to a wavelength of $\lambda = 240$ nm. Nevertheless, the photophysical analysis were performed inducing the excitation irradiating at $\lambda = 300$ nm, which would be insufficient for the monomer to be responsible for the singlet fission. Conversely, the radiative decay of the double triplet coupled into a singlet occurring at $\lambda \sim 680$ nm, could fulfil the aforementioned condition. It was thus concluded that the initial dimer excitation and the subsequent interaction with a neighboring pair of coupled chromophores in the ground state could explain the assessed quantum yield values.

The versatile nature of the developed Pt(II) emitters, which allows to finely tune the color of emission through proper choice of the functional groups introduced on the 4-position of the pyridine rings, together with the outstanding and unprecedented data collected, opened up to new horizons in the contest of cyclometalated Pt(II) luminophores design.

3.1.3 Ir(III) cyclometalated complexes for bioimaging: state of the art

In 1987, King and Watts reported the synthesis of the archetypal cyclometalated Ir(III) complex, $[Ir(ppy)_2(bpy)]^+$.[70] (**Figure 42**)

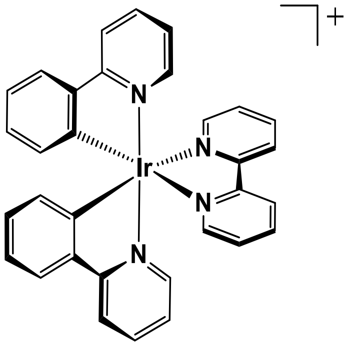

Figure 42. Molecular structure of $[Ir(ppy)_2(bpy)]^+$.

The photoluminescent properties of the cationic complex have been assessed in a CH_2Cl_2:MeOH, 9:1 mixture at room temperature.[70] The complex displayed a wavelength of emission of λ_{max}= 583 nm, associated to a life-time of the excited state equal to τ = 0.34 µs and to a phosphorescence quantum yield of Φ = 0,07.

The analysis of the photosensitizing properties[71] highlighted that the archetypal complex produces the singlet oxygen very efficiently, with a singlet oxygen quantum yield of 0.97. This evidence suggested the potential application of the cationic cyclometalated Ir(III) complex in the living cells as a photosensitizer for photodynamic therapy.

Over the following years, Lo *et al.* reported studies concerning a series of Ir(III) complexes bearing the 2-phenylpyridine (N^C) moiety and the bipyridine (N^N) ligand in the coordination sphere, modified with a variety of substituents. In this context, biotin[72] (**Figure 43, a**) aliphatic chains[73] (**Figure 43, b**), poly(ethylene glycol) (PEG)[74] (**Figure 43, c**) were introduced on the bipyridine N^N moiety aiming to design optimal emitters meant to be inserted in the biological media.

The molecular representation of the evaluated complexes is given in **Figure 43**.

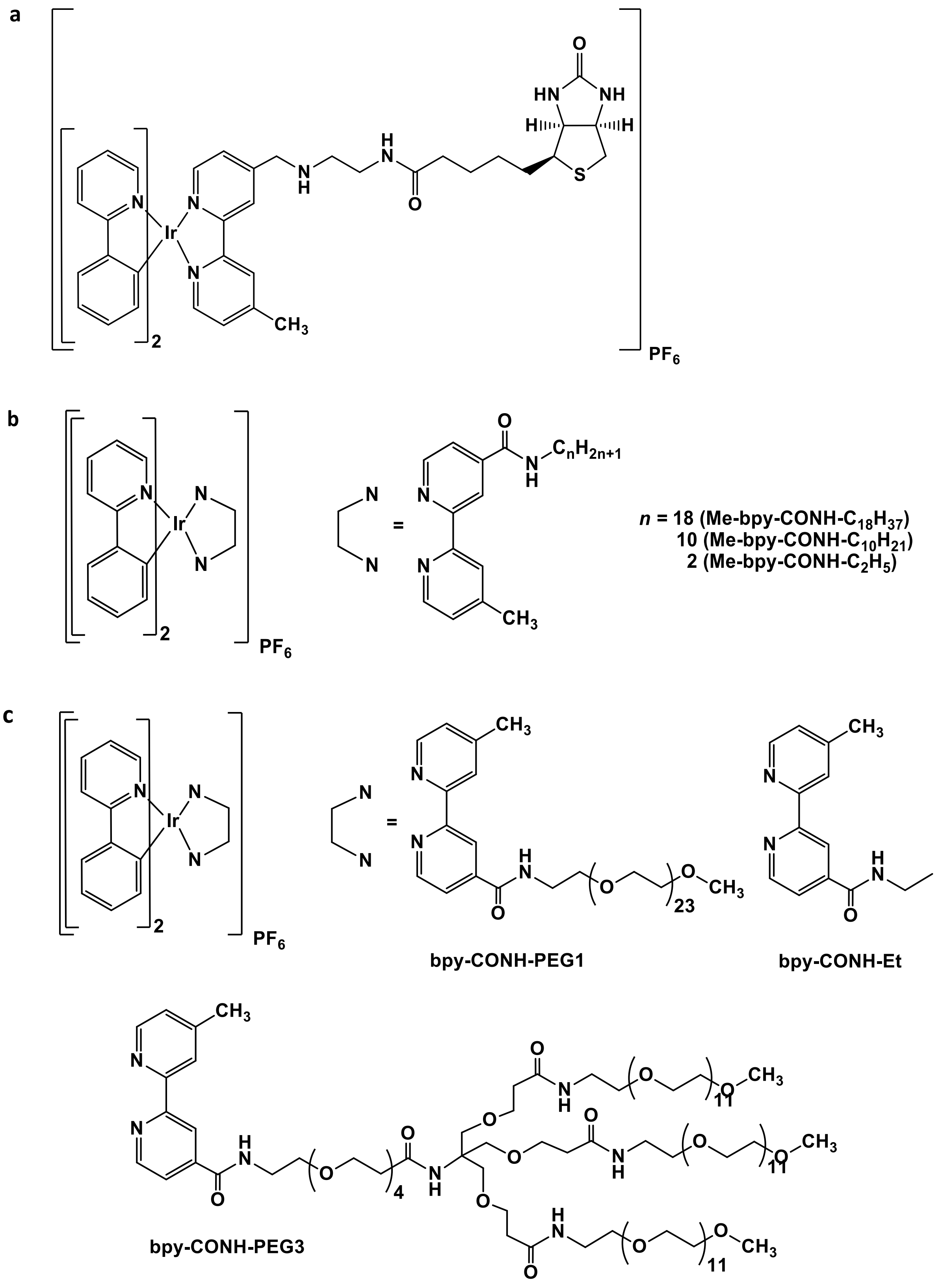

Figure 43. Cyclometalated Ir(III) complexes developed in the context of biological application. a) Biotin-conjugated Ir(III) complex. b) Aliphatic chains' functionalized Ir(III) complexes. c) PEG-modified Ir(III) complexes.

Whilst the luminescent properties of the biotin-conjugated complex were assessed in fluid solution[72], the effect of the introduction of the PEG moiety and various length alkyl chains in the coordination sphere, was mainly investigated in HeLa cells.

The studies[73] revealed an inclination of the luminophores to accumulate inside the cells and in particular, in the perinuclear region. Unfortunately, most of the Ir(III) probes bearing long alkyl chains displayed an elevated cytotoxicity, evaluated by the IC_{50} value.

Conversely, complexes functionalized with PEG chains bpy-CONH-PEG1 and bpy-CONH-PEG3,[74] showed a lower cytotoxicity due to the long chain substituents, which provide protection to the complex. This prevents the interaction between the Ir(III) emitters and the biomolecules, thus avoiding a response from the immune system to be triggered.

Velders *et al.*[75] investigated a series of modified $Ir(ppy)_3$ (ppy = 2-phenylpyrydine) complexes obtained introducing one, two and three amino acid fragments respectively on the ligands. In particular, the 5-position of the pyridine was functionalized with either alanine, lysine or glycine. The complexes reported in the study are depicted in **Figure 44**.

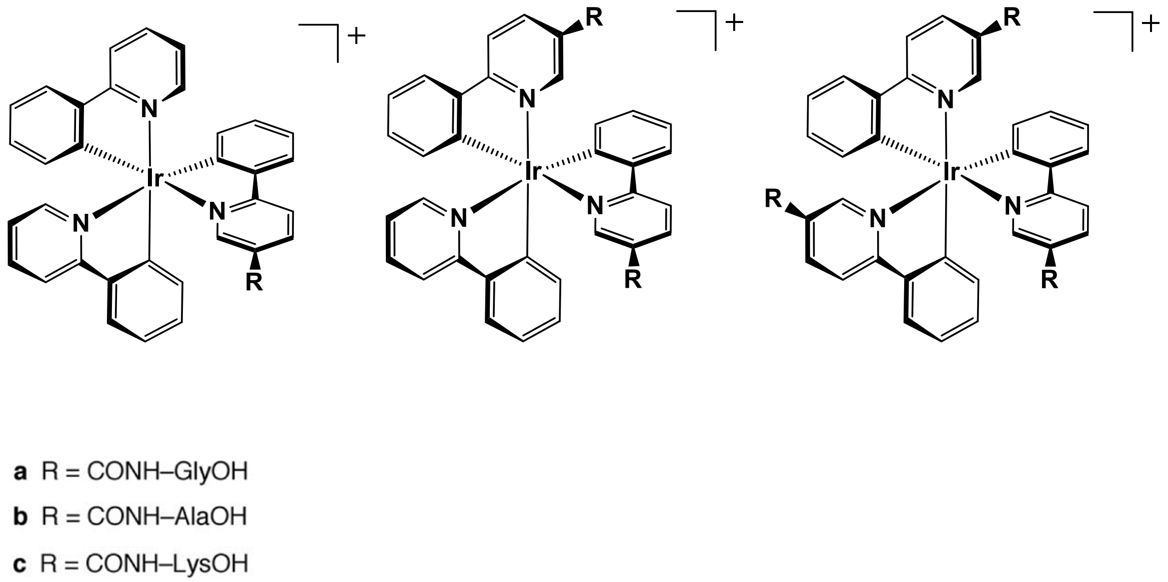

Figure 44. Molecular structure of the amino acids conjugated Ir(III) complexes developed by Velders et *al*.

The amino acid conjugates were investigated in mouse breast cancer cells to assess their cellular uptake,[75] their cell distribution and their photophysical properties in the biological media.

The bio-conjugation performed through introduction of a variable number of amino acid units allows to properly tune the water solubility of $Ir(ppy)_3$. Indeed, the backbone of the archetypal complex is hydrophobic, whilst the substituents are hydrophilic.

The experiments highlighted that the Ir(III) complexes bearing only one amino acid display a 20-fold more efficient cellular uptake with respect to the bis- and tris-substituted complexes. This evidence could be explained considering that the spontaneous cellular membrane crossing is more likely for small hydrophobic species thus, for the mono-functionalized complexes. The gradual increase in the number of the amino acids on the backbone, limits the passive diffusion process efficiency. In this context, the hydrophobicity of each complex was evaluated through theoretical calculations of the logarithm of the partition coefficient, indicated as LogP. LogP measures the hydrophilicity or hydrophobicity of a compound, relying on the partition of the considered solute in two immiscible solvents, namely a non-polar solvent and water.

The LogP values supported the aforementioned hypothesis. Furthermore, among the mono-substituted complexes, the one bearing the lysine moiety showed a higher hydrophobicity with respect to the alanine and glycine functionalized ones. Additionally, lysine could undergo protonation conferring a cationic nature to the probe, leading to an easier cellular uptake, since positive charges generally favor cells penetration.

The mono-amino acid conjugated complexes were then incubated in the cells at 37°C for 1h in a concentration equal to 10 μM to observe cells staining.[75] The complex functionalized with lysine displayed a homogenous distribution of the probe all over the cell, except for the nucleus, where no staining was observed. On the other hand, glycine and alanine conjugates preferentially localized in the lysosomes.

Lastly, the photoluminescent properties of the amino acid conjugated Ir(III) complexes were investigated in vitro.[75] The study revealed that all the variously functionalized probes display emission in the range of 564-585 nm and the quantum yield values have led to the conclusion that Ir(III) cyclometalated complexes preserve their optimal photophysical features in the biological media.

Overall, the modification of the archetypal $Ir(ppy)_3$ complex through conjugation with various molecules, provides a promising strategy to improve biocompatibility of Ir(III) based emitters with the purpose to design excellent bright luminophores for biological applications.

The aforementioned investigations prompted us to design, synthesize and characterize a series of Ir(III) complexes meant to be used as luminescent labels for bioimaging. In this context, three tryptophan conjugated Ir(III) luminophores complexed with various cyclometalated ligands and a glucose-conjugated Ir(III) complex were developed. Additionally, two Ir(III) based emitters bearing proper anchoring functional groups such as hydroxymethyl and azide, were prepared aiming to exploit them as backbones for the introduction of biologically relevant substrates.

The molecular structure of the designed compounds is reported in **Figure 45.**

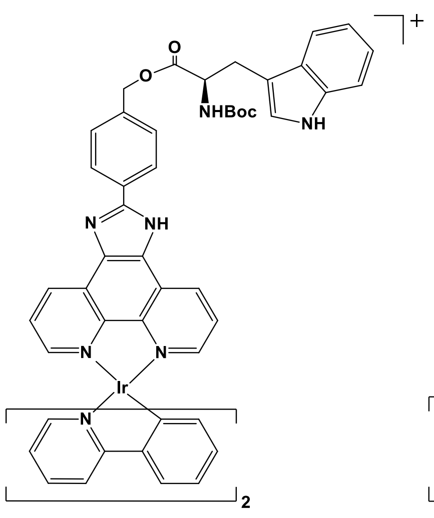

Ir-1

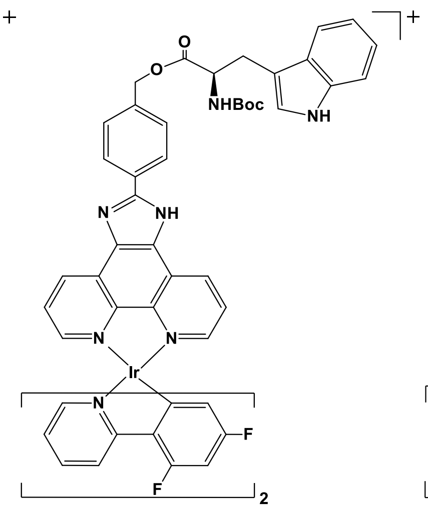

Ir-2

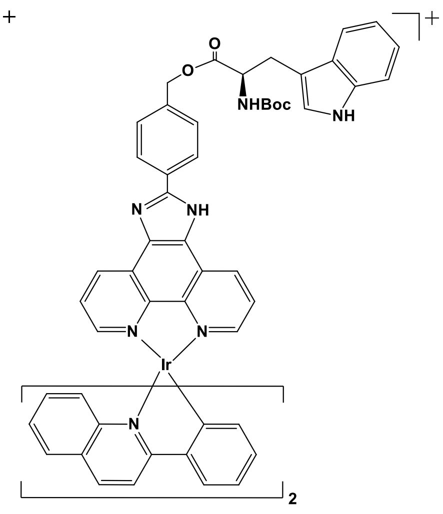

Ir-3

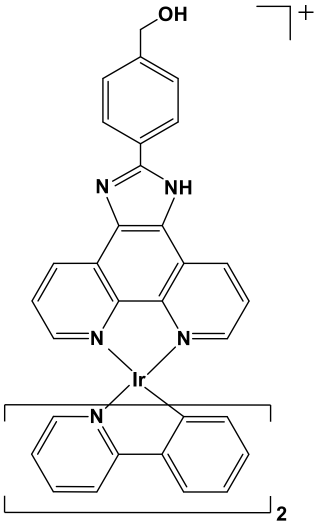

Ir-4

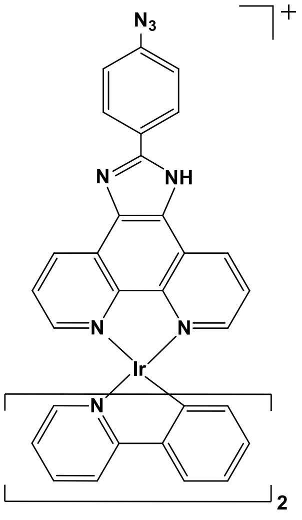

Ir-5

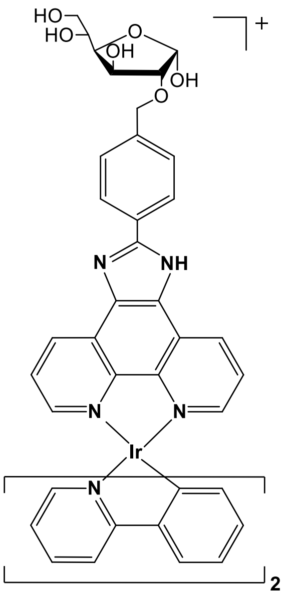

Ir-6

Figure 45. Molecular structure of the developed Ir(II) based emitters for bioimaging.

3.2 Targeting cancer metabolism to selectively address emitters in the biological environment

Tumorigenesis, namely the indiscriminate cellular proliferation mechanism that leads to metabolic alterations, gathered significant attention over the past decades.[76] In this context, cancer cells require a considerable amount of nutrients and metabolites to fulfill the energy requirement for replication and preservation. Hence, the cellular metabolism results reprogrammed, aiming to maintain the tumorigenic state. Concerning the biosynthetic pathways, glucose and glutamine play a crucial role, since they are catabolized to create the carbon intermediates used as building blocks for the biosynthesis of biologically relevant substrates.

In the 1920s Otto Warburg[77] set a milestone in the context of cancer metabolism, discovering that glucose consumption to produce lactate was considerable and more rapid in tumor cells with respect to healthy cells, independently from the oxygen availability within the surrounding tissues. The phenomenon observed was named Warburg effect or aerobic glycolysis.

Subsequently, Harry Eagle[78] observed an analogous process involving glutamine. The amount of glutamine supply required for malignant cells proliferation resulted significantly enhanced. Indeed, glutamine plays a central role in the biological environment, being involved in the biosynthesis of nitrogen-containing substrates as nucleotides and non-essential amino acids. In addition, glutamine is also implicated in the assimilation of essential amino acids, which are taken up from external sources. In particular, it was observed that the intake of leucine, an essential amino acid, is accompanied to an efflux of glutamine.[79]

Consequently, the concentration of intracellular glutamine promotes the uptake of amino acids through the corresponding transporter which is mainly the L-type amino acids transporter LAT1.

Along with these discoveries, the alteration of other significant biological substrates was assessed, including a series of amino acids.[76]

Given these premises, studies concerning tumorigenesis and cancer cells metabolism gained remarkable interest in the context of the development of agents for cancer therapy and for bioimaging.

3.2.1 Targeting cancer cells through L-tryptophan transporters

The altered metabolism of amino acids in tumoral tissues involves various modifications that are common to all cancers, independently from the subtype.[76] In-depth studies reported that:

- The requirement of nitrogen needed for the biosynthesis of metabolites and macromolecules results increased;
- The rapid consumption of the amino acids is associated with the overexpression of their transporters to provide the appropriate income of amino acids;
- The enzymes involved in the biochemistry of the amino acids are produced in altered concentrations.

L-type amino acids transporters (LATs), are responsible for the uptake of amino acidic substrates inside the cells. Until now, four types of LATs have been identified, namely LAT1, LAT2, LAT3 and LAT4. Among them, LAT1 transporters play a central role since they assist the uptake of large neutral aromatic amino acids.

In healthy cells of some organs such as brain or spleen, LAT1 transporters are poorly expressed. Conversely, studies highlighted their strong overexpression in various tumors such as in malignant cells of mouth, breast and cervix.[80, 81]

Furthermore, it was observed that the upregulation of LAT1 transporters in malignant cancers is enhanced with respect to benign cancers.[82]

LAT1 transporters conformation consists of twelve transmembrane domains bond through a sulfur bridge to a glycoprotein macromolecule which confers stability to the cylindrical structure inserted inside the cell membrane (**Figure 46**).[83, 84]

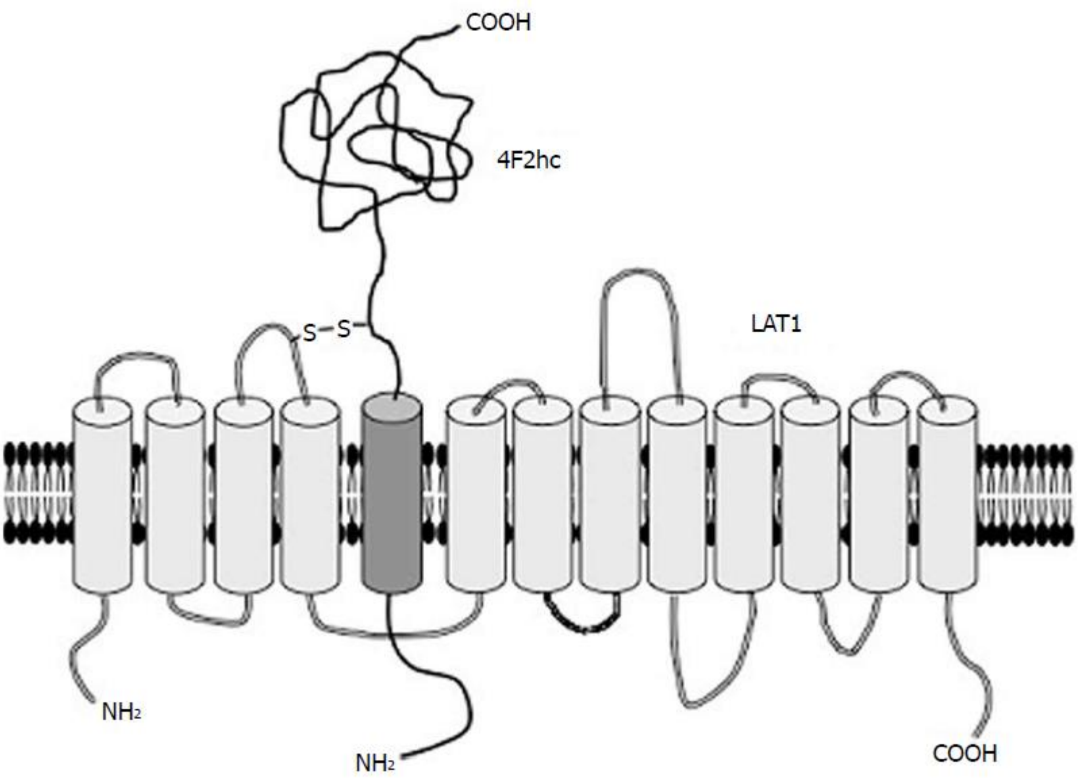

Figure 46. Illustration of the transmembrane LAT1 transporter configuration, that is associated with the 4F2hc transmembrane protein, which confers stability to LAT1.

LAT1 represents an efficient transporter for polar uncharged amino acids and this explains why it plays such a crucial role in the tumorigenesis. In particular, it was assessed that the binding affinity provided by LAT1 for leucine is significantly larger[85] with respect to that of LAT2, even though the concentration of LAT2 in healthy tissues is much higher.[86]

Besides leucine, tryptophan represents another biologically relevant substrate, since it is involved in various biosynthetic pathways.

Remarkably, tryptophan is the precursor of two significant biomolecules: serotonin and L-kynurenine. Studies revealed that 95% of tryptophan enters in the kynurenine pathway and it is converted in kynurenines, the metabolites produced in the synthetic route.[87]

As depicted in **Scheme 1**, the very first reaction encountered in the path is the conversion of tryptophan into N-formyl-L-kynurenine through the rate-limiting enzymes 2,3-dioxygenase (TDO) and indoleamine 2,3-dioxygenase (IDO).[88, 89]

N-formyl-L-kynurenine then undergoes a degradation to L-kynurenine by formamidase. L-kynurenine provides a crucial substrate especially in the central nervous system (CNS), since it can be channeled in three different pathways, giving rise to the generation of other biologically significant biomolecules as schematically shown in **Scheme 1**.[88]

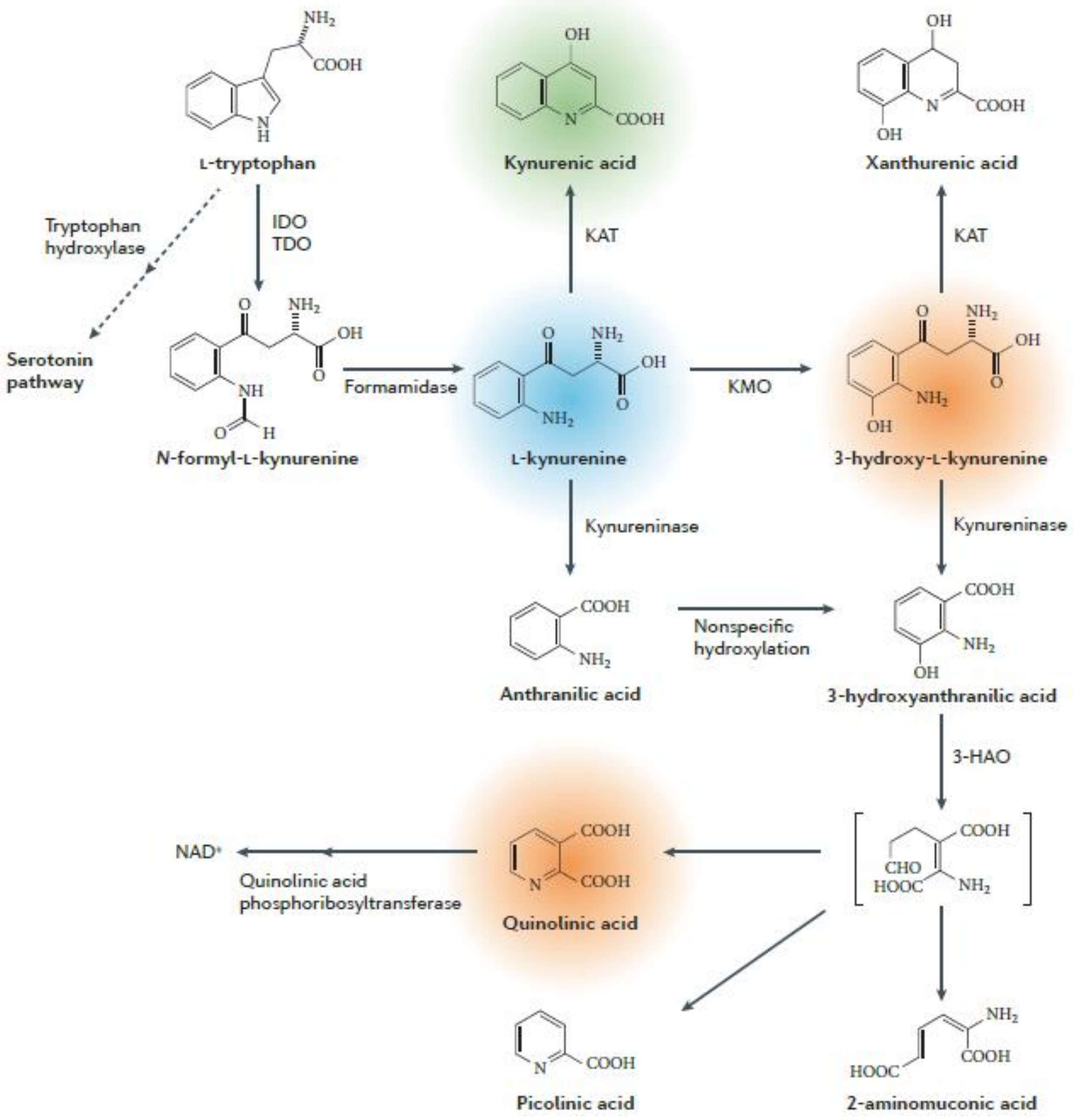

Scheme 1. Schematic representation of the kynurenine pathway, in which tryptophan plays a central role.

Notably, the kynurenine pathway and the serotonin biosynthesis take place in the brain, implying that tryptophan penetrates in the blood-brain-barrier (BBB).[90]

Brain cells uptake of amino acids from the blood stream involves two steps: the permeation through the brain capillary endothelial wall, which constitutes the BBB, and the penetration of the cellular membrane of the brain cells. Considering that the surface area of the BBB is considerably lower than that of the brain cells plasma membranes, the rate-limiting process during the transport of the species is represented by the penetration of the BBB. BBB is indeed constituted by two membranes, namely luminal and abluminal membranes, thus the uptake of substrates has to be regulated through carriers.[90]

Specifically, tryptophan exploits the transporters for neutral aromatic amino acids mainly LAT1, as depicted above.

The possibility to channel tryptophan, a key biomolecule, inside brain cells through facile BBB permeation, represents an outstanding point for the design of molecules meant for bioimaging or cancer therapy applications.

In addition, the contribution given by LAT transporters in the context of a tumorous condition leads to the overexpression of this type of carriers, enabling the influx of an increased concentration of tryptophan with respect to healthy tissues.

Taken together, these premises highlight the potential of tryptophan as a targeting vector for the design of innovative bio-conjugated emitters.

3.2.1.1 Binding L-tryptophan to Ir(III) complexes: state of the art

Iridium cyclometalated complexes provide a remarkable class of emitters, due to their proven outstanding photophysical properties. The highly efficient intersystem crossing involved in the photoluminescent phenomenon and the long life-time of the excited state makes these typology of organometallic compounds very appealing for a wide range of applications.[38, 91, 92, 93, 95, 96]

Nevertheless, the emission induced upon irradiation with a light source, can be affected by the selected ligands composing the coordination sphere, or by other neighboring substrates that can interact with the emitter. This feature offers the possibility to design chemosensors, aiming to detect specific substrates in the surrounding environment.

In particular, Pang *et al.*[97] investigated a water soluble Ir(III) complex responsive to tryptophan in cells media. The molecular structure of the cationic complex involves two 2-phenylquinoline as the cyclometalated ligands and a 2,2′-bipyridine bearing two carboxylates as functional groups on the 4 and 4′ positions of the rings. The molecular representation of the described complex is reported below (**Figure 47**).

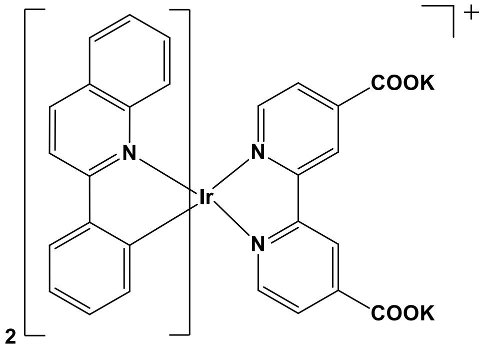

Figure 47. Molecular structure of the cyclometalated Ir(III) sensor for tryptophan detection developed by Pang *et al.*.

Photoluminescent analysis were performed[97] in Phosphate Buffered Saline (PBS) at physiological pH (7.4) to recreate the biological environment and the most intense emission was observed at λ = 577 nm. Then, tryptophan was gradually introduced in the PBS solution, slowly increasing the concentration starting from 1 x 10^{-9} to 1 x 10^{-4} M. Remarkably, phosphorescence intensity is affected by the presence of tryptophan, evidencing a gradual quenching accompanied by a shift of the emission band at λ = 589 nm. Plotting the phosphorescence intensity data and the corresponding concentration of tryptophan, a good linear relationship was assessed, meaning that the water soluble Ir(III) complex displays an excellent selectivity towards tryptophan. Aiming to achieve a complete investigation, Pang *et al.*[97] carried out the quenching assay using a variety of amin acids, concluding that besides tryptophan, no other amino acid influences the photoluminescence intensity of the Ir(III) complex. This represents a very promising result, suggesting its potential as a selective chemosensor for tryptophan.

Density functional theory (DFT) calculation clarified the underlying reason behind the phosphorescence quenching. Upon excitation of the Ir complex, the nitrogen on the indole of tryptophan interacts with the carboxylates introduced on the backbone, giving rise to the formation of hydrogen bonds. Considering that, the Ir(III) complex represents an electron acceptor, whilst tryptophan is a donor. Consequently, the formation of a donor-acceptor complex occurs enabling the photoinduced electron-transfer (PET) process.

Notably, DFT studies determined that in the absence of a quencher, the transition induced by irradiation of the fluorophore involves the displacement of the electron from the HOMO (-4.90 eV) to the LUMO (-5.72 eV). Conversely, when tryptophan is introduced, an electron from the HOMO of the amino acidic substrate is transferred to the HOMO of the Ir(III) complex, leading to the extinction of phosphorescence through photoinduced electron-transfer. Indeed, tryptophan's HOMO displays an energy of -5.09 eV, thus it is located in-between the Ir(III) complex molecular orbitals. The schematic representation of the described mechanism is reported in **Figure 48**.

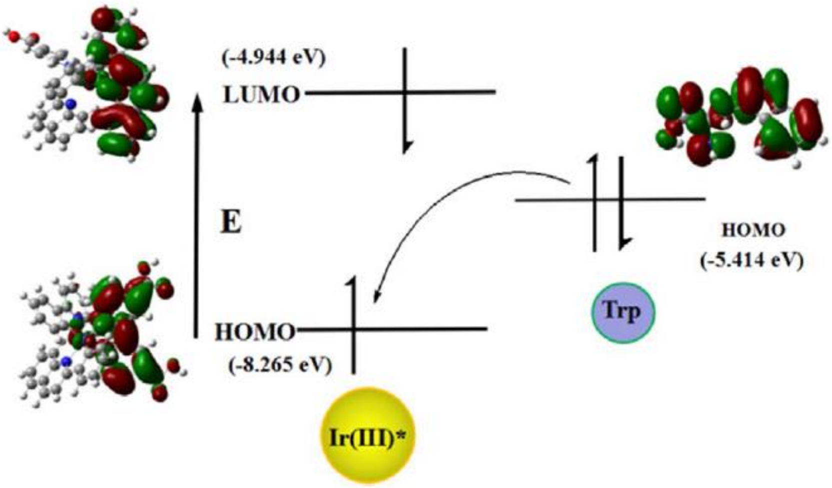

Figure 48. Scheme representing the electron-transfer induced upon photo-excitation as a consequence of the interaction between the Ir(III) complex and tryptophan.

Pang *et al.*[97] also studied the interplay between the designed water soluble Ir(III) complex and the bovine serum albumin (BSA). In contrast with the observations made in the context of the interactions with tryptophan, a significant enhancement of the photoluminescent intensity was assessed as a consequence of the encapsulation in the BSA.

Overall, the possibility to evaluate a remarkable modification of the Ir(III) complexes emission properties through the interaction with specific substrates, represents a very useful tool to control the photoluminescence intensity.

The reported investigation concerning the modulation of the Ir(III) complex emission provided by tryptophan, represents an example of weak interaction occurring within the considered substrates. Nevertheless, to our knowledge, no cationic Ir(III) complexes covalently functionalized through ester bond with tryptophan have been reported in literature to date.

Given these premises, a series of covalently modified tryptophan-conjugated cyclometalated Ir(III) complexes (**Figure 49**) were designed, synthesized and characterized, aiming to enhance the already optimal photoluminescent properties displayed by these typology of emitters.

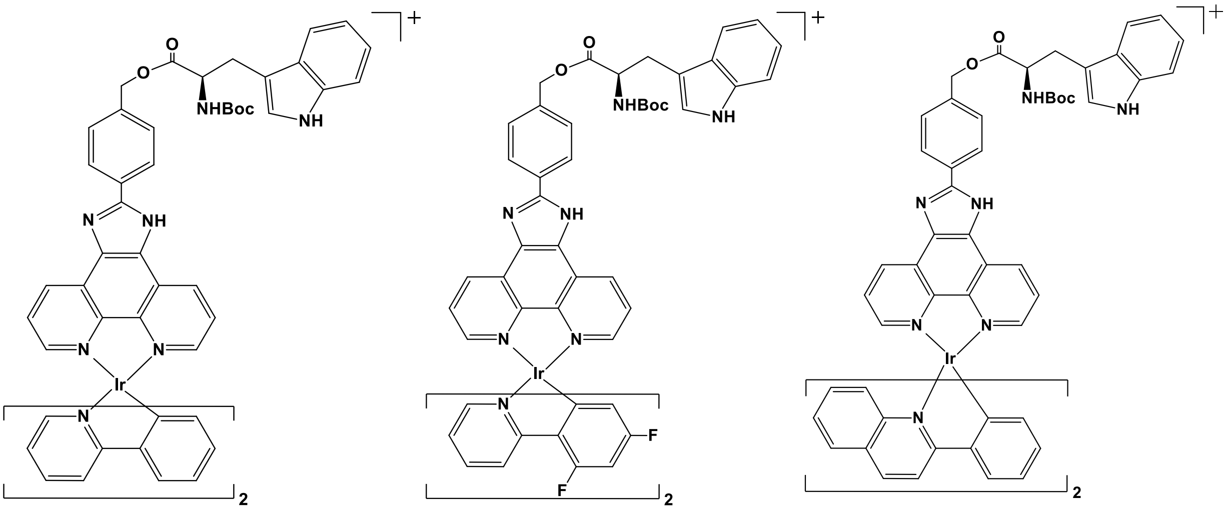

Ir-1 **Ir-2** **Ir-3**

Figure 49. Molecular structure of the designed cationic tryptophan conjugated Ir(III) complexes.

3.2.2 The role of glucose in tumorigenesis: an overview

Metabolic alterations induced by tumorigenesis play a significant role for the development of efficient cancer therapies. Remarkable consumption of glucose represents a sign of the increased demand of nutrients supply required for the proliferation and survival of tumorous cells.

In healthy cells, a glucose molecule is metabolized *via* glycolysis, a process occurring in the cytoplasmic region of the cells in which the sugar molecule is finally converted into two molecules of ATP to produce energy and a molecule of pyruvate.[98] Pyruvate in turn enters the Krebs cycle, also known as tricarboxylic acid (TCA) cycle or citric acid cycle, taking place in the mitochondria where it undergoes a series of biochemical reactions to drastically increase the amount of ATP up to 36-38 molecules. In particular, pyruvate is firstly converted into Acetyl-coenzyme A (Acetyl-CoA) through decarboxylation with concomitant generation of reduced nicotinamide adenine dinucleotide (NADH).

Nevertheless, acetyl-CoA derives from the oxidation of biological relevant substrates such as fatty acids, acetate, amino acids and ketone bodies as well. The thus produced acetyl-CoA is then converted into citrate, which represents a key substrate, since it is regenerated at the end of the cycle. Indeed, citrate undergoes several reactions to be transformed into oxalacetate which is then reconverted into citrate through the citrate synthase enzyme.

Throughout the process, the biosynthesis of NADH plays a crucial role, providing the reduction potential for the further production of ATP through oxidative phosphorylation, a process involving the electron transfer through the mitochondrial respiratory chain complexes.[99]

Oxidative phosphorylation leads to the complete degradation of glucose into CO_2 and H_2O. The depicted process is aerobic, thus is strongly oxygen-dependent. The schematic representation of glycolysis and TCA cycle is reported in **Figure 50**.

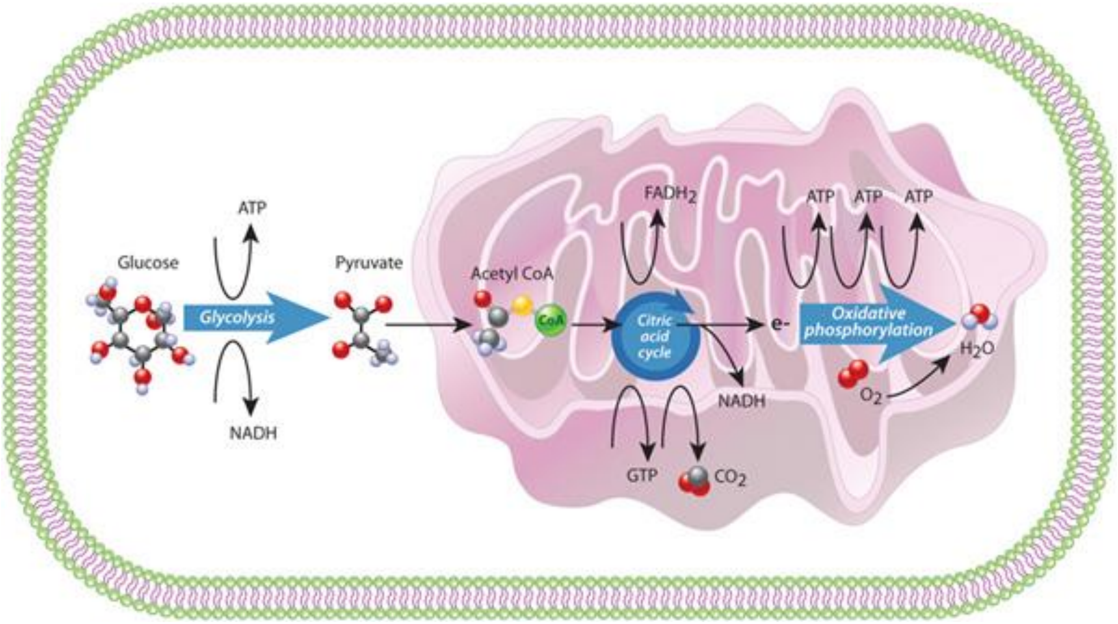

Figure 50. Illustration of the metabolic pathways involving glucose in the eukaryotic cells: the glycolysis is followed by the citric acid cycle, to finally allow the oxidative phosphorylation.

Conversely, when oxygen is not available in the surrounding environment, pyruvate is directly converted into lactic acid rather than enter the Krebs' cycle. Alterations within the TCA cycle have been observed with the occurrence of numerous diseases.[100] Specifically, the significant conversion of pyruvate into lactic acid has been assessed and that's further supported by the ascertained decreased NADH concentration, leading to the conclusion that anaerobic pathways are favored over TCA cycle. The described mechanism is known as Warburg effect, which was noticed even with perfectly functioning mitochondria.[101]

Overall, huge amounts of glucose are readily taken up and consumed giving rise to generation of two ATP molecules and lactate, resulting in a very inefficient and wasteful process. In addition, the increased concentration of lactate provokes the acidification of the surrounding environment which is very deleterious for healthy cells. Hence, glucose is quickly metabolized, and the pace of glycolysis is altered. In healthy oxygenated tissues, lactate shouldn't be present.[102]

As a consequence, the energy metabolism results compromised, and the amount of glucose required to compensate its quick consumption results drastically increased. In this context, the glucose plasma membrane transporter GLUT1 was found overexpressed in a variety of cancers (ovary, kidney, breast, brain, colon).[103, 104, 105]

The huge influx of glucose observed within malignant cells opens up to new strategies for the development of therapeutic agents. The appendage of the glucose moiety on the backbone of a functional substrate can be exploited as a targeting vector to selectively address the therapeutics inside tumor cells through the upregulated transporters.

In this context, Pt(II) and Ir(III) based glucose-conjugated emitters (**Figure 51**) were designed and synthesized aiming to develop efficient luminescent labels for bioimaging and targeted photosensitizers for photodynamic therapy.

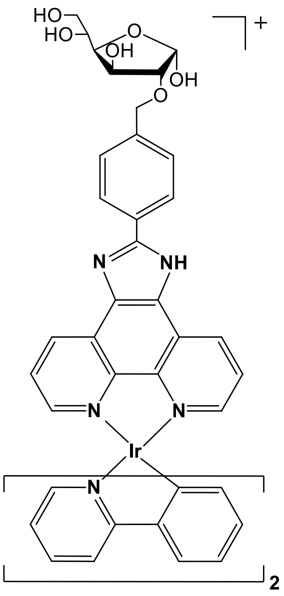

Ir-6

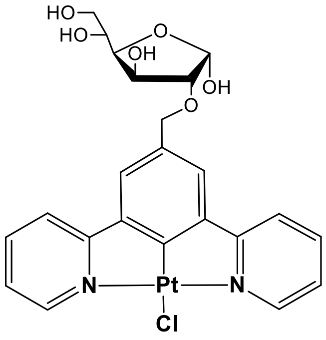

Pt-11

Figure 51. Molecular structure of the developed Ir(III) and Pt(II) glucose-appended complexes.

3.2.3 Synthesis and characterization of bioconjugated Pt(II) and Ir(III) complexes

3.2.3.1 Synthesis of a tryptophan conjugated Pt(II) cyclometalated complex

The importance of bioconjugation prompted us to design and synthesize a tryptophan conjugated cyclometalated Pt(II) complex (**Figure 52**).

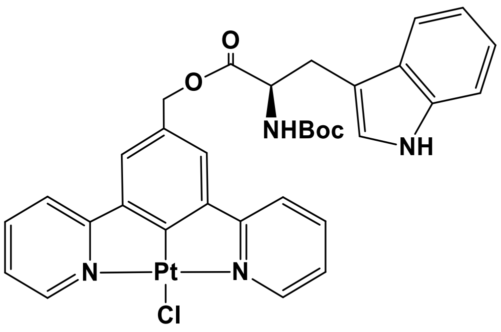

Pt-10

Figure 52. Molecular structure of the tryptophan conjugated emitter Pt-10.

The introduction of the amino acid moiety was performed on the ligand backbone, through the hydroxyl group. The detailed synthetic procedure is reported in Chapter III.

At first, the ligand backbone was prepared starting from 3,5-dibromobenzyl alcohol and 2-(tri-*n*-butylstannyl)pyridine through a Stille coupling, according to literature.[106] The cyclometalated moiety was then functionalized with the Boc-protected tryptophan, using HOBt, EDCI and Et_3N dissolved in dry DCM.[107]

The purified tryptophan-conjugated compound was fully characterized through NMR analysis and mass spectrometry.

Finally, the complexation was attempted combining the synthesized N^C^N ligand with K_2PtCl_4 in an acetonitrile:water mixture (9/1, v/v) under inert atmosphere and then heating under reflux for 72h.

In the end, a brown suspension was obtained and isolated through filtration on a Nylon membrane. The brown solid was washed with water, MeOH and diethyl ether. The product displayed poor solubilty towards any organic and water-based solvent. Aiming to perform the characterization of the product, it was solubilized in d_6-DMSO but no clear peaks were observed, even after optimization of the acquisition parameters.

3.2.3.2 Synthesis of a glucose conjugated cyclometalated Pt(II) complex

The central role played by glucose in multiple biological pathways, encouraged the design of a glucose conjugated cyclometalated Pt(II) complex (**Figure 53**). In this context, the glucose moiety was introduced on the chelating ligand through a multi-step synthetic route. The details concerning the synthetic procedure are reported in Chapter III.

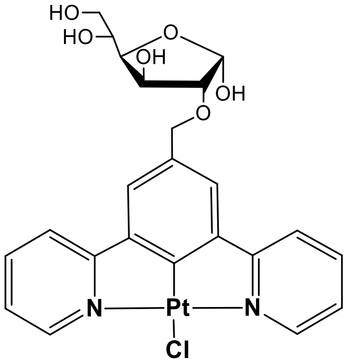

Pt-11

Figure 53. Molecular structure of the designed glucose conjugated emitter.

The assembly of the ligand backbone was achieved through a Stille coupling combining 3,5-dibromobenzyl alchol and 2-(tri-*n*-butylstannyl)pyridine.[106] The hydroxymethyl group was then treated with a 48% HBr solution in MeOH aiming to convert the oxygenated function into a bromine atom, crucial to carry out a nucleophilic substitution.

In parallel, the glucose moiety was prepared performing a series of protections with benzyl groups and selective deprotections starting from 1,2-*O*-isopropylidene-α-D-glucofuranose to obtain the suitable substrate for the subsequent bioconjugation.[108]

In the end, the nucleophilic substitution between the two building blocks in the presence of NaH in DMF was performed, accomplishing the synthesis of the desired glucose conjugated ligand.

Two synthetic approaches were equally possible to afford **Pt-11**: either to deprotect the glucose moiety before the complexation, or to perform the deprotection as the very last step of the synthetic route.

Due to potential solubility issues arising from the free hydroxyl groups on the sugar, the platination was attempted using the protected glucose moiety, reacting the cyclometalated ligand and K_2PtCl_4 in an acetonitrile:water mixture (9/1, v/v), heating at 110°C for 72h. The suspension obtained was filtered and washed with water, MeOH and diethyl ether.

The collected solid was analyzed through NMR, which highlighted the presence of impurities. Despite the poor solubility displayed by the product, consecutive crystallizations with a mixture of DCM and diethyl ether were attempted aiming to isolate the pure Pt(II) complex.

Nevertheless, ^{1}H-NMR confirmed the persisting presence of impurities. Alternative purification approaches were adopted, but due to the solubility issues, the isolation of the glucose conjugated Pt(II) complex was not achieved.

Hence, alternatively, the free ligand was dissolved in MeOH and treated with H_2 in the presence of palladium on carbon (Pd/C) to attempt the deprotection of the glucose moiety prior complexation but no deprotection was assessed. Thus, the debenzylation was carried out through the combination of ammonim formate and Pd/C under H_2 atmosphere. ^{1}H-NMR characterization evidenced the presence of the benzyl groups. As the final attempt, the deprotection of the glucose moiety was attempted under hydrogen atmosphere, using $Pd(OH)_2$ on carbon in MeOH. Even in this case, the benzyl groups removal was not achieved.

Purification and deprotection issues didn’t allow to obtain the targeted glucose conjugated Pt(II) complex **Pt-11.**

3.2.3.3 Synthesis of a Pt complex for bioconjugation through exchange of the ancillary ligand

With the purpose to insert the glucose moiety on the organometallic complex, an alternative approach with respect to the functionalization of the cyclometalated backbone was adopted. In particular, a specifically designed ancillary ligand containing an hydroxyl anchoring group was synthesized, (**Figure 54**) aiming to subsequently perform the exchange of the chlorine atom with the developed substrate. The introduction of the hydroxyl group allows to further modify the ancillary ligand through glucose conjugation, making the designed system very appealing.

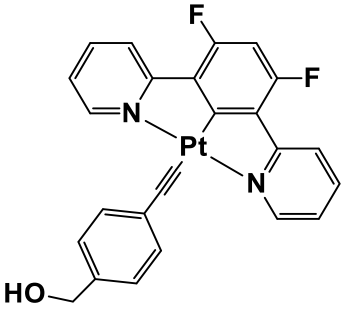

Pt-9

Figure 54. Molecular structure of the Pt-9, developed for further functionalization with a biologically relevant substrate.

The starting fluorinated cyclometalated Pt(II) complex has been extensively described in literature[109] due to its excellent photophysical properties and versatility. The synthetic route followed to obtain it, is described in detail in the Experimental Section (Chapter III).

The ligand backbone was prepared through a Suzuki coupling between the 2-Bromopyridine and the pinacol ester of benzene-1,3-difluoro-4,6-diboronic acid. Subsequently, the platination was performed reacting the fluorinated ligand with K_2PtCl_4 in an acetonitrile:water mixture (9/1, v/v), heating at 110°C for 72h.

In the end, the exchange of the chlorine in the coordination sphere was achieved introducing (4-ethynylphenyl)methanol in the presence of CuI and freshly distilled iPr_2NH in dry DCM.[110] The reaction was run for 72h heating at 80°C and a blue suspension was obtained.

The solid was isolated through filtration, washed many times with abundant MeOH and dried. A complete characterization of the compound couldn't be performed due to severe solubility issues. ^{1}H-NMR spectrum was recorded in d_6-DMSO, but the peaks couldn't be clearly assigned.

3.2.3.4 Synthesis of a cyclometalated Pt(II) complex for bioconjugation

The successful achievement obtained with the highly hindered functionalized Pt complexes **Pt-1** to **Pt-8,** prompted us to profit from the developed synthetic route to accomplish the synthesis of an innovative Pt(II) complex built to subsequently perform bioconjugation. In particular, the project aimed to prepare a cyclometalated Pt(II) complex introducing the hydroxymethyl moiety on the para position of the pyridin rings, in order to create an appendage for the insertion of a biologically relevant substrate (**Figure 55**).

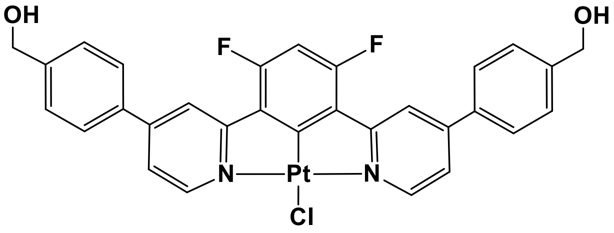

Pt-12

Figure 55. Molecular structure of Pt-12, functionalized two hydroxymethyl groups on the pyridine rings.

The procedure envisaged three steps, as briefly described for **Pt-1** to **Pt-8** and as discussed in detail in Chapter III.

At first, the reaction between p-Bromobenzylalcohol and 2-chloro-pyridine-4-boronic acid was perfomed to obtain the desired modified pyridinic substrate. Then, the intermediate was combined with the pinacol ester of benzene-1,3-difluoro-4,6-diboronic acid to build the backbone of the cyclometalated ligand. The NMR analisys performed on the species collected following the purification through chromatrography, highlighted that the major product obtained from the second Suzuki coupling was the N^C derivative, resulting from the coupling and the subsequent deborylation (**Figure 56**)

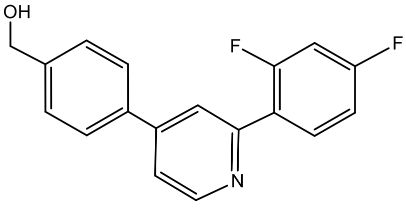

Figure 56. Molecular structure of the N^C species obtained as the main product of the second Suzuki coupling performed.

Given the outcome of the reaction, the platination couldn't be performed.

Nevertheless, the bidentate species provides a good candidate for the complexation of Ir(III) thus, the complexation with the Ir(III) dimer $[Ir(ppy)_2Cl]_2$ (ppy: 2-phenylpyridine) was attempted. The isolated N^C ligand and the 2-pyridylbenzene Ir dimer were thus combined in a DCM:MeOH mixture (1/1, v/v) and heated at 50°C overnight to achieve the synthesis of the corresponding Ir(III) complex. The suspension was cooled down to room temperature and filtered. The poor solubility of the isolated product prevented the characterization to be performed.

3.2.3.5 Synthesis of a series tryptophan-conjugated cyclometalated Ir(III) complexes

Tryptophan provides a relevant substrate within the biological environment due to the numerous biochemical pathways in which it is involved. The relevant role played in the cellular equilibrium prompted us to design and synthesize a series of cationic tryptophan conjugated Ir(III) complexes (**Figure 57**).

Ir-1, **Ir-2** and **Ir-3** were prepared following a common pathway, introducing various cyclometalated ancillary ligands with the purpose to tune their photophysical properties and optimize their efficiency. The detailed synthetic procedure is reported in Chapter III.

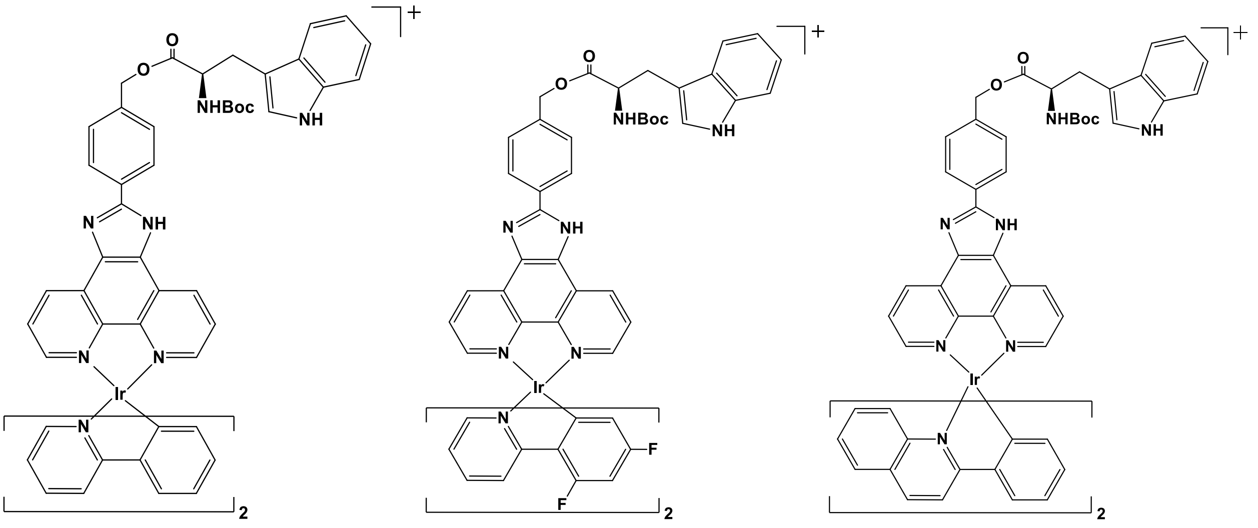

Ir-1 **Ir-2** **Ir-3**

Figure 57. Molecular structure of the designed tryptophan conjugated Ir(III) complexes Ir-1, Ir-2 and Ir-3.

The three complexes were obtained starting from the assembly of the phenanthroline-based scaffold, which was synthesized through reaction between 1,10-phenanthroline-5,6-dione and 4-(4-hydroxymethyl)benzaldehyde.[38]

The formation of the acetylated derivative as the by-product was assessed, thus the mixture was treated with a 30% solution of MeONa in MeOH to displace the acetyl group and deprotect the hydroxymethyl moiety, crucial for the following step.

Then, Boc-protected tryptophan was introduced on the anchoring hydroxyl group through condensation, performed in the presence of HOBt, EDCI and Et_3N in a solution of amine free DMF.[107]

In parallel, the three Ir based precursors necessary for the subsequent complexation reaction were prepared.[111]

Specifically, $IrCl_3 \bullet xH_2O$ was combined with the cyclometalated ligands 2-phenylpyridine, 2-(2,4-Difluorophenyl)pyridine and 2-Phenylquinoline, respectively. In the end, a suspension was obtained and the desired Ir dimers were isolated through filtration. The impurities were then removed dissolving the crude products in concentrated solutions of DCM and inducing the precipitation of the pure fractions with diethyl ether.

To complete the synthetic pathway, the tryptophan-conjugated backbone and the suitable dimer were let react in a mixture of DCM:MeOH (1/1, v/v) overnight at 50°C.[112]

The desired Ir(III) complexes were afforded as an orange or yellow powder after treatment of the reaction mixture with a 6-fold excess of KPF_6. The final products were purified through crystallization with DCM and diethyl ether.

The achievement of the desired complexes synthesis can be assessed through ^{1}H-NMR, where the introduction of Ir(III) and its coordination sphere, display significant differences with respect to the free ligand pattern. As a reference, the ^{1}H-NMR of the tryptophan conjugated free ligand (**19**) and of **Ir-1** are reported in **Figure 58** aiming to underline the modifications occurring as a consequence of complexation. Specifically, a shift of the signal arising from the resonance of the hydrogens placed in the 2 and 9 position of the phenanthroline moiety can be observed.

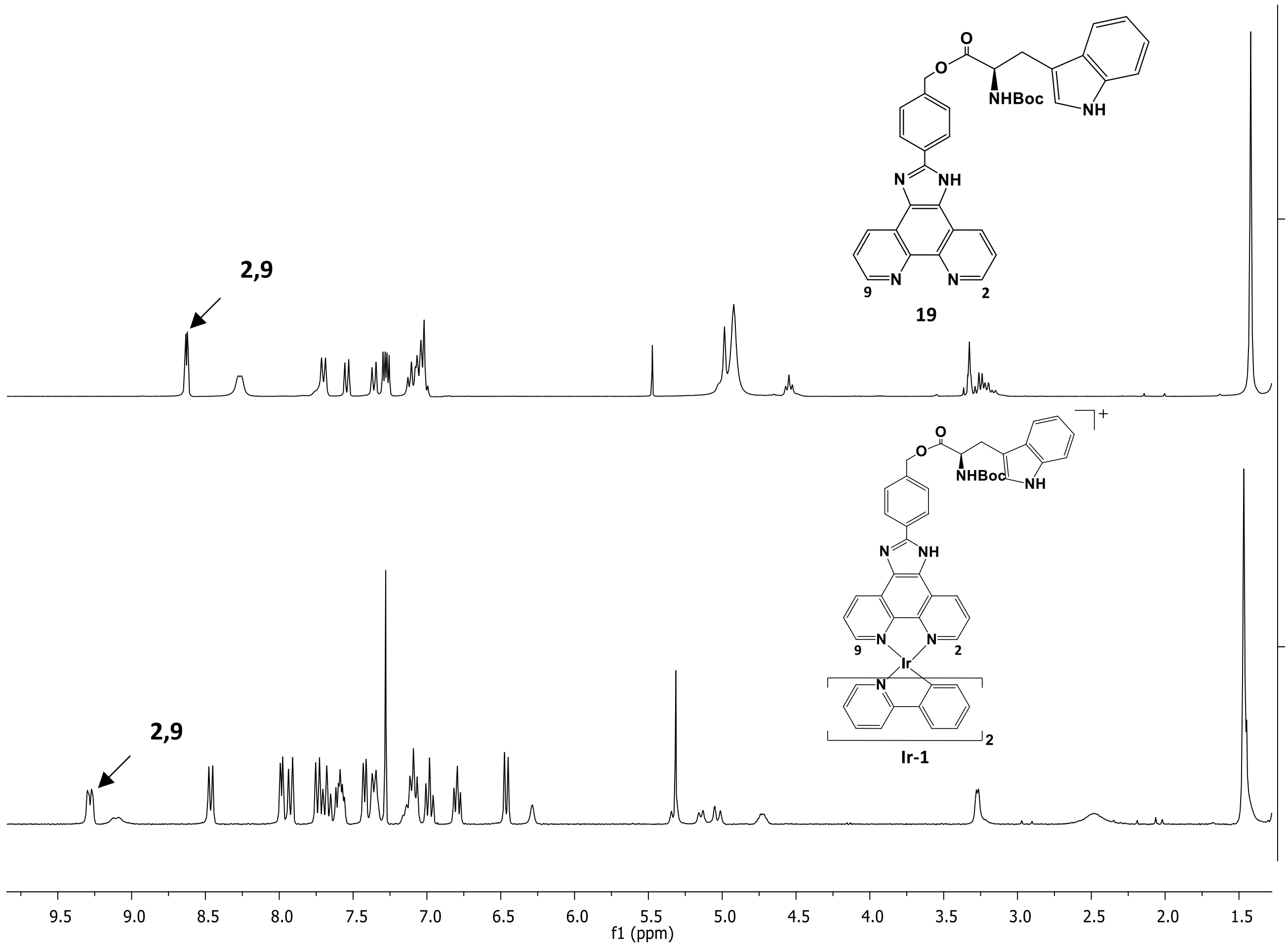

Figure 58. ^{1}H-NMR spectra of compound 19 and the related Ir(III) complex. The comparison between the two patterns highlights a significant difference within the observed signals. Specifically, the doublet at ~ 8.5 ppm arising from the resonance of the hydrogens in 2 and 9 position, tend to shift after complexation with the Ir(III) ion.

Ir-1, **Ir-2** and **Ir-3** were fully characterized *via* ^{1}H-NMR, ^{13}C-NMR spectroscopy, mass spectrometry and elemental analysis. Additional information regarding the purity of **Ir-2** were obtained recording the ^{19}F-NMR.

Furthermore, photophysical analysis were performed to assess their effectiveness as emitters and to investigate the effect induced by the different ancillary ligands on the electronic structure of the Ir(III) complexes. The photoluminescent properties will also be tested *in vitro* in the biological environment *via* insertion in the brain cells. The biological assays are still in progress.

3.2.3.6 Synthesis attempt of a glucose-conjugated cyclometalated Ir(III) complex

The potential use of glucose to significantly increase the influx of targeted emitters inside cancer cells, and the promising photophysical properties displayed by the phenanthroline-based Ir(III) complexes, prompted us to design a glucose conjugated luminophore (**Ir-6**, **Figure 59**).

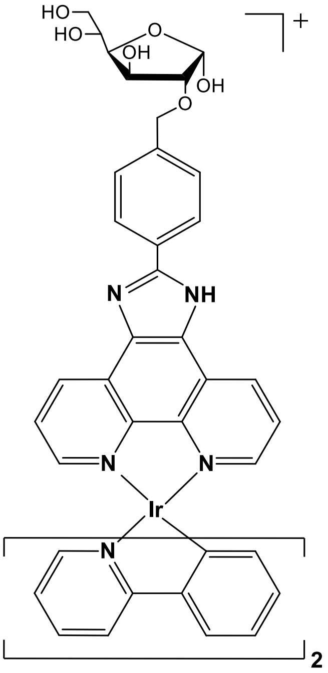

Ir-6

Figure 59. Molecular structure of the glucose conjugated Ir(III) complex Ir-6.

The synthetic pathway involved many steps:

- The assembly of the imidazolyl modified phenanthrolinic ligand and its bromination;
- The preparation of the glucose moiety, suitable for the subsequent conjugation to the N^N scaffold;
- The introduction of the benzyl-protected glucose through the bromine anchoring group inserted on the imidazolyl modified N^N ligand;
- The deprotection of the sugar moiety;
- The complexation of the synthesized backbone with the heavy metal ion.

Specifically, the imidazolyl modified phenanthroline-based ligand was synthesized as discussed in paragraph 3.2.3.5.[38]

The hydroxymethyl group was then treated with a 48% HBr solution in MeOH aiming to convert the hydroxyl function into a bromine atom, crucial to carry out the nucleophilic substitution.

In parallel, the 1,2-*O*-isopropylidene-α-D-glucofuranose was treated with subsequent protection and selective deprotection steps aiming to prepare the suitable substrate to perform the following glucose conjugation.

The hydrogen abstraction of the properly modified sugar moiety to carry out the bioconjugation was achieved solubilizing it in dry DMF with NaH and then adding the brominated phenantroline-based scaffold.

After the glucose appendage, deprotection was attempted on the free ligand in order to avoid potential complications arising from the presence of the Ir(III) ion. Indeed, the treatment of the Ir(III) complex with H_2 could affect the emitter stability.

Thus, multiple attempts were performed, involving the use of either Pd/C or $Pd(OH)_2$ in MeOH under an H_2 atmosphere but the benzyl groups removal couldn’t be achieved.

Given the difficulties encountered in the context of deprotection of the glucose moiety, the synthesis of the desired Ir(III) complex couldn’t be accomplished.

3.2.3.7 Synthesis of phenanthrolinine-based Ir(III) complexes for bioconjugation

With the purpose to broaden the frontiers of bioimaging and photodynamic therapy, two Ir(III) complexes bearing interesting functional groups designed to subsequently perform bio-conjugation were prepared.

In particular, **Ir-4** (**Figure 60**) was designed with an hydroxymethyl group, which is crucial for the insertion of a wide variety of biological substrates, such as amino acids *via* condensation. On the other hand, **Ir-5** (**Figure 60**) presents an azide (N_3) group, useful to perform click chemistry reactions.

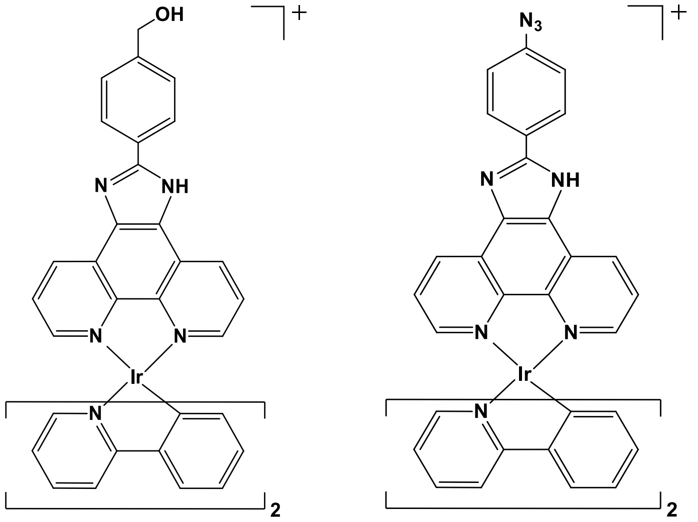

Ir-4 **Ir-5**

Figure 60. Molecular structure of complexes Ir-4 and Ir-5, designed with the purpose to be further functionalized with biologically relevant substrates.

The detailed procedures followed to achieve **Ir-4** and **Ir-5** is reported in the Experimental Section (Chapter III). The synthetic pathway to obtain **Ir-4** involved the preparation of the phenanthroline-based scaffold as briefly described for **Ir-1** to **Ir-3** in paragraph 3.2.3.5. The hydroxymethyl functionalized ligand was thus directly complexed using the 2-phenylpyridine Ir dimer and treated with a 6-fold excess of KPF_6, filtered and finally crystallized with a mixture of DCM and diethyl ether to afford the cationic species as a pure yellow solid.

The formation of the desired complex was assessed through complete NMR characterization, mass spectrometry and elemental analysis. Additionally, the photophysical properties of **Ir-4** were investigated in deoxygenated DCM solutions, aiming to test its efficiency as emitter. Extensive biological assays will be carried out to evaluate the photophysical properties of **Ir-4** in brain tissues, as well as its ability to serve as luminescent label for bioimaging. The analysis are still in progress.

Ir-5 was prepared starting from the introduction of the azide function on 4-Formylbenzene-boronic acid, performed in the presence of NaN_3 and $Cu(OAc)_2$. Then, the reaction of 4-azido-benzaldehyde with 1,10-phenanthroline-5,6-dione with ammonium acetate in glacial acetic acid afforded the ligand backbone.

In the end, the phenanthrolinic scaffold was combined with the 2-phenylpyridine Ir(III) dimer in a MeOH:DCM mixture (v/v, 1/1) at 50°C overnight and the desired complex was obtained. Despite numerous attempts of purification, the ^{1}H-NMR spectrum highlighted the presence of a second species and thus further evaluations were prevented.

3.2.3.7.1 Photophysical properties

The tryptophan conjugated ligand (**Figure 61**) was analyzed investigating the photophysical properties with the purpose to assess the effect induced by the subsequent introduction of Ir(III) and of a coordination sphere made up of both various typologies of cyclometalated ligands and of a rigid N^N bioconjugated ligand.

UV-visible spectra were obtained using a Shimadzu UV3600 spectrophotometer. Steady state and time-resolved fluorescence data were collected using a FLS980 spectrofluorometer (Edinburg Instrument Ltd). Quantum yields were measured with a C11347 Quantaurus Hamamatsu Photonics K.K spectrometer.

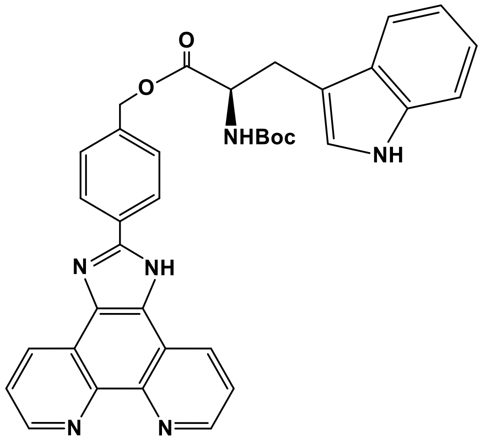

19

Figure 61. Molecular structure of the imidazolyl modified phenanthroline based tryptophan conjugated ligand.

The ligand was dissolved in dichloromethane obtaining a $1*10^{-5}$ M solution and analysed at room temperature (298.15 K) without additional treatments. The absorption and emission spectra were obtained irradiating at different wavelengths. The collected data are reported in **Figure 62**.

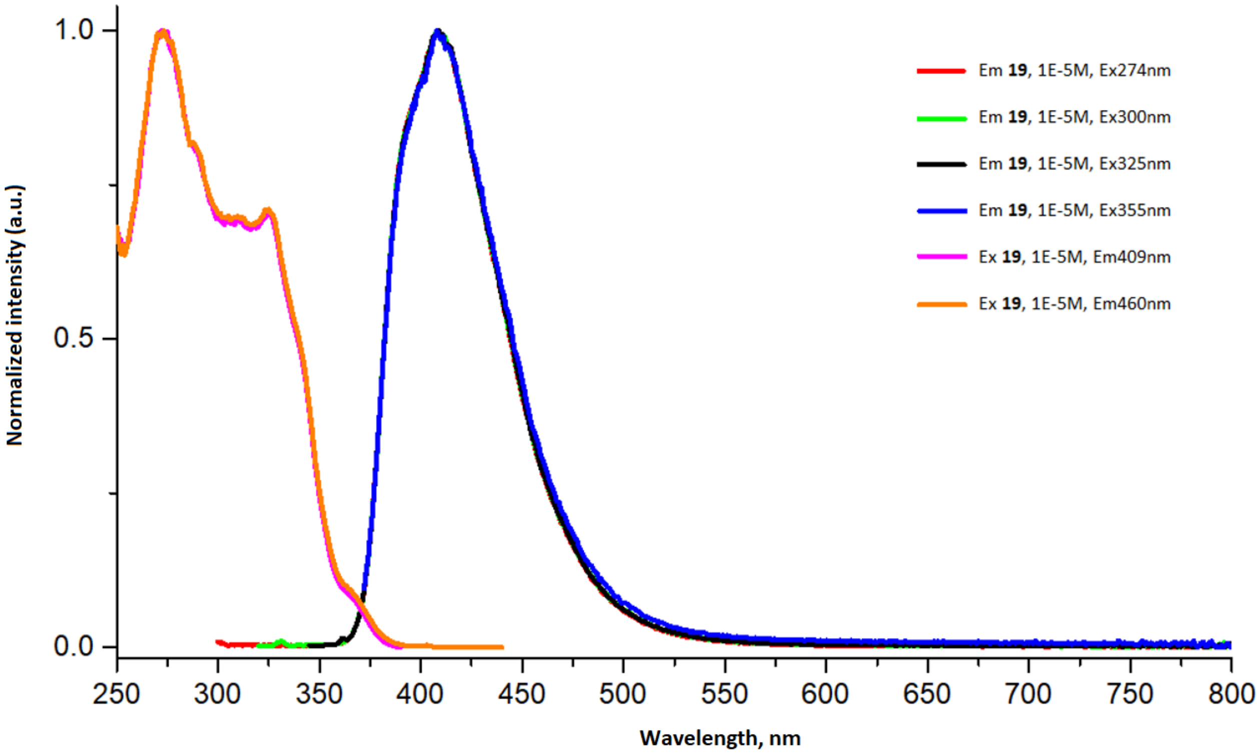

Figure 62. UV-vis absorption and emission spectra of 19 recorded in 10^{-5} M CH_2Cl_2 solutions at 298K.

In conformity with the investigation conducted by Zhao *et al.*[114] concerning an analogous phenanthroline based ligand, the maximum of absorption was recorded at λ = 273 nm, associated to a molar extinction coefficient of ε = 26.0 (**ε** × 10^3/M^{-1} cm^{-1}). Upon excitation, the tryptophan conjugated ligand gives rise to emission at λ = 408 nm, with a quantum yield of Φ_{em} = 11.5% and a measured lifetime of the excited state of τ = 3.76 ns.

The photophysical properties of **Ir-1**, **Ir-2** and **Ir-3** were assessed dissolving the complexes in dichloromethane at room temperature (298.15 K). **Ir-1**, **Ir-2**, **Ir-3** were used to prepare solutions of various concentrations, aiming to investigate potential modifications arising as a consequence of the emitters increased concentration.

Before irradiation, the solutions were subject to freeze-pump-thaw cycle treatment in order to remove oxygen, which can affect the photoluminescent phenomena quenching the complexes emission through energy transfer.

The photophysical parameters of each complex are listed in **Table 3.**

Table 3. Photophysical data collected for Ir-1 to Ir-3. [a] Data obtained in 10^{-5}M CH_2Cl_2 solution at 298K. [b] Data obtained in 10^{-5}M deoxygenated CH_2Cl_2 solution at 298K (λ_{ex}= 300 nm).

Complex	λ_{abs} / nm ($\varepsilon \times 10^3$ / $M^{-1}cm^{-1}$)[a]	λ_{em} / nm[b]	$\tau/\mu s$[b]	Φ_{lum} %[b]
Ir-1	302 (70.7), 342 (48.3), 400 (8.7), 474 (3.9)	560	1.02	51.2
Ir-2	281 (71.5), 320 (38.6), 360 (12.2), 413 (5.1)	522	4.97	33.0
Ir-3	283 (102.1), 330 (45.5), 414 (8.8)	556	2.76	98.1

To our knowledge, structurally analogous Ir(III) complexes either functionalized with an hydroxymethyl moiety or conjugated to tryptophan have never been reported in literature. Nevertheless, an Ir(III) complex bearing an hydroxyl group on the phenyl ring (**Figure 63**) has been characterized.[38]

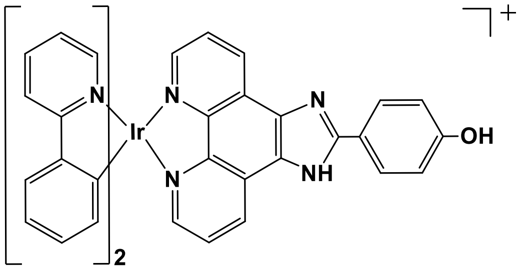

Figure 63. Molecular structure of the Ir(III) emitter bearing the hydroxyl group on the scaffold investigated by Gurta et *al.*.

With reference to the cited cyclometalated Ir(III) complex (**Figure 63**), the strong absorptions observed between 220-300 nm are attributed to the ^{1}IL ligand centred transitions ($^1\pi \rightarrow \pi^*$) from the 2-phenylpyridine and the phenanthroline moiety. This evidence is supported by the elevated extinction coefficient values arising from the spin-allowed nature of the transition. Moving towards 400 nm, the presence of a shoulder has been observed as the result of two photophysical contributions.

Specifically, a ligand-to-ligand charge transfer (^{1}LLCT) implicating the cyclometalated ligands and the phenantroline fragments (π(ppy) ⟶ π*(phen)), and a metal-to-ligand charge-transfer (^{1}MLCT) leading to the displacement of electronic density form the Ir(III) ion to the phenanthroline (dπ ⟶ π*(phen)), are involved.

The transitions centred around λ~ 460 nm, displaying a low intensity, can be associated to spin-forbidden metal-to-ligand charge transfer (^{3}MLCT) and ligand-to-ligand charge transfer (^{3}LLCT) transitions (**Figure 64**).[34]

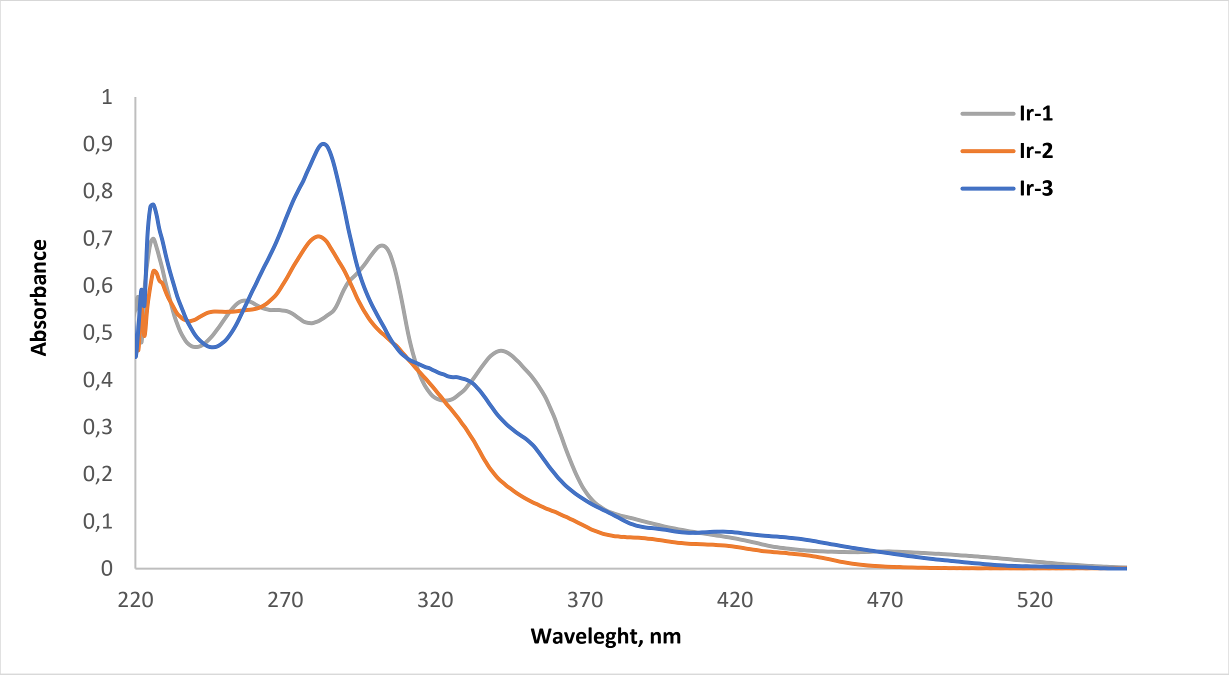

Figure 64. Absorption spectra of Ir-1 to Ir-3 recorded in 10^{-5}M CH_2Cl_2 solutions at 298K.

The photoluminescent analysis highlighted emissions in the range of 522-560 nm owing to their high ligand field stabilization energy as a consequence of the selected strong σ-donor cyclometalated ligands and of the elevated oxidation state of the Ir(III) ion. Additionally, the heavy metal ion significantly contributes to the promotion of the intersystem crossing, a phenomenon considerably enhanced by the strong spin-orbit coupling induced by the heavy metal ion. The induced phosphorescence is attributed to a ^{3}LLCT transition, combined with a ^{3}MLCT transition. The emission phenomenon is associated to variable quantum yields, with an outstanding value for **Ir-3** (Φ_{PL}: 98.1). The photoluminescence spectra recorded for **Ir-1**, **Ir-2**, **Ir-3** are depicted in **Figure 65**. The comparison of the patterns highlighted a blue shift of **Ir-2** emission with respect to **Ir-1**, **Ir-3**. This evidence finds explanation considering the HOMO stabilizing effect played by the introduction of the fluorine atoms on the cyclometalated phenyl rings. The overall increase in the HOMO-LUMO energy gap, results in a shorter wavelength of emission.

Remarkably, the enhanced π-conjugation within the cyclometalated ligand **Ir-3** confers excellent photoluminescence associated to an excellent quantum yield, close to unity (Φ_{PL}: 98.1).

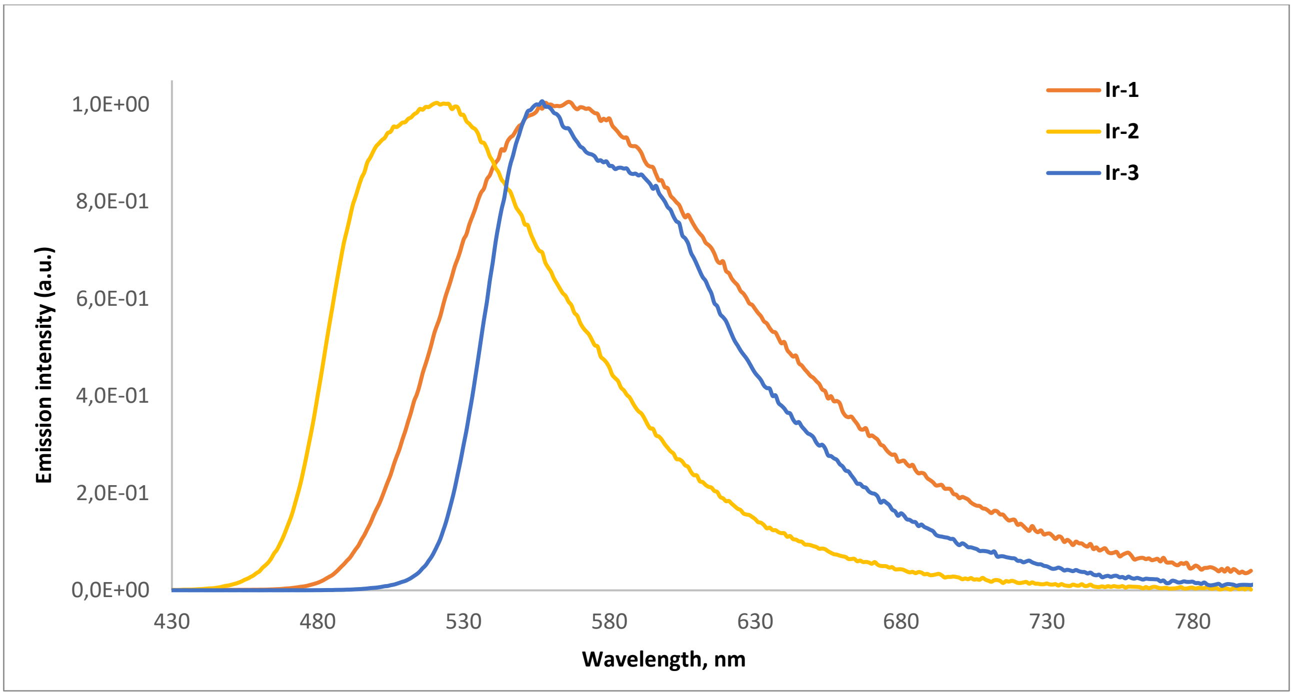

Figure 65. Emission spectra of Ir-1 to Ir-4 in 10^{-5}M degassed CH_2Cl_2 solutions at 298K. Ir-1, λ_{ex} = 300 nm; Ir-2, λ_{ex} = 300 nm, Ir-3, λ_{ex} = 330 nm.

The study performed on the lifetime of the excited state of **Ir-1** highlighted a significant difference within the data collected in relation to the selected concentration values. Specifically, at low concentrations ($2*10^{-6}$ M) the observed phenomenon relies on the emission of the monomer, giving rise to a lifetime of the excited state of τ = 1.02 µs. The observation of the emission spectra obtained gradually increasing the concentration evidences a change in the pattern, highlighting the formation of a red shifted band at 620 nm ($2*10^{-4}$ M).

Aiming to further investigate the nature of the species responsible for the newly observed emission, the absorption spectrum of the species emitting at 620 nm was recorded. As shown in **Figure 66**, the acquired absorption pattern evidences a great difference with respect to the absorption spectrum attributed to the monomer. Given these premises, the collected data suggest that the aggregates are responsible for the arising red shifted emission, characterized by a life-time of the excited state of τ = 16 µs.

The collected data in the context of the investigations carried out for **Ir-2** and **Ir-3** highlighted their inclination to undergo the formation of aggregates as the concentration of the emitter in solution is increased. As a model, the UV-Vis absorption and emission spectra collected at various concentrations of **Ir-1** are reported in **Figure 66**.

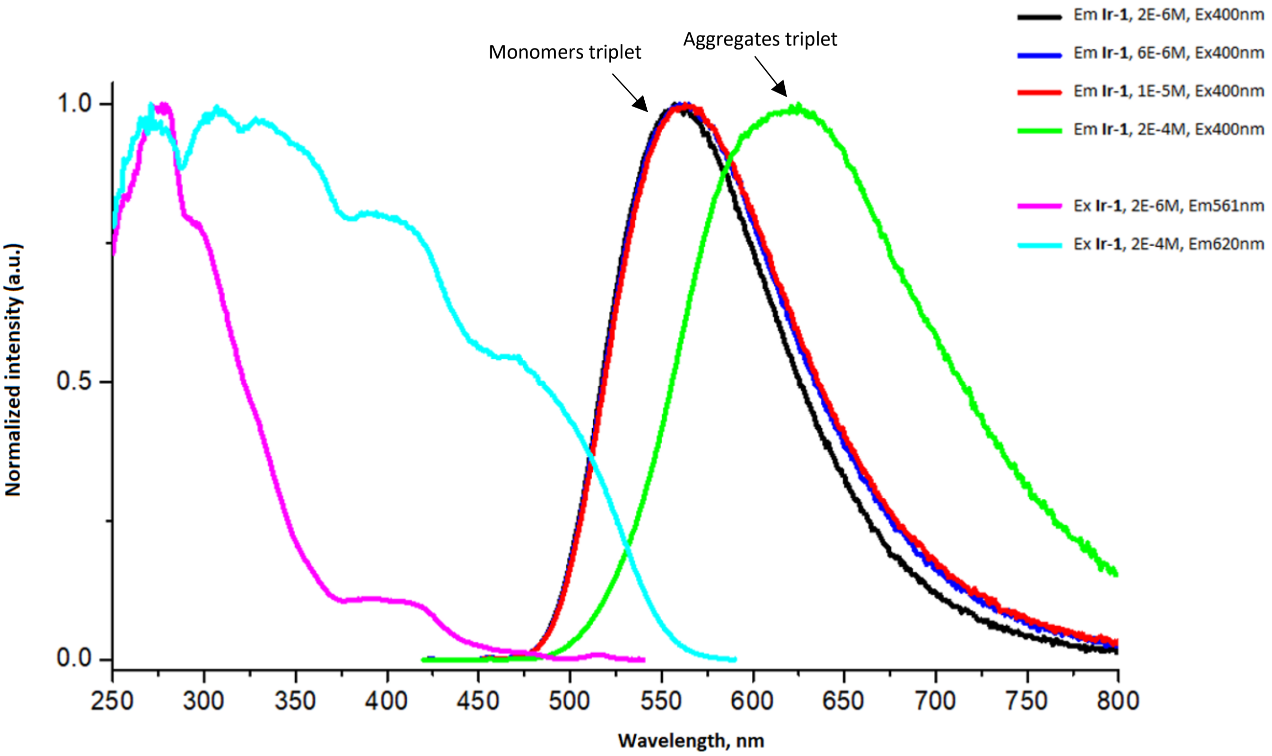

Figure 66. UV-Vis absorption and emission spectra of Ir-1 in degassed CH_2Cl_2 in the range of $2 \cdot 10^{-6}$ to $2 \cdot 10^{-4}$ M.

3.2.3.7 Conclusion

The relevant role played by bioconjugation encouraged the design of a series of cyclometalated Pt(II) and Ir(III) based emitters either functionalized with biological substrates such as glucose and tryptophan, or developed with an hydroxyl anchoring vector exploitable for further functionalization.

The series of tryptophan-conjugated Ir(III) complexes were synthesized completing the coordination sphere with a variety of cyclometalated ligands, in order to investigate their effect on the photophysical properties of the emitters.

Within the investigated compounds, **Ir-3** displays the highest values of molar absorption coefficient and a quantum yield close to unity in solution. The enhanced π-conjugation of the phenyl-quinoline moiety makes a significant contribution to the emitter efficiency.

The photophysical properties of **Ir-1, Ir-2** and **Ir-3** will be investigated in the biological media, specifically inserting them in the brain cells. The biological assays over **Ir-1, Ir-2** and **Ir-3** are still in progress.

3.3 Photodynamic therapy: introduction

Photodynamic therapy (PDT) is a light-based therapeutic modality used for the treatment of many non-oncological diseases and cancer.[115] Photodynamic therapy relies its efficacy on the cytotoxicity induced among the biological tissues via generation of reactive oxygen species (ROS) accomplished through the combination of two non-toxic components: a photosensitizer and a light source.

The photosensitizer (PS) is a light absorbing molecule that undergoes activation upon excitation, able to transfer the exceeding energy collected to another chemical species. The treatment involves the administration of the photosensitizer, mainly intravenously, which is localized and accumulated in the targeted cells. The photosensitizer is then activated through exposition to a specific wavelength radiation, which causes its excitation. Thus, the energy absorbed is subsequently transferred to the triplet oxygen $^3O_2$, naturally present in the biological tissues, which is converted in the highly reactive singlet oxygen $^1O_2$. A series of cascade reactions occurs and many other reactive oxygen species such as radicals are released in the cellular environment, giving rise to cells death. (**Figure 67**)

The mechanism of action of photodynamic therapy relies on a basic photophysical process.[115] When a source of photons of a specific wavelength is turned on, the photosensitizer, which at first is in the ground state (S_0), absorbs the energy carried by the photons and goes to the excited singlet state (S_1). Then, through intersystem crossing, the photosensitizer switches from the excited singlet state (S_1) to the excited triplet state (T_1). Finally, the exceeding energy is released in order to restore the photosensitizer. The radiative decay that involves an excited triplet state and a singlet ground state is spin forbidden but, due to the strong spin-orbit coupling, this rule is partially circumvented and a slow emission of photons results. The energy released via phosphorescence triggers cascade reactions, that leads to the generation of highly reactive and cytotoxic species. In particular, two main pathways can be outlined:

1. Type I reaction: the photosensitizer interacts with the biomolecules in the surrounding environment and generates radicals through hydrogen or electron transfer. In turn, these species activate the $^3O_2$ and form many ROS, such as the superoxide anion ($O_2^{\bullet-}$), the hydroxyl radical ($OH^\bullet$) and hydrogen peroxide (H_2O_2).
2. Type II reaction: the photosensitizer transfers the energy deriving from the excited triplet state directly to the $^3O_2$ producing the highly reactive $^1O_2$.

Figure 67 depicts the outlines photodynamic therapy mechanisms and their effect on the biological tissues.

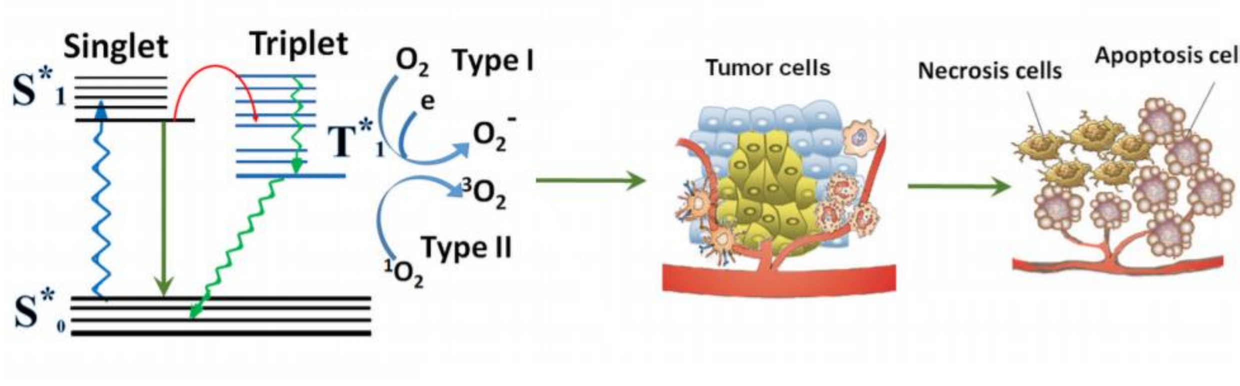

Figure 67. Schematic illustration of the photodynamic therapy mechanism (left) in tumor cells, where the cascade reactions lead to necrosis and apoptosis (right).

ROS induce oxidative stress which cause severe cells' damage and lastly cells' death. The cytotoxicity induced by ROS is particularly advantageous: given their high reactivity, their half-time is very short and the destruction of the cellular components involves a limited area. For instance, the lifetime of $^1O_2$ in the biological media is around 0.04 µs and its diffusion radius is equal to 0.02 µm.[116] Additionally, the activation of the photosensitizer through light irradiation, allows to selectively generate ROS in a specific area thus avoiding an invasive release of cytotoxic species.

The limited radius of action represents a major advantage because it makes it possible to control the treatment and to confine the cells death. In this context, the main purpose of photodynamic therapy is to selectively destroy the tumor cells in order to avoid the side effects shown by the conventional anticancer agents.

Photodynamic therapy leads to cells death through two main pathways: apoptosis and necrosis.[117] Necrosis is a violent and uncontrolled mechanism, characterized by the disruption of cytoplasmic membranes and cellular fragmentation. The disintegration process causes the release of the intracellular content in the extracellular environment, leading to inflammation and induced toxic effect on the surrounding tissues. Apoptosis, also known as "programmed cellular death", is a very complex regulated process in which mitochondria plays a key role. Indeed, oxidative stress provokes the release of cytochrome c from mitochondria in the cytosol, leading to a non-toxic cascade of reactions. In fact, apoptosis doesn't involve the release of the cellular constituents in the extracellular tissues, since they are promptly engulfed by surrounding cells or macrophages and no inflammation occurs. Therapeutically, a controlled cells' death mechanism is desirable in order to avoid side effects associated with violent cellular disruption and consequent immune system response. The cells death pathway depends on the localization of the photosensitizer: mitochondrial photosensitizers provoke apoptosis, whilst cellular membrane photosensitizers lead to necrosis.

Thus, the design of photosensitizers able to selectively accumulate in a specific cellular substructure is crucial, but many factors affect the efficiency of the treatment:[118]

- The type of targeted tumor cells;
- The nature of the photosensitizer;
- The concentration and the distribution of the photosensitizer.

Hence, the selectivity required could be achieved through two strategies:

- Functionalization of the photosensitizer introducing a biomolecule able to address it inside a specific subcellular structure of the tumor cells;
- Design of a photosensitizer that is non-toxic in the dark and that could be activated only via irradiation.

Photodynamic therapy could be further enhanced using red light wavelengths to excite the photosensitizer. Indeed, another aspect that has to be taken into account is the photon penetration through the biological tissues. In this context, the UV-visible light can be absorbed by the chromophores contained inside the tissues and so the efficiency in the photophysical process is compromised, since only a part of the irradiated light reaches the target. In order to enhance the quantum yield, near-infrared light should be exploited: previous studies discovered that wavelengths ranging from 500 to 600 nm has a depth penetration of 4 mm, whilst 8 mm could be reach using 600-800 nm wavelengths.[117]

The first photosensitizer approved for photodynamic therapy was Photofrin, a mixture of oligomers of porphyrins. In this context, porphyrins are considered very promising light absorbing fragments due to their highly delocalized π-conjugated system. Nevertheless, Photofrin revealed many limits as photosensitizer agent. First of all, it’s a mixture of more than 60 oligomers so its composition and pureness aren’t easy to control. Photofrin showed also a poor light absorbing ability in the red region, a limited tumor cells targeting capacity and finally, prolonged side-effects.[119] Thus, new photosensitizers were designed and investigated in order to obtain ideal near-infrared light activated agents with optimal features:

- Excellent chemical stability;
- Ability to localize and accumulate in a specific tumor’s cellular structure;
- Non-toxic in the dark and activated upon irradiation only;
- Great photophysical properties and high singlet oxygen yield;
- High absorbance in the red region (600-800 nm).

3.3.1 Pt(II) complexes as anticancer agents: an overview

Metal complexes display a key role in many biological processes, suffice it to say that haemoglobin and myoglobin are made up of a porphyrin organic ligand coordinating a central iron ion.

Historically, a wide variety of organometallic complexes have been used for the treatment of many diseases.

In medicinal inorganic chemistry, anticancer Pt(II) complexes represent a great achievement.[120] The first Pt(II) based cancer agent discovered is the diamminedichloroplatinum(II), a Pt(II) square planar complex also known as cisplatin.

The mechanism of action of cisplatin consists of three steps:

a) Substitution of the chloride ligands with water molecules and activation of the Pt(II) complex, which switches from a neutral to a positively charged complex;
b) Electrostatic attraction between the positively charged Pt(II) complex and the negatively charged DNA;
c) Inhibition of the DNA replication.

The effectiveness of cisplatin led to the design and synthesis of analogous Pt(II) complexes, made up of two cis-ammine and two cis-monodentate or a bidentate anionic leaving group ligands. **Figure 68** represents the molecular structures of the clinically approved Pt(II) based drugs.

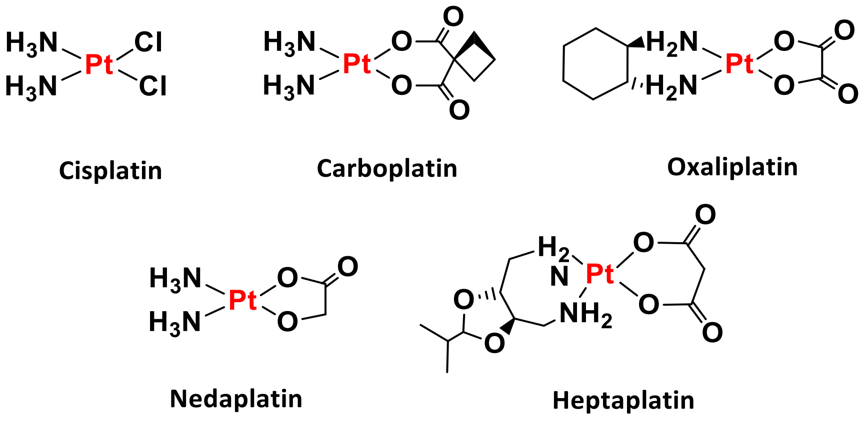

Figure 68. Molecular structure of the developed Pt(II) complexes displaying anticancer activity.

Pt(II) complexes containing targeting groups able to address the anticancer agent to specific cellular organelles, were subsequently synthesized. In this respect, carbohydrates were taken into account as biological vectors due to their ability to establish multiple hydrogen interactions with the structures inserted into the cellular membrane.[121]

Glucose provides a very promising strategy for the functionalization of these anticancer agents since it plays a central role in the cellular metabolism. The proliferation of a tumor throughout the biological tissues, requires a high amount of energy[122], which is supplied by glucose. As a consequence, in order to guarantee the dramatically increased rate of glucose cellular uptake, the malignant cells give rise to the overexpression of the glucose membrane transporters GLUT1. The glucose altered metabolism is known as the Warburg effect.[123] The Warburg effect can be exploited to provide a selective treatment against cancer and to overcome the side effects of cisplatin and its analogues. Indeed, these first-generation drugs are administered intravenously and unwanted interactions with blood and cellular components, such as blood human albumin and glutathione could occur. Thus, the cytotoxic effect could be altered. The introduction of a targeting group on the ligands of Pt(II) complexes increases the selectivity of the treatment, exploiting the interaction with the GLUT1 receptors and favoring the drugs uptake inside the cancer cells. Moreover, the glucose moiety imparts hydrophilicity to Pt(II) emitters, a feature that further improves the selectivity in the context of cellular uptake. Indeed, cell membranes are composed of a hydrophobic phospholipid bilayer which can be crossed spontaneously by small lipophilic neutral charged molecules only. Thus, hydrophilic molecules can’t permeate the biological membranes without the aid of specific transporters.[124]

Additionally, the conjugation of a Pt(II) complex with glucose results in increased water solubility, which is advantageous for the elimination process. Indeed, if the glucose-conjugated drug is stable enough in water, slow hydrolysis occurs and the complex can be excreted directly via kidney, avoiding the release of the heavy metal center. Conversely, the dissociation of the heavy metal ion from the organic backbone, provokes systemic toxicity. The accumulation of metals like Pt(II) in biological tissues thus represents a serious side-effect in the administration of organometallic therapeutic agents.[124]

Several Pt(II) complexes bearing glucose as a vector were synthesized, inserting the sugar moiety on the diamino chelating ligand or, in alternative, on the anionic leaving group. The studies carried out highlighted the role of the glucose linker length. Indeed, long carbon chains prevent the optimal interaction with the glucose receptor.[125] **Figure 69** represents the molecular structure of the evaluated glucose conjugated Pt(II) complexes.

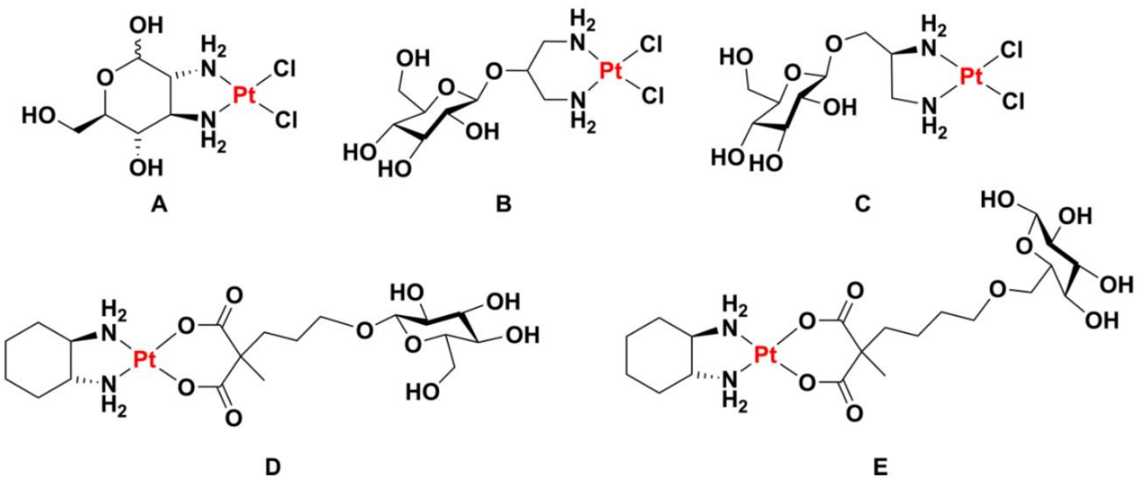

Figure 69. Molecular structure of the glucose-conjugated Pt(II) complexes developed by Lippard et *al.*.

The pharmacological advantage given by the introduction of a vector fragment in the complex was also exploited using other typologies of biological relevant molecules.

In this context, the folate moiety was covalently linked to the anionic ligand of the Pt(II) complex due to the importance of the pteroic unit contained in the folic acid, which is involved in many biological processes.[126] The molecular structure of the investigated complex is represented in **Figure 70**.

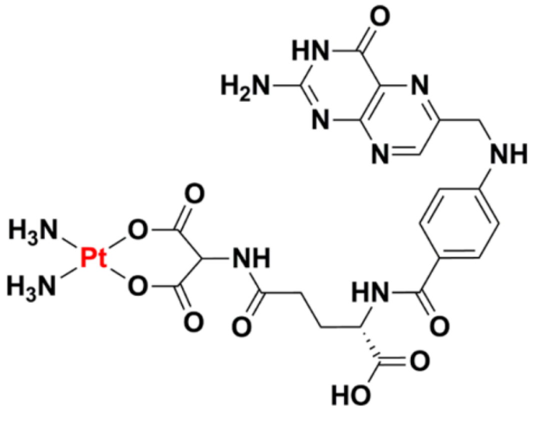

Figure 70. Molecular structure of the folate-conjugated Pt(II) complex.

The uncontrolled tumor cells growth requires higher amounts of folate substrates and the glycoprotein that serves as the folate receptor results overexpressed.[127] Nevertheless, the use of the folate moiety gives rise to water solubility issues and consequently the complex can't be used in a biological medium.[128]

3.3.1.1 Pt(II) complexes as photosensitizers for photodynamic therapy

The design of rigid terdentate Pt(II) complexes is considered a successful strategy to develop bright emitters for bioimaging and photodynamic therapy's applications. In this respect, N^C^N and N^N^N ligands for the coordination of Pt(II) ions have been investigated as photosensitizers for photodynamic therapy[129, 130], highlighting their outstanding and appealing photophysical properties.

N^C^N cyclometalated Pt(II) complexes have already been reported in literature due to their advantageous features:[26, 27]

- Optimal phosphorescent emitters;
- Long lived triplet excited state;
- Easily tunable photophysical properties through a proper choice of the coordination sphere;
- Large Stokes shift;
- Great photochemical stability and limited chemical degradation.

Aiming to further improve the efficiency of luminophores through the introduction of a targeting vector, an N^N^N terdentate Pt(II) complex conjugated with glucose has been reported in literature.[131]

The Pt(II) coordination sphere is characterized by a glucose-appended terpyridine linked to the sugar moiety through a short carbon chain and by a 4,4-Difluoro-5,7-dimethyl-4-bora-3a,4a-diaza-s-indacene-3 (BODIPY) ligand (**Figure 71**). Glucose introduction on the organometallic backbone provides a promising approach both to selectively address the emitter inside cancer cells over healthy cells and to improve its water solubility.

Additionally, upon red light irradiation, the Pt(II) acetylenic bond is cleaved and the BODIPY ligand released in the biological environment. BODIPY is responsible for the photogeneration of the singlet oxygen in the cells' media, serving as a PDT agent itself. Furthermore, the Pt(II) unit provides a potential DNA intercalator.

The therapeutical efficiency of the system was assessed comparing the designed glycoconjugate Pt(II) luminophore and the complex displaying a benzene ring in place of the sugar moiety on the terpyridine (**Figure 71**). The two complexes appeared to be both optimal red-light activated photodynamic therapy agents, with a much higher cancer cellular uptake displayed by the glucose appended complex.

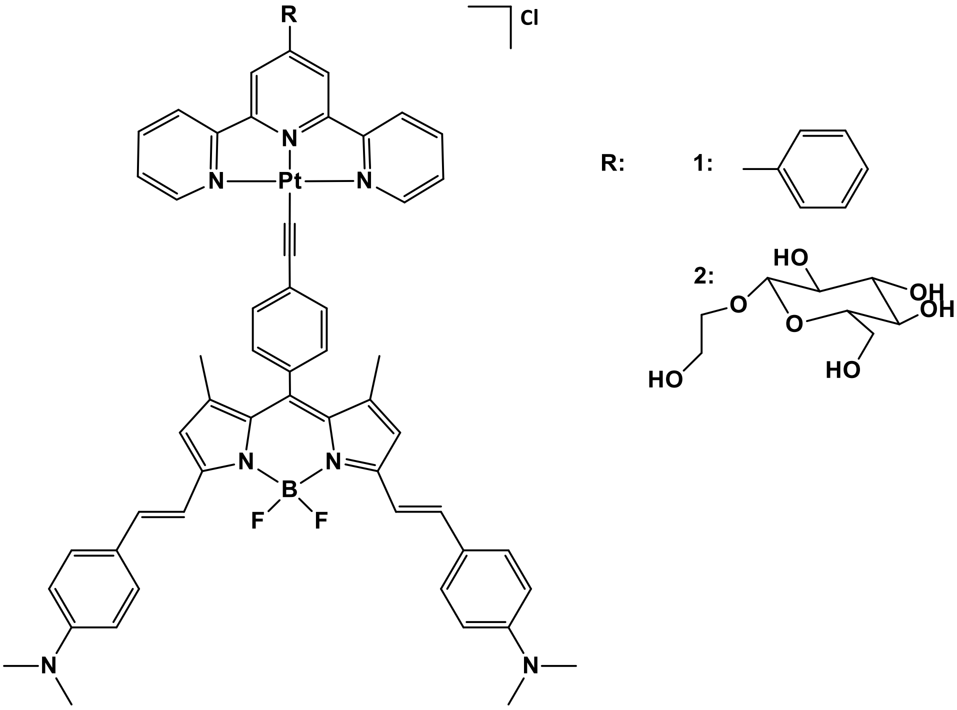

Figure 71. Pt(II) complex investigated by Chakravarty et *al.* bearing the BODIPY moiety.

Overall, the study highlighted and confirmed the key role fulfilled by the glucose moiety introduced on the ligand.

Given the importance to develop anticancer agents able to selectively address tumor cells, a cyclometalated N^C^N Pt(II) complex functionalized with the glucose moiety linked through a short carbon chain was designed and synthesized in the present thesis (**Figure 72**), aiming to overcome the many side effects limiting first generation Pt(II) based drugs.

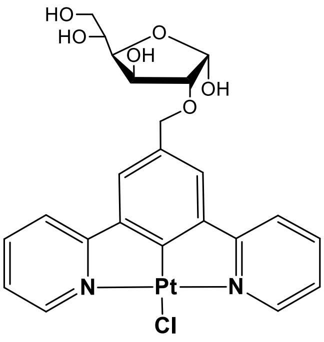

Pt-11

Figure 72. Molecular representation of the targeted glucose-appended emitters.

To our knowledge, no N^C^N cyclometalated Pt(II) complex made up of the glucose-appended 1,3-(2-dipyridyl)benzene moiety has been reported in literature yet.

In this context, Patra, Awuah and Lippard[108] reported a study concerning the effect of the diverse positional isomers of glucose, appended on the scaffold of Pt(II) complexes. The molecular representation of the investigated complexes is reported in **Figure 73**.

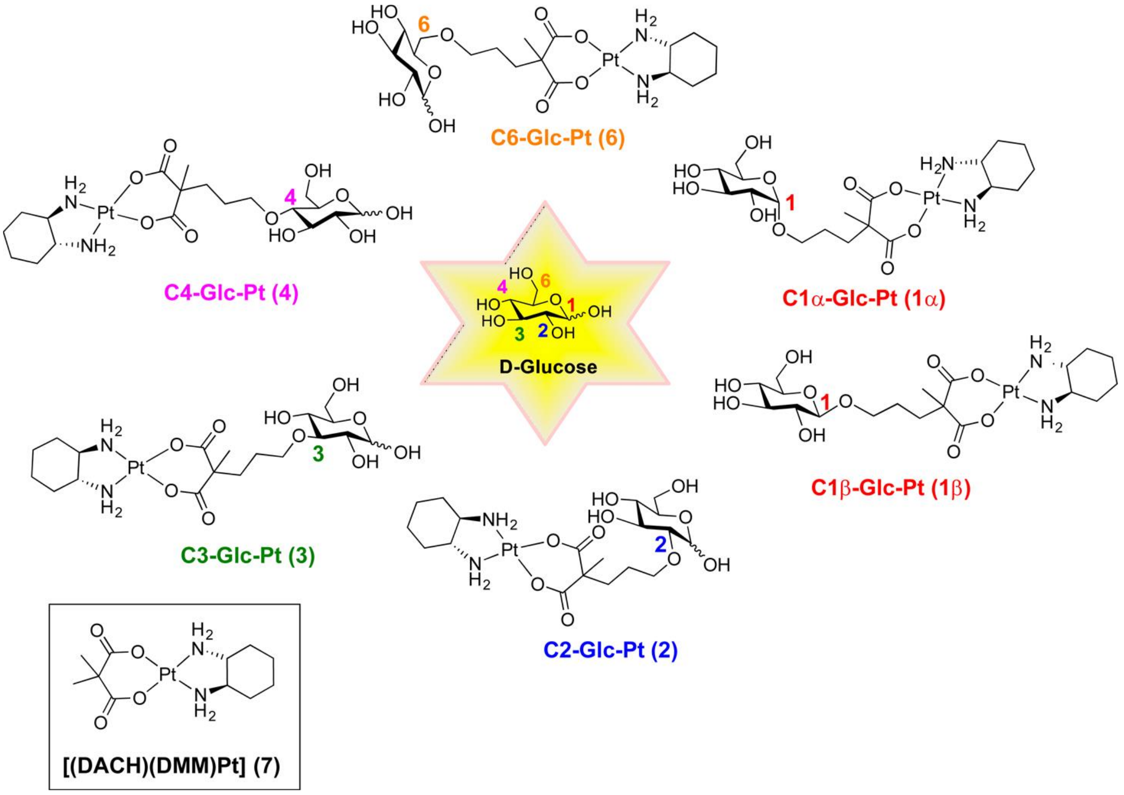

Figure 73. Molecular representation of the Pt(II) complexes' series investigated by Lippard et *al.*.

Glucose has indeed four secondary hydroxyl groups and a primary hydroxyl group that could be exploited to perform the conjugation of the sugar moiety on a variety of molecules' backbone.

In the biological environment, the hydroxyl groups play a key role for the recognition process since they form hydrogen bonds with specific amino acid residues of the glucose transporters GLUTs, localized in the cell membranes. The three-dimensional spatial arrangement of biological transporters induces the selectivity observed as part of the interaction occurring with their substrates. Consequently, biological activity and recognition processes are affected by the position of the hydroxyl group on the glucose moiety, selected as anchoring group for the Pt(II) complex bioconjugation.

The study investigated the cytotoxicity and the internalization ability of the glucose appended organometallic complexes, obtained binding each of the five hydroxyl groups to the backbone. The evaluation was carried out relying on the analysis of the crystals' structure of GLUT1 and GLUT3 transporters bond to D-glucose, obtained in the context of previous studies reported in literature.[132, 133]

The results led to the conclusion that the glucose-conjugated Pt(II) complex obtained attaching the sugar moiety via the C2 carbon atom provides the most promising anticancer agent of the series. Indeed, it tends to efficiently accumulate in tumor cells with respect to the complexes obtained with the other positional isomers.

3.3.2 Cyclometalated Ir(III) complexes for photodynamic therapy

The design of second and third row transition metal complexes provide a promising approach as photosensitizers for photodynamic therapy.[134] In addition to Pt(II) based anticancer agents, the medical application of cyclometalated Ir(III) complexes gained increasing interest over the years due to their optimal photophysical properties and due to their versatility.

3.3.2.1 Ir(III) complexes as singlet oxygen sensitizers: introduction and state of the art

3.3.2.1.1 Bis-cyclometalated Ir(III) complexes

The design of an ideal photosensitizer for the generation of singlet oxygen is crucial to induce an effective and non-invasive death of the cancer cells. The first photosensitizers developed, among them porphyrins, phthalocyanines, fullerene derivatives and organic dyes, have highlighted many limitations.[135] In particular, low quantum efficiency for the singlet oxygen production, poor photochemical stability and an inability to selectively address cancer cells were assessed. Additionally, their propensity to aggregate in water further decreases the quantum yield of the photophysical processes. With the purpose to overcome these limitations, new improved photosensitizers were investigated.

Cyclometalated Ir(III) complexes display optimal properties as phosphorescent luminophores. Indeed, heavy metals are associated with strong spin-orbit coupling, which induce an efficient intersystem crossing, resulting in a long-lived triplet excited state. The photoluminescent properties could be further enhanced selecting proper ligands to prevent the heavy distortion of the backbone upon excitation and to make the metal centered excited state inaccessible. Moreover, the wavelength of absorption and emission can be further tuned introducing electron-donating or electron-withdrawing functional groups on the ligands. Indeed, the penetration of the light in biological tissues is maximum around $\lambda = 800$ nm and thus near-infrared light should be employed to increase the singlet oxygen generation quantum yield.[135]

Another aspect that has to be taken into consideration in biological applications, is the poor water solubility displayed by conventional Ir(III) complexes[70] and their consequent tendency to aggregate. For the purpose, a proper coordination sphere should be provided.

In 2002 Gao *et al.*[134] reported a series of neutral bis-cyclometalated Ir(III) complexes used as singlet oxygen activators. In particular, the three investigated complexes represented in **Figure 74** displayed encouraging photophysical properties for biological application.

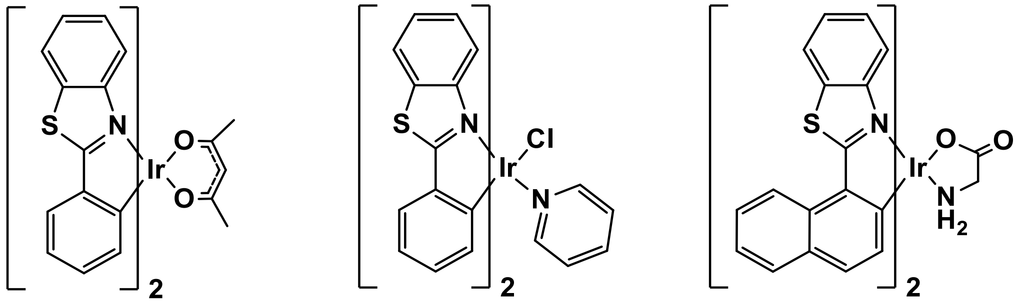

BT **BT - py** **BSN - G**

Figure 74. Molecular structure of the Ir(III) complexes investigated by Gao et *al.*.

The quantum yield for singlet oxygen generation was determined for each complex, irradiating with λ = 355 nm and λ = 532 nm light in air-saturated C_6H_6 solutions.

The study also revealed the nature of the electronic state involved in the transition for BT: the lowest excited state, whose main contribution is given by the C^N ligand, was attributed to a mixture of MLCT and $^3(\pi\text{-}\pi^*)$ states.

With the purpose to investigate the effect of the ancillary ligands on the singlet oxygen generation quantum yield, the β-diketonate fragment was substituted with ligands that could serve as significant biological models. In this context, an Ir(III) complex bearing a monodentate Lewis base was synthesized and analyzed.[134] Pyridine indeed, acts as a model for the side chain of histidine, a relevant amino acid involved in many biological processes. Subsequently, the β-diketonate was replaced with glycine, a bidentate amino acid that provides a model for amino acids containing amine or carboxylic acids in the side chain. Comparing the singlet oxygen generation quantum yield of the three complexes, the highest values were obtained upon excitation with the longer wavelength radiation, λ = 532 nm. A quantum yield equal to one was obtained for BT-py. Also, no degradation was assessed within 60 min of irradiation, meaning that the complexes are photostable.[134]

In 2011, Murata *et al.*[135] stated they reported the first cationic Ir(III) based photosensitizers for the release of singlet oxygen.

The study investigated six neutral and cationic Ir(III) emitters complexed by cyclometalated ligands and either N^N or O^O bidentate ligands. The molecular representation of the evaluated Ir(III) complexes is reported in **Figure 75**.

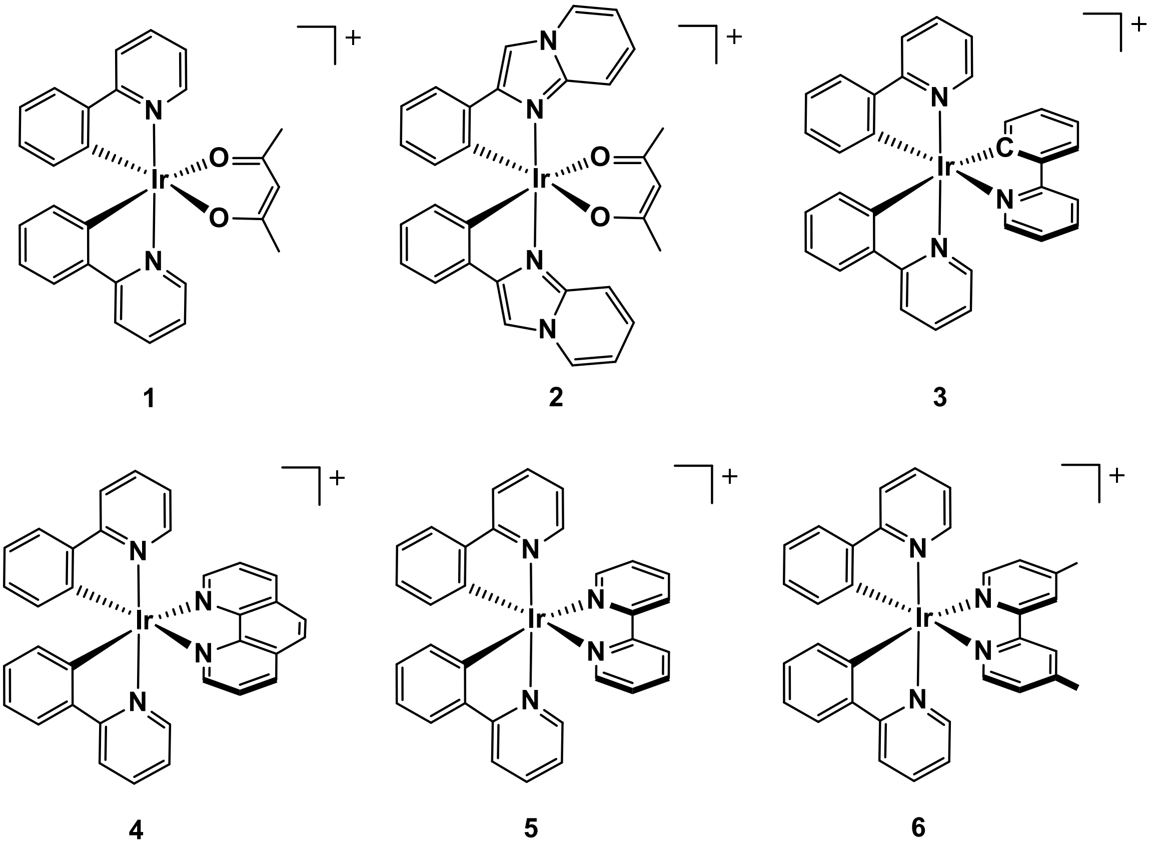

1 **2** **3**

4 **5** **6**

Figure 75. Molecular structure of the cyclometalated Ir-based emitters developed by Murata et *al.*.

The UV-vis absorption spectra of each complex, recorded in a solution of CH_2Cl_2:MeOH, 9:1, at room temperature, are provided in **Figure 76**. The most intense peaks fall in the range of 250-350 nm and arise from the spin allowed ligand-centered transition (^{1}LC). Between 350 nm and 400 nm, the bands associated to the ^{1}MLCT transition are displayed. Complex **3** shows an intense absorption in this region, with respect to the other five complexes. This peak is attributed to a ^{1}MLCT or to a ^{3}MLCT transition. Finally, the weak spin forbidden transitions which derive from a mixture of ^{3}LC and ^{3}MLCT states lay in the region around λ = 500 nm.

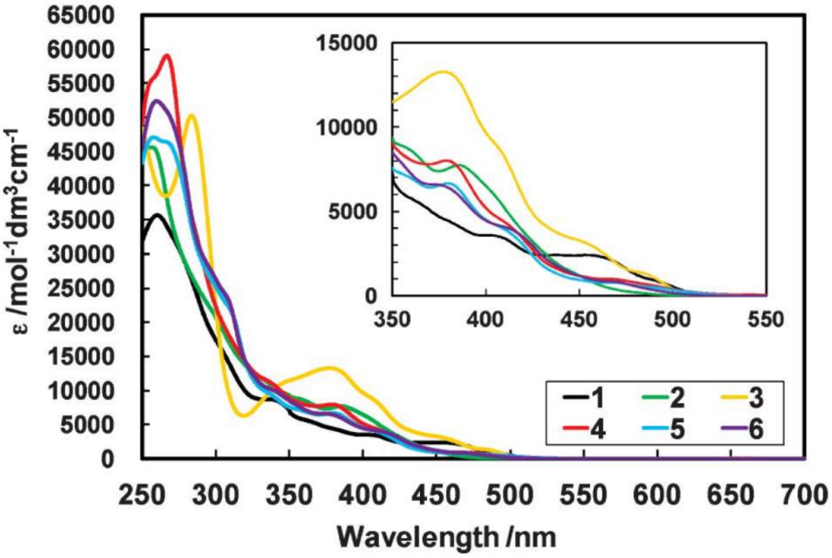

Figure 76. UV-Vis absorption spectra of the evaluated Ir (III) emitters 1-6 recorded in a CH_2Cl_2:MeOH (9:1, v/v) mixture. Inset: Absorption peaks between 350-550 nm.

Additionally, the study[135] evaluated the photophysical parameters of the six complexes: wavelength of emission, phosphorescence quantum yield and life-time of the excited state. Overall, all the complexes emit in the 510-583 nm range, giving rise to a green-yellow phosphorescence. Among the six complexes, complex **3** shows the highest quantum yield (Φ = 0.97) and the longest emission time (τ = 1.9 µs). On the other hand, complex **2** is characterized by the lowest phosphorescence efficiency, Φ = 0.02. This could be explained considering that the metal centered MC excited state is probably highly distorted and thermally accessible thus, a non-radiative release of the exceeding energy occurs.[136]

Finally, singlet oxygen generation efficiency was determined through the photooxidation of 1,5-dihydroxynaphthalene (DHN) to form Juglone, following the pathway represented below (**Figure 77**).

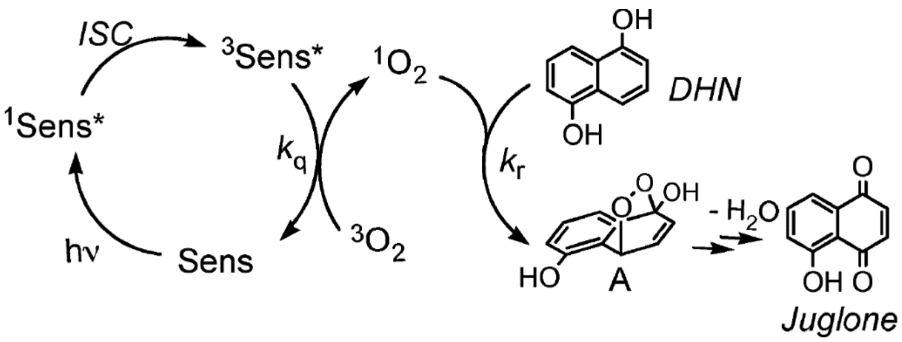

Figure 77. Illustration of the photooxidation of 1,5-dihydroxynaphthalene (DHN) to form Juglone.

The experiments were carried out adding complexes **1-6** to an oxygen-saturated mixture of CH_2Cl_2:MeOH, 9:1, containing 1,5-dihydroxynaphthalene (DHN) at room temperature, upon excitation at 350 nm. The study highlighted that the highest singlet oxygen generation yields are supplied by the three cationic Ir(III) complexes, ranging from 78% to 97%. Specifically, it was observed that **5** and **6** display quite different singlet oxygen generation yields, despite their structural similarity and the fact that they are characterized by comparable electrochemical and photophysical properties. This evidence suggested that the two methyl groups introduced on the dipyridine ligand of **6** could give rise to steric hindrance and prevent the efficient conversion of $^3O_2$ to form $^1O_2$. Thus, steric hindrance has to be taken into account to design ideal photosensitizers.

Overall, the study revealed that cationic cyclometalated Ir(III) complexes display optimal properties for the application as photosensitizers and high photochemical stability. Furthermore, the positive charge allows to associate water soluble counter anions to the Ir(III) complexes. This feature provides a very appealing strategy to overcome the solubility issues arising when photosensitizers are inserted inside the biological media.[135]

Furthermore, the possibility to modify the organometallic backbone conjugating the Ir(III) based emitters with biologically relevant substrates, makes them even more attractive for the application as photosensitizers.

3.3.2.1.2 Ir(III) complexes bearing imidazolyl modified phenanthroline ligands

Cyclometalated Ir(III) complexes display enhanced photophysical properties with respect to first generation photosensitizers. The selection of the coordination sphere for the metal center is crucial: strong field ligands contribute to stabilize the d^6 low spin configuration, making the complex kinetically inert and consequently preventing the heavy metal ion to induce toxicity in the biological media.

Given these premises, both the high oxidation state of the Ir(III) ion and C^N ligands provide a high splitting energy and thus high complex stability. The study reported by Gupta *et al.*[94] in 2014 investigates the photophysical properties of a series of Ir(III) complexes bearing imidazolyl modified phenanthroline ligands, systematically substituted with different functional groups. Furthermore, an insight about the localization of the photosensitizers inside the subcellular structures is provided. The molecular representation of the analyzed complexes is reported below (**Figure 78**).

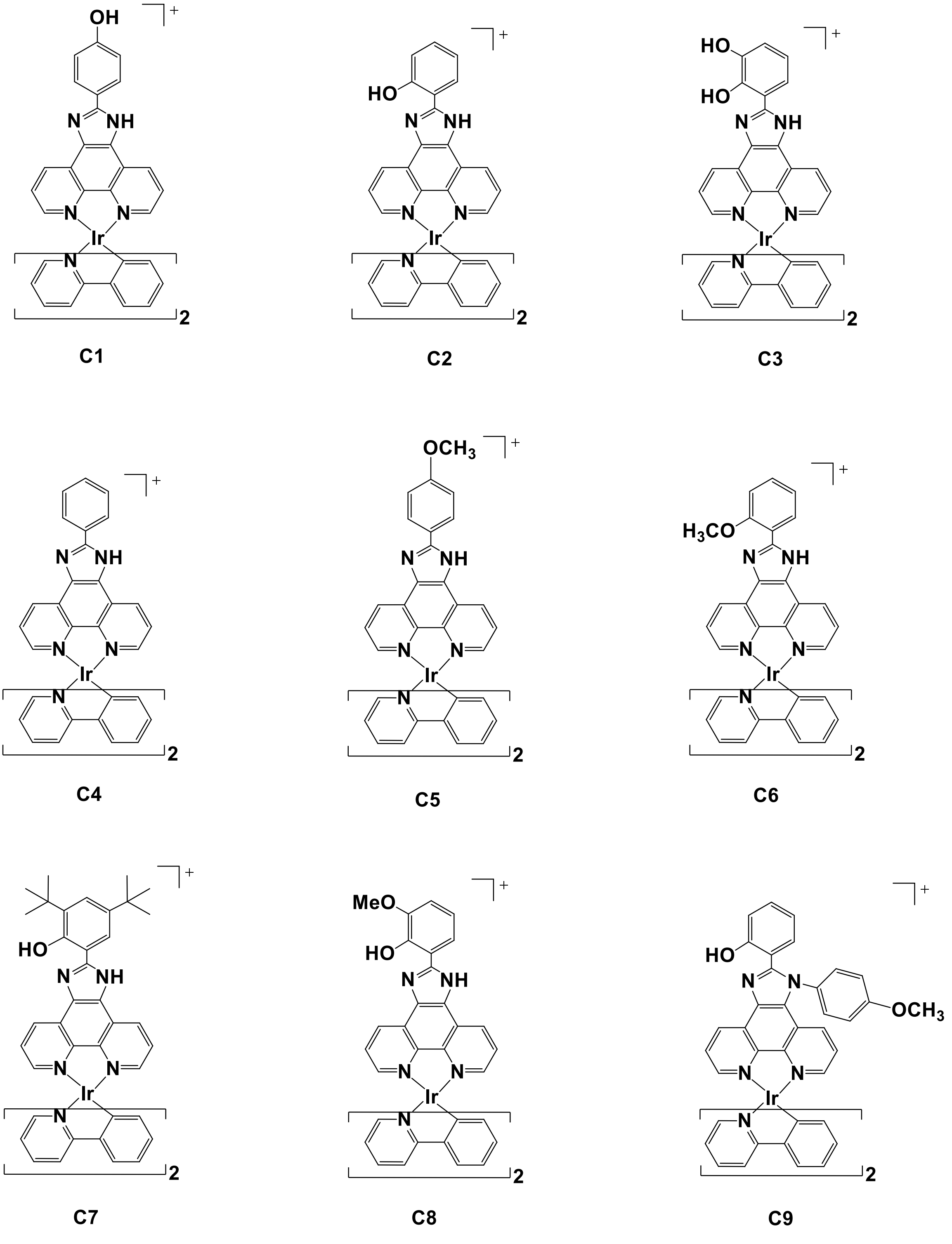

C1 C2 C3

C4 C5 C6

C7 C8 C9

Figure 78. Molecular structure of the imidazolyl modified phenanthroline-based Ir emitters C1-C9 investigated by Mandal et *al.*.

The photophysical analysis were carried out solubilizing the complexes in an acetonitrile solution at 298K, exciting at λ = 390 nm. The complexes displayed emission in the range of 570-615 nm, associated to a variable quantum yield *Φ* = 6.74-41.21% and a life-time of the excited state ranging from 8.60 μs to 14.47 μs.

Among the nine complexes studied, **C2** turned out to be the most promising to accomplish specific localization of the photosensitizer inside the endoplasmic reticulum. The authors suggested that the hydroxyl group in the 2 position of the phenyl ring plays a central role for the creation of intramolecular interactions and for the recognition process in the endoplasmic reticulum. In this context, **C4** was analyzed in order to make a comparison with the results obtained for **C2**. The absence of the hydroxyl group on the 2' position of the phenyl ring prevents quenching mechanisms and thus gives rise to a higher luminescence. Moreover, the accumulation in the endoplasmic reticulum is less selective with respect to **C2**. These evidences highlighted the importance of intramolecular interactions within the complex backbone.[94]

Cells assays in the dark revealed that **C2** displays minimum cytotoxicity when not irradiated, resulting in a very appealing complex for photodynamic therapy treatments.

3.3.2.1.3 Imidazolyl modified phenanthroline Ir(III) complex functionalized with a biological vector

The development of innovative Ir(III) emitters to accomplish the ideal photosensitizer, highlighted the importance of selecting proper rigid and high ligand-splitting energy ligands for the metal center coordination. Considering the promising photophysical properties displayed by imidazolyl modified phenanthroline, a series of cationic cyclometalated Ir(III) complexes built on the phenanthroline based ligands were designed, synthesized and tested.

At first, two Ir(III) complexes **Ir-4** and **Ir-5** bearing interesting functional groups introduced to subsequently perform the conjugation with a biologically relevant substrate were developed. (**Figure 79**)

Then, the photosensitizers selectivity was further improved introducing a targeting vector aiming to facilitate the recognition process and the permeation into the subcellular structures. In this context, the insertion of the tryptophan moiety on the hydroxylated N^N ligand scaffold was attempted, aiming to achieve three Ir(III) complexes stabilized with a variety of cyclometalated ancillary ligands (**Ir-1, Ir-2, Ir-3, Figure 79**) .

Lastly, a glucose-conjugated Ir(III) emitter (**Ir-6, Figure 79**) was designed with the purpose to exploit the enhanced sugar molecule uptake observed within tumor cells. The increased glucose influx inside malignant cells, arising as a consequence of the Warburg effect represents an interesting approach to dramatically improve the selectivity, being able to discriminate between healthy and cancerous cells.

The molecular representation of the investigated complexes is in **Figure 79**.

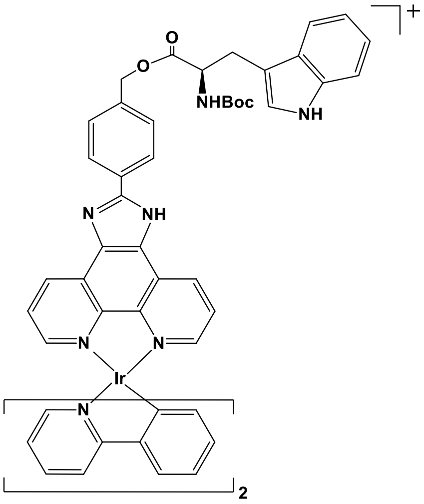

Ir-1

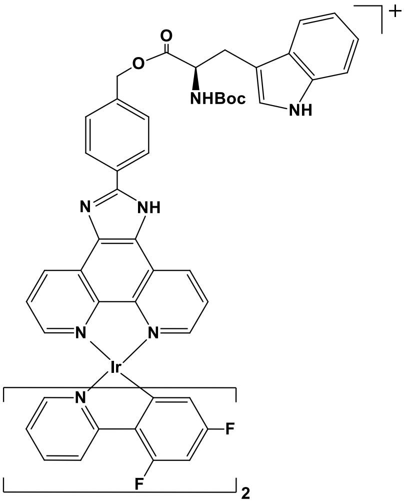

Ir-2

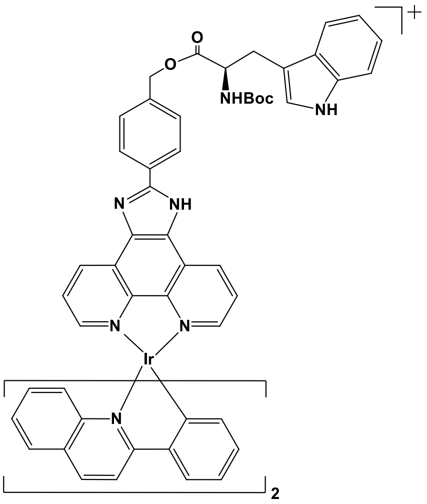

Ir-3

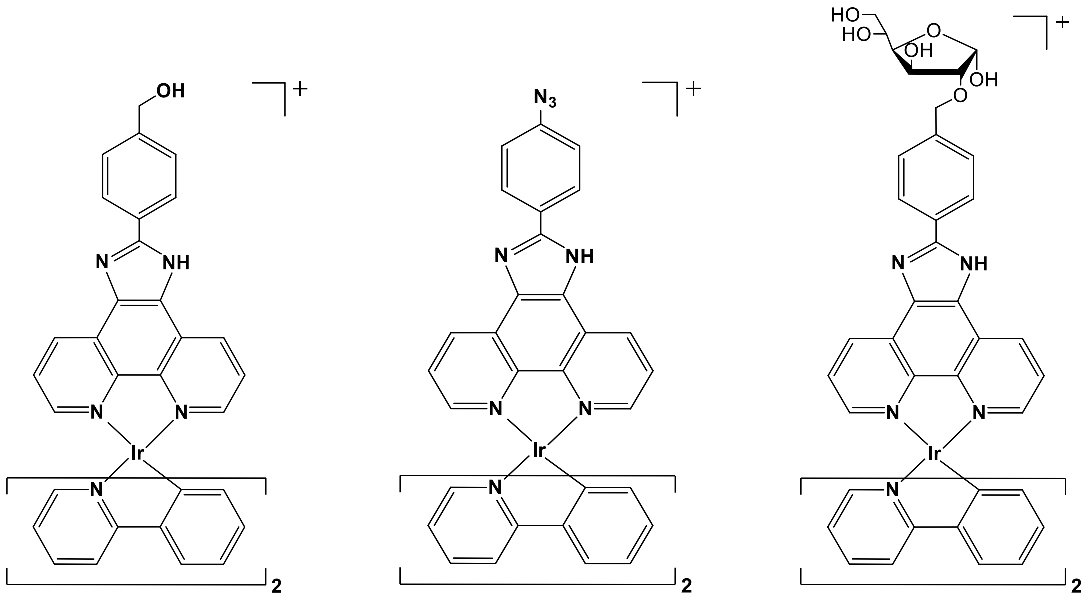

Ir-4 **Ir-5** **Ir-6**

Figure 79. Molecular structure of the designed Ir(III) complexes functionalized with a biological vector.

A briefly description of the followed synthetic pathways is provided in paragraphs 3.2.3.5, 3.2.3.5, 3.2.3.5. The detailed synthetic procedures are reported in the Experimental Section.

3.3.2.1.2.1 Photophysical properties

The investigation concerning the photophysical properties of **Ir-1**, **Ir-2** and **Ir-3**, were performed in degassed dichloromethane at 298.15 K. Specifically, variable amounts of the emitters were dissolved in dichloromethane with the purpose to evaluate the effect of the gradually increasing concentration on the photoluminescence phenomenon. Given the sensibility displayed by Ir complexes towards molecular oxygen, freeze-pump-thaw cycles were performed aiming to prevent undesired quenching.

The collected data have been extensively discussed in paragraph 3.2.3.7.1.

Chapter II- Phosphorescent organometallic complexes for OLEDs

1. OLEDs: introduction and principles

Organic light-emitting diodes (OLEDs) gained increasing attention over the last decades due to their optimal photophysical properties for a wide range of applications, such as solid-state lighting and flat panel displays. OLEDs technology relies on electroluminescence, a phenomenon discovered in 1936 in ZnS phosphors[137], that involves the emission of light in response to the application of a potential difference to a photo-electron functional semiconductor. The recombination of electrons and holes generated applying the voltage gives rise to the emission of electromagnetic radiation.

In the early 1960s, Martin Pope *et al.*[138, 139] reported the design of the first electroluminescent device made up of a layer of anthracene single crystals. The radiative emission was obtained applying a high voltage under vacuum. Unfortunately, the high voltage and the large size of single crystals required for the process, represented a hindrance for large scale application.

The first well-functioning OLED was developed in 1987 by Tang and VanSlyke.[140] The device consisted of two organic thin films embedded between an anode and a cathode. The two organic layers had a specific function: the film made of aromatic diamine served as an efficient hole transporter, conversely, the tris(8-hydroxyquinoline) aluminum (Alq_3) microcrystals act both as emitting layer and electron transporters. The molecular representation of the Alq_3 structure is reported in **Figure 80**.

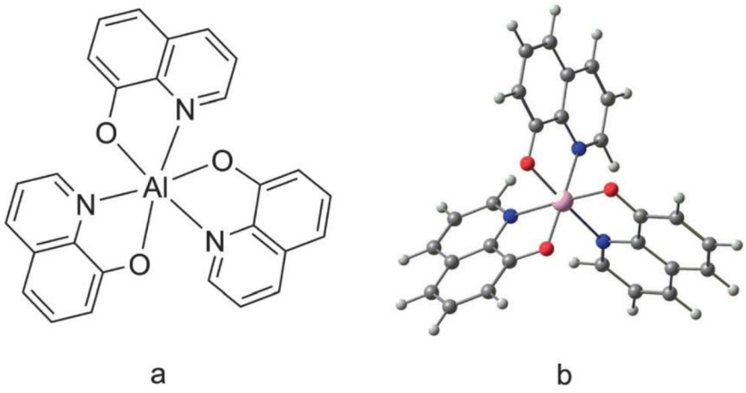

Figure 80. (a) Molecular structure of Alq_3; (b) 3D model of Alq_3.

The promising performance observed in the designed device, encouraged further studies aimed at improving the OLED components. Moreover, the use of separated organic layers as electrons and holes transporters, suggested that the recombination of the charge carriers takes place in the device core. This basic principle is at the basis of the reduced voltage necessary to induce the emission phenomenon.

The first OLED were made of polymeric emissive layers:[141] the unsaturated backbone of organic molecules was considered an efficient electron conductor, due to the delocalization of the electrons provided by conjugation. The polymeric layer, for instance polyphenylene vinylene (PPV), was typically attached to an indium oxide layer, serving as the anode of the system and a cathode, which was made of magnesium silver alloys, aluminum, or amorphous silicon hydrogen alloys.

Initially, the conjugated aromatic molecules are in their ground state, so the electrons are all paired up in the HOMO. When a bias is applied, the charge carriers are injected in the device and start flowing through the layers towards the anode and the cathode. Since electrons and holes bear negative and positive charges respectively, they tend to attract each other in close proximity via electrostatic interactions and the formation of excitons occurs. Two types of excitons can be generated: singlet excitons and triplet excitons. Indeed, when an electron is injected from the cathode to the LUMO, a spin-up or a spin-down orientation is equally probable.[142]

According to quantum mechanics, the triplet state is divided into three sublevels, thus the triplet excitons are statistically produced with a ratio of 3:1 with respect to singlet excitons. As a consequence, triplet excitons play a crucial role in imparting the efficiency of the system.

The recombination of the charge carriers involving the singlet excited state ($S_1 \rightarrow S_0$) is spin allowed according to the selection rules, thus it results in a fluorescent emission. On the other hand, the transition starting from the triplet excited state ($T_1 \rightarrow S_0$) gives rise to a non-radiative decay, dissipating the exceeding energy through the release of heat. The transition is indeed spin-forbidden and phosphorescence has such a low rate constant that intramolecular vibrations quench the radiative emission. Overall, a great part of the applied voltage is converted in heat and the device increases its internal temperature, resulting in an inefficient process. In the ideal OLED, the rate constant of the radiative deactivation has to be enhanced in order to become competitive with the vibrational energy dissipation rate constant.[142]

The restrictions imposed by the spin selection rules can be circumvented when the light absorbing substrate is characterized by a strong spin-orbit coupling. In this context, organometallic complexes made of heavy transition metals of the second and third row such as Pt and Ir, provide a promising alternative to organic π-conjugated molecules.

The insertion of heavy metal organometallic complexes in the emitting layer of the device can theoretically achieve the 100% of the internal quantum efficiency. Indeed, the strong spin-orbit coupling provided by the metal center ensures a huge increase in the probability of the $T_1 \rightarrow S_0$ transition, leading to an efficient phosphorescent emission. Thus, the triplet excitons (75%) result in a radiative long-lived emission whilst the singlet excitons produced (25%) can either give rise to direct radiative decay or convert into triplet state via intersystem crossing and deactivate through phosphorescence.[142] In principle, the 100% of the generated excitons releases electromagnetic radiations and nonradiative deactivation is no longer competitive.

Nevertheless, phosphorescent emitters pose various issues in the design of the device: the use of high voltage to increase the stability of the triplet state, can induce competitive quenching mechanism that affect the OLEDs efficiency.[143]

Nowadays, OLEDs consist of multilayer devices in which the material and the width of each layer are variable, in order to finely tune the properties required for the developed system.[144] The schematic representation of an OLED, the charges migration through the device and the light emission are reported in **Figure 81**.

A

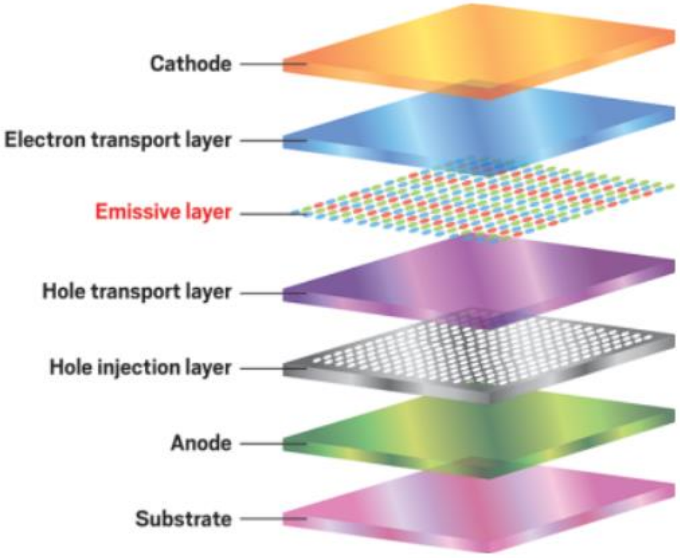

B

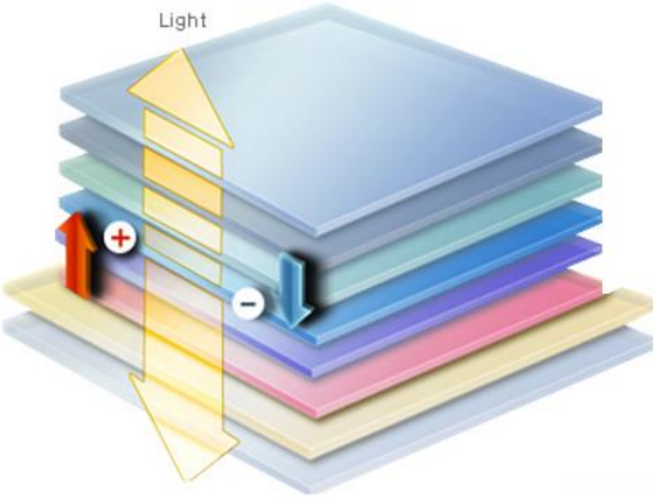

Figure 81. (A) Illustration of an OLED devices architecture; (B) Charge carriers and light flow through the multilayer structure.

Generally, a transparent glass is coated with tin-doped indium oxide (ITO) to form the anode.[142] On the opposite side of the device, electrons are generated by a low work function material such as aluminum or alkaline earth metals, serving as the cathode. The hole-injection layer and the electron-injection layer are stacked on the anode and cathode, respectively, to favor the charge carriers flow towards the electrodes.

In the middle of the device, the emission layer (EML) is surrounded by a hole-transport layer (HTL) and an electron-transfer (ETL) layer. The HTL and the ETL are organic layers that usually include the arylamine, carbazole or fluorene fragments. The most frequently used component of ETL layers is Tris (8-hydroxyquinoline)aluminium(III) (Alq_3), due to the promising emissive properties displayed. To further improve the charge carriers' flow through the device, a hole-blocker layer (HBL) can be inserted in order to avoid the holes to access to the ETL.[142]

The device core plays a central role in the electroluminescence process efficiency: in the emission layer the guest, a photoluminescent compound, is dispersed in the host, a solid matrix. The most popular host constituent is the 4,4'-N,N'-dicarbazolebiphenyl (CBP) molecule, due to its suitable electronic band structure and photophysical properties.[142] Heavy metal organometallic complexes appear to be ideal guests for the emission layer, since they display optimal emission properties, and they can be further modified to finely tune the wavelength of emission. This last feature is particularly interesting: the proper modification of the coordination sphere of the metal center provides the organometallic complexes to be able to emit at different specific wavelengths. The dopants selected are responsible for the color of the device, thus the design of a variety of organometallic complexes would allow the production of OLEDs with a wide range of colors.

However, the exciton formation could be followed by undesirable processes that result in the quenching of the luminescence, affecting the efficiency of the OLEDs. In this context, the guest doped into the host matrix has to be highly dispersed. Indeed, once a bias is applied to the device, the host generates single excitons (D*) and the exceeding energy could be accepted by the guest (A). When the emission spectrum of the host overlaps the absorption spectrum of the guest, a long range-Förster energy transfer occurs.[142] The mechanism is represented in **Figure 82** and it is promoted by the interaction between the dipole transition moments associated to the two species (M_1 and M_2).

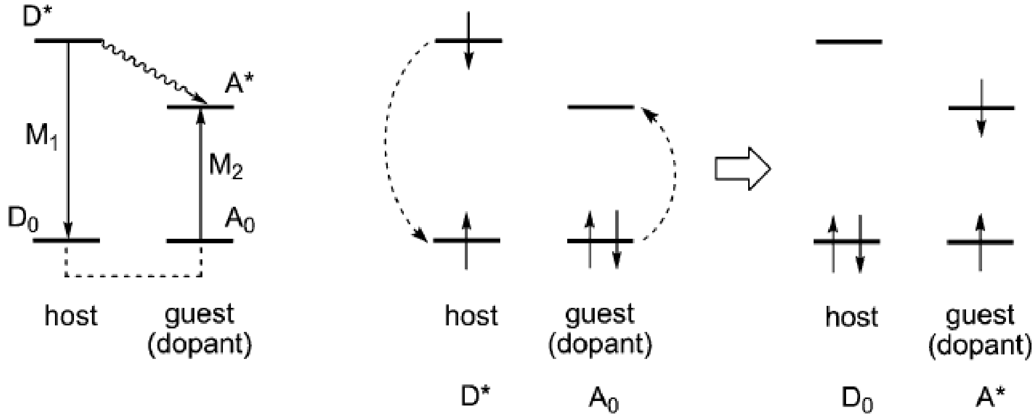

Figure 82. Schematic mechanism of the long range Förster energy transfer involving the host matrix and the guest.

The short-range Dexter energy transfer consists of electron exchanges that involve both the HOMO and the LUMO orbitals of the donor and of the acceptor. The overlap of the wavefunctions of the guest and the host is crucial and thus the distance between the two species heavily affects the efficiency of the process. The Dexter energy transfer involves either singlet-singlet energy transfer or triplet-triplet energy transfer. In **Figure 83** the singlet-singlet electron exchange is represented.

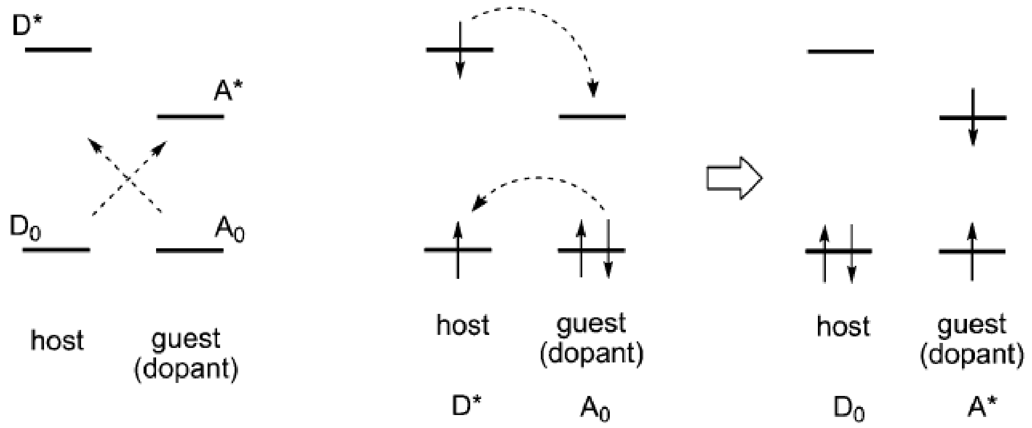

Figure 83. Schematic mechanism of the short-range Dexter energy transfer involving the host matrix and the guest.

The applied voltage can lead to the formation of singlet and triplet excitons directly generated by the guest. Thus, the host matrix isn't involved in energy transfer processes and only serves as a charge transporter.

In this context, the efficiency of the devices is enhanced when electrons and holes are stuck on the organometallic phosphor.

Given these premises, the design of the ideal OLED must take into account many aspects:[142]

- The host has to show a good photo- and chemical stability;
- The emission layer matrix has to allow an efficient charge carrier flow;
- The electronic structure of the host matrix has to match the electronic structure of the guest;
- Selection of the proper host and guests in order to avoid quenching mechanisms and the release of heating.

Multilayer devices provide a convenient strategy to overcome many limitations, since they allow to enhance the performance of each layer. The efficiency of the OLED can be further improved introducing a hole-blocker layer.

Although the improvements made in the development of the ideal OLED, two main objectives have yet to be achieved:

- Obtaining bright blue-light emitters;
- Optimizing the photo-functional material.

In particular, with regard to the blue emission, Pt(II) complexes have been investigated[145, 146, 147]

due to their optimal photophysical properties.

2. Cyclometalated Pt(II) complexes for OLEDs: introduction and state of the art

The third-row transition metal ions provide a suitable metal center for the development of organometallic compounds meant to be inserted in the emissive layer of OLEDs. In this context, Pt(II) based emitters made up of 6-phenyl-2,2′-bipyridine and N^N^C ligands the have been widely investigated over the years.[48, 50, 148, 149, 150, 151]

Thompson *et al.*[152] reported a study concerning a series of variously modified bidentate cyclometalated Pt(II) complexes in order to demonstrate the fine-tuning of the emission color resulting from the introduction of different atoms and functional groups. In particular, the Pt(ppy)(dmp) complex, where ppy stands for 2-phenylpyridine and dmp for dipivaloylmethane, was taken as the reference and the 2-phenylpyridine ligand was gradually modified with either electron-donating or electron-withdrawing substituents. The complexes displayed a strong and bright emission in the solid state at 77K associated to a lifetime of the excited state of microseconds, displaying a wide range of colors in the visible spectrum.

The introduction of a strong electron-donating dimethylamine group on the pyridine ring and of electron-withdrawing fluorine atoms on the benzene ring (**4,6-dFp-4-dmapyPt(dpm)**) results in a blue emitting complex, displaying a wavelength of emission of λ_{max} = 440 nm and a life-time of the excited state of τ = 6.1 µs in 2-methyltetrahydrofuran at 77K. The molecular representation of the investigated complex is given in **Figure 84**.

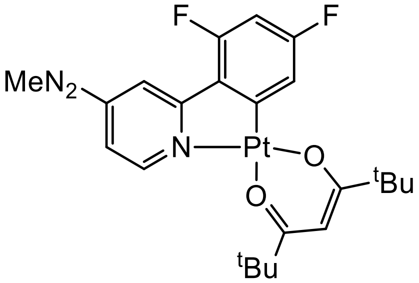

Figure 84. Molecular structure of the 4,6-dFp-4-dmapyPt(dpm) complex evaluated by Thompson et *al.*.

The studies conducted over the obtained emission spectra are coherent with the assumption that the excited state involved in the radiative decay derives from a combination of the ^{3}LC and MLCT excited states. The redox properties and consequently the emission properties of the complex can be heavily affected by the substituents introduced on the 2-phenylpyridine ligand. Electron-withdrawing fluorine atoms inserted on the phenyl ring give rise to a hypsochromic shift, decreasing the reduction potential. On the other hand, the functionalization of the pyridyl ring with a strong electron-donating group as dimethylamine, raises the

LUMO energy, further increasing the energy gap between the molecular orbitals involved in the radiative decay. As a consequence, the wavelength of emission decreases, thus resulting in a blue emission.

Pt(II) blue emitters have gained great interest for OLED application, leading to the development of improved luminescent Pt(II) complexes. Indeed, the aforementioned complex displays a drastic decline in the quantum yield at room temperature.[152] This evidence could be explained considering that the bidentate ligand is not rigid enough and, upon excitation, the excited state of the complex is heavily distorted and the metal centered (MC) excited state thermally accessible, thus resulting in a non-radiative deactivation.

With the purpose to overcome the described limitations, terdentate cyclometalated chelators for Pt(II) complexation were designed and investigated.

In this context,[48] 1,3-di(2-pyridyl)benzene ligands provide a suitable coordinating moiety for Pt(II), giving rise to bright emitters: the structure of the ligand can't twist, thus ensures a rigid backbone. Moreover, the Pt-C bond is shorter compared to the Pt-C bond in the bidentate N^C ligand, resulting in a stronger covalent interaction and consequently in a higher ligand-field stabilization energy. The molecular representation of the developed terdentate complex is given in **Figure 85**.

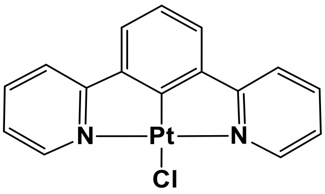

Figure 85. Molecular structure of the Pt(II) based emitter built with the 1,3-di(2-pyridyl)benzene pincer.

The Pt(II) complex made up of the cyclometalated 1,3-di(2-pyridyl)benzene ligand, bearing the chloride anion as the ancillary ligand, has been widely investigated[48] and its photophysical properties turned out to be optimal: the wavelength of emission λ_{max} = 491 nm, the quantum yield Φ = 0.60 and the lifetime of the excited state τ = 7.2 µs were obtained in a deoxygenated dichloromethane solution at room temperature. The emission spectra analysis highlighted that the emitting excited state has mainly a ligand centered $^3\pi$-π^* character.

Taking as a reference the aforementioned Pt(II) luminophore, the introduction of proper functional groups in the 1,3-di(2-pyridyl)benzene moiety provides a successful strategy to produce different color devices covering a wide range of wavelengths and to maximize the photoluminescence efficiency.

In this context, a modified 1,3-di(2-pyridyl)benzene Pt(II) complex obtained introducing two fluorine atoms on the central benzene ring and two dimethylamine groups on the pyridine rings (PtL^{30}Cl) was investigated,[47] and a pronounced blue-shift effect was observed. The molecular structure of the complex is represented in **Figure 86**.

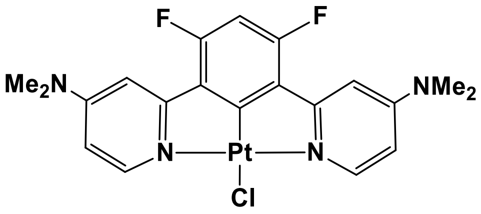

Figure 86. Molecular structure of the cyclometalated Pt(II) complex (PtL^{30}Cl) functionalized with dimethylamino groups on the 4-position of the pyridine rings.

Previous studies concerning the electronic structure of the reference complex (**Figure 85**) revealed the roles played by the 4-position of the pyridine rings[47] and the meta position[151] with respect to the metal, on the benzene ring within the ligand. The 4-position of the heterocyclic rings is strictly related to the LUMO energy thus, the introduction of a strong electron-donating group as dimethylamine leads to a raised LUMO energy and to a subsequent increase in the HOMO-LUMO gap. On the other hand, the meta position on the benzene ring relative to the metal ion affects the energy of the HOMO. The substitution with two fluorine atoms of the aromatic hydrogens localized in the meta positions with respect to the Pt(II) ion, gives rise to a lowering of the HOMO energy. Overall, the energy gap between the HOMO and the LUMO further increases, resulting in the blue shift.

The electronic structure studies were further confirmed[47] by the evaluation of the photophysical properties. For the purpose, the complex was solubilized at low concentration in a deoxygenated solution at room temperature, resulting in a sky-blue emission, λ_{max} = 453 nm, with a good quantum yield Φ = 0.60 and a life-time of the excited state equal to τ = 4.7 µs.

The presence of the methyl groups on the pyridines are important in the context of interaction between molecules in the media as well. The planar geometry of Pt(II) complexes favors the formation of weak interactions between close molecules: the orbitals orthogonal to the molecular plane tend to overlap, giving rise to face-to-face interactions. Ground-state stacked complexes display absorption and emission bands that are shifted to lower energies compared to the isolated complex. The interaction between a ground-state complex and an excited one can also occur, leading to the formation of excimers, species characterized by red shifted emission with respect to the monomer. The cyclometalated Pt(II) based emitter functionalized with the dimethylamine groups seems to discourage the aggregation process, because of the steric hindrance provided by the methyl groups.

The design of OLED containing blue emitters require a detailed study of the materials used for each layer. In particular, the host matrix has to be characterized by high triplet energy states in order to avoid quenching provoked by the energy transfer from the excited guest to the host.

Williams J. A. G. *et al.*[47] reported the fabrication of the OLED device doped with the described blue emitting Pt(II) complex (PtL^{30}Cl). The OLED architecture is reported in **Figure 87**.

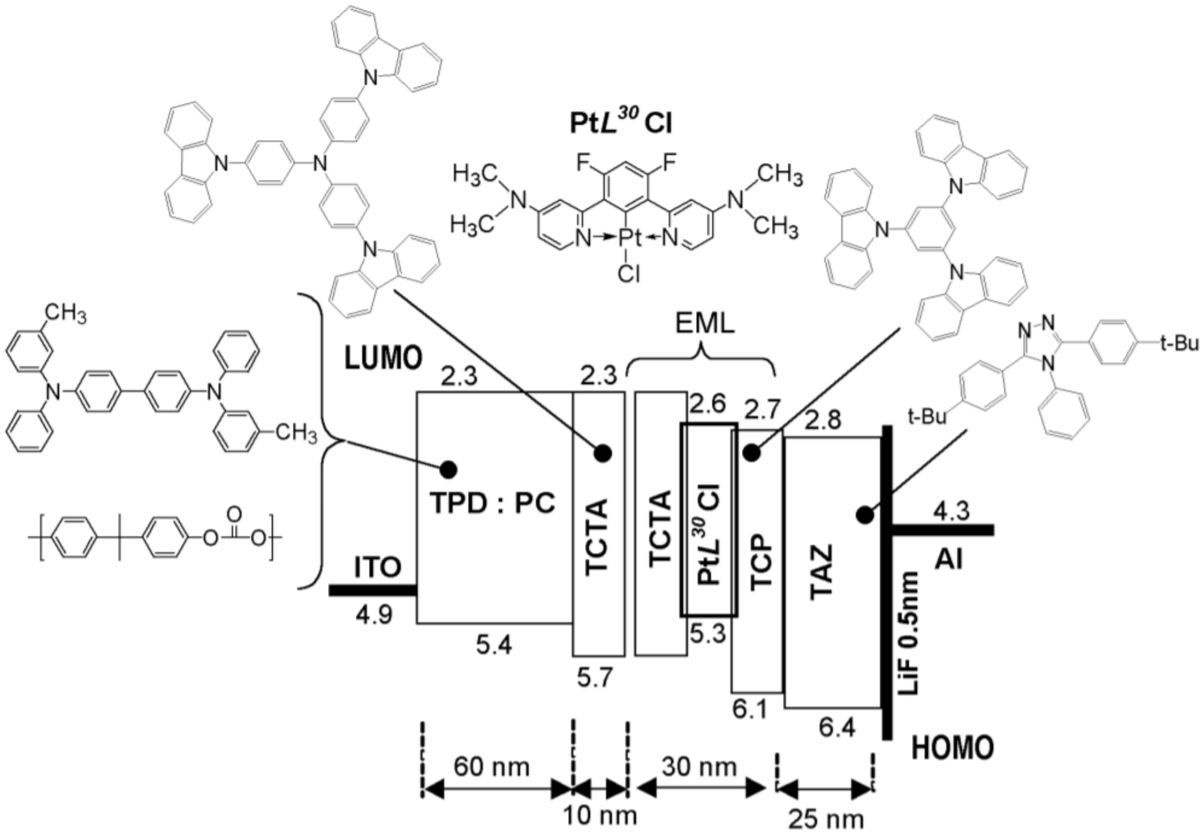

Figure 87. Illustration of the OLED device fabricated by Williams et *al.*.

The emissive layer composition was investigated in order to maximize the electroluminescence efficiency. The study highlighted that the greatest results were obtained using a 1:1 mixture of 4,4',4''-tris-(N-carbazolyl)-triphenylamine (TCTA) and 1,3,5-tris(N-carbazolyl)benzene (TCP) as the host matrix.

Having fixed the optimal composition of the host, the concentration of the Pt(II) complex was gradually varied to assess the effect of the excimer formation on the emission color. Low dopant concentration results in the blue emission deriving from the radiative deactivation of the isolated complex triplet excited state. Upon gradual raise of the emitter concentration, an increase of the red emission contribution associated with the radiative decay of excimers or aggregates, was assessed. Conversely, the insertion of the Pt(II) based phosphor in a concentration equal to 100% suppresses the blue emission completely. The electroluminescence spectra depicting the emission bands for each Pt(II) complex concentration is reported in **Figure 88** with an inset representing the Commission Internationale de l'Eclairage (CIE) diagram.

Plotting the different dopant concentration in the CIE diagram, an almost linear trend is outlined. The analysis of the chromaticity diagram highlights that concentrations of the Pt(II) emitter equal to 20 wt% and 25 wt% correspond to CIE coordinates near white.

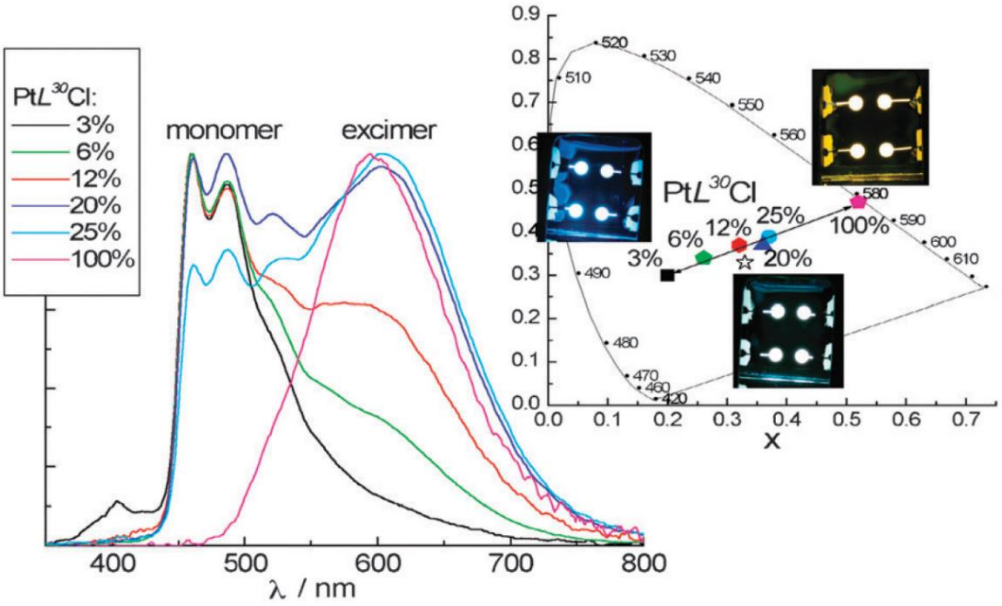

Figure 88. Electroluminescence spectra obtained increased concentration of $PtL^{30}Cl$ embedded in the emitting layer (TCTA:TCP, 1:1). Inset: CIE diagram.

In conclusion, the cyclometalated Pt(II) emitter functionalized with the dimethylamine on the pyridine rings designed and investigated by Williams J. A. G. *et al.* displays optimal photophysical properties as a blue phosphor for OLED application. Indeed, the terdentate N^C^N ligand provides a rigid backbone able to prevent the thermal deactivation of the triplet state, leading to a 600 fold more emissive complex compared to the analog bidentate organometallic dopant bearing the modified 2-phenylpyridine ligand.

Furthermore, the possibility to control the formation of excimers represents a promising approach to exploit the combination of monomeric and excimeric emissions to obtain a wide range of colors. In particular, the choice of the proper composition of the emissive layer can produce white light, achieving White Organic Layer Emitting Diodes (WOLED).

2.1 Pt(II) emitters for OLEDs fabrication displaying outstanding quantum yield

Che et *al.*[153] synthesized a series of tridentate cyclometalated Pt(II) complexes variously functionalized, aiming to develop bright and efficient emitters both for bioimaging and OLEDs fabrication purposes.

The molecular representation of the investigated complexes is reported in **Figure 89**.

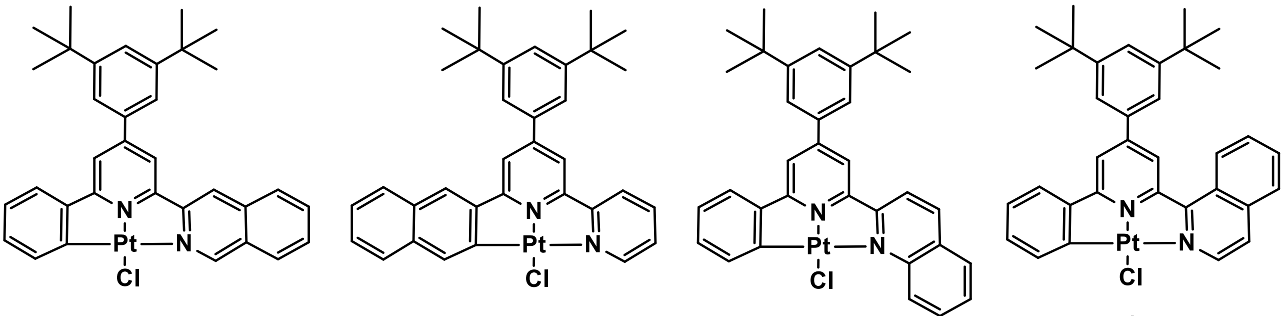
1 **2** **3** **4**

Figure 89. Molecular structure of the Pt(II) complexes 1-4 investigated by Che et *al.*.

The complexes were designed with a robust and rigid pincer, in order to investigate the effect of the structure on the deactivation pathway and to enhance the efficiency of the radiative emission, discouraging potential distortions of the excited-state backbone. The introduction of a 3,5-ditert-butylbenzene moiety on the central pyridine rings, further enriches the electronic structure of the complex, contributing to enhance the π-conjugation of the system.

The positional isomers show strong phosphorescence in a degassed dichloromethane solution, where **1** displays a value of quantum yield equal to unity.

Overall, a strong absorption around λ = 250-350 nm related to the singlet intraligand (^{1}IL) $\pi \rightarrow \pi^*$ transition was observed, accompanied by a weaker absorption at λ = 400-470 nm attributed to the ^{1}IL/^{1}MLCT (metal to ligand charge transfer) transition. Concerning the emission, the peaks maxima are centered between λ = 521-653 nm, displaying a significant redshift as highlighted in **Figure 90**.

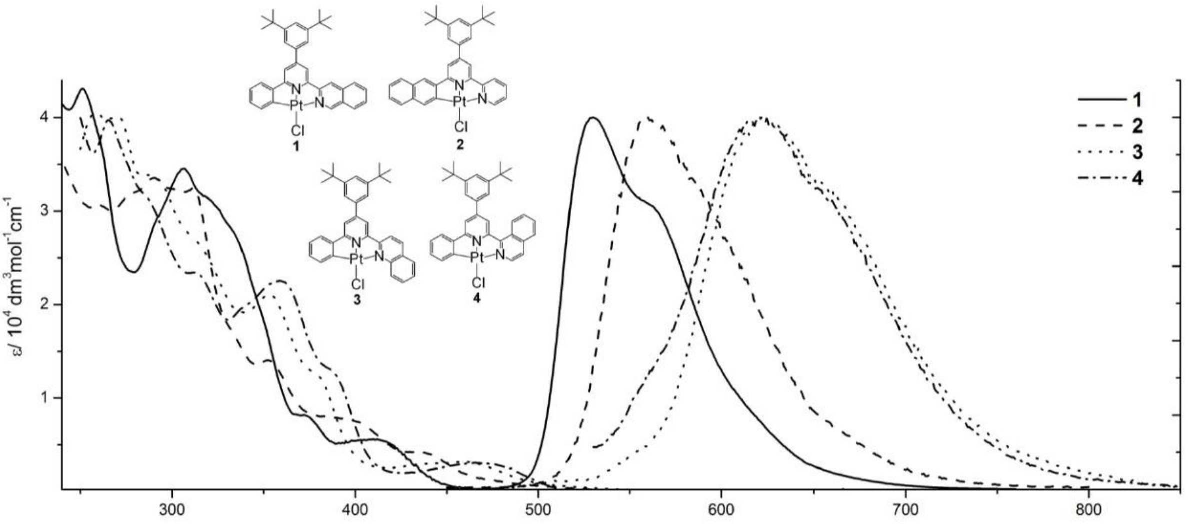

Figure 90. UV-Vis absorption spectra of complexes 1-4 recorded at room temperature in $2\cdot 10^{-5}$M CH_2Cl_2 solution. Emission spectra of 1-4 recorded in $2\cdot 10^{-5}$M CH_2Cl_2 solution. 1, λ_{ex} = 410 nm; 2, λ_{ex} = 433 nm; 3, λ_{ex} = 459 nm; 4, λ_{ex} = 460 nm.

The phenomenon could be explained relying on the distorted geometry of the triplet excited state with respect to the ground state, which displays a perfectly coplanar arrangement. In particular, the triplet excited state of **3** and **4** undergoes a significant distortion, leading to a huge decrease in the quantum yield. On the other hand, the rigid structure of **1** ensures the coplanarity even after the intersystem crossing, giving rise to a quantum yield equal to unity.

Aiming to fully characterize the potential of complex **1**, it was embedded as emitter in the OLED device, constructed sequentially depositing indium tin oxide (ITO), (4,4'-cyclohexylidenebis[*N,N*-bis(4-methylphenyl)benzamine]) (TAPC) as the hole-transporting layer, (4,4',4''-tri(9-carbazoyl)triphenylamine) (TCTA) hosting the Pt(II) complex, (3,3'-[5'-[3-(3-pyridinyl)phenyl][1,1':3',1''-terphenyl]-3,3''-diyl] bispyridine) (TmPyPB) used as the electron transporter and finally LiF and Al. The organic substrates used for the device fabrication are depicted in **Figure 91**.

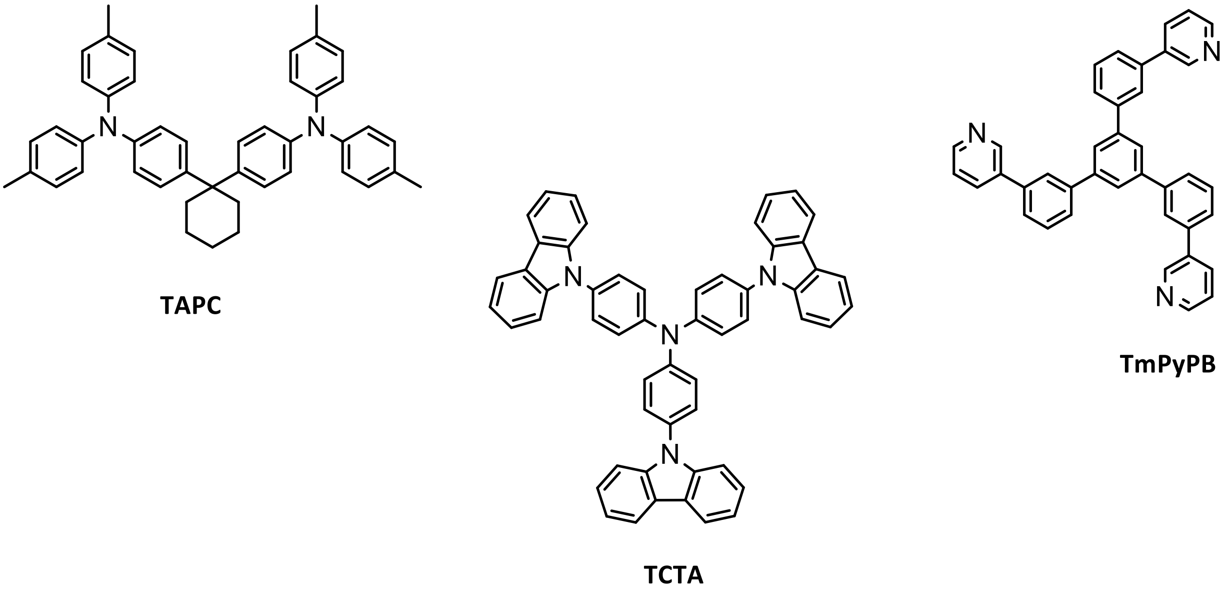

Figure 91. Molecular structures of TAPC, TCTA, TmPyPB.

The wavelength of emission observed in the solid-state results slightly red shifted with respect to the emission maximum determined in solution at ambient temperature, giving rise to a green-yellow emission with CIE coordinates of (0.431, 0.557). The external quantum efficiency value is optimal, with a maximum of 21%. In addition, the emission of the hosting material, which should be assessed at λ = 400 nm, was not observed thus implying a highly efficient energy transfer from the organic TCTA matrix to the dopant.

In conclusion, the promising studies conducted on the designed Pt(II) complexes, prompted us to assess the effect of highly hindered substituents introduced on the robust 1,3-di(2-pyridyl)benzene moiety, performing the functionalization in the para position of the pyridine rings, rather than on the central ring of the backbone aiming to investigate its impact on the aggregation process in the solid state. The detailed discussion concerning the developed emitters is reported in paragraph 2.2.

2.2 Fluorinated cyclometalated Pt(II) phosphors bearing highly hindered substituents

The optimal photophysical properties displayed by the fluorinated cyclometalated Pt(II) complex functionalized with dimethylamine groups on the pyridine rings, the promising results obtained by Che *et al.,* and the possibility to tune the emission color varying the dopant concentration, encouraged further investigations in this context.

To our knowledge, a detailed evaluation reporting the effect of highly hindered aromatic substituents introduced in the 4-position of the pyridyl rings, as part of the 3,5-difluoro-2,6-di(2-pyridinyl)phenyl ligand, for OLED and WOLED application, has not been published yet.

The synergy between the optimal photophysical properties provided by the rigid terdentate 1,3-di(2-pyridyl)benzene moiety and the tuning of the electronic structure achieved through the backbone modification with proper functional groups, represents a successful strategy to fulfill bright blue emission for OLED application. Specifically, strong electron-donating functional groups inserted on the 4-position of the heterocyclic rings raise the LUMO energy, leading to a pronounced blue shifted emission. A key role is also played by the steric hindrance provided by the substituents. The excimers or aggregates formation could be controlled achieving the proper spatial arrangement of the bulky functional groups.

In this context, a series of fluorinated cyclometalated Pt(II) emitters bearing sterically hindered aromatic substituents on the pyridyl moiety of the ligand were designed, synthesized and investigated for OLEDs and WOLEDs fabrication. The molecular structure of the analyzed complexes is reported in **Figure 92**.

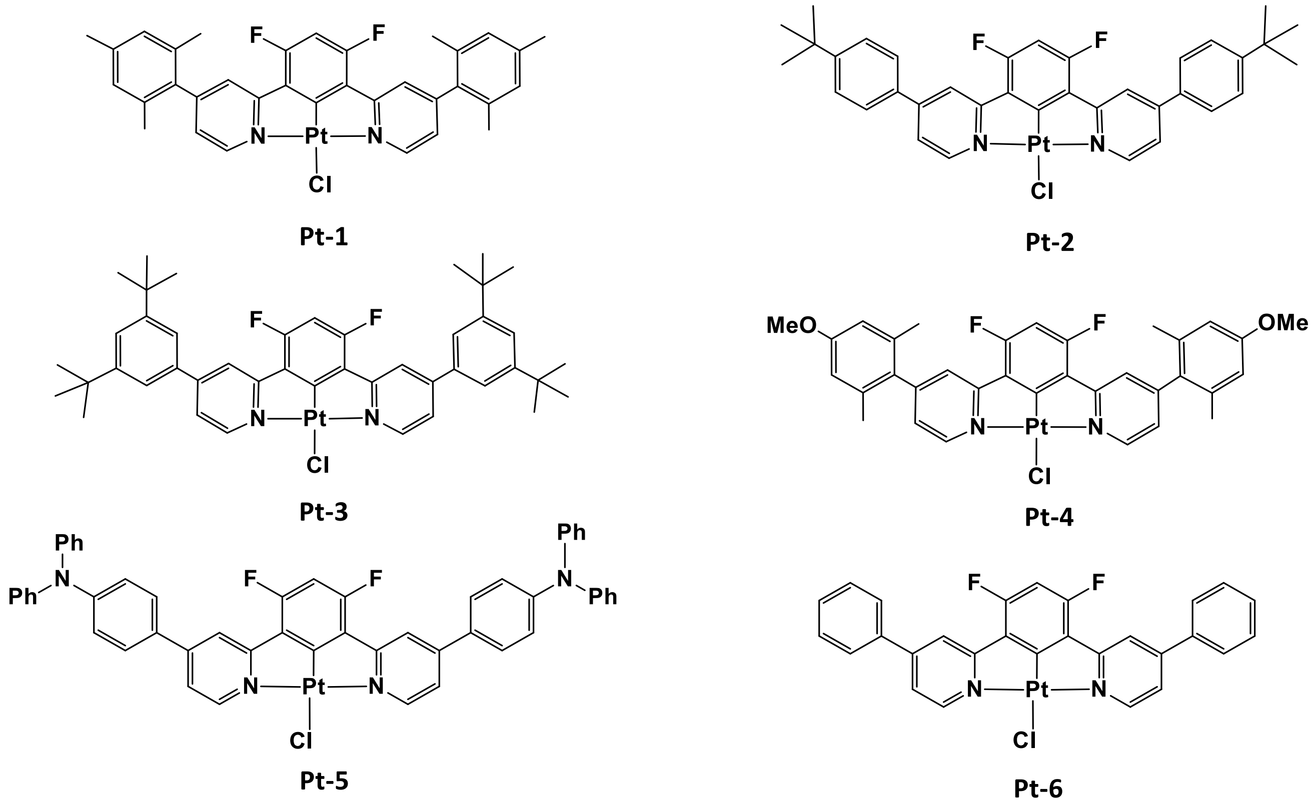

Figure 92. Molecular structure of Pt-1 to Pt-6.

The introduction of highly hindered aromatic groups is expected to discourage the Pt(II) complexes stacking, that leads to the formation of aggregates and excimers. Indeed, it has been hypothesized that in the solid state the substituent could be twisted with respect to the molecular plane, outlined by the planar cyclometalated ligand coordinated to the Pt(II) ion and the ancillary ligand. The hypothesis was then confirmed by the X-ray analysis performed on the crystals obtained from **Pt-1**. The X-ray structure of **Pt-1** is reported in **Figure 93**.

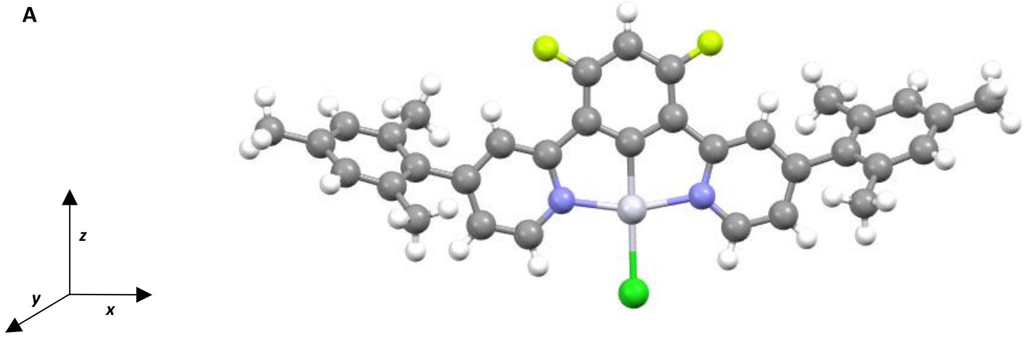

B

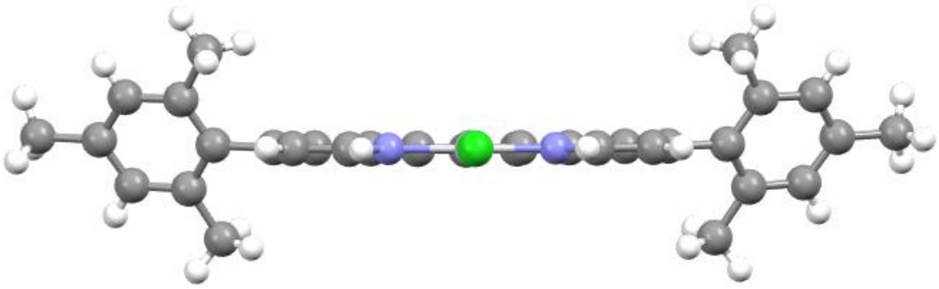

Figure 93. X-ray structure of Pt-1 embedded in needle crystals. A) Frontal view of Pt-1. B) Pt-1 with the molecular plane lying on the xy plane to highlight the orientation of the mesityl groups.

The structural arrangement of **Pt-1** embedded in the crystal displays the mesityl groups twisted of 61.7° with respect to the molecular plane.

The inclination of the sterically hindered substituents to undergo rotation around the bond that links them to the cyclometalated scaffold was further supported by the crystalline structure obtained for the pincer of **Pt-6**.

Even though the N^C^N moiety isn't perfectly coplanar due to the absence of the metal ion that provides rigidity fixing the structure, the twisted spatial configuration of the phenyl rings has been evidenced (**Figure 94**). Specifically, the torsion angle measured 46.9°.

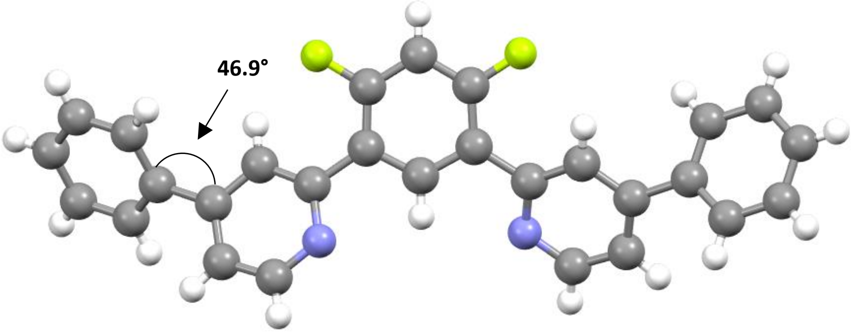

Figure 94. X-ray structure of the pincer of Pt-6, displaying a twisted arrangement of the phenyl rings with respect to the molecular plane.

The electroluminescence analysis concerning **Pt-2**, **Pt-3**, **Pt-4** and **Pt-6** are still in progress.

2.2.1 Synthesis and characterization of the developed sterically hindered Pt(II) emitters

2.2.1.1 Synthesis of the fluorinated highly hindered Pt(II) complexes

The synthetic pathway followed for the preparation of the sterically hindered Pt(II) complexes has been briefly outlined in paragraph 3.1.2.1. The detailed description is provided in the Experimental Section, Chapter III.

Pt-1 to **Pt-6** were synthesized following a common route, involving three steps:

- The modification of the pyridine rings through functionalization with the proper aryl substituent;
- The construction of the rigid terdentate N^C^N chelating ligand;
- The complexation through combination with the Pt(II) salt.

The synthesis of the backbone was achieved through two subsequent Suzuki couplings, which are very versatile and can be performed combining different sets of starting materials. In particular, **Pt-1** to **Pt-4** were obtained starting from the 2-chloro-4-iodopyridine and the boronic acid of the desired aryl functional group,[51] whilst **Pt-5** and **Pt-6** were synthesized combining the 2-chloro-pyridine-4-boronic acid with the suitable bromine derivative of the sterically hindered substituent.[52]

The introduction of the highly hindered substituent on the pyridine ring was followed by the synthesis of the cyclometalated moiety though reaction of the modified 2-chloropyridine and the pinacol ester of 1,3-difluoro-4,6-diboronic acid.[47]

Finally, **Pt-1** to **Pt-6** were obtained refluxing each sterically hindered fluorinated ligand with K_2PtCl_4 in a 9:1 mixture of acetonitrile and water under inert atmosphere.

The successful isolation of the desired Pt(II) complexes was assessed recording the ^{1}H-NMR, were characteristic signals arise as a consequence of the Pt(II) ion insertion into the cyclometalated pincer. An insight in this regard is provided in paragraph 3.1.2.1.

Additional information concerning the purity of the emitters were obtained from ^{19}F and ^{13}C-NMR spectra. Elemental analysis and mass spectrometry were carried out to finalize the characterization.

2.2.1.2 Photoluminescent properties in solution

The evaluation concerning the photophysical properties of **Pt-1** to **Pt-6** was performed at room temperature, dissolving the emitters in dichloromethane. Specifically, solutions of variable concentration were prepared for each complex, aiming to carry out an in-depth investigation to assess the effect induced by the increasing concentration on the photoluminescent phenomena. Freeze-pump-thaw cycles were performed prior irradiation, in order to prevent phosphorescence quenching through molecular oxygen removal.

The detailed collected data have been discussed in paragraph 3.1.2.2.

2.2.1.3 Highly hindered Pt(II) complexes: OLEDs fabrication

The extraordinary photophysical properties displayed by **Pt-1**, **Pt-5** in dichloromethane solution at room temperature, encouraged further investigations in the solid state. Specifically, the complexes were embedded as dopants in the emissive layer of the OLED devices. The devices were fabricated according to a multilayer structure, sequentially depositing each layer starting from the anode. The configuration involved the application of tin-doped indium oxide as the anode on the radiation-transparent glass substrate. Aiming to promote the efficient hole-injection, a 2 nm-thick Molybdenum oxide (MoO_x) layer was deposited. Subsequently, a 4,4’,4’’-tri(9-carbazoyl)triphenylamine (TCTA) layer was positioned, either used as host matrix or as hole transporter. Indeed, BCPO (bis-4- (N-carbazolyl)phenylphosphine oxide) was also used as the host material for the insertion of the Pt(II) based emitters. The device was further improved with a 30 nm-thick coating of 2,2',2''-(1,3,5-Benzinetriyl)-tris(1-phenyl-1-H-benzimidazole) (TPBi) (**Figure 95**) that acted as electron-transporter and with a thin electron-injector layer of LiF (0.5 nm). Finally, the system was closed depositing the cathode, a 100 nm-thick layer of Al.

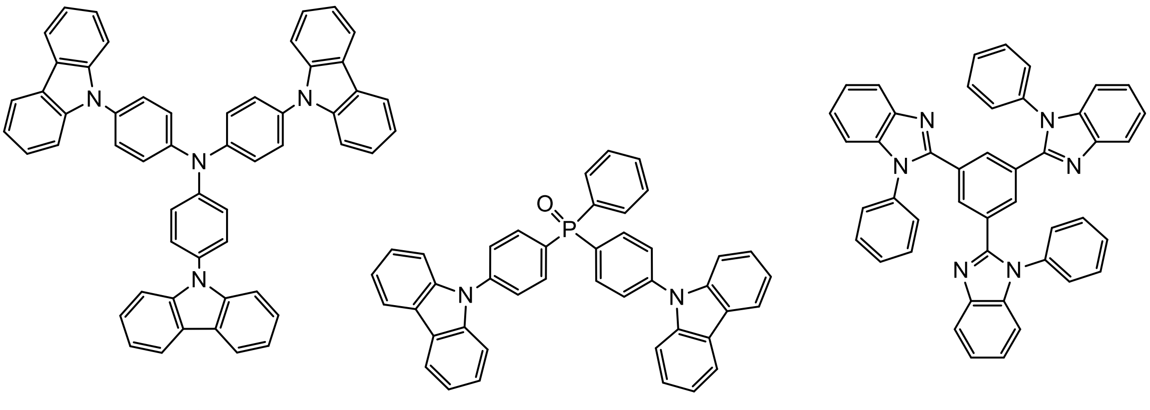

TCTA **BCPO** **TPBi**

Figure 95. Molecular structure of TCTA, BCPO and TPBi.

The devices were designed embedding diverse concentrations of the phosphors, aiming to assess the effect of increasing doping concentration on the electroluminescence properties of the device.

2.2.1.3.1 OLEDs fabrication: Pt-1

The fabrication of the devices were performed following the configuration: ITO/ MoOx(2nm)/ TCTA(50nm)/ BCPO: Pt(II) (30nm, x%)/ TPBi(30nm)/ LiF(0.5nm)/ Al(100nm) where x% stands for the concentration of the embedded Pt(II) based emitter. The host material was indeed doped using three different concentrations of the phosphor: 8% (Device I), 70% (Device II) and 100% (Device III). The schematic representation of the fabricated OLED is depicted in **Figure 96**.

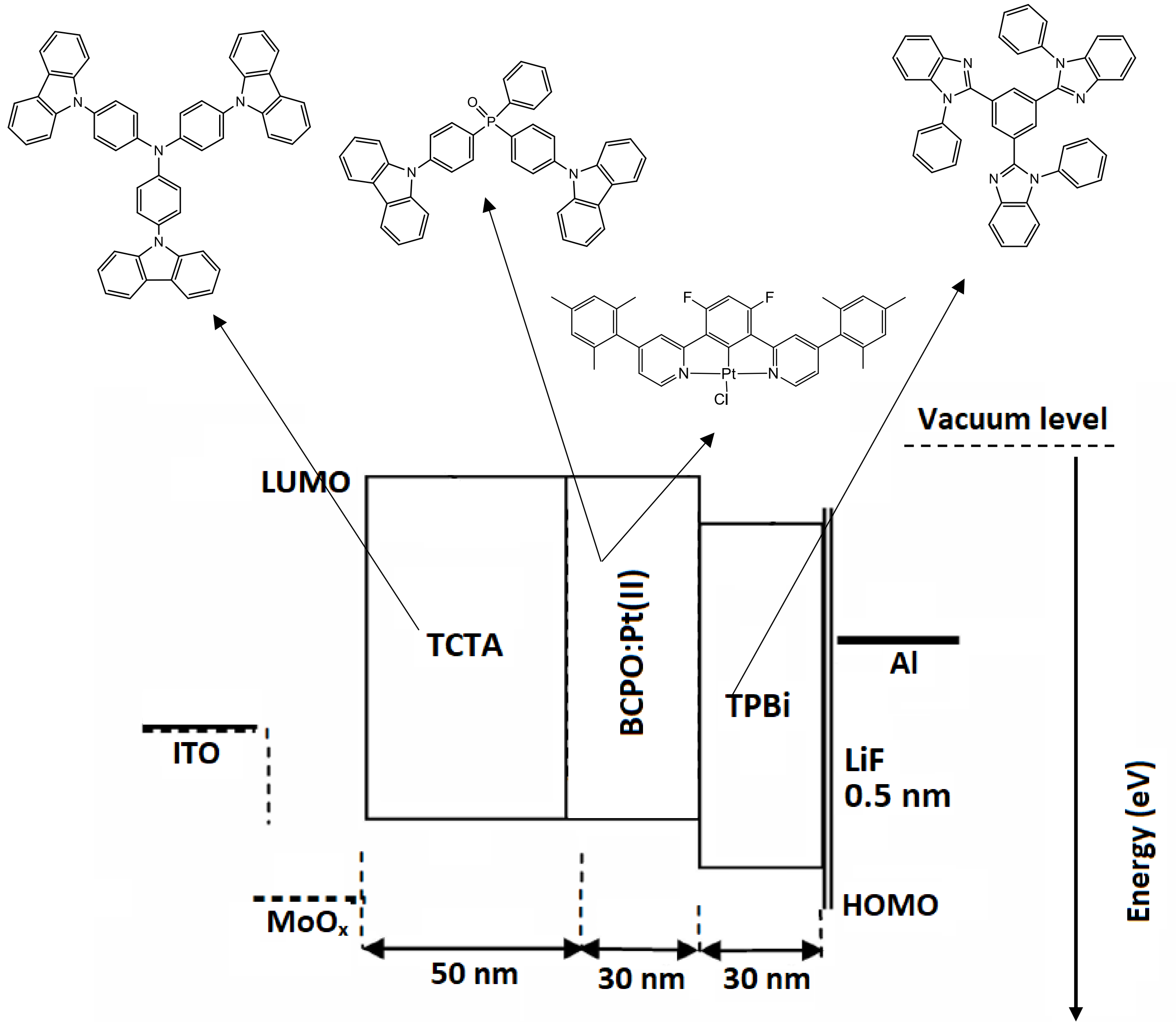

Figure 96. Illustration of the multilayer structure of the OLEDs fabricated embedding Pt-1 in the emissive layer.

The observation of the electroluminescent spectra (**Figure 97**) highlights a significant difference in the emission pattern related to the phosphor concentration. Specifically, at low doping levels (8%) the intense peak at λ = 477 nm displaying a shoulder at λ = 506 nm, can be attributed to the monomeric emission arising from the triplet excited state deactivation.

Conversely, increasing the concentration up to 70%, the monomer emission is accompanied by a second band centered at λ = 666 nm, attributable to the excimer radiative decay. Eventually, at high doping levels (100%) the peak at λ = 477 nm becomes considerably less intense with concomitant rising of the large band at λ = 666 nm. Hence, increasing the concentration of the emitter leads to the formation of excimers, which become responsible for the observed luminescence phenomenon.

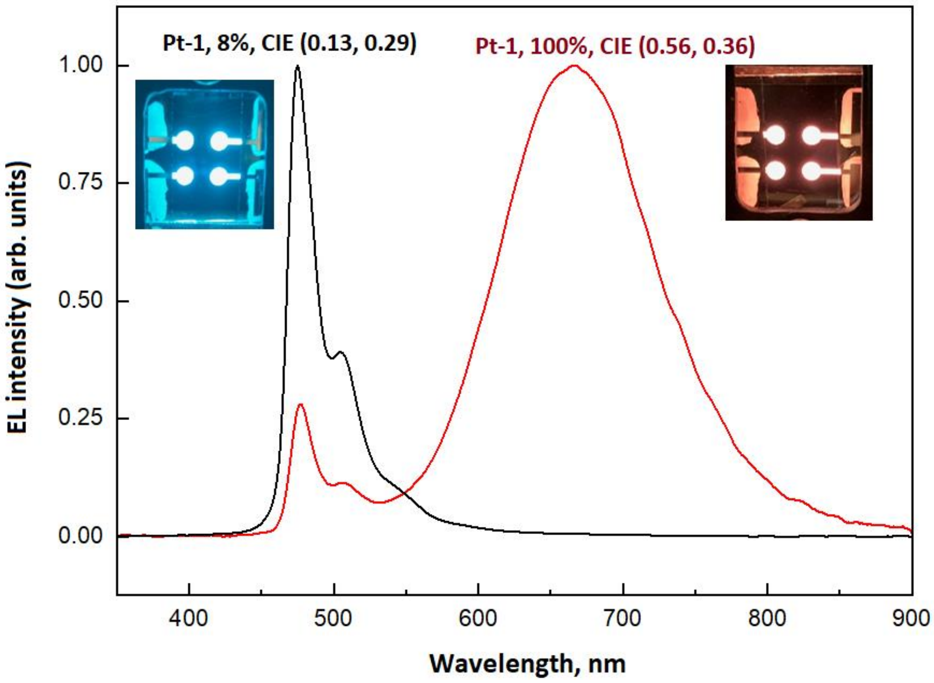

Figure 97. Electroluminescence spectra obtained inserting 8% (black line) and 100% (red line) of Pt-1 in the emissive layer of the device. Inset: Blue emission displayed by Device I (Pt-1: 8%) and red emission displayed by Device III (Pt-1: 100%).

The variable doping degree gives also rise to a modification of the color of the emission. In particular, a bright blue emission is displayed by the sole monomer (Device I), associated to CIE coordinates of (0.13, 0.29). On the other hand, the predominant contribution of the excimers' emission at higher concentration of Pt-1 (Device III), results in a red emission, ascribed to CIE coordinates of (0.56, 0.36).

The combination of the simultaneous radiative decay of the two species (Device II), observed inserting 70% of Pt-1 in the matrix, generates white light, associated to CIE coordinates of (0.36, 0.33) (**Figure 98**).

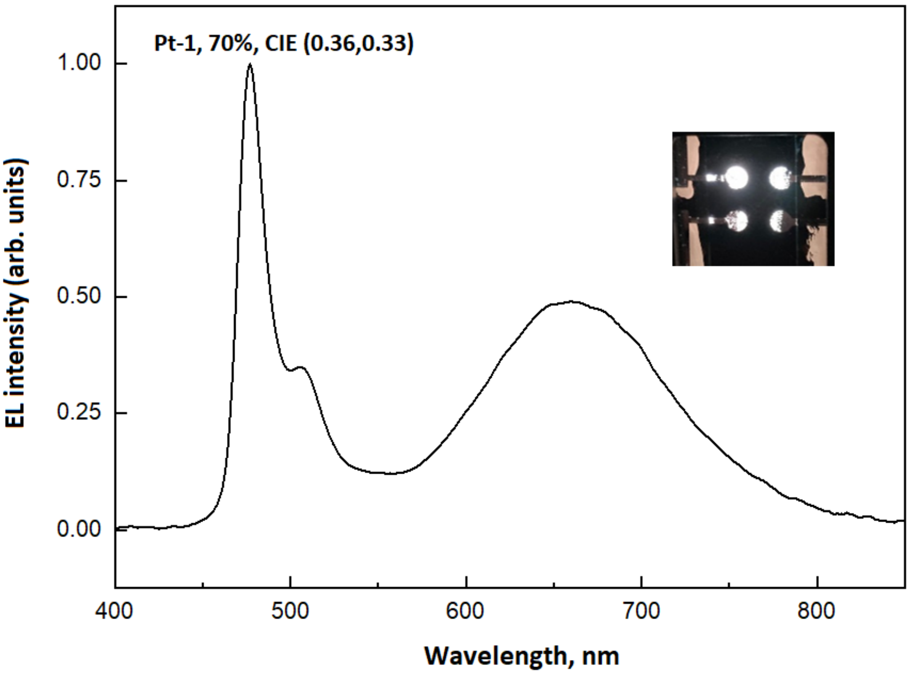

Figure 98. Electroluminescence spectra obtained inserting 70% of Pt-1 in the emissive layer of the device. Inset: White emission displayed by Device II (Pt-1: 70%).

White light emission is the key for the design of WOLEDs, which represent a crucial issue for the generation of bright white artificial light. Indeed, the design of efficient WOLEDs is still a challenge since the exciton manipulation requires the development of more sophisticated and complex multilayer structures.

The quality of the fabricated devices was investigated through the application of a bias between the anode and the cathode, collecting the luminescence and electroluminescence data in relation to the applied voltage and the current density, respectively (**Figure 99**).

Applying a bias of 4.8 V, the maximum luminescence was observed for the device containing Pt-1 in a concentration equal to 8% (585.79 cd/m^2), whilst high doping levels (Device III) lead to the lowest luminescence (52.34 cd/m^2). The curve then reaches a plateau, displaying the maximum at 9 V with a luminescence of 13 267.87 cd/m^2 for the device doped with the 8% of Pt-1, whereas for the emissive layer containing 100% of the phosphor, the luminescence is significantly lower (1196.76 cd/m^2).

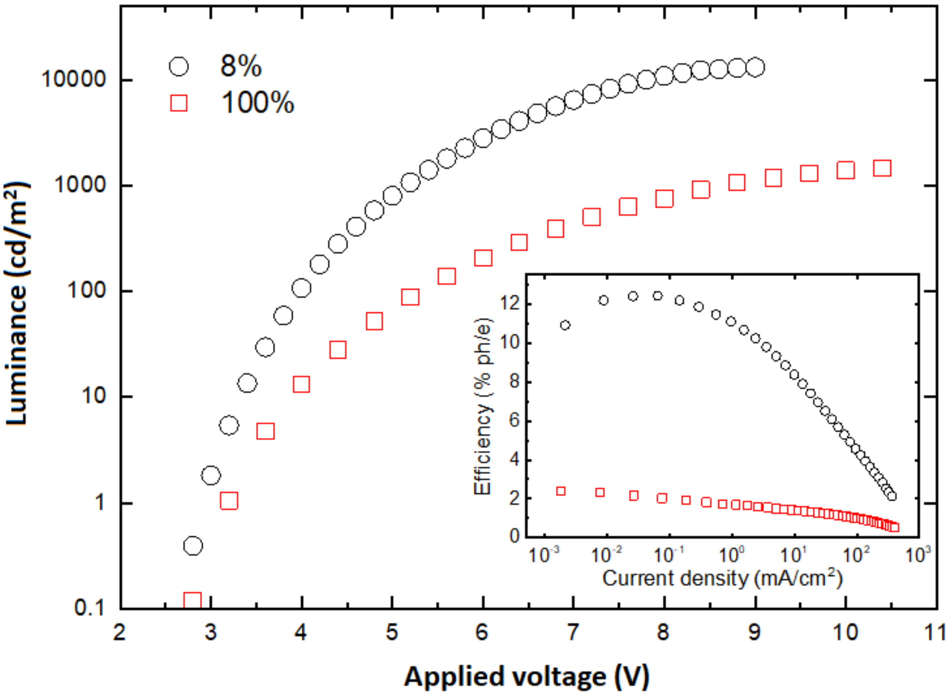

Figure 99. Luminance vs applied voltage measured for Device I and Device III. Inset: EL quantum efficiency vs current density.

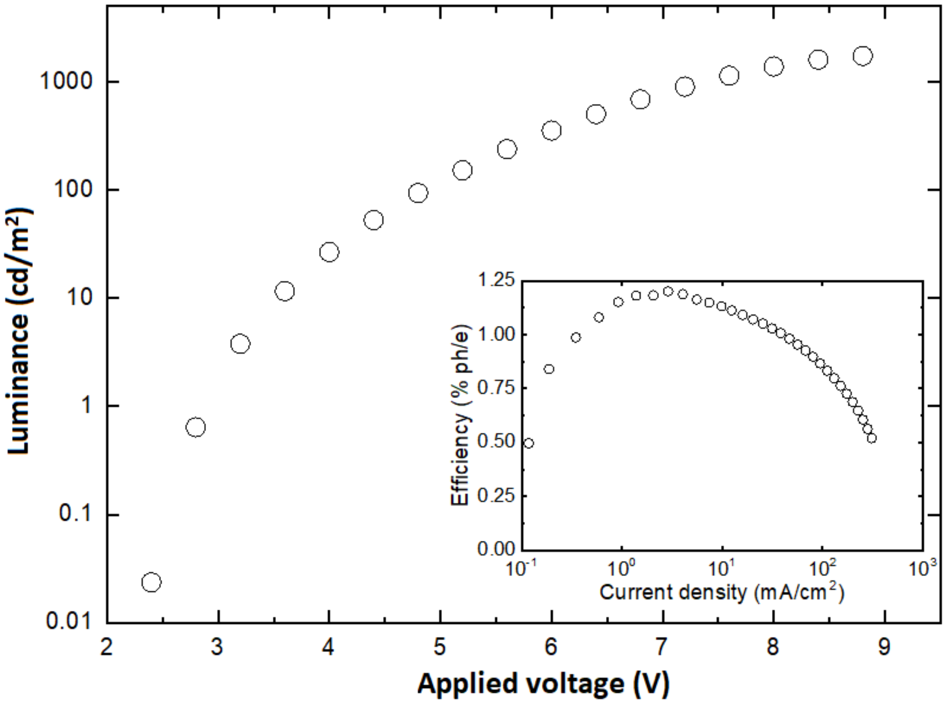

Figure 100. Luminance vs applied voltage measured for Device II. Inset: EL quantum efficiency vs current density.

The quantum efficiency (% ph/e) of each configuration was assessed as a function of the applied current density (mA/cm^2). Comparing the obtained values, Device I turned out to be the most performant, displaying a quantum efficiency of 12.39% ph/e with the application of a reduced current density (0.025 mA/cm^2). Conversely, Device III is characterized by the maximum efficiency (2.38% ph/e) at 0.0018 mA/cm^2 and Device II represents the less performant of the series, with a quantum efficiency of 1.20% ph/e at 2.88 mA/cm^2.

2.2.1.3.2 OLEDs fabrication: Pt-5

Two OLED devices were fabricated with Pt-5, displaying a configuration of ITO/ MoOx(2nm)/ TCTA(50nm)/ BCPO: Pt(II) (30nm, x%)/ TPBi(30nm)/ LiF(0.5nm)/ Al(100nm), where the percentage of the emitter inserted in the TCTA layer was 8% for Device IV and 100% for Device V. The schematic representation of the fabricated OLED is depicted in **Figure 101**.

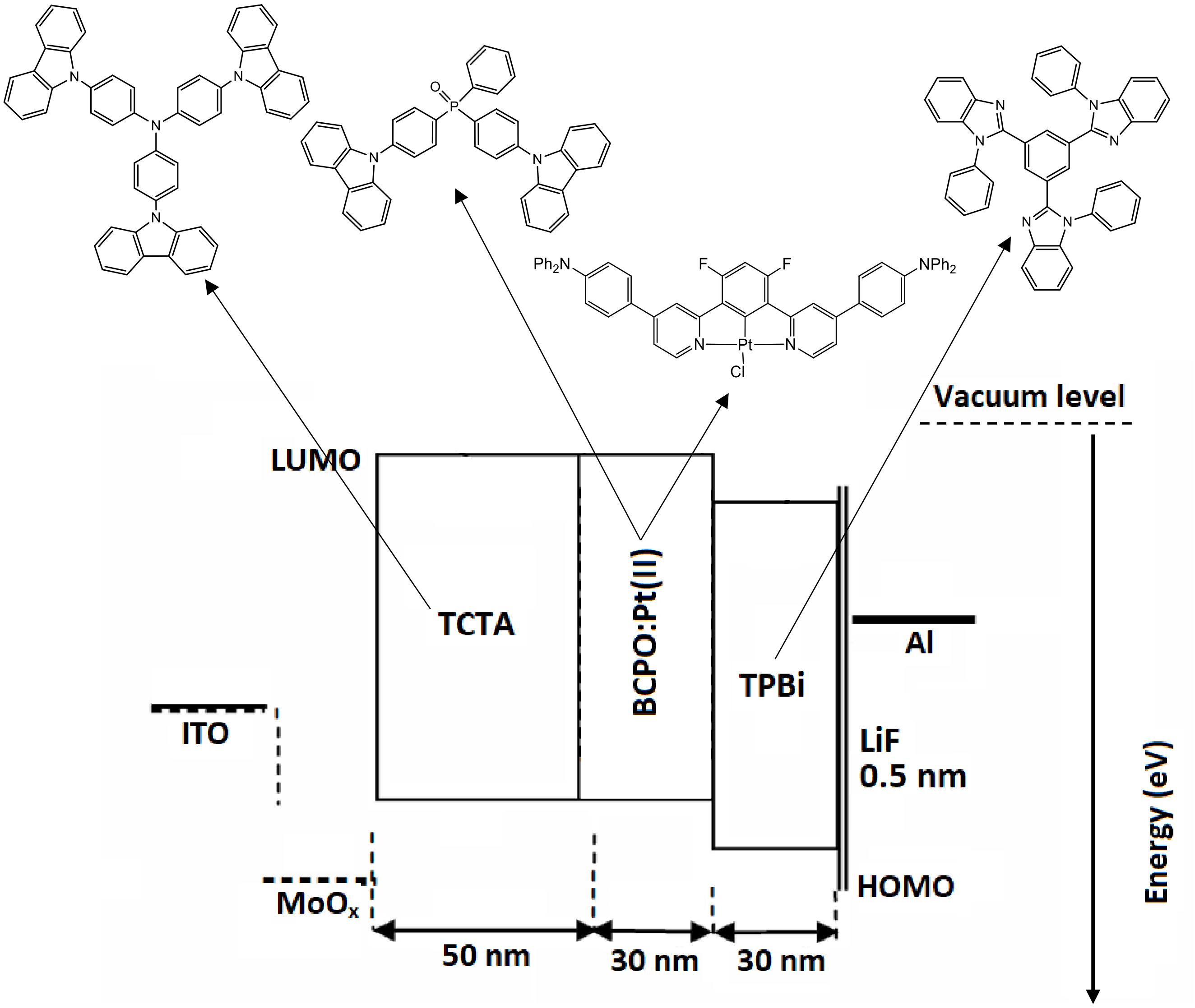

Figure 101. Illustration of the OLEDs architecture fabricated embedding Pt-5 in the emissive layer

The application of the bias between the electrodes induced the electrons and holes injection, leading to the electroluminescent phenomenon. In particular, Device IV displayed a bright green-yellow emission (**Figure 102**) with the maximum intensity at λ = 539 nm, attributable to the monomer emission and CIE coordinates of (0.38, 0.56) (**Figure 102**). Drastically increasing the concentration of Pt-5 in the emissive layer, the spectrum undergoes a serious change in the pattern. As a matter of fact, high doping levels privilege the formation of excimers which exhibit a significantly red-shifted emission band centered at λ = 690 nm.

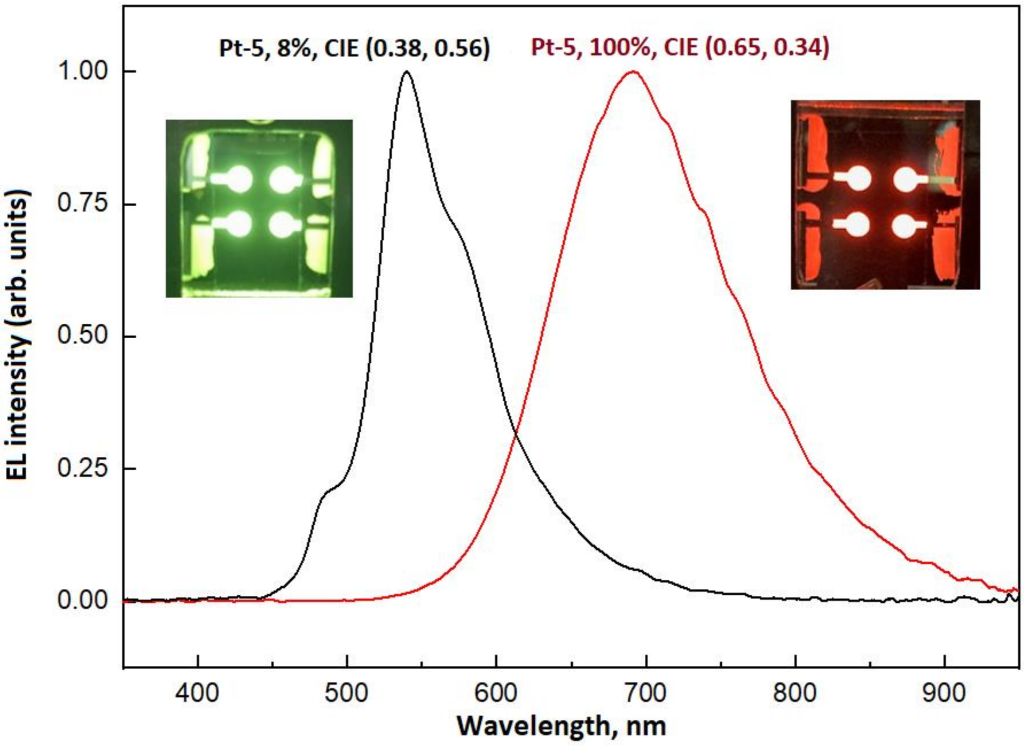

Figure 102. Electroluminescence spectra obtained inserting 8% (black line) and 100% (red line) of Pt-5 in the emissive layer of the device. Inset: Green-yellow emission displayed by Device IV (Pt-5: 8%) and red emission displayed by Device V (Pt-5: 100%).

Device V is characterized by a strong red emission corresponding to CIE coordinates of (0.65, 0.34), to which no contribution given by the monomer emission was assessed. Analyzing the luminance variation as a function of the applied voltage, an increasing raise was observed for Device IV leading to a maximum of 5 606.7 cd/m^2 at 10.4 V (**Figure 103**) whilst even though Device V shows the same trend, it reaches the maximum of 1 745.3 cd/m^2 at 8.4 V.

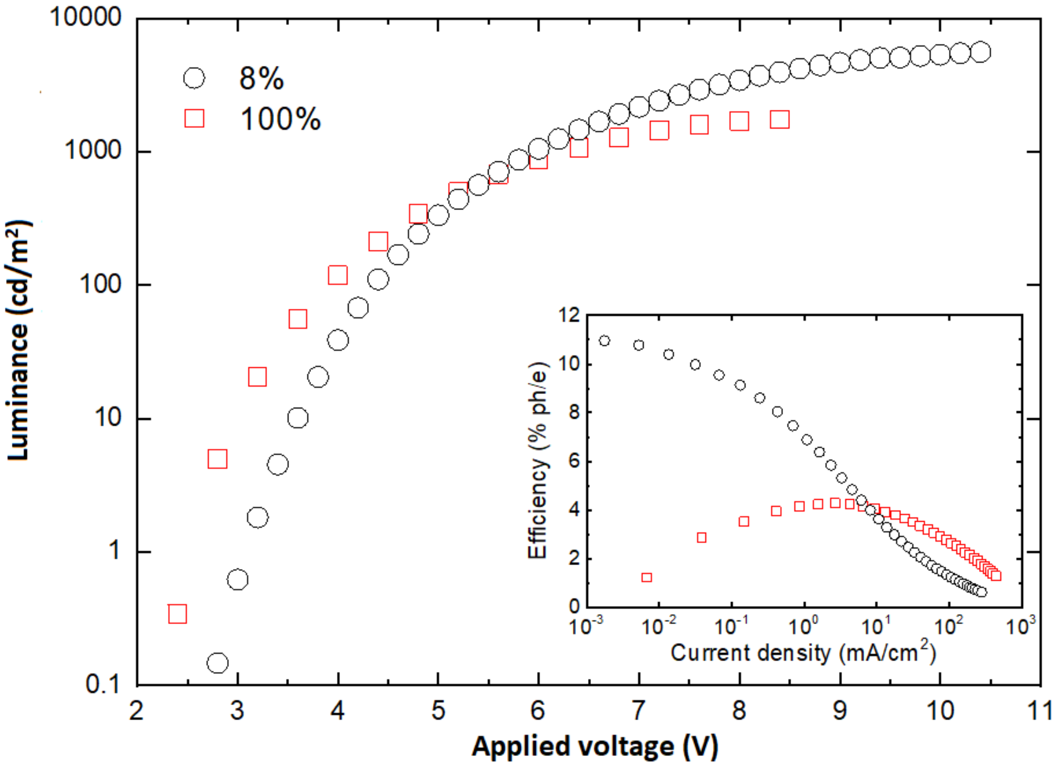

Figure 103. Luminance vs applied voltage measured for Device IV and Device V. Inset: EL quantum efficiency vs current density.

The quantum efficiency of Device IV results very high at low values of current density, showing the maximum (10.96% ph/e) at 0.0018 mA/cm^2. Conversely, Device V is characterized by a completely different pattern of the curve. Specifically, it slowly increases reaching the maximum (4.27% ph/e) at 2.67 mA/cm^2 to subsequently undergo a rapid decrease.

2.2.1.3.3 Conclusions

The promising photoluminescent properties displayed by **Pt-1** and **Pt-5** prompted us to embed the sterically hindered Pt(II) complexes as dopants in the emissive layer of OLEDs devices. In particular, five devices were constructed modulating the concentration of the phosphors aiming to investigate the electroluminescent properties and their efficiency in the generation of light. In summary, the optimal composition is displayed by Device I, owing to the highest luminous intensity (585.79 cd/m^2) applying a bias of 4.8 V. Conversely, Device IV resulted to be the most highly performing device relying on the value of efficiency, expressed in % ph/e, as a function of the applied current density. Indeed, right after the injection of electrons and holes inside the system (0.0018 mA/cm^2), the observed efficiency results equal to 10.96% ph/e.

The operating voltage of OLED represents one of the major limitations concerning the lifetime of the devices. Indeed, in order to produce bright light, a high current has to be applied. Nevertheless, intense electric fields provoke the generation of Joule heating, which affects the structure stability. Thermal degradation is responsible for the morphology alteration of the polymeric matrix and for the consequent decrease in the luminance efficacy.

The development of bright, stable OLEDs, emitting intense light at low driving voltage with a long lifetime, represents a looming challenge. In this context, given the remarkable data collected, the design of Device IV doped with a low concentration of **Pt-5** provides an extremely promising device.

The electroluminescence analysis performed on **Pt-1** and **Pt-5** evidenced a significant difference in the emission spectra at variable concentrations. Specifically, it was assessed that at low doping level (8%), monomers are responsible for the observed phenomenon whilst increasing the concentration, the formation of the excimers is privileged with consequent red shift of the wavelength of emission. Considering Device III and Device V, the contribution given by the monomers and excimers emission is dissimilar for the two synthesized Pt(II) complexes. In particular, doping the polymeric matrix with 100% of **Pt-1**, the electroluminescence spectrum highlights the presence of an excimeric intense broad band at λ = 666 nm accompanied by a minor signal given by the single molecule emission. Conversely, Device V fabricated inserting **Pt-5** at high concentration is characterized by the sole emission of the excimers. Hence, **Pt-1** shows a more complex emission pattern, owed to the combined monomeric and excimeric signals.

WOLEDs represent a promising source of high-quality white light, especially in the context of energy-saving indoor lighting and displays. Thus, the development of highly efficient devices with optimized electroluminescent properties and a long lifetime, is currently a burning issue that gains great interest. Given these premises, the fabrication of a WOLED was also achieved using 70% of **Pt-1** as the dopant, aiming to obtain the white light through the manipulation of the excitons. The performed analysis highlighted great results, attributing CIE coordinates of (0.36, 0.33) to the fabricated device, considerably close to the ideal white point, represented by CIE coordinates of (0.33, 0.33).

In this context, a cyclometalated Pt(II) complex designed bearing the mesityl ring on the central benzene ring of the N^C^N pincer rather than on the pyridine rings (**Figure 104**) was investigated as dopant for the fabrication of OLEDs.[25] The introduction of the hindered aryl substituent on the terdentate backbone, makes it structurally comparable with **Pt-1**.

Specifically, considering the external quantum efficiency measured for **Pt-1** and the previously studied analog, a significant improvement was made with the insertion of **Pt-1** in the emissive layer. Indeed, doping at low concentration with **Pt-1** (Device I), the maximum quantum efficiency results very high (12.39% ph/e) whilst the analog displays a maximum quantum efficiency of 4% ph/e.

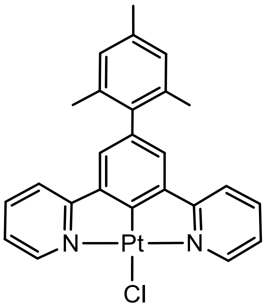

Figure 104. Molecular structure of the Pt emitter investigated by Williams et *al.*.

Conversely, no comparable Pt(II) complexes bearing the diphenylaniline moiety on the cyclometalated scaffold were reported in literature in the context of OLEDs fabrication. Nevertheless, a Pt(II) phosphor functionalized introducing two dimethylamino groups on the para position of the pyridine rings (**Figure 105**) was investigated by Williams *et al.*.[47]

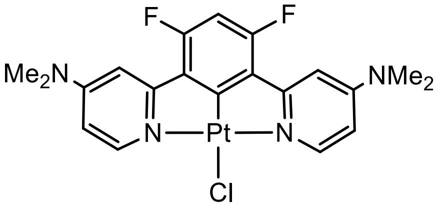

Figure 105. Molecular structure of the Pt-NMe$_2$ emitter investigated by Williams et *al.* functionalized with dimethylamino groups on the 4-position of the pyridine rings.

Despite the fact that at low doping levels both **Pt-5** and the dimethylamino functionalized Pt(II) complex display the same external quantum efficiency (11% ph/e), the applied current density results considerably different. Specifically, Device IV reaches the maximum efficiency at 0.0018 mA/cm^2, whilst the device fabricated using the less bulky analog needs a current density of 2.5 mA/cm^2 to achieve the same value. Hence, **Pt-2** displayed promising results for the development of bright and performant OLEDs using low onset current. Indeed, the devices' short lifetime is mainly due to the effect of repeatedly applied high voltages, which are associated with material degradation. The operational voltage thus represents an ongoing crucial challenge to overcome, making the obtained result even more interesting.

In the context of aggregation, the presence of sterically hindered functional groups seems to be promising in preventing the π-π stacking interaction occurring between neighboring square planar Pt(II) complexes. Indeed, WOLEDs fabrication was achieved both with the emitter developed by Williams et *al.* and with **Pt-1**, using significantly diverse concentrations. Specifically, Williams et *al.* obtained the white light doping the emissive layer with 20% of the developed Pt(II) complex. Conversely, Device II was fabricated embedding 70% of the Pt(II) based emitter. Even though the OLEDs architecture designed by Williams *et al.* and the multilayer structure of Devices II display a different composition, and thus a direct comparison is prevented, the remarkable difference in the doping level suggests the inclination of Pt-NMe$_2$ to easily undergo aggregation with respect to **Pt-1**. The presence of the bulky and twisted mesityl groups discourages the interaction between neighboring emitters. Thus, white light generation is achieved increasing the concentration of **Pt-1**, to allow the formation of red emitting aggregates.

Additionally, the remarkable versatility provided by the designed Pt(II) complexes opens up new perspectives for the development of further enhanced and optimized dopants. Indeed, the structural arrangement of the Pt(II) based emitters plays a crucial role on the electroluminescence mechanism, owing to the formation of monomeric, bimolecular excited species (excimers) and even of aggregates. The fine tailoring of the phosphors cyclometalated backbone through introduction of various functional group, displaying a different degree of bulkiness, and the modulation of the doping level of the emissive layer, allows to precisely control the color tunability.

Overall, the great potential displayed by **Pt-1** and **Pt-5** could provide the solution to fulfil the design of cost-effective, bright and long-lived OLED devices.

Chapter III- Experimental section

1. General comments

All the commercially available reagents and solvents were used as received from the supplier. Anhydrous solvents were obtained via distillation under argon, performing preliminary water traces removal in the presence of either NaH or CaH_2. Toluene was distilled over sodium/benzophenone. Air- and water-sensitive reactions were performed in flame-dried glassware under argon atmosphere.

The purifications were performed through column chromatography on silica gel (Merck Geduran 60, 0.063-0.200 mm). Flash chromatography was carried out using Grace Reveleris^{TM} with Puriflash^{TM} 40µm flash cartridges (Buchi). Analytical thin layer chromatography was performed on Merck Silica Gel 60 F254 plates.

The characterization of each intermediate and of the final products was performed recording the NMR spectra on a Bruker AV III 300 MHz or AV III 400 MHz spectrometers. Chemical shifts of ^1H, ^{19}F and ^{13}C NMR spectra are reported in parts per million (ppm) and the coupling constants are measured in Hertz (Hz). Signals' multiplicities are listed as singlet (s), d (doublet), t (triplet), quartet (q), multiplet (m). High-resolution mass spectrometry (HRMS) was performed at the Centre Regional de Mesures Physiques de l'Ouest, University of Rennes 1, either on a LC-MS Agilent 6510, a Brucker MaXis 4G or a Thermo Fisher Q-Exactive using positive or negative ion Electron-Spray ionization techniques (respectively ESI+, ESI-).

Elemental analysis of Pt(II) and Ir(III) complexes were obtained at the Centre Regional de Mesures Physiques de l'Ouest, University of Rennes 1.

X-ray analysis were performed at 150 K collecting the data with a D8 VENTURE Bruker AXS diffractometer using Mo-Kα (λ= 0.71073 Å).

The photophysical properties evaluation was carried out at the University of Milan. The emitters were dissolved in dichloromethane and variable concentration solutions were prepared. Prior irradiation, freeze-pump-thaw cycles were performed to remove the dissolved molecular oxygen. UV-visible spectra were obtained using a Shimadzu UV3600 spectrophotometer. Quantum yields were measured with a C11347 Quantaurus Hamamatsu Photonics K.K spectrometer. Steady state and time-resolved fluorescence data were collected using a FLS980 spectrofluorimeter (Edinburg Instrument Ltd). Diluted solutions were analysed in quartz cuvettes with 1 cm optical path length, whereas quartz cuvettes of 1 mm optical path length were used for concentrated solutions.

2. Synthesis of cyclometalated Pt(II) and Ir(III) complexes

2.1 Synthesis of the fluorinated Pt(II) complexes bearing highly hindered substituents

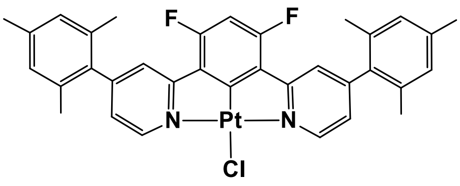

Pt-1

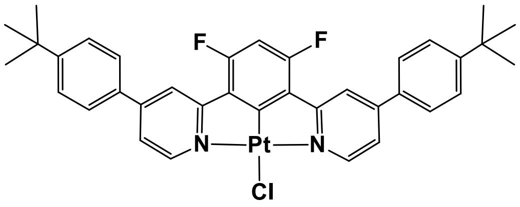

Pt-2

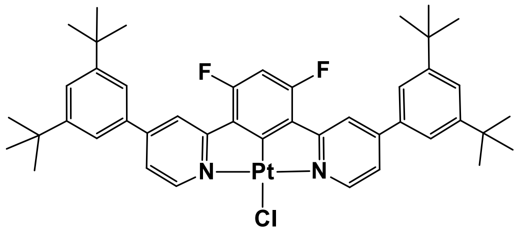

Pt-3

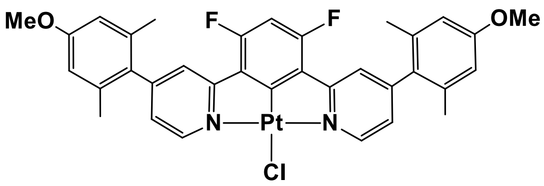

Pt-4

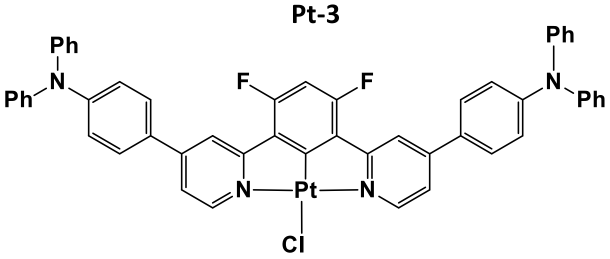

Pt-5

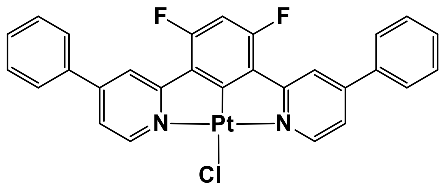

Pt-6

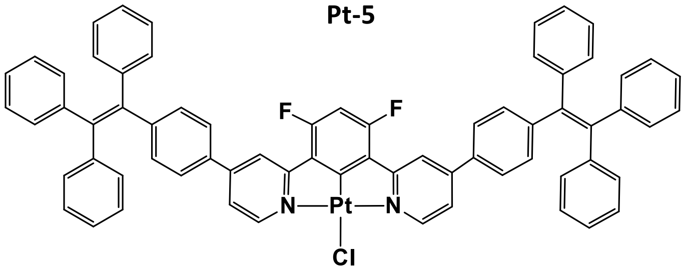

Pt-7

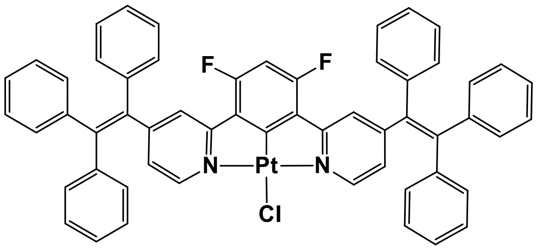

Pt-8

Figure 106. Molecular structure of the designed sterically hindered Pt(II) complexes.

2.1.1 Synthesis of Pt-1 to P-4

Pt-1 to **Pt-4** were synthesized according to literature, firstly introducing the sterically hindered substituents on the pyridine ring through the use of the boronic acid of the aryl function and 2-chloro-4-iodopyridine,[51] followed by reaction with the pinacol ester of benzene-1,3-difluoro-4,6-diboronic acid to give the N^C^N ligand.[47]

The general synthetic route is decited in **Scheme 2**.

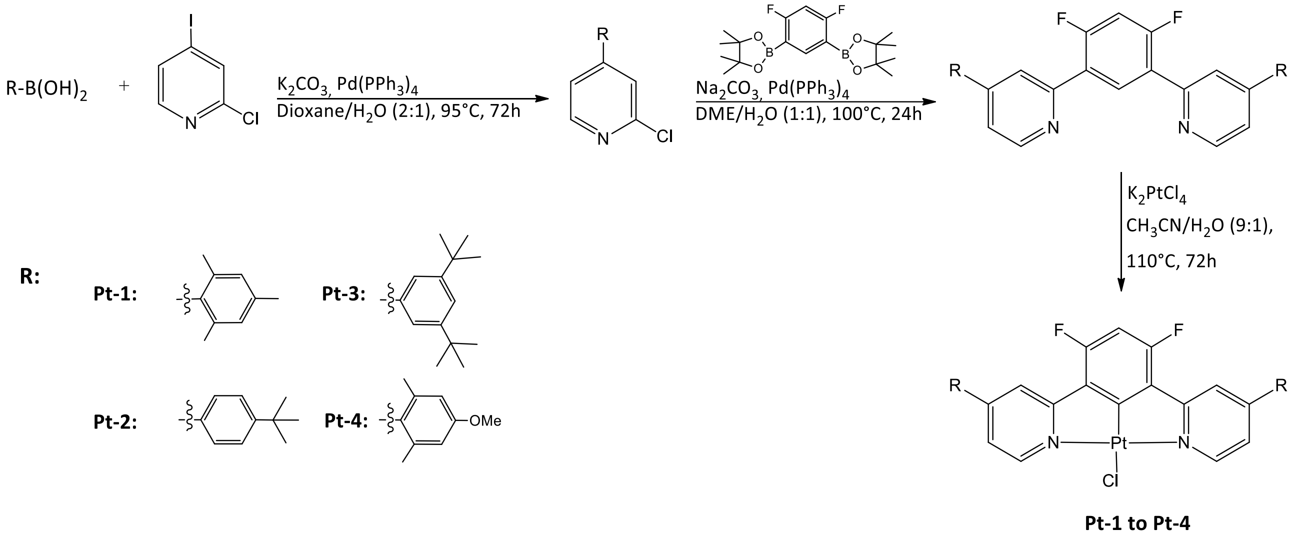

Scheme 2. Schematic illustration of the synthetic route followed to achieve the synthesis of Pt-1 to Pt-4.

2.1.1.1 Synthesis of 2,2'-(4,6-difluoro-1,3-phenylene)bis(4,4,5,5-tetramethyl-1,3,2-dioxaborolane)

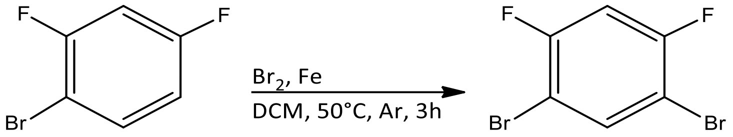

Under an Argon atmosphere, Fe (0.80 g, 14.1 mmol) and 1-bromo-2,4-difluorobenzene (13.66 g, 70.8 mmol) were solubilized in 18 mL of dry dichloromethane in a three neck round bottom flask. The solution was stirred at 50°C for 30 min before adding Br_2 (4.0 mL, 77.8 mmol) and let reflux for additional three hours.

Upon completion of the reaction, the solvent was evaporated *in vacuo* and the desired compound was isolated via distillation at 65°C under reduced pressure to obtain a white solid (12.8 g). **Yield:** 71%. **^{1}H-NMR** (300 MHz, $CDCl_3$, δ): 7.74 (t, *J* = 7.2 Hz, 1H), 6.99 (t, *J* = 8.1 Hz, 1H).

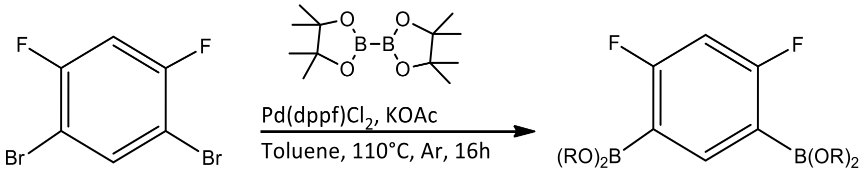

1,3-dibromo-4,6-difluorobenzene (0.50 g, 1.8 mmol), bis(pinacolato)diboron (1.02 g, 4.0 mmol), KOAc (0.92 g, 9.4 mmol) and Pd(dppf)Cl_2 (0.08 g, 0.1 mmol) were placed in a two neck round bottom flask under an inert atmosphere and dissolved in 8.4 mL of anhydrous toluene. The mixture was heated at 110°C overnight and subsequently let cool to room temperature. Then, the reaction mixture was diluted with 25 mL of AcOEt and washed with 25 mL of water. The collected organic phase was further washed twice with a mixture of 30 mL of water and 50 mL of brine, dried over anhydrous $MgSO_4$ and concentrated *in vacuo*.

The crude product was thus filtered on a pad of silica gel using a mixture of cyclohexane:AcOEt (8:2, v/v) as the eluent, in order to remove the insoluble species and most of the impurities. The solvent was then removed under reduced pressure and the residue dissolved in pentane. The flask was finally placed in the freezer to let crystallize overnight.

The colorless crystalline solid was filtered through a paper filter with a büchner funnel and dried under vacuum (1.74 g). **Yield:** 65%. **^{1}H-NMR** (300 MHz, $CDCl_3$, δ): 8.15 (t, *J* = 7.5 Hz, 1H), 6.75 (t, *J* = 9.7 Hz, 1H), 1.37 (s, 24H). **^{19}F-NMR** (282.36 MHz, $CDCl_3$, δ): -94.28 (s, 2F).

2.1.1.2 Synthesis of Pt-1

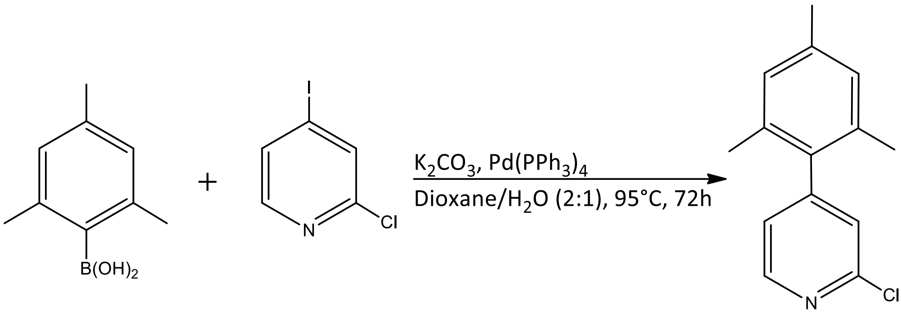

1

1. 2,4,6-trimethylphenylboronic acid (1.16 g, 7.1 mmol), 2-chloro-4-iodopyridine (1.00 g, 4.2 mmol), K_2CO_3 (1.65 g, 16.7 mmol), were added in a round bottom flask under an Ar atmosphere and solubilized in a 2:1 mixture of 1,4-dioxane and water. A needle for Ar supply was thus placed in the reaction mixture for 30 min in order to remove the oxygen traces. $Pd(PPh_3)_4$ (0.17 g, 0.15 mmol) was finally added and the vessel sealed. The reaction mixture was heated to reflux. Since the presence of 2-chloro-4-iodopyridine was assessed after 4 days, even after addition of a supplementary amount of 2,4,6-trimethylphenylboronic acid to favour its consumption, it was concluded that the reaction was over and the vessel was thus allowed to cool to room temperature. Then, toluene was poured into the reaction mixture and the two phases were separated. The organic layer was washed three times with 30 mL water and 20 mL brine, dried over anhydrous $MgSO_4$ and concentrated *in vacuo.*

The crude product couldn't be purified through flash chromatography since the desired compound and the 2-chloro-4-iodopyridine displayed the same polarity. Thus, the displacement of the iodine atom from the starting reagent was attempted using *n*-Bu-Li.

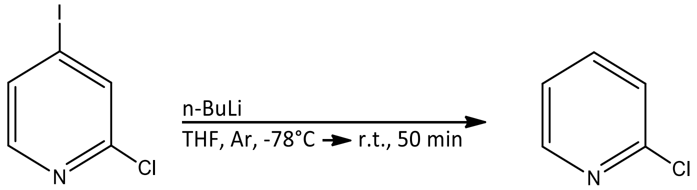

The crude product was placed in a two neck round flask previously dried with a heat gun and, under an Argon atmosphere, it was dissolved in 20 mL of anhydrous THF. The vessel was then immersed in a liquid nitrogen bath, keeping the temperature at -78°C and *n*-BuLi (2.5 M in hexane, 1.3 eq.) was added. The reaction was run for 50 min and finally quenched with 200 µL of water. The vessel was then cool down to room temperature and diluted with 20 mL of ethylacetate. The organic layer was separated, washed three times with 30 mL of water, dried over anhydrous $MgSO_4$ and evaporated under reduced pressure.

Once the consumption of the 2-chloro-4-iodopyridine was assessed, the crude product was purified using a silica gel flash column chromatography. The purification was carried out using hexane:AcOEt, 10:0 to 8:2 (v/v) as the eluent to obtain a colorless oil (302 mg). **Yield:** 31% (brsm). **^{1}H-NMR** (300 MHz, $CDCl_3$, δ): 8.46 (d, *J*= 5.0 Hz, 1H), 7.18 (s, 1H), 7.06 (dd, *J* = 5.0, 1.2 Hz, 1H), 6.97 (s, 2H), 2.35 (s, 3H), 2.03 (s, 6H).

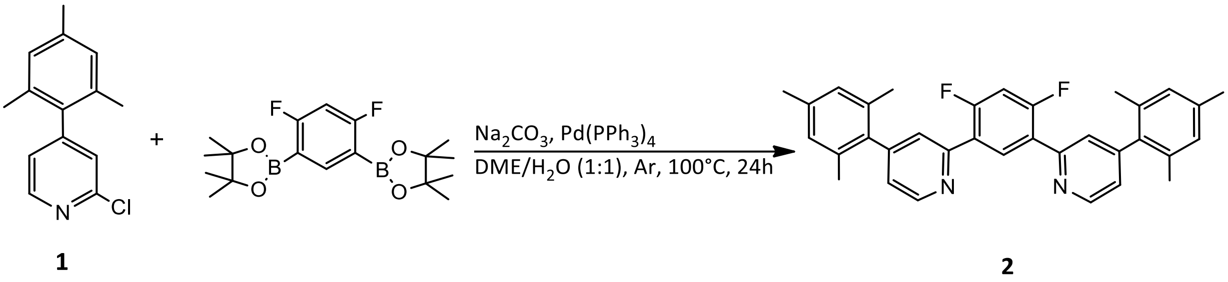

2. 1 (0.18 g, 0.77 mmol), the pinacol ester of benzene-1,3-difluoro-4,6-diboronic acid (0.12 g, 0.34 mmol), an aqueous solution of Na_2CO_3 (1 M, 4.6 mL) and $Pd(PPh_3)_4$ (0.06 g, 0.06 mmol) were placed in a Schlenk tube and solubilized in 4.6 mL of DME. Before sealing the vessel, it was degassed for 10 min by letting the Argon flow. The reaction mixture was then heated at 100°C overnight. The vessel was then allowed to cool to ambient temperature and the solvent concentrated *in vacuo*. The oily residue was dissolved in a mixture of dichloromethane (30 mL) and water (20 mL). The organic phase was collected, dried over anhydrous $MgSO_4$ and evaporated under reduced pressure.

The purification of the crude product was carried out using a puriflash instrument, loading the sample in a silica gel column. The eluition was carried out using a mixture of cyclohexane:AcOEt, 10:0 to 7:3 (v/v) to obtain a yellow oil (200 mg). **Yield:** 70%. **^{1}H-NMR** (300 MHz, $CDCl_3$, δ): 8.80 (d, *J* = 5.0 Hz, 2H), 8.72 (t, *J* = 8.9 Hz, 1H), 7.62 (s, 2H), 7.12 (dd, *J* = 5.0, 1.5 Hz, 2H), 6.98-7.08 (m, 5H), 2.37 (s, 6H), 2.08 (s, 12H). **^{19}F-NMR** (282.36 MHz, $CDCl_3$, δ): -113.27 (s, 2F). **^{13}C-NMR** (75.48 MHz, $CDCl_3$, δ): 160.5 (dd, *J* = 255.5 and 12.4 Hz), 152.7, 150.0, 149.9, 137.6, 136.2, 135.2, 133.8 (t, *J* = 4.2 Hz), 128.4, 125.4 (t, *J* = 4.3 Hz), 124.7 (dd, *J* = 9.8 and 6.1 Hz), 123.6, 104.9 (t, *J* = 27.1 Hz), 21.0, 20.6. **HRMS (ESI+):** $(M+H)^+$ calcd for $C_{34}H_{31}N_2F_2$, 505.2449; found: 505.2450.

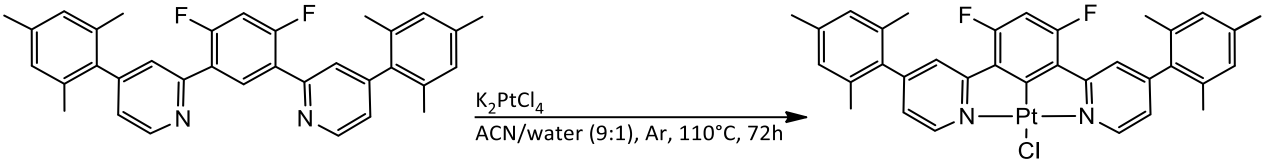

2 **Pt-1**

Pt-1. To a Schlenk tube, **2** (0.07 g, 0.14 mmol) was added and dissolved in 4.8 mL of acetonitrile. Then, K_2PtCl_4 (0.11 g, 0.28 mmol) was solubilized in 0.8 mL of water and then added to the reaction mixture with a pasteaur pipette. The vessel was degassed by directly bubbling Argon in the solvent with a needle for 40 min. The reaction mixture was then sealed and heated at reflux at 110°C for 3 days, until the reaction mixture became a yellow suspension. Upon cooling to room temperature, the reaction mixture was filtered through a nylon membrane filter. A yellow solid was separated and washed with water and diethyl ether. The thus obtained yellow solid was then collected and dried (88 mg). **Yield:** 30%. **^{1}H-NMR** (300 MHz, $CDCl_3$, δ): 9.42 (dd, *J* = 5.9, 0.7 Hz, $^3J(^{195}Pt)$ = 40.4 Hz, 2H), 7.81-7.76 (m, 2H), 7.17 (dd, *J* = 4.0, 1.9 Hz, 2H), 7.03 (s, 4H), 6.73 (t, *J* = 11.2 Hz, 1H), 2.38 (s, 6H), 2.11 (s, 12H). **^{19}F-NMR** (282,36 MHz, $CDCl_3$, δ): -107.90 (s, 2F). **^{13}C-NMR** (75.48 MHz, $CDCl_3$, δ): 164.3, 154.1, 151.9, 138.4, 135.1, 134.8, 128.7, 124.5, 123.7, 99.4, 29.7, 21.1, 20.6. (An accurate analysis of the ^{13}C NMR spectrum could not be performed. The peaks corresponding to certain carbons are not visible. **Elem. Anal.** calcd. for $C_{36}H_{33}Cl_5F_2N_2Pt$, 2 CH_2Cl_2: C, 47.83; H, 3.68; N, 3.10; found: C, 47.64; H, 3.64; N, 3.05.

2.1.1.3 Synthesis of Pt-2

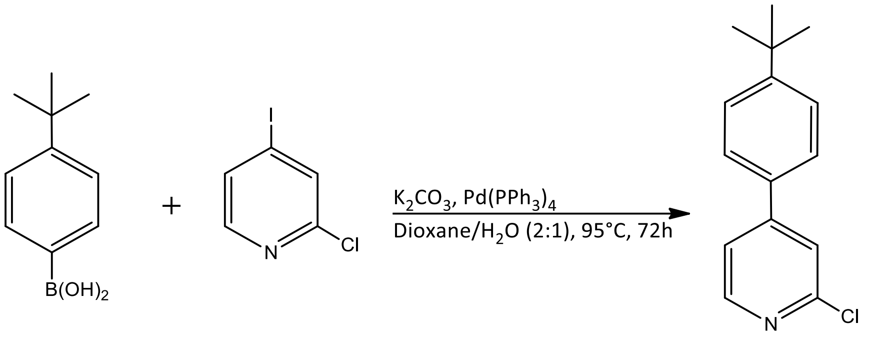

3

3. 4-tert-Butylbenzeneboronic acid (1.49 g, 8.4 mmol), 2-chloro-4-iodopyridine (1.00 g, 4.2 mmol), K_2CO_3 (1.73 g, 12.5 mmol), were added in a round bottom flask under an Ar atmosphere and solubilized in a 2:1 mixture of 1,4-dioxane and water. A needle for Ar supply was thus placed in the reaction mixture for 30 min in order to remove the oxygen traces. $Pd(PPh_3)_4$ (0.24 g, 0.2 mmol) was finally added and the vessel sealed. The reaction mixture was heated at reflux for 72h. The vessel was finally allowed to cool to room temperature. Then, toluene was poured into the reaction mixture and the two phases were separated. The organic layer was washed three times with 30 mL of water and 20 mL of brine, dried over anhydrous $MgSO_4$ and concentrated *in vacuo.*

The crude was purified using a silica gel chromatography (cyclohexane:AcOEt, 20:1, v/v) to obtain the desired compound as a colourless oil (547 mg). **Yield:** 53%. **^{1}H-NMR** (300 MHz, $CDCl_3$, δ): 8.43 (d, *J* = 5.2 Hz, 1H), 7.48-7.64 (m, 5H), 7.44 (dd, *J* = 5.2, 1.6 Hz, 1H), 1.39 (s, 9H). **^{13}C-NMR** (75.48 MHz, $CDCl_3$, δ): 153.2, 152.2, 151.4, 150.0, 133.8, 126.7, 126.2, 121.9, 120.3, 34.8, 31.2.

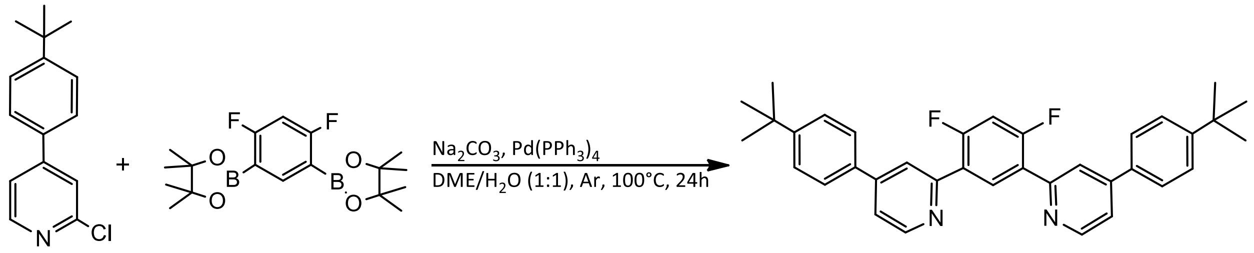

3

4

4. 3 (0.55 g, 2.2 mmol), the pinacol ester of benzene-1,3-difluoro-4,6-diboronic acid (0.36 g, 0.99 mmol), an aqueous solution of Na_2CO_3 (1 M, 13 mL) and $Pd(PPh_3)_4$ (0.19 g, 0.17 mmol) were placed in a Schlenk tube and solubilized in 13 mL of DME. Before sealing the vessel, it was degassed for 10 min by letting the Argon flow. The reaction mixture was then heated at 100°C overnight. The vessel was then allowed to cool and the solvent concentrated *in vacuo*. The oily residue was dissolved in a mixture of dichloromethane (30 mL) and water (20 mL). The organic phase was collected, dried over anhydrous $MgSO_4$ and evaporated under reduced pressure.

The crude was purified using silica gel chromatography (cyclohexane/AcOEt, 16/1) to obtain a colorless oil (501 mg). **Yield:** 95%. **^{1}H-NMR** (300 MHz, $CDCl_3$, δ): 8.77 (d, J = 5.1 Hz, 2H), 8.70 (t, J = 9 Hz, 1H), 8.01 (s, 2H), 7.68 (d, J = 8.5 Hz, 4H), 7.56 (d, J = 8.5 Hz, 4H), 7.51 (dd, J = 5.2, 1.7 Hz, 2H), 7.10 (t, J = 10.7 Hz, 1H), 1.41 (s, 18H). **^{13}C-NMR** (75.48 MHz, $CDCl_3$, δ): 153.1, 152.5, 150.2, 148.9, 135.4, 134.0, 126.8, 126.2, 122.1, 120.6, 105.1, 34.9, 34.7, 34.4, 31.5, 31.3, 30.2, 29.7. **^{19}F-NMR** (282.36 MHz, $CDCl_3$, δ): -112.42 (s, 2F). **HRMS (ASAP):** $(M+H)^+$ calcd for $C_{36}H_{34}N_2F_2$, 533.2763; found: 533.2764.

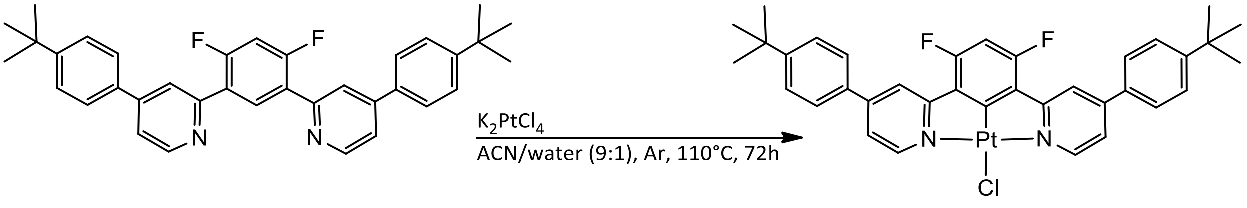

4

Pt-2

Pt-2. To a Schlenk tube, **4** (0.10 g, 0.19 mmol) was added and dissolved in 9 mL of acetonitrile. Then, K_2PtCl_4 (0.16 g, 0.38 mmol) was solubilized in 1 mL of water and then added to the reaction mixture with a pasteaur pipette. The vessel was degassed by directly bubbling Argon in the solvent with a needle for 40 min. The reaction mixture was then sealed and heated at reflux at 110°C for 3 days, until the reaction mixture became a yellow suspension. Upon cooling to room temperature, the reaction mixture was filtered through a nylon membrane filter. A yellow solid was separated and washed with water and diethyl ether. The thus obtained yellow solid was then collected and dried (77 mg). **Yield:** 41%. **^{1}H-NMR** (300 MHz, $CDCl_3$, δ): 9.27 (d, J = 5.9 Hz, $^3J(^{195}Pt)$ = 39.3 Hz, 2H), 8.10 (s, 2H), 7.69 (d, J = 8.3 Hz, 4H), 7.58 (d, J = 8.3 Hz, 4H), 7.46 (dd, J = 5.9, 1.9 Hz, 2H), 6.73 (t, J = 11.2 Hz, 1H), 1.41 (s, 18H). **^{13}C-NMR** (75.48 MHz, $CDCl_3$, δ): 153.7, 151.7, 133.6, 126.6, 126.3, 120.3, 34.7, 31.1, 27.1. **^{19}F-NMR** (282 MHz, $CDCl_3$, δ): -109.00 (s, 2F). **HRMS (ASAP):** $(M+H_2O)^+$ calcd for $C_{36}H_{35}N_2OF_2{}^{195}Pt$, 744.2360; found: 744.2367. **Elem. Anal.** calcd. for $C_{36}H_{33}ClF_2N_2Pt$: C, 56.73; H, 4.36; N, 3.68; found: C, 56.77; H, 4.35; N, 3.70.

2.1.1.4 Synthesis of Pt-3

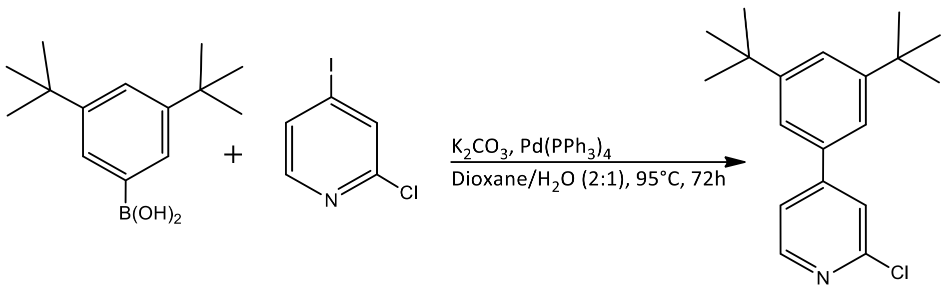

5

5. (3,5-di-tert-butylphenyl)boronic acid (0.88 g, 3.8 mmol), 2-chloro-4-iodopyridine (0.50 g, 2.1 mmol), K_2CO_3 (0.87 g, 6.3 mmol), were added in a round bottom flask under an Ar atmosphere and solubilized in a 2:1 mixture of 1,4-dioxane and water. A needle for Ar supply was thus placed in the reaction mixture for 30 min in order to remove the oxygen traces. $Pd(PPh_3)_4$ (0.24 g, 0.2 mmol) was finally added and the vessel sealed. The reaction mixture was heated to reflux for 72h. The vessel was finally allowed to cool to room temperature. Then, toluene was poured into the reaction mixture and the two phases were separated. The organic layer was washed three times with 30 mL of water and 20 mL of brine, dried over anhydrous $MgSO_4$ and concentrated *in vacuo.*

The crude was purified using a silica gel chromatography (cyclohexane:AcOEt, 20:1, v/v) to obtain the desired compound as a colourless oil (847 mg). **Yield:** 67%. **^{1}H-NMR** (300 MHz, $CDCl_3$, δ): 8.47 (d, *J* = 5.2 Hz, 1H), 7.55-7.60 (m, 2H), 7.43-7.48 (m, 3H), 1.42 (s, 18H).

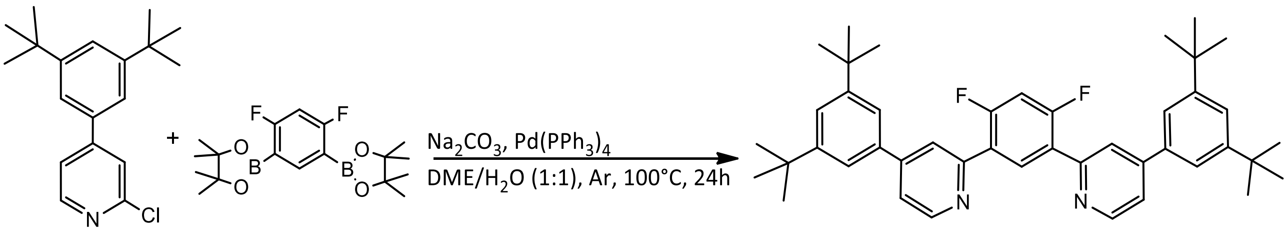

5 **6**

6. 5 (0.42 g, 1.4 mmol), the pinacol ester of benzene-1,3-difluoro-4,6-diboronic acid (0.23 g, 0.6 mmol), an aqueous solution of Na_2CO_3 (1 M, 8 mL) and $Pd(PPh_3)_4$ (0.12, 0.1 mmol) were placed in a Schlenk tube and solubilized in 8 mL of DME. Before sealing the vessel, it was degassed for 10 min by letting the Ar flow. The reaction mixture was then heated at 100°C overnight. The vessel was then allowed to cool and the solvent concentrated *in vacuo*. The oily residue was dissolved in a mixture of dichloromethane (30 mL) and water (20 mL). The organic phase was collected, dried over anhydrous $MgSO_4$, filtered and evaporated under reduced pressure. The crude was purified using silica gel chromatography (cyclohexane:AcOEt, 16:1, v/v) to obtain a colorless oil (438 mg). **Yield:** 68%. **^{1}H-NMR** (300 MHz, $CDCl_3$, δ): 8.79 (d, *J* = 5.1 Hz, 2H), 8.70 (t, J= 8.9 Hz, 1H), 8.0 (s, 2H), 7.47-7.62 (m, 8H), 7.11 (t, *J* = 10.6 Hz, 1H),1.43 (s, 36H). **^{13}C-NMR** (75.48 MHz, $CDCl_3$, δ): 162.5, 159.2, 152.9, 151.7, 150.4, 150.0, 137.8, 133.8, 124.7, 123.3, 122.7, 121.6, 121.1, 105.4, 105.1, 104.7, 35.0, 31.5, 30.2, 29.7. **^{19}F-NMR** (282.36 MHz, $CDCl_3$, δ): -112.92 (s, 2F). **HRMS (ESI+):** $(M+H)^+$ calcd for $C_{44}H_{51}N_2F_2$, 645.4015; found: 645.4008.

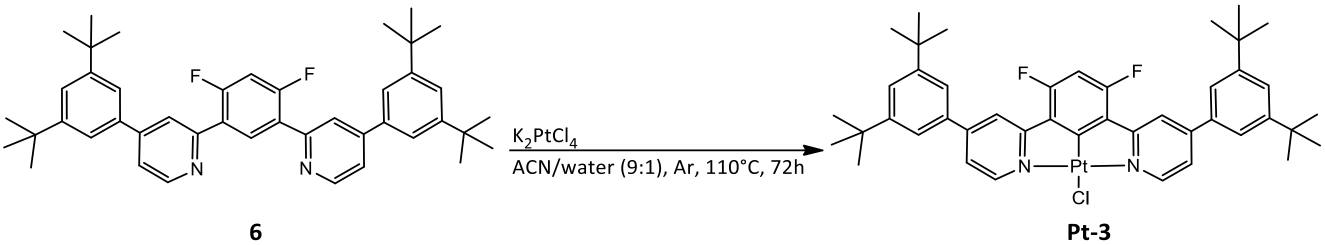

6

Pt-3

Pt-3. To a Schlenk tube, **6** (0.17 g, 0.27 mmol) was added and dissolved in 11.7 mL of acetonitrile. Then, K_2PtCl_4 (0.22 g, 0.54 mmol) was solubilized in 1.3 mL of water and then added to the reaction mixture with a pasteaur pipette. The vessel was degassed by directly bubbling Argon in the solvent with a needle for 40 min. The reaction mixture was then sealed and heated at reflux at 110°C for 3 days, until the reaction mixture became a yellow suspension. Upon cooling to room temperature, the reaction mixture was filtered through a nylon membrane filter. A yellow solid was separated and washed with water, MeOH and diethyl ether. The thus obtained yellow solid was then collected and dried (148 mg). **Yield:** 85%. **^{1}H-NMR** (300 MHz, $CDCl_3$, δ): 9.34 (d, *J* = 6.0 Hz, $^3J(^{195}Pt)$ = 39.4 Hz, 2H), 8.13 (s, 2H), 7.63 (s, 2H), 7.45-7.59 (m, 6H), 6.74 (t, *J* = 11.2 Hz, 1H), 1.43 (s, 36H). **^{13}C-NMR** (75.48 MHz, $CDCl_3$, δ): 164.3, 153.3, 152.0, 151.7, 136.6, 124.5, 121.5, 121.1, 35.2, 31.4. **^{19}F-NMR** (282 MHz, $CDCl_3$, δ): -108.48 (s, 2F). **HRMS (ESI+):** $(M+Na)^+$ calcd for $C_{44}H_{49}N_2F_2{}^{35}Cl\,Na^{195}Pt$, 896.3092; found: 896.3085. **Elem. Anal.** calcd. for $C_{44}H_{49}ClF_2N_2Pt$: C, 60.44; H, 5.65; N, 3.20; found: C, 60.48; H, 5.66; N, 3.23.

2.1.1.5 Synthesis of Pt-4

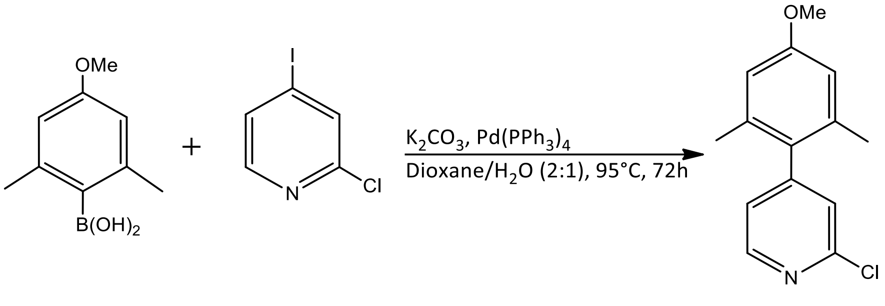

7

7. 2,6-Dimethyl-4-methoxybenzeneboronic acid (0.90 g, 5.0 mmol), 2-chloro-4-iodopyridine (0.60 g, 2.5 mmol), K_2CO_3 (1.04 g, 7.5 mmol), were added in a round bottom flask under an Ar atmosphere and solubilized in a 2:1 mixture of 1,4-dioxane and water. A needle for Ar supply was thus placed in the reaction mixture for 30 min in order to remove the oxygen traces. $Pd(PPh_3)_4$ (0.14 g, 0.1 mmol) was finally added and the vessel sealed. The reaction mixture was heated to reflux for 72h. The vessel was finally allowed to cool to room temperature. Then, toluene was poured into the reaction mixture and the two phases were separated. The organic layer was washed three times with 30 mL of water and 20 mL of brine, dried over anhydrous $MgSO_4$, filtered and concentrated *in vacuo.*

The crude was purified using a silica gel chromatography (cyclohexane:AcOEt, 20:1, v/v) to obtain the desired compound as a colourless oil (602 mg). **Yield:** 59%. **^{1}H-NMR** (300 MHz, $CDCl_3$, δ) (ppm): 8.42 (d, *J* = 5.0 Hz, 1H), 7.15 (s, 1H), 7.03 (d, *J* = 5.0 Hz, 1H), 6.67 (s, 2H), 3.81 (s, 3H), 2.02 (s, 6H). **^{13}C-NMR** (75.48 MHz, $CDCl_3$, δ): 159.2, 152.9, 151.8, 149.8, 136.5, 130.3, 125.6, 124.0, 113.1, 55.3, 20.9. **HRMS (ESI+):** $(M+Na)^+$ calcd for $C_{14}H_{14}NO^{35}Cl$ Na, 270.0656; found: 270.0659.

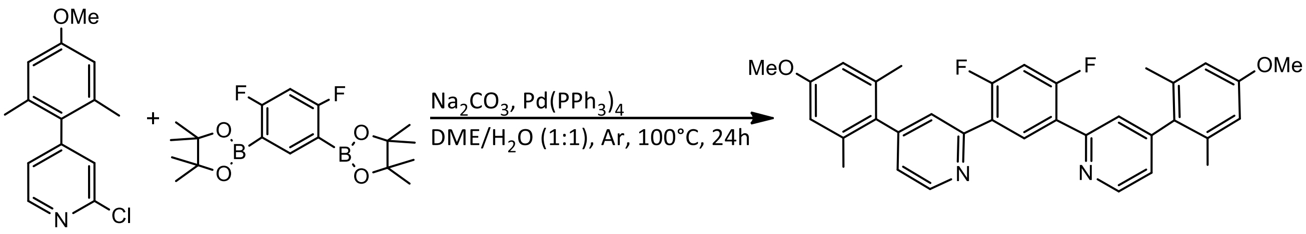

7 **8**

8. **7** (0.36 g, 1.5 mmol), the pinacol ester of benezene-1,3-difluoro-4,6-diboronic acid (0.24 g, 0.7 mmol), an aqueous solution of Na_2CO_3 (1 M, 9 mL) and $Pd(PPh_3)_4$ (0.13, 0.1 mmol) were placed in a Schlenk tube and solubilized in 8 mL of DME. Before sealing the vessel, it was degassed for 10 min by letting the Argon flow. The reaction mixture was then heated at 100°C overnight. The vessel was then allowed to cool and the solvent concentrated *in vacuo*. The oily residue was dissolved in a mixture of dichloromethane (30 mL) and water (20 mL). The organic phase was collected, dried over anhydrous $MgSO_4$ and evaporated under reduced pressure. The crude was purified using silica gel chromatography (cyclohexane:AcOEt, 16:1, v/v) to obtain a colorless oil (413 mg). **Yield:** 79%. **^{1}H-NMR** (300 MHz, $CDCl_3$, δ): 8.79 (d, *J* = 4.9 Hz, 2H), 8.70 (t, *J* = 8.9 Hz, 1H), 7.61 (s, 2H), 7.12 (d, *J* = 5.0 Hz, 2H), 7.03 (t, *J* = 10.6 Hz, 1H), 6.74 (s, 4H), 3.86 (s, 6H), 2.09 (s, 12H).**^{13}C-NMR** (75.48 MHz, $CDCl_3$, δ): 162.1, 158.9, 152.7, 150.1, 149.8, 136.9, 133.9, 131.6, 125.5, 124.6, 123.8, 112.8, 105.6, 105.1, 104.5, 55.2, 20.9. **^{19}F-NMR** (282.36 MHz, $CDCl_3$, δ): -113.43 (s, 2F). **HRMS (ESI+):** $(M+H)^+$ calcd for $C_{34}H_{31}N_2O_2F_2$, 537.2348; found: 537.2346.

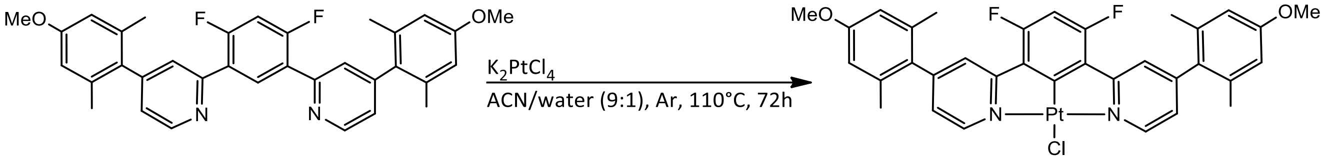

8 **Pt-4**

Pt-4. To a Schlenk tube, **8** (0.14 g, 0.27 mmol) was added and dissolved in 11.7 mL of acetonitrile. Then, K_2PtCl_4 (0.22 g, 0.53 mmol) was solubilized in 1.3 mL of water and then added to the reaction mixture with a pasteaur pipette. The vessel was degassed by directly bubbling Argon in the solvent with a needle for 40 min. The reaction mixture was then sealed and heated at reflux at 110°C for 3 days, until the reaction mixture became a yellow suspension. Upon cooling to room temperature, the reaction mixture was filtered through a nylon membrane filter. A yellow solid was separated and washed with water, MeOH and diethyl ether. The thus obtained yellow solid was then collected and dried (124 mg). **Yield:** 81%. **^{1}H-NMR** (300 MHz, $CDCl_3$, δ): 9.40 (d, *J* = 5.9 Hz, $^{3}J(^{195}Pt)$ = 40.2 Hz, 2H), 7.76 (s, 2H), 7.17 (d, *J* = 5.8, 2H), 6.68-6.80 (m, 5H), 3.87 (s, 6H), 2.13 (s, 12H). **^{13}C-NMR** (75.48 MHz, $CDCl_3$, δ): 164.2, 159.4, 153.8, 151.9, 136.3, 130.7, 124.9, 124.1, 113.3, 55.2, 21.2. **^{19}F-NMR** (282 MHz, $CDCl_3$, δ): -108.10 (s, 2F). **HRMS (ESI+):** $(M+Na)^+$ calcd for $C_{34}H_{29}N_2O_2F_2{}^{35}Cl\,Na^{195}Pt$, 788.1426; found: 788.1436. **Elem. Anal.** calcd. for $C_{34}H_{29}ClF_2N_2O_2Pt$: C, 53.30; H, 3.82; N, 3.66; found: C, 53.55; H, 3.83; N, 3.64.

2.1.2 Synthesis of Pt-5 to P-8

The functionalization of pyridine for **Pt-5** to **Pt-8** was achieved combining the bromine derivative of the highly hindered aryl substituent with the boronic acid of 2-chloropyridine[52] which was then used to perform a second Suzuki coupling with the pinacol ester of the benzene-1,3-difluoro-4,6-diboronic acid to build the ligand scaffold.[47]

The schematic representation of the general synthetic route is reported in **Scheme 3.**

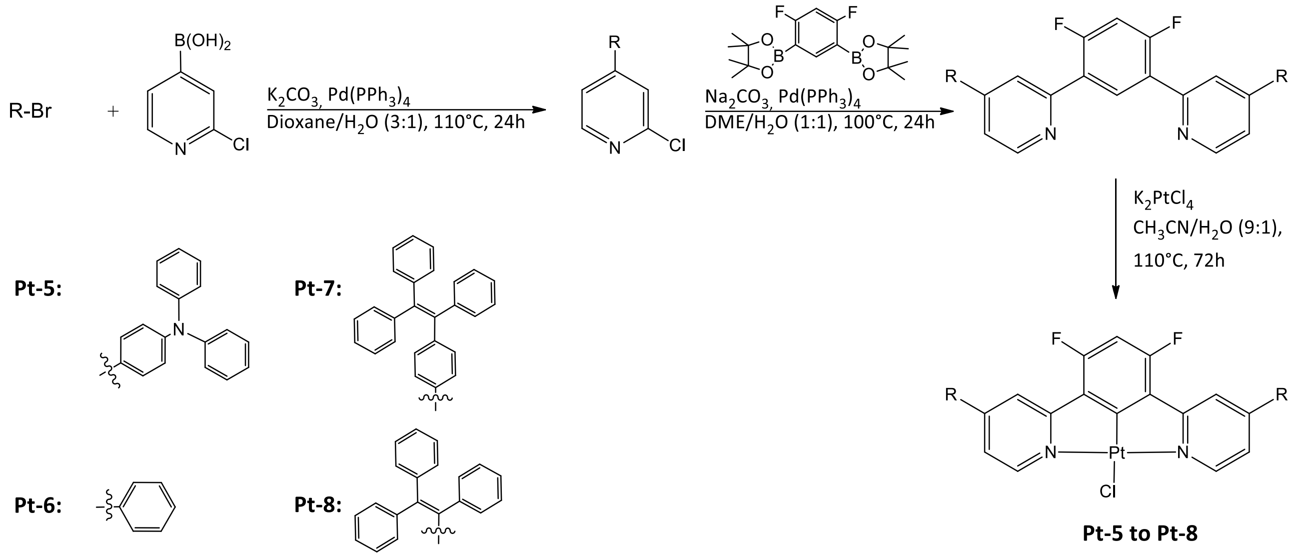

Scheme 3. Schematic illustration of the synthetic route followed to accomplish the synthesis of Pt-5 to Pt-8.

2.1.2.1 Synthesis of Pt-5

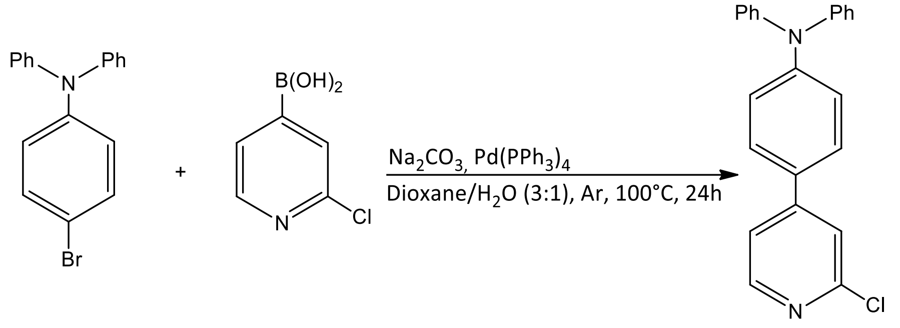

9

9. 2-chloro-pyridine-4-boronic acid (0.41 g, 2.6 mmol), (4-Bromophenyl)-diphenylamine (0.60 g, 1.85 mmol), $Pd(PPh_3)_4$ (0.11 g, 0.09 mmol), Na_2CO_3 (0.59 g, 5.6 mmol) were placed in a Schlenk tube and solubilized in a mixture made up of 4.5 mL of distilled water and 13.6 mL of 1,4-dioxane. The air was completely removed from the reaction vessel by vigorously bubbling argon for 10 min and sealed. The reaction mixture was then stirred and heated to reflux at 100°C overnight. The vessel was thus let cool to ambient temperature. The mixture was then acidified with HCl_{aq} and exctracted three times with 50 mL of ethyl acetate. The organic layer was separated and washed three times with 50 mL of water and 20 mL of brine. The solvent was finally dried over anhydrous $MgSO_4$ and evaporated under reduced pressure.

The crude product was then purified using a puriflash instrument loaded with a silica gel column. The purification was carried out eluting the sample with a mixture of cyclohexane:AcOEt, 10:0 to 8:2 (v/v) to obtain a colorless oil (480 mg). **Yield:** 44%. **^{1}H-NMR** (300 MHz, $CDCl_3$, δ): 8.39 (d, *J* = 5.2 Hz, 1H), 7.47-7.53 (m, 3H), 7.40 (dd, *J* = 5.3, 1.6 Hz, 1H), 7.29-7.36 (m, 4H), 7.08-7.20 (m, 8H). **^{13}C-NMR** (75.48 MHz, $CDCl_3$, δ): 206.9, 152.2, 150.9, 149.9, 149.5, 147.0, 129.3, 127.7, 125.2, 123.9, 122.5, 121.1, 119.6. **HRMS (ESI+):** $(M+H)^+$ calcd for $C_{23}H_{18}N_2{}^{35}Cl$, 357.1153; found: 357.1154.

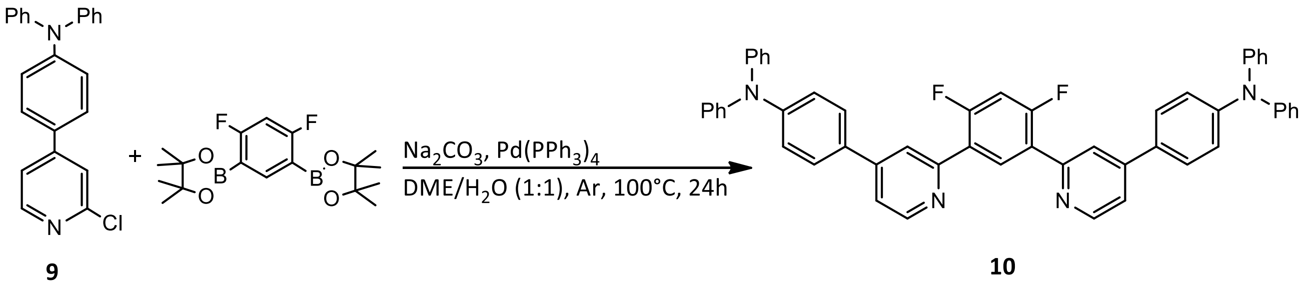

9

10

10. To a two neck round bottom flask, **9** (0.17 g, 0.49 mmol), the pinacol ester of benzene-1,3-difluoro-4,6-diboronic acid (0.08 g, 0.22 mmol), an aqueous Na_2CO_3 solution (1 M, 3.5 mL), $Pd(PPh_3)_4$ (0.04 g, 0.04 mmol) and 3.5 mL of DME, were added under an argon atmosphere. The air was fully removed by bubbling Ar for 20 min. The vessel was then sealed and heated to reflux at 100°C overnight. Upon cooling to ambient temperature, the reaction mixture was finally evaporated under reduced pressure and dissolved in a mixture of dichloromethane (30 mL) and water (20 mL). The organic phase was collected, dried over anhydrous $MgSO_4$, filtered and concentrated *in vacuo*. The pure compound was obtained after purification performed using a puriflash instument loaded with a silica gel column and a mixture of cyclohexane:AcOEt 10:0 to 8:2 (v/v), as the eluent to obtain a colorless oil (190 mg). **Yield:** 42%. **^{1}H-NMR** (300 MHz, $CDCl_3$, δ): 8.74 (d, *J* = 5.2 Hz, 2H), 8,68 (t, *J* = 9.0 Hz, 1H), 7.98 (s, 2H), 7.57-7.63 (m, 4H), 7.47 (dd, *J* = 5.2, 1.7 Hz, 2H), 7.29-7.36 (m, 8H), 7.15-7.22 (m, 12H), 7.04-7.14 (m, 5H). **^{13}C-NMR** (75.48 MHz, $CDCl_3$, δ): 153.1, 150.1, 149.0, 148.3, 147.3, 133.8, 131.9, 129.4, 127.8, 125.0, 123.6, 122.9, 121.6, 119.8, 105.0 (t, *J* = 27.0 Hz). **^{19}F-NMR** (282.36 MHz, $CDCl_3$, δ): -112.52 (s, 2F). **HRMS (ESI+):** $(M + H)^+$ calcd for $C_{52}H_{37}N_4F_2$, 755.2981; found: 755.2978.

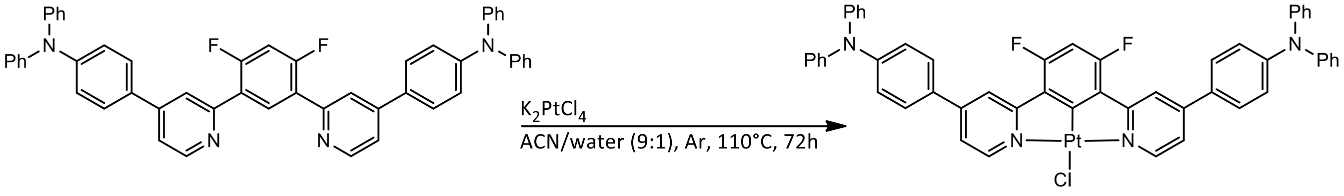

10

Pt-5

Pt-5. A Schlenk tube was charged with **10** (0.11 g, 0.15 mmol) dissolved in 5 mL of acetonitrile and K_2PtCl_4 (0.13 g, 0.30 mmol) solubilized in 0.5 mL of water. The reaction vessel was then filled with argon and a needle was inserted in the solvent in order to directly bubble the Ar in the reaction mixture. After 40 min, the vessel was sealed and heated at reflux at 110°C for 72h. In the end, the reaction mixture was let cool. Afterwards, the solid was isolated after filtration through a nylon membrane filter and washed with water and diethyl ether to obtain a yellow solid (200 mg). **Yield:** 82%. **^{1}H-NMR** (300 MHz, $CDCl_3$, δ): 9.27 (d, *J* = 6.4 Hz, $^3J(^{195}Pt)$ = 43.7 Hz, 2H), 8.09 (s, 2H), 7.64-7.61 (m, 4H), 7.45 (dd, *J* = 4.2, 2.2 Hz, 2H), 7.38-7.31 (m, 8H), 7.22-7.10 (m, 16H), 6.77 (t, *J* = 11.3 Hz, 1H). **^{19}F-NMR** (282.36 MHz, $CDCl_3$, δ): -108.99 (s, 2F). It was not possible to record a ^{13}C NMR spectrum due to a very low solubility whether in $CDCl_3$ or DMSO. **HRMS (ESI+):** $(M+H)^+$ calcd for $C_{52}H_{35}N_4F_2{}^{35}Cl^{195}Pt$, 983.2161; found: 983.219. **Elem. Anal.** calcd. for $C_{52}H_{35}ClF_2N_4Pt$: C, 63.45; H, 3.58; N, 5.69; found: C, 63.58; H, 3.60; N, 5.71.

2.1.2.2 Synthesis of Pt-6

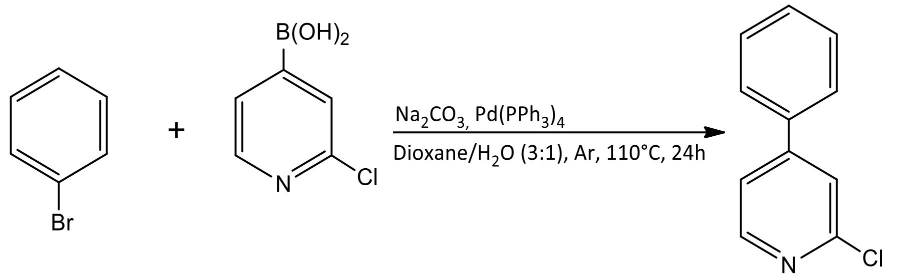

11

11. 2-chloro-pyridine-4-boronic acid (1.12 g, 7.1 mmol), Bromobenzene (0.80 g, 5.1 mmol), Pd(PPh$_3$)$_4$ (0.29 g, 0.2 mmol), Na_2CO_3 (1.62 g, 15.3 mmol) were placed in a Schlenk tube and solubilized in a mixture made of 10 mL of distilled water and 30 mL of 1,4-dioxane. The air was completely removed from the reaction vessel by vigorously bubbling argon for 10 min and sealed. The reaction mixture was then stirred and heated to reflux at 110°C overnight. The vessel was thus let cool to ambient temperature. The mixture was then acidified with HCl_{aq} and exctracted three times with 50 mL of ethyl acetate. The organic layer was separated and washed three times with 50 mL of water and 20 mL of brine. The solvent was finally dried over anhydrous $MgSO_4$ and evaporated under reduced pressure.

The crude was purified using silica gel chromatography (cyclohexane:AcOEt, 20:1, v/v) to obtain a colorless oil (150 mg). **Yield:** 19%. **^{1}H-NMR** (300 MHz, $CDCl_3$, δ): 8.42 (d, *J* = 5.2 Hz, 1H), 7.55-7.64 (m, 2H), 7.44-7.55 (m, 4H), 7.42 (dd, J= 5.1, 1.1 Hz, 1H). **^{13}C-NMR** (75.48 MHz, $CDCl_3$, δ): 152.2, 151.5, 150.0, 136.8, 129.7, 129.3, 127.0, 122.0, 120.5. **HRMS (ESI+):** $(M+Na)^+$ calcd for $C_{11}H_8N^{35}ClNa$, 212.0238; found: 212.0237.

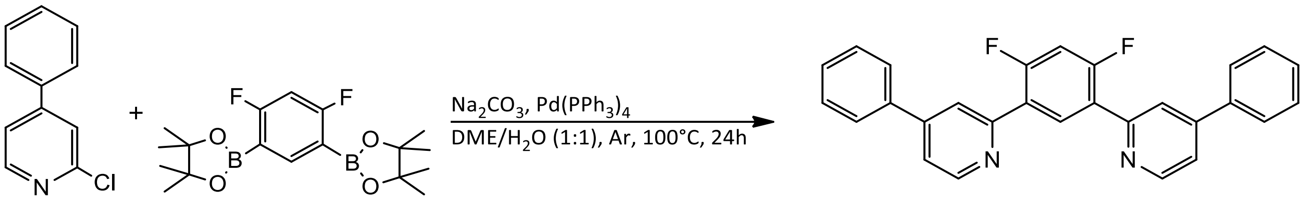

11 **12**

12. To a two neck round bottom flask, **11** (0.19 g, 0.98 mmol), the pinacol ester of benzene-1,3-difluoro-4,6-diboronic acid (0.16 g, 0.44 mmol), an aqueous Na_2CO_3 solution (1 M, 7 mL), Pd(PPh$_3$)$_4$ (0.08 g, 0.07 mmol) and 7 mL of DME, were added under an argon atmosphere. The air was fully removed by bubbling Ar for 20 min. The vessel was then sealed and heated to reflux at 100°C overnight. Upon cooling to ambient temperature, the reaction mixture was finally evaporated under reduced pressure and dissolved in a mixture of dichloromethane (30 mL) and water (20 mL). The organic phase was collected, dried over anhydrous $MgSO_4$, filtered and concentrated *in vacuo*. The crude was purified using silica gel chromatography (cyclohexane:AcOEt, 16:1, v/v) to obtain a colorless oil (227 mg). **Yield:** 55%. **^{1}H-NMR** (300 MHz, $CDCl_3$, δ): 8.80 (d, *J* = 5.2 Hz, 2H), 8.71 (t, *J* = 9.0 Hz, 1H), 8.02 (s, 2H), 7.72 (d, *J* = 6.8 Hz, 4H), 7.45-7.59 (m, 8H), 7.11 (t, *J* = 10.6 Hz, 1H).**^{13}C-NMR** (75.48 MHz, $CDCl_3$, δ): 162.2 (d, *J* = 12.4 Hz), 158.9 (d, *J* = 12.5 Hz), 153.1, 150.1, 149.0, 138.2, 133.8, 129.1, 127.2, 124.7, 124.5, 122.3, 120.6, 105.1 (t, *J* = 27.2 Hz). **^{19}F-NMR** (282.36 MHz, $CDCl_3$, δ): -112.43 (s, 2F). **HRMS (ESI+):** $(M+H)^+$ calcd for $C_{28}H_{19}N_2F_2$, 421.1511; found: 421.1509.

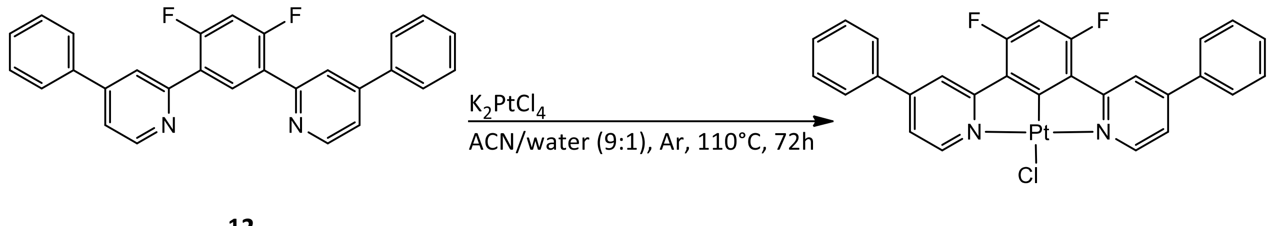

12

Pt-6

Pt-6. A Schlenk tube was charged with **12** (0.10 g, 0.24 mmol) dissolved in 9 mL of acetonitrile and K_2PtCl_4 (0.16 g, 0.38 mmol) solubilized in 1 mL of water. The reaction vessel was then filled with Argon and a needle was inserted in the solvent in order to directly bubble the Ar in the reaction mixture. After 40 min, the vessel was sealed and heated at reflux at 110°C for 72h. In the end, the reaction mixture was let cool. Afterwards, the solid was isolated after filtration through a nylon membrane filter and washed with water and diethyl ether. The yellow solid was then collected and dried (121 mg). **Yield:** 93%. **^{1}H-NMR** (300 MHz, $CDCl_3$, δ): 9.32 (d, *J* = 6.1 Hz, $^3J(^{195}Pt)$ = 39.1 Hz, 2H), 8.11 (s, 2H), 7.67 – 7.78 (m, 4H), 7.53-7.71 (m, 6H), 7.49 (dd, *J* = 6.0, 1.9 Hz, 2H), 6.77 (t, *J* = 11.3 Hz, 1H). **^{13}C-NMR** (75.48 MHz, $CDCl_3$) δ: 151.8, 136.7, 130.3, 129.4, 127.2, 120.7. Due to the poor solubility, not all the carbon atoms can be observed in the spectrum. **^{19}F-NMR** (282.36 MHz, $CDCl_3$, δ): -108.32 (s, 2F). **HRMS (ESI+):** $(M+Na)^+$ calcd for $C_{28}H_{17}N_2F_2{}^{35}ClNa^{195}Pt$, 672.0588; found: 672.0584. **Elem. Anal.** calcd. for $C_{28}H_{17}ClF_2N_2Pt$: C, 51.74; H, 2.64; N, 4.31; found: C, 51.83; H, 2.67; N, 4.33

2.1.2.3 Synthesis of Pt-7

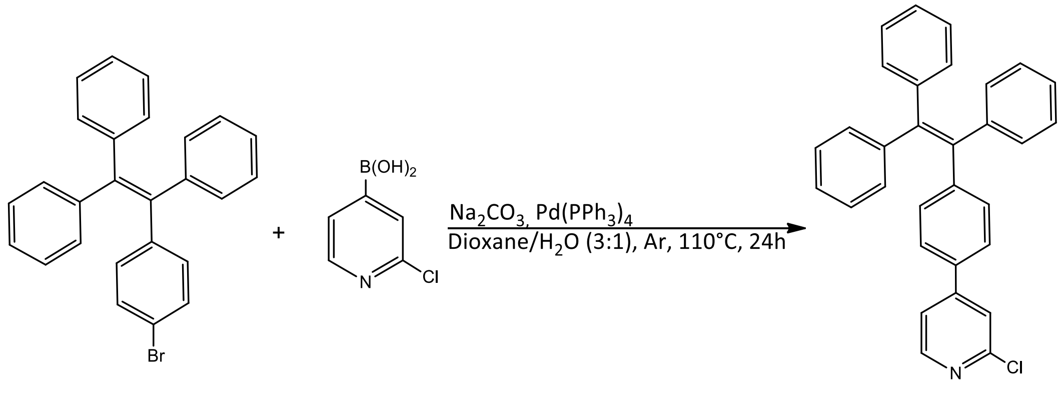

13

13. 2-chloro-pyridine-4-boronic acid (0.23 g, 1.5 mmol), 1-(4-Bromophenyl)-1,2,2-triphenylethylene (0.50 g, 1.2 mmol), $Pd(PPh_3)_4$ (0.07 g, 60 µmol), Na_2CO_3 (0.39 g, 3.6 mmol) were placed in a Schlenk tube and solubilized in a mixture made of 5 mL of distilled water and 15 mL of 1,4-dioxane. The air was completely removed from the reaction vessel by vigorously bubbling Argon for 10 min and it was then sealed. The reaction mixture was then stirred and heated to reflux at 110°C overnight. The vessel was thus let cool to ambient temperature. The mixture was then acidified with HCl_{aq} and exctracted three times with 50 mL of ethyl acetate. The organic layer was separated and washed three times with 50 mL of water and 20 mL of brine. The solvent was finally dried over anhydrous $MgSO_4$, filtered and evaporated under reduced pressure.

The crude was purified using silica gel chromatography (cyclohexane:AcOEt, 20:1, v/v) to obtain a colorless oil (253 mg). **Yield:** 47%. **^{1}H-NMR** (300 MHz, $CDCl_3$, δ): 8.40 (d, *J* = 5.2 Hz, 1H), 7.51 (d, *J* = 1.1 Hz, 1H), 7.39 (dd, *J* = 6.1, 2.1 Hz, 3H), 7,03-7,20 (m, 17H).**^{13}C-NMR** (75.48 MHz, $CDCl_3$, δ): 152.2, 151.0, 149,.9, 145.6, 143.4, 143.3, 142.1, 139.8, 134.4, 132.2, 131.3, 131.2, 127.9, 127.8, 127.7, 126.8, 126.7, 126.2, 121.7, 120.1. **HRMS (ESI+):** $(M+Na)^+$ calcd for $C_{31}H_{22}N^{35}ClNa$, 466.1333; found: 466.1335.

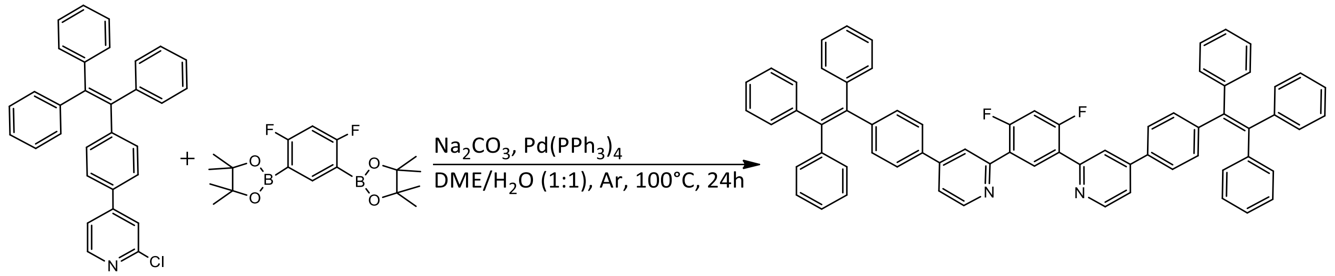

13

14

14. To a two neck round bottom flask, **13** (0.15 g, 0.3 mmol), the pinacol ester of benzene-1,3-difluoro-4,6-diboronic acid (0.06 g, 0.15 mmol), an aqueous Na_2CO_3 solution (1 M, 3 mL of H_2O), $Pd(PPh_3)_4$ (0.03 g, 0.03 mmol) and 3 mL of DME, were added under an argon atmosphere. The air was fully removed by bubbling Ar for 20 min. The vessel was then sealed and heated to reflux at 100°C overnight. Upon cooling to ambient temperature, the reaction mixture was finally evaporated under reduced pressure and dissolved in a mixture of dichloromethane (30 mL) and water (20 mL). The organic phase was collected, dried over anhydrous $MgSO_4$, filtered and concentrated *in vacuo*. The crude was purified using silica gel chromatography (cyclohexane:AcOEt, 16:1, v/v) to obtain a colorless oil (80 mg). **Yield:** 56%. **^{1}H-NMR** (300 MHz, $CDCl_3$, δ): 8.74 (d, *J* = 5.2 Hz, 2H), 8.64 (t, *J* = 8.9 Hz, 1H), 7.96 (s, 2H), 7.43-7.52 (m, 6H), 7.02-7.22 (m, 35H).**^{13}C-NMR** (75.48 MHz, $CDCl_3$, δ): 145.0, 143.4, 143.2, 141.8, 140.0, 132.1, 131.4, 131.3, 131.2, 127.8, 127.7, 126.7, 126.6, 126.3, 120.3. **^{19}F-NMR** (282.36 MHz, $CDCl_3$, δ): -112.92 (s, 2F). **HRMS (ESI+):** $(M+Na)^+$ calcd for $C_{68}H_{46}N_2F_2Na$, 951.3521; found: 951.3521.

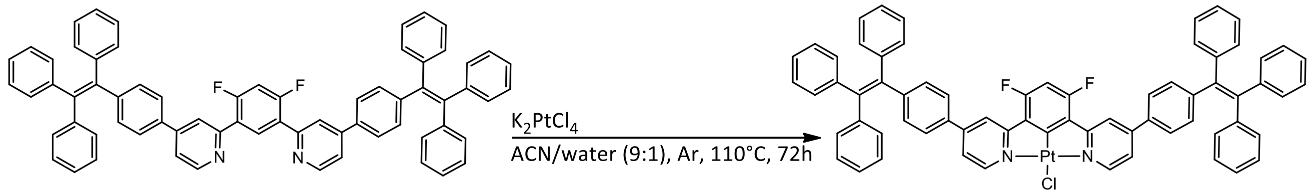

14

Pt-7

Pt-7. A Schlenk tube was charged with **14** (0.09 g, 0.1 mmol) dissolved in 9 mL of acetonitrile and with K_2PtCl_4 (0.08 mg, 0.2 mmol) solubilized in 1 mL of water. The reaction vessel was then filled with argon and a needle was inserted in the solvent in order to directly bubble Ar in the reaction mixture. After 40 min, the vessel was sealed and heated at reflux at 110°C for 72h. In the end, the reaction mixture was let cool. Afterwards, the solid was isolated after filtration through a nylon membrane filter and washed with water, MeOH and diethyl ether. The orange solid was then collected and dried (50 mg). **Yield:** 78%. **^{1}H-NMR** (300 MHz, $CDCl_3$, δ): 9.23 (d, *J* = 6.1 Hz, $^3J(^{195}Pt)$ = 36.0 Hz, 2H), 8.02 (s, 2H), 7.48 (d, *J* = 8.4 Hz, 4H), 7.39 (dd, *J* = 6.1, 2.0 Hz, 2H), 7.03-

7.23 (m, 34H), 6.69 (t, *J* = 11.3 Hz, 1H). **^{13}C-NMR** (75.48 MHz, $CDCl_3$, δ): 151.1, 146.3, 143.3, 143.2, 142.3, 139.8, 134.1, 132.3, 131.3, 131.3, 127.9, 127.8, 127.7, 126.9, 126.8, 126.4. Due to the poor solubility, ^{13}C-NMR spectrum didn't allow to clearly observe the C atoms. **^{19}F-NMR** (282.36 MHz, $CDCl_3$, δ): -108.50 (s, 2F). **HRMS (ESI+):** $(M+Na)^+$ calcd for $C_{68}H_{45}N_2F_2{}^{35}ClNa^{195}Pt$, 1180.2780; found: 1180.2784. **Elem. Anal.** calcd. for $C_{68}H_{45}ClF_2N_2Pt$: C, 70.49; H, 3.91; N, 2.42; found: C, 70.85; H,3.93; N, 2.44.

2.1.2.4 Synthesis of Pt-8

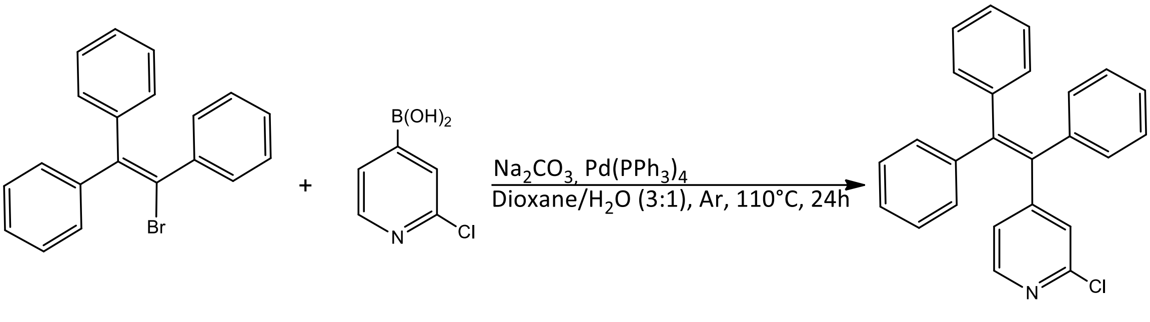

15

15. 2-chloro-pyridine-4-boronic acid (0.22 g, 1.4 mmol), 1-(4-Bromophenyl)-1,2,2-triphenylethylene (0.30 g, 0.9 mmol), $Pd(PPh_3)_4$ (0.05 g, 0.04 mmol), Na_2CO_3 (0.28 g, 2.7 mmol) were placed in a Schlenk tube and solubilized in a mixture made of 2.5 mL of distilled water and 7.5 mL of 1,4-dioxane. The air was completely removed from the reaction vessel by vigorously bubbling Argon for 10 min and it was then sealed. The reaction mixture was then stirred and heated to reflux at 110°C overnight. The vessel was thus let cool to ambient temperature. The mixture was then acidified with HCl_{aq} and exctracted three times with 50 mL of ethyl acetate. The organic layer was separated and washed three times with 50 mL of water and 20 mL of brine. The solvent was finally dried over anhydrous $MgSO_4$ and evaporated under reduced pressure.

The crude was purified using silica gel chromatography (cyclohexane:AcOEt, 20:1, v/v) to obtain a colorless oil (83.8 mg). **Yield:** 25%. **^{1}H-NMR** (300 MHz, $CDCl_3$, δ): 8.11 (d, *J* = 5.2 Hz, 1H), 6.95-7.25 (m, 16H), 6.86 (d, *J* = 5.2 Hz, 1H). **^{13}C-NMR** (75.48 MHz, $CDCl_3$, δ): 155.0, 151.3, 149.0, 144.7, 142.1, 141.7, 137.0, 131.2, 131.0, 128.2, 127.8, 127.7, 127.3, 126.3, 124.8. **HRMS (ESI+):** $(M+H)^+$ calcd for $C_{25}H_{19}N^{35}Cl$, 368.1200; found: 368.1200.

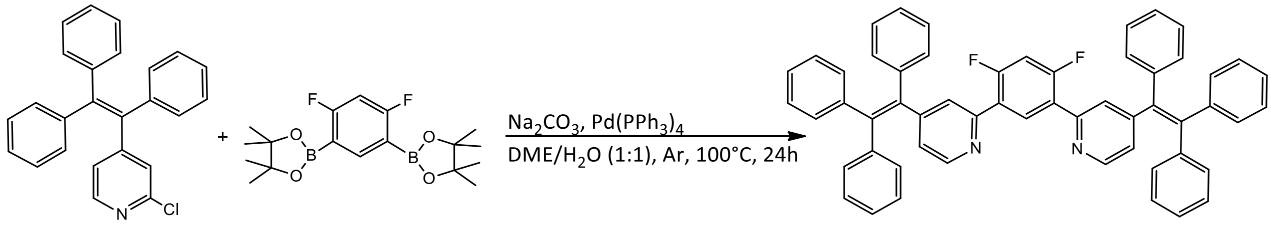

15 **16**

16. To a two neck round bottom flask, **15** (0.12 g, 0.3 mmol), the pinacol ester of benzene-1,3-difluoro-4,6-diboronic acid (0.05 g, 0.15 mmol), an aqueous Na_2CO_3 solution (1 M, 3 mL), $Pd(PPh_3)_4$ (0.03 g, 0.02 mmol) and 3 mL of DME, were added under an argon atmosphere. The air was fully removed by bubbling Ar for 20 min. The vessel was then sealed and heated to reflux at 100°C overnight. Upon cooling to ambient temperature, the reaction mixture was finally evaporated under reduced pressure and dissolved in a mixture of dichloromethane (30 mL) and water (20 mL). The organic phase was collected, dried over anhydrous $MgSO_4$, filtered and concentrated *in vacuo*. The crude was purified using silica gel chromatography (cyclohexane:AcOEt, 16:1, v/v) to obtain a colorless oil (75 mg). **Yield:** 65%. **^{1}H-NMR** (300 MHz, $CDCl_3$, δ): 8.45 (d, *J* = 5.1 Hz, 2H), 8.19 (t, *J* = 8.9 Hz, 1H), 7.37 (s, 3H), 6.96-7.23 (m, 29H), 6.92 (d, *J* = 5.1 Hz, 2H), 6.81 (t, *J* = 10.5 Hz, 1H). **^{13}C-NMR** (75.48 MHz, $CDCl_3$, δ): 163.4, 152.3, 152.1, 149.2, 143.7, 142.7, 142.5, 142.2, 138.2, 131.2, 131.1, 128.1, 128.0, 127.7, 127.3, 126.9, 124.8, 119.1, 34.9, 34.8, 34.4, 31.9, 31.5, 31.4, 30.3, 30.2, 30.1, 29.7, 29.4. **^{19}F-NMR** (282.36 MHz, $CDCl_3$, δ): -112.79 (s, 2F). **HRMS (ASAP):** $(M)^+$ calcd for $C_{56}H_{38}N_2F_2$, 776.2998; found: 776.3006.

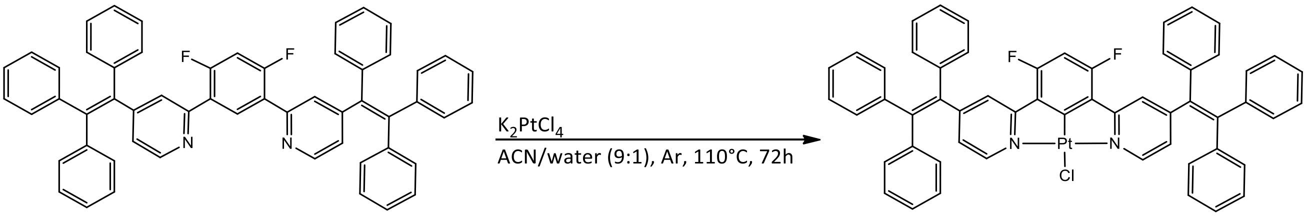

16 **Pt-8**

Pt-8. A Schlenk tube was charged with **16** (0.20 g, 0.3 mmol) dissolved in 9.0 mL of acetonitrile and with K_2PtCl_4 (0.21 mg, 0.5 mmol) solubilized in 1 mL of water. The reaction vessel was then filled with argon and a needle was inserted in the solvent in order to directly bubble Ar in the reaction mixture. After 40 min, the vessel was sealed and heated at reflux at 110°C for 72h. In the end, the reaction mixture was let cool. Afterwards, the solid was isolated after filtration through a nylon membrane filter and washed with water, MeOH and diethyl ether. The orange solid was then collected and dried (70.8 mg). **Yield:** 35%. **^{1}H-NMR** (300

MHz, $CDCl_3$, δ): 8.99 (d, *J* = 6.0 Hz, $^{3}J(^{195}Pt)$ = 37.2 Hz, 2H), 7.47, (s, 2H), 7.0-7.25 (m, 30H), 6.88 (d, *J* = 6.0 Hz, 2H), 6.50 (t, *J* = 11.1 Hz, 1H). Due to the poor solubility, ^{13}C couldn't be obtained. **^{19}F-NMR** (282.36 MHz, $CDCl_3$, δ): -108.94 (s, 2F). **HRMS (ESI+):** $(M+Na)^+$ calcd for $C_{56}H_{37}N_2F_2{}^{35}ClNa{}^{195}Pt$, 1028.2153; found: 1028.2160. **Elem. Anal.** calcd. for $C_{56}H_{37}ClF_2N_2Pt$: C, 66.83; H, 3.71; N, 2.78; found: C, 66.86; H,3.73; N, 2.76.

2.2 Synthesis of cationic tryptophan-conjugated Ir(III) complexes

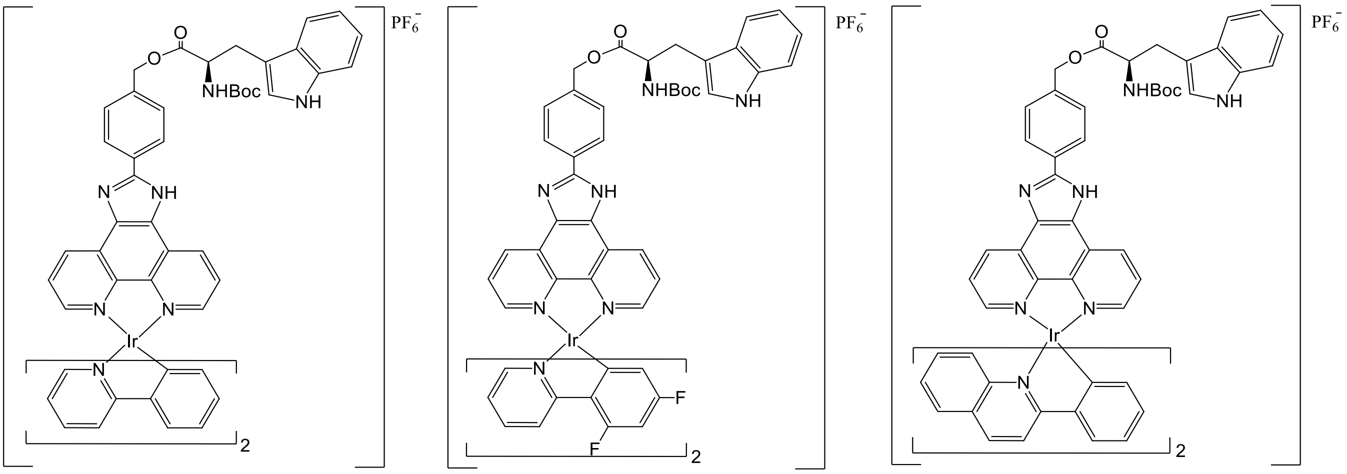

Ir-1 **Ir-2** **Ir-3**

Figure 107. Molecular structure of the synthesized tryptophan conjugated Ir(III) complexes.

The tryptophan-conjugated Ir(III) complexes were prepared following the procedures reported in literature[112,113] The synthesis of the imidazolyl modified phenanthroline-based scaffold was synthesized according to literature[38] Then, the tryptophan conjugation was achieved as previously reported.[107] **Ir-1**, **Ir-2**, **Ir-3** and the dimer precursors were synthesized according to literature.[111]

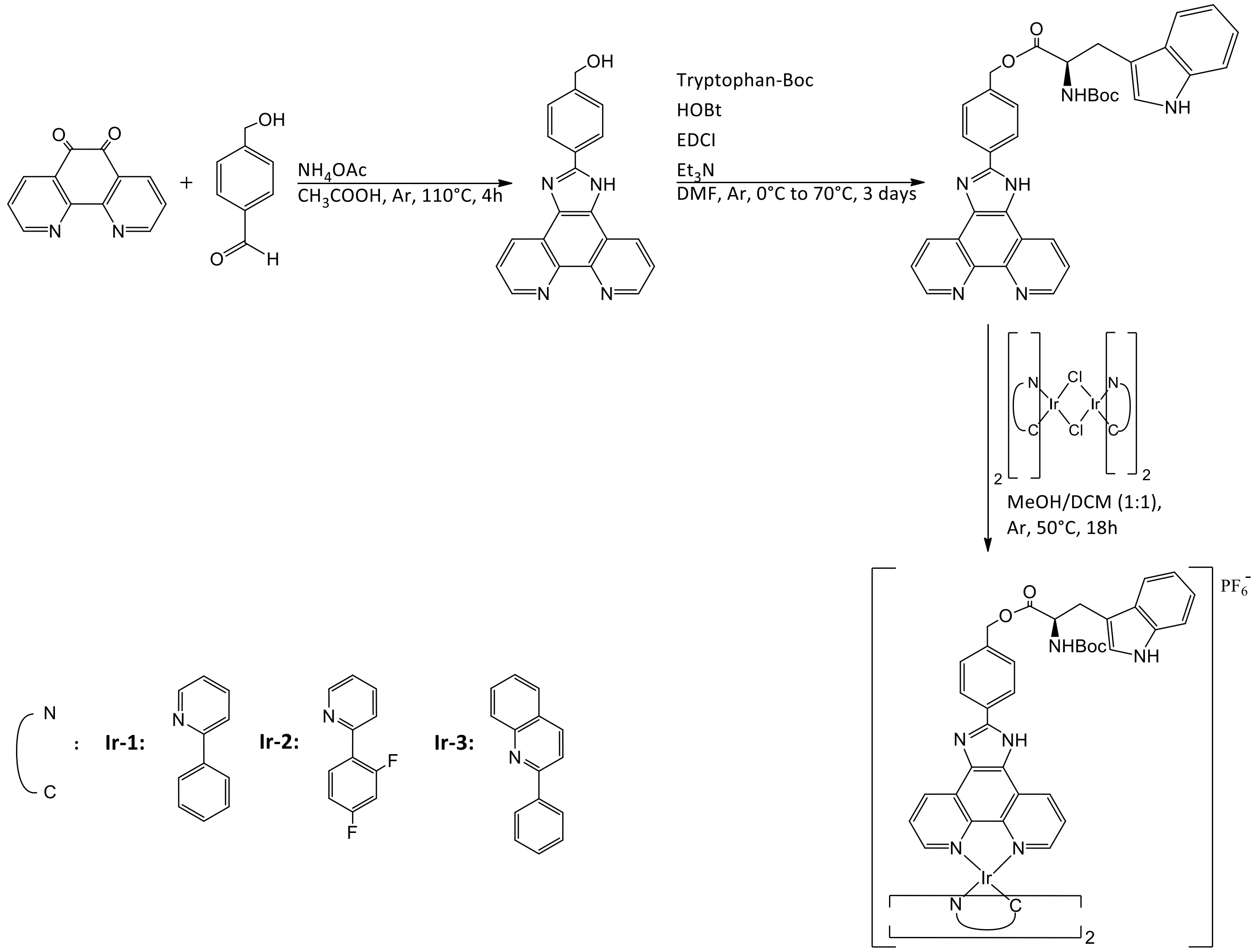

Ir-1 to Ir-3

Scheme 4. Illustration of the synthetic pathway followed for the preparation of Ir-1 to Ir-3.

2.2.1 Synthesis of the tryptophan-conjugated phenanthroline-based ligand

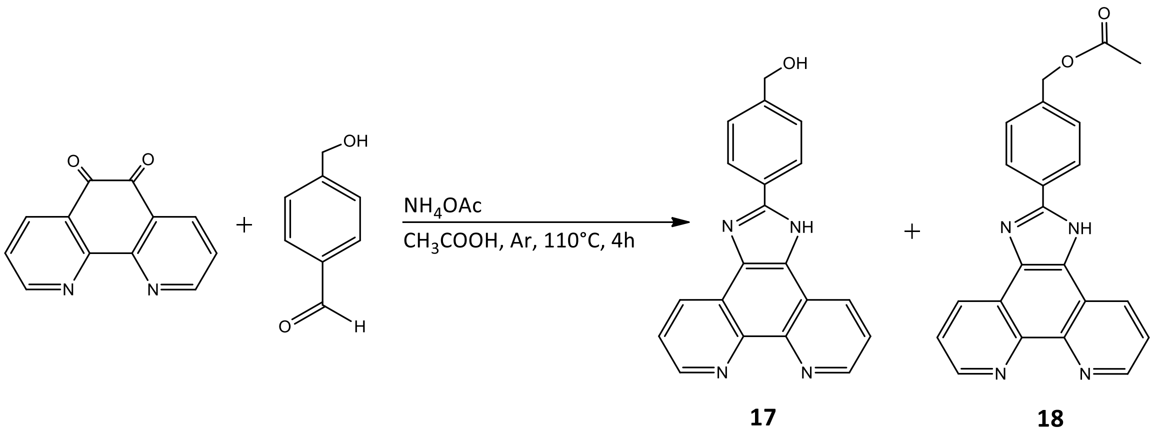

17+18. A Schlenk tube fitted with a condenser, filled with Ar, was charged with 1,10-phenanthroline-5,6-dione (0.24 g, 1.1 mmol), 4-(4-hydroxymethyl)benzaldehyde (0.18 g, 1.3 mmol), ammonium acetate (1.74 g, 22.5 mmol) and glacial acetic acid (4.0 mL). The mixture was heated under reflux for 4h, cooled to room temperature and neutralized with aqueous ammonia. In the end a lacquer deposited on the glassware was obtained. The solvent was thus collected apart, and the lacquer was washed pouring water (10 mL) under sonication. The precipitation of a yellow powder was observed. The suspension was filtered, and the isolated yellow solid washed with diethyl ether (15 mL) and dried under vacuum.

The NMR spectrum recorded on the powder in d$_6$-DMSO highlighted the presence of two species: the desired complex **17** and the acetylated derivative **18**.

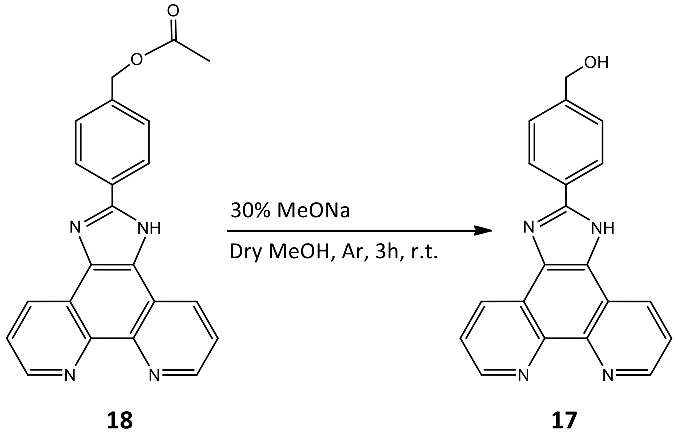

17. The mixture made of **17+18** (388 mg) was placed in a two neck round-bottomed flask under Ar and solubilized in 5 mL of dry MeOH. Then, then 3 mL of a 30% solution of MeONa in MeOH was added in a dropwise manner. The solution was let stir for three hours at room temperature. The desired ligand was obtained through precipitation with 1 mL of a saturated solution of NH_4Cl. The suspension was filtered. The isolated yellow solid was washed with 5 mL of water, 10 mL of diethyl ether and dried under vacuum (200 mg). **Yield:** 54%. **^{1}H-NMR** (400 MHz, DMSO, δ): 9.04 (d, *J* = 3.8 Hz, 2H), 8.94 (d, *J* = 7.9 Hz, 2H), 8.27 (d, *J* = 8.0 Hz, 2H), 7.80-7.89 (m, 2H), 7.57 (d, *J* = 8.0 Hz, 2H), 5.34 (t, *J* = 5.6 Hz, 1H), 4.63 (d, *J* = 5.3 Hz, 2H).

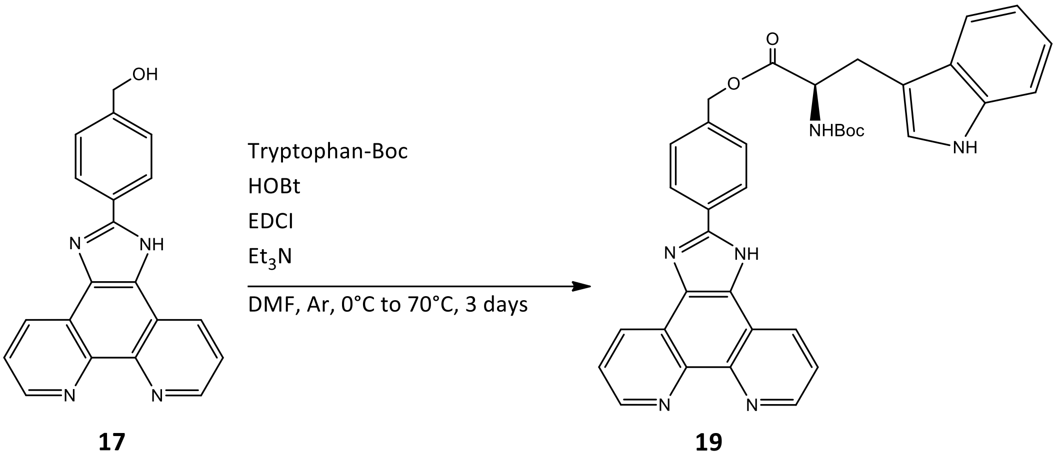

19. In a Sclenk tube under inert atmosphere, Boc protected tryptophan (0.47 g, 1.5 mmol), HOBt (0.21 g, 1.5 mmol) and EDCI (0.30 g, 1.5 mmol) were dissolved in 8 mL of dry DMF amine free at 0°C. Then, Et_3N (0.21 mL, 1.5 mmol) was added and the mixture was let stirring for one hour, before the ligand (0.20 g, 0.6 mmol) was dissolved in the mixture as well. The vessel was finally sealed and heated at 70°C for 72h. Upon cooling to room temperature, the solvent was evaporated *in vacuo.* The crude product was purified through silica gel flash chromatography, using a mixture of DCM:MeOH, 19:1, v/v, as the eluent. The desired compound was obtained as a yellow solid (266 mg). **Yield:** 69% . **^{1}H-NMR** (300 MHz, MeOD, δ): 8.63 (dd, *J* = 4.3, 1.5 Hz, 2H), 8.20-8.33 (m, 2H), 7.70 (d, *J* = 8.0 Hz, 2H), 7.54 (d, *J* = 7.8 Hz, 1H), 7.36 (d, *J* = 8.0 Hz, 1H), 7.24-7.32 (m, 2H), 6.98-7.15 (m, 6H), 4.99 (s, 2H), 4.55 (t, *J* = 6.9 Hz, 1H), 3.14-3.30 (m, 2H), 1.42 (s, 9H). **^{13}C-NMR** (75.48 MHz, $MeOD_3$, δ): 172.8, 156.4, 150.3, 147.0, 142.6, 137.2, 136.7, 129.3, 128.8, 127.9, 127.4, 126.0, 123.2, 122.7, 121.1, 118.5, 117.9, 111.1, 109.3, 79.3, 65.9, 55.0, 53.4, 27.5. **HRMS (ESI+):** $(M+Na)^+$ calcd for $C_{36}H_{32}N_6O_4Na$, 635.2377; found: 635.2384.

2.2.2 Synthesis of the Ir-dimers

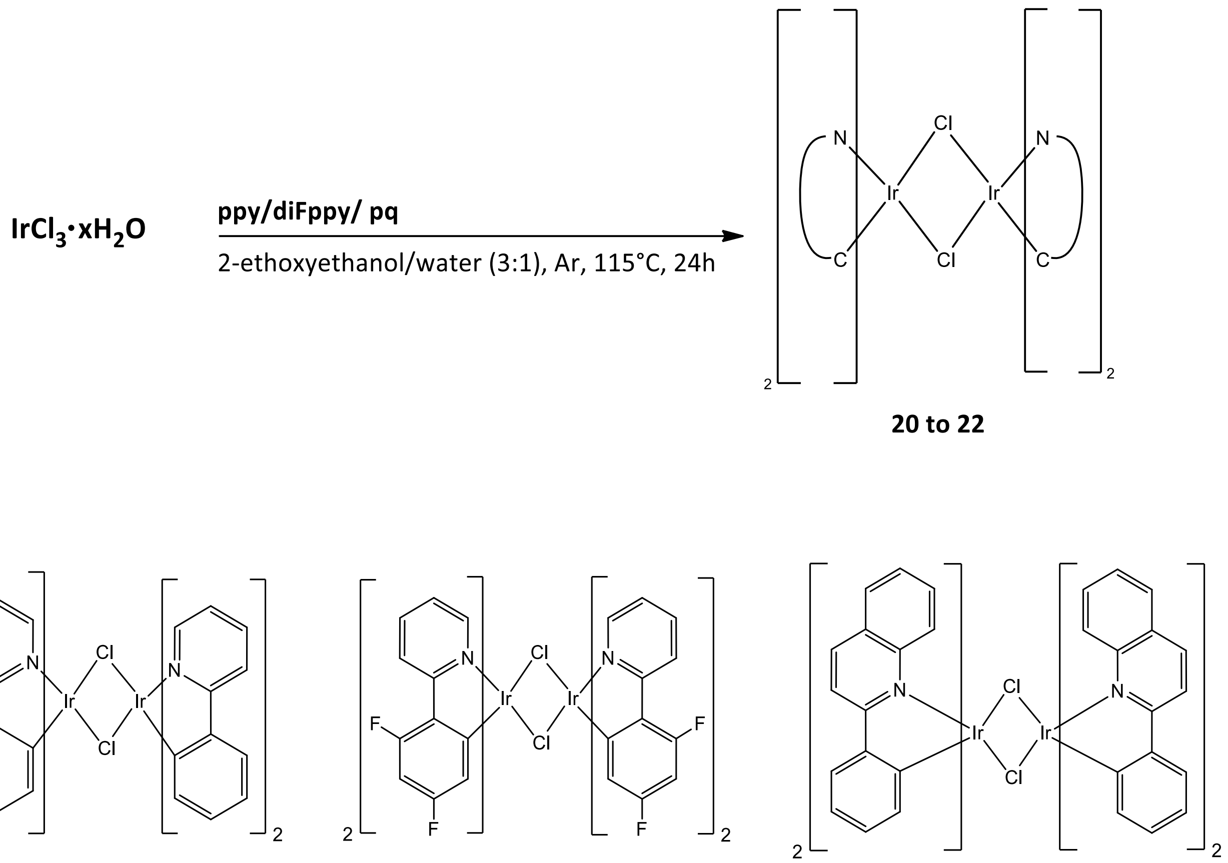

20 to 22

20

21

22

Scheme 5. General synthetic route followed to prepare the Ir dimers 20, 21 and 22.

General procedure:

$IrCl_3{\bullet}xH_2O$, 2-phenilpyridine (ppy), 2-(2,4-Difluorophenyl)pyridine (diFppy), or 2-phenylquinoline (pq) were placed in a three neck round-bottomed flask fitted with a condenser and dissolved in a 2-ethoxyethanol:water mixture (3/1, v/v). The solution was then deaerated bubbling Ar inside the solution for 30 min. The vessel was finally sealed and heated at 115°C for 24h. The thus obtained yellow or red suspension was let cool down to room temperature, diluted with 5 mL of water and filtered. The isolated solid was washed with MeOH, diethyl ether and dried under vacuum. The Ir dimers were finally precipitated with DCM/diethyl ether in order to remove the major impurities.

20. Reagents: $IrCl_3{\bullet}xH_2O$ (0.30 g, 1.0 mmol), 2-phenylpyridine (0.36 mL, 2.5 mmol). Solvents: 2-ethoxyethanol (15 mL), water (5 mL). The desired complex was obtained as a yellow solid (371 mg). **Yield:** 69%. **^{1}H-NMR** (300 MHz, $CDCl_3$, δ): 9.26 (d, *J* = 5.0 Hz, 4H), 7.89 (d, *J* = 7.8 Hz, 4H), 7.71-7.81 (m, 4H), 7.51 (dd, *J* = 11.1 Hz, 4.4 Hz, 4H), 6.72-6.83 (m, 8H), 6.53-6.63 (m, 4H), 5.95 (d, *J* = 7.8 Hz, 4H).

21. Reagents: $IrCl_3$•xH_2O (0.30 g, 1.0 mmol), 2-(2,4-Difluorophenyl)pyridine (0.38 mL, 2.5 mmol). Solvents: 2-ethoxyethanol (15 mL), water (5 mL). The desired complex was obtained as a yellow solid (386 mg). **Yield:** 63%. **^{1}H-NMR** (300 MHz, $CDCl_3$, δ): 9.14 (d, *J* = 4.9 Hz, 3H), 8.33 (d, *J* = 8.6 Hz, 3H), 7.85 (t, *J* = 7.4 Hz, 4H), 6.81-6.88 (m, 3H), 6.28-6.42 (m, 4H), 5.31 (dd, *J* = 9.1, 2.3 Hz, 3H).

22. Reagents: $IrCl_3$•xH_2O (0.30 g, 1.0 mmol), 2-Phenylquinoline (0.52 g, 2.5 mmol). Solvents: 2-ethoxyethanol (15 mL), water (5 mL). The desired complex was obtained as a red solid (280 mg). **Yield:** 44%. **^{1}H-NMR** (400 MHz, CD_2Cl_2, δ): 8.59 (d, *J* = 9.1 Hz, 4H), 8.03-8.06 (m, 4H), 7.95-7.96 (m, 4H), 7.70 (d, *J* = 7.8 Hz, 4H), 7.63-7.66 (m, 4H), 7.40-7.41 (m, 4H), 7.14-7.18 (m, 4H), 6.84 (t, *J* = 7.4 Hz, 4H), 6.37 (m, 4H), 5.80 (d, *J* = 7.6 Hz, 4H).

2.2.3 Synthesis of the tryptophan-conjugated Ir(III) complexes

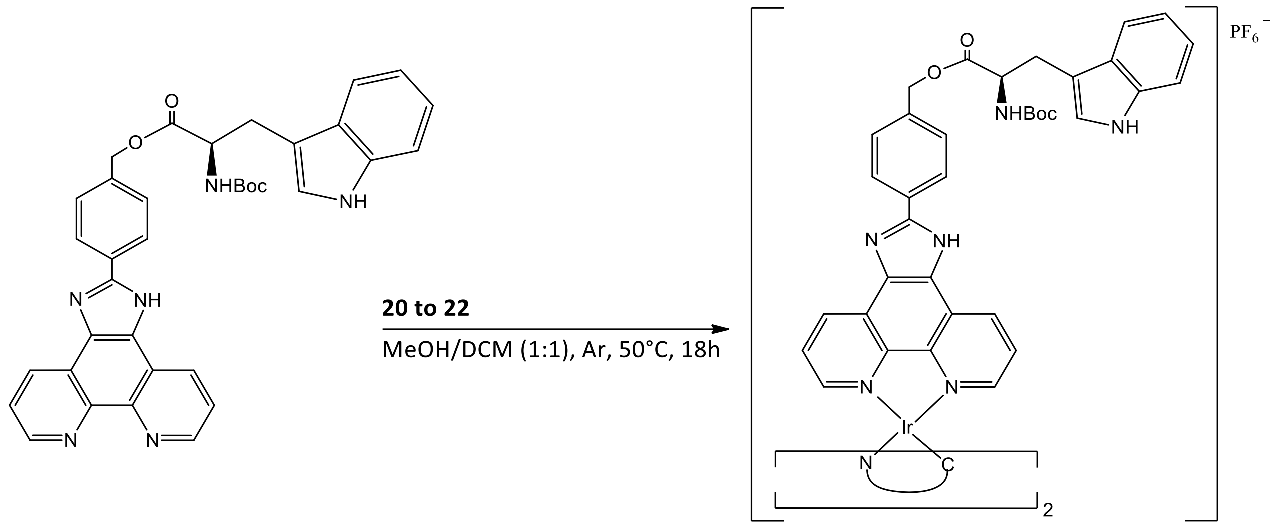

19 **Ir-1 to Ir-3**

General procedure:

The proper Ir-dimer and the tryptophan-conjugated ligand were dissolved in a MeOH:DCM mixture (1/1, v/v) in a Schlenk tube filled with argon. Before sealing the vessel and heating at 50°C overnight, the solution was deaerated bubbling Ar inside the solution for 30 min. The mixture was then cooled to room temperature and a 6-fold excess of KPF_6 was added, letting the mixture stir for 1.5 h. In the end, the suspension was filtered to remove insoluble salts and the recovered solution was thus evaporated to dryness *in vacuo* to get the crude product.

Ir-1. Reagents: **20** (0.09 g, 0.08 mmol), **19** (0.10 g, 0.16 mmol). Solvents: DCM (5 mL), MeOH (5 mL). The crude product was purified through silica gel chromatography (DCM:MeOH, 19:1, v/v) to obtain an orange solid (118 mg). **Yield:** 57%. **^{1}H-NMR** (300 MHz, $CDCl_3$, δ): 9.29 (dd, *J* = 7.9, 2.5 Hz, 2H), 9.08 (s, 1H), 8.46 (d, *J* = 8.0 Hz, 2H), 7.98 (d, *J* = 4.9 Hz, 2H), 7.92 (d, *J* = 8.1 Hz, 2H), 7.79 – 7.50 (m, 7H), 7.42 (d, *J* = 5.7 Hz, 2H), 7.36 (d, *J* = 7.8 Hz, 3H), 7.04-7.17 (m, 4H), 6.98 (t, *J* = 7.4 Hz, 2H), 6.79 (t, *J* = 6.6 Hz, 2H), 6.46 (d, *J* = 7.5 Hz, 2H), 6.29 (s, 1H), 4.96-5.19 (m, 2H), 4.74 (m, 1H), 3.27 (d, J = 4.2 Hz, 2H), 1.47 (s, 9H). **^{13}C-NMR** (75.48 MHz, $CDCl_3$, δ): 168.2, 151.8, 148.7, 145.4, 143.8, 143.1, 137.6, 132.2, 131.8, 130.6, 129.3, 127.3, 124.7, 124.4, 123.7, 122.7, 122.3, 119.3, 119.1, 28.5. **HRMS (ESI+):** $(M)^+$ calcd for $C_{58}H_{48}N_8O_4{}^{193}Ir$, 1113.3422; found: 1113.3425. **Elem. Anal.** calcd. for $C_{58}H_{48}N_8O_4{}^{193}Ir$: C, 55.50; H, 3.61; N, 8.93; found: C, 55.77; H, 3.62; N, 8.97.

Ir-2. Reagents: **21** (0.09 g, 0.07 mmol), **19** (0.09 g, 0.14 mmol). Solvents: DCM (8 mL), MeOH (8 mL). The crude product was purified through precipitation with a mixture of DMC/diethyl ether to obtain a yellow solid (60 mg). **Yield:** 31%. **^{1}H-NMR** (300 MHz, $CDCl_3$, δ): 8.32-8.48 (m, 5H), 8.21 (d, *J* = 4.9 Hz, 2H), 7.76-7.94 (m, 5H), 7.56 -7.64 (m, 2H), 7.35 (d, *J* = 5.6 Hz, 2H), 7.02-7.14 (m, 3H), 6.88-6.96 (m, 3H), 6.61-6.73 (m, 4H), 5.83 (d, *J* = 7.9 Hz, 3H), 4.97-5.28 (m, 3H), 4.81 (s, 1H), 3.20-3.41 (m, 1H), 1.50 (s, 9H). **^{19}F-NMR** (282.36 MHz, $CDCl_3$, δ): -106.52 (d, *J* = 967.4 Hz, 2F), -71.07 (d, *J* = 717.7 Hz, 2F). **^{13}C-NMR** (126 MHz, $CDCl_3$, δ): 164.9, 164.4, 162.9, 160.6, 155.2, 153.7, 148.5, 148.0, 139.1, 136.6, 128.4, 127.6, 127.5, 124.0, 123.8, 123.5, 121.7, 119.0, 118.5, 114.2, 114.1, 112.0, 99.5 (t, *J* = 27.0 Hz), 66.1, 65.7, 54.8, 53.4, 31.0, 28.4. **HRMS (ESI+):** $(M)^+$ calcd for $C_{58}H_{44}N_8F_4O_4{}^{193}Ir$, 1185.3046; found: 1185.3044. **Elem. Anal.** calcd. for $C_{58}H_{44}N_8O_4F_4{}^{193}Ir$: C, 62.13; H, 3.96; N, 9.99; found: C, 62.31; H, 3.98; N, 10.03.

Ir-3. Reagents: **22** (0,09 g, 0.07 mmol), **19** (0,09 g, 0.14 mmol). Solvents: DCM (10 mL), MeOH (10 mL). The crude product was purified through precipitation with a mixture of DMC/diethyl ether to obtain an orange solid (70 mg). **Yield:** 35%. **^{1}H-NMR** (300 MHz, $CDCl_3$, δ): 9.10 (d, *J* = 8.0 Hz, 1H), 8.34-8.49 (m, 2H), 8.06-8.32 (m, 8H), 7.71-7.87 (m, 2H), 7.52-7.66 (m, 4H), 6.63-7.27 (m, 20H), 4.91-5.29 (m, 3H), 4.76 (s, 1H), 3.14-3.43 (m, 1H), 1.48 (s, 9H). **^{13}C-NMR** (126 MHz, $CDCl_3$, δ): 172.3, 170.1, 155.3, 153.8, 151.4, 147.9, 145.6, 145.5, 139.9, 136.6, 135.0, 130.9, 127.4, 127.0, 124.1, 123.7, 123.1, 121.5, 119.1, 118.3, 117.4, 112.1, 108.5, 66.0, 54.7, 30.8, 28.6. **HRMS (ESI+):** $(M)^+$ calcd for $C_{66}H_{52}N_8O_4{}^{193}Ir$, 1213.3735; found: 1213.3736. **Elem. Anal.** calcd. for $C_{66}H_{52}N_8O_4{}^{193}Ir$: C, 65.33; H, 4.32; N, 9.23; found: C, 65.57; H, 4.34; N, 9.27.

2.3 Synthesis of cationic phenanthroline-based Ir(III) complexes for bioconjugation

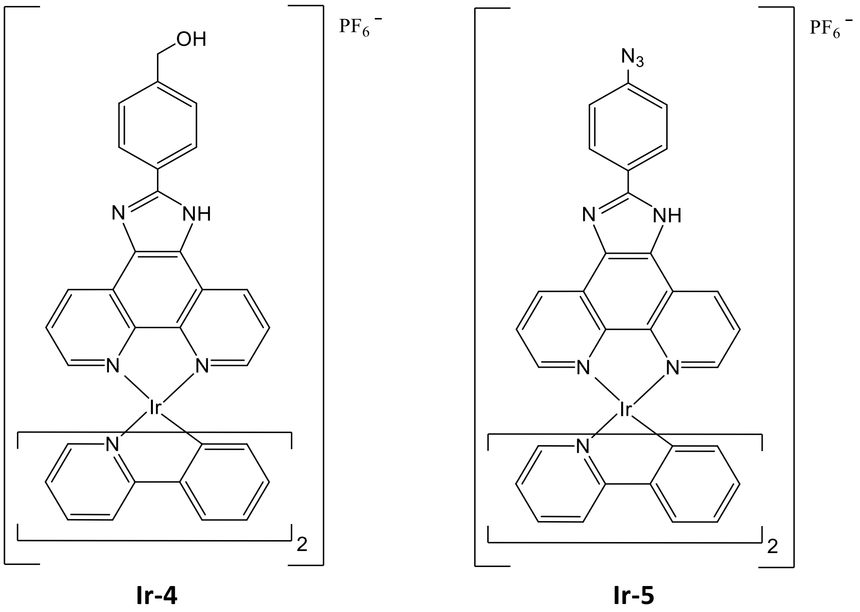

Figure 108. Molecular structure of Ir-4 and Ir-5.

2.3.1 Synthesis of Ir-4

Complex **Ir-4** was synthesized according to the previously discussed procedures. Specifically, **17** and **20** were obtained as described in paragraphs 2.2.1 and 2.2.2, respectively.

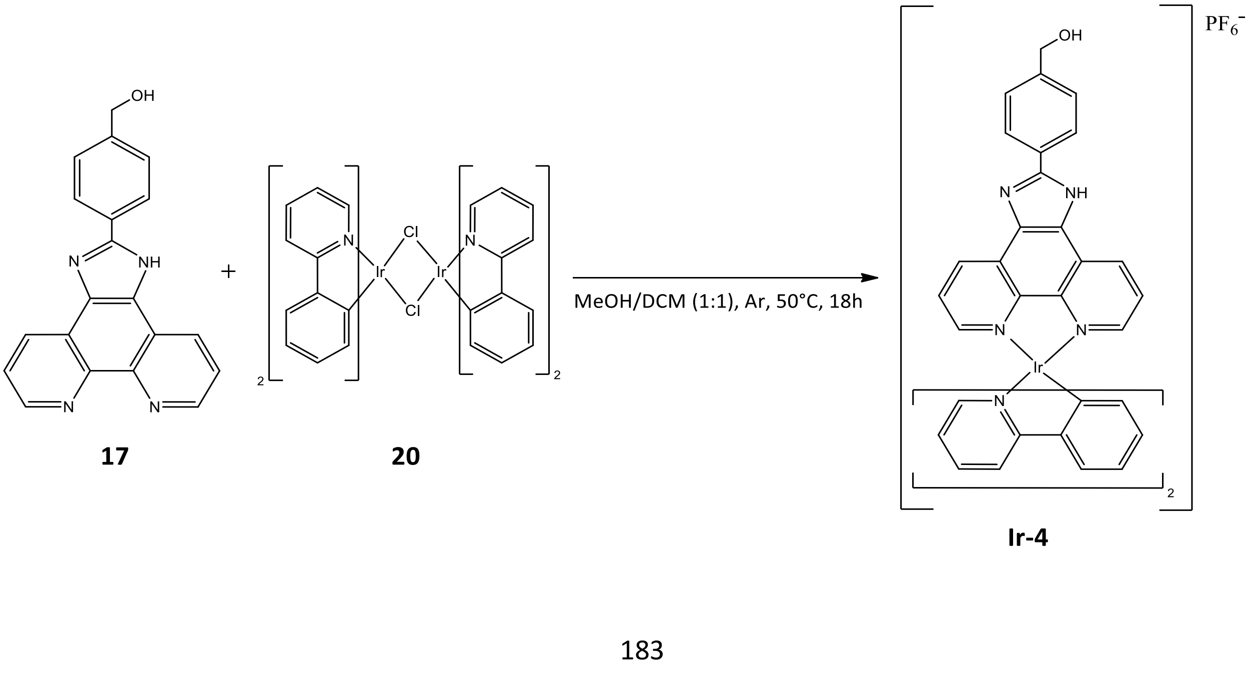

A Schlenk tube filled with Ar was charged with **18** (0.06 g, 0.17 mmol), **20** (0.09 g, 0.08 mmol) and 16 mL of a DCM:MeOH mixture (1/1, v/v). Before sealing the vessel and heating at 50°C, the solution was deaerated with Ar for 30 min. Upon cooling to room temperature, a 6-fold excess of KPF_6 was added and the suspension was let stir at room temperature for 3 h. In the end, the solvent was evaporated under reduced pressure and the residue taken up with 20 mL of DCM. The suspension was then filtered to remove the insoluble salts and the solvent was concentrated *in vacuo.*

The crude product was purified inducing the precipitation of the desired complex with a DCM/diethyl ether mixture to obtain the pure compound as an orange powder (100 mg). **Yield:** 58%. **^{1}H-NMR** (300 MHz, $CDCl_3$, δ): 8.51 (d, *J* = 7.8 Hz, 2H), 8.14-8.24 (m, 2H), 7.96 (d, *J* = 7.9 Hz, 2H), 7.69-7.86 (m, 6H), 7.53 (d, *J* = 8.0 Hz, 2H), 7.31-7.44 (m, 5H), 7.12 (t, *J* = 7.6 Hz, 2H), 7.01 (t, *J* = 7.3 Hz, 2H), 6.83-6.94 (m, 2H), 6.44 (d, *J* = 7.3 Hz, 2H), 4.78 (s, 2H). Due to poor solubility issues, the ^{13}C-NMR couldn't be recorded. **HRMS (ESI+):** $(M)^+$ calcd for $C_{42}H_{30}N_6O^{193}Ir$, 827.2105; found: 827.2107. **Elem. Anal.** calcd. for $C_{42}H_{30}N_6O^{193}Ir$: C, 61.00; H, 3.66; N, 10.16; found: C,61.33; H, 3.68; N, 10.19.

2.3.2 Synthesis of Ir-5

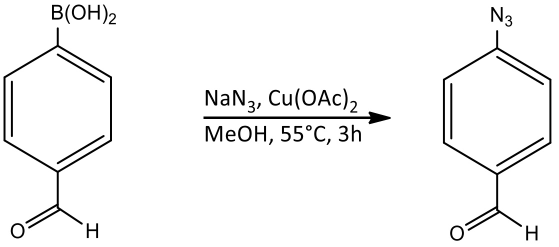

23

23. 4-Formylbenzene-boronic acid (1.00 g, 6.7 mmol), NaN_3 (0.65 g, 10.0 mmol) and $Cu(OAc)_2$ (0.12 g, 0.7 mmol) were dissolved in 10 mL of MeOH in a two neck round bottomed flask fitted with a refrigerator. The vessel was then heated at 55°C for 3 h. Upon cooling to ambient temperature, the reaction mixture was concentrated on celite. The crude product was directly purified through silica gel chromatography with a cyclohexane:AcOEt mixture (9:1, v/v) to obtain the pure aldehyde as a colourless oil (270 mg). **Yield:** 28%. **^{1}H-NMR** (300 MHz, $CDCl_3$, δ): 9.96 (s, 1H), 7.90 (d, *J* = 8.4 Hz, 2H), 7.17 (d, *J* = 8.4 Hz, 2H).

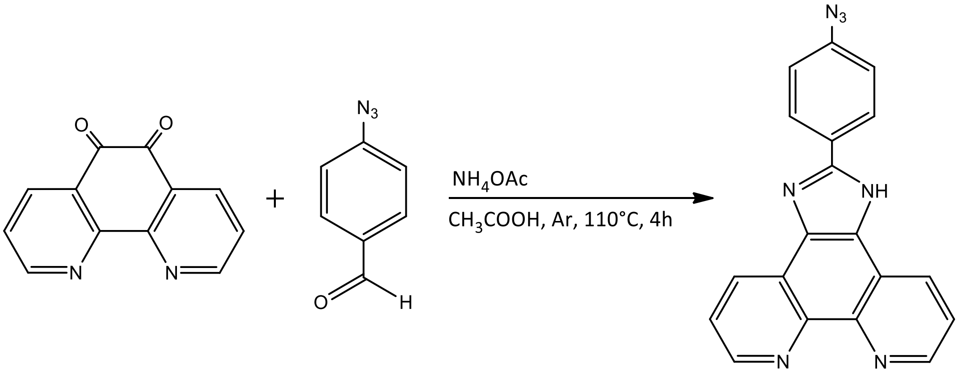

23 **24**

24. A Schlenk tube fitted with a condenser, filled with Ar, was charged with 1,10-phenanthroline-5,6-dione (0.27 g, 1.3 mmol), 4-azido-benzaldehyde (0.23 g, 1.6 mmol), ammonium acetate (1.99 g, 25.8 mmol) and glacial acetic acid (8 mL). The mixture was heated under reflux for 4h, cooled to room temperature and neutralized with aqueous ammonia. In the end, a lacquer deposited on the glassware was obtained. The solvent was thus collected apart, and the lacquer was washed pouring water (10 mL) under sonication. The precipitation of a red powder was observed. The suspension was filtered, and the isolated red solid washed with diethyl ether (15 mL) and dried under vacuum (311 mg). **Yield:** 71% **^{1}H-NMR** (300 MHz, DMSO, δ): 9.05 (d, *J* = 2.9 Hz, 2H), 8.93 (d, *J* = 8.2 Hz, 2H), 8.33 (d, *J* = 8.4 Hz, 2H), 7.86 (s, 2H), 7.40 (d, *J* = 8.5 Hz, 2H).

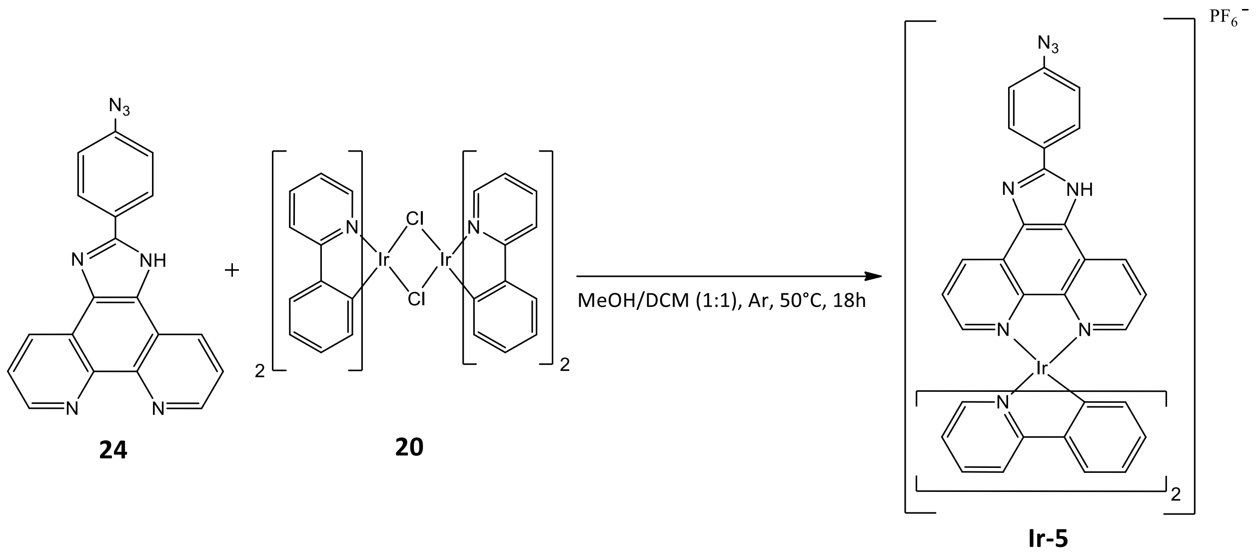

Ir-5. 24 (0.10 g, 0.3 mmol) and **20** (0.16 g, 0.15 mmol) were dissolved in 10 mL of a MeOH:DCM mixture (1:1 v/v) in a Schlenk tube filled with Argon. Before sealing the vessel and heating at 50°C overnight, the solution was deaerated bubbling Ar inside the solution for 30 min. The mixture was then cooled to room temperature and a 6-fold excess of KPF_6 was added, letting the mixture stir for additional 1.5 h. In the end, the suspension was filtered to remove insoluble salts and the recovered solution evaporated to dryness *in vacuo* to get the crude product. The crude product was then purified through silica gel chromatography using a mixture of DCM:MeOH (19:1, v/v) as the eluent. The NMR spectrum highlighted the presence of a second species in the purified batch, thus two subsequent crystallizations with a mixture of DMC and diethyl ether were attempted. It was not possible to isolate the desired complex.

2.4 Synthesis of a Pt complex for bioconjugation through exchange of the ancillary ligand

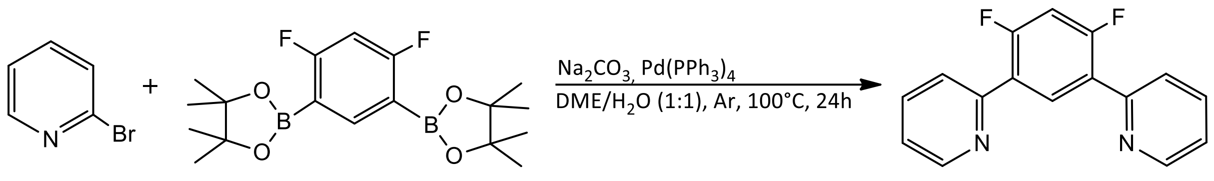

25

25. To a two neck round bottom flask, 2-Bromopyridine (0.82 g, 5.2 mmol), the pinacol ester of benzene-1,3-difluoro-4,6-diboronic acid (0.85 g, 2.3 mmol), an aqueous Na_2CO_3 solution (1 M, 38.5 mL), $Pd(PPh_3)_4$ (0.44 g, 0.4 mmol) and 38.5 mL of DME, were added under an argon atmosphere. The air was fully removed by bubbling Ar for 30 min. The vessel was then sealed and heated to reflux at 100°C overnight. Upon cooling to ambient temperature, the reaction mixture was finally evaporated under reduced pressure and dissolved in a mixture of dichloromethane (30 mL) and water (20 mL). The organic phase was collected, dried over anhydrous $MgSO_4$, filtered and concentrated *in vacuo*. The crude was purified using silica gel chromatography (cyclohexane:AcOEt, 9:1, v/v) to obtain a pale yellow solid (418 mg). **Yield:** 67%. **^{1}H-NMR** (300 MHz, $CDCl_3$, δ): 8.75 (d, *J* = 4.7 Hz, 2H), 8.65 (t, *J* = 9.0 Hz, 1H), 7.77-7.84 (m, 4H), 7.25-7.33 (m, 2H), 7.06 (t, *J* = 10.7 Hz, 1H).

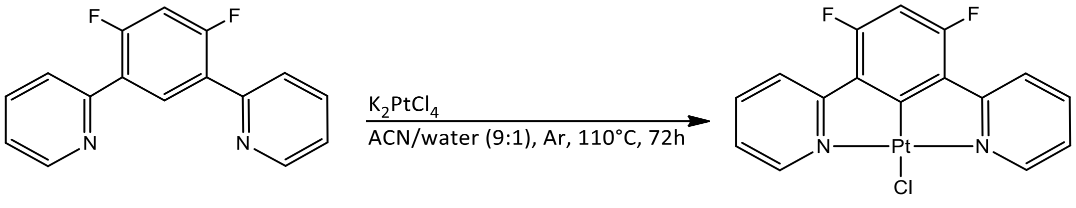

25 **26**

26. A Schlenk tube was charged with **25** (0.08 g, 0.3 mmol) dissolved in 9 mL of acetonitrile and with K_2PtCl_4 (0.19 g, 0.5 mmol) solubilized in 1 mL of water. The reaction vessel was then filled with argon and a needle was inserted in the solvent in order to directly bubble Ar in the reaction mixture. After 40 min, the vessel was sealed and heated at reflux at 110°C for 72h. In the end, the reaction mixture was let cool. Afterwards, the solid was isolated through filtration carried out on a nylon membrane filter and washed with water, MeOH and diethyl ether. The orange solid was then collected and dried (113 mg). **Yield:** 72%. **^{1}H-NMR** (400 MHz,

$CDCl_3$, δ): 9.37 (d, *J* = 5.7 Hz, $^3J(^{195}Pt)$ = 40.3 Hz, 2H), 7.88-8.03 (m, 3H), 7.30-7.37 (m, 3H), 6.73 (t, *J* = 11.2 Hz, 1H).

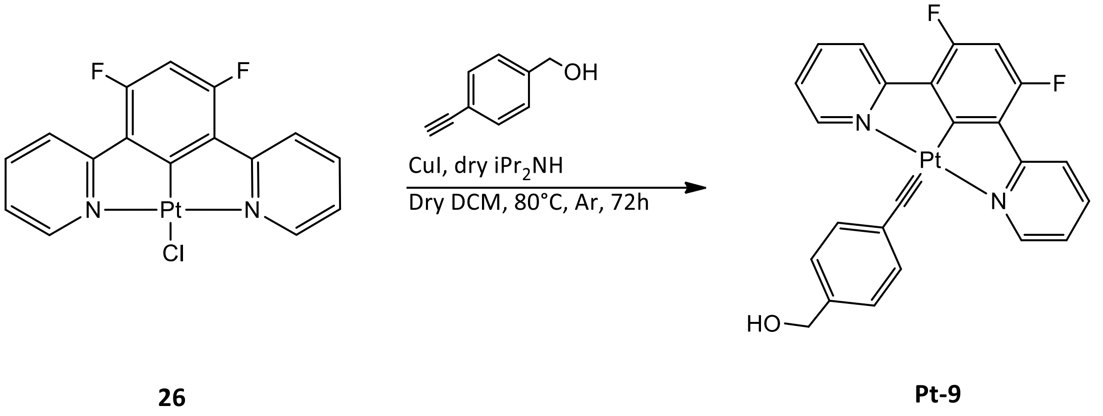

Pt-9. A Schlenk tube filled with Argon was charged with (4-ethynylphenyl)methanol (0.05 g, 0.3 mmol), **26** (0.08 g, 0.2 mmol) and CuI (1.5 mg, 0.01 mmol) dissolved in 20 mL of dry DCM. Finally, dry iPr_2NH (5 mL) was added and the mixture was deaerated vigorously bubbling Ar for 10 min. The flask was then sealed and heated at 80°C for 72h. In the end, the obtained blue suspension was filtered through a Nylon membrane and the solid washed with MeOH (10 x 3 mL). The blue solid was then collected and dried (51 mg). **Yield:** 55%. **^{1}H-NMR** (300 MHz, DMSO, δ): 8.89 (d, *J* = 5.0 Hz, 2H), 7.99 (t, *J* = 7.7 Hz, 2H), 7.38-7.63 (m, 4H), 7.09-7.33 (m, 4H), 6.89 (t, *J* = 11.4 Hz, 1H), 5.27 (t, *J* = 5.7 Hz, 1H), 4.53 (d, *J* = 5.6 Hz, 2H). Due to severe solubility issue encountered even in DMSO, further analysis couldn't be performed. **HRMS (ESI+):** $(M+Na)^+$ calcd for $C_{25}H_{16}N_2OF_2Na^{195}Pt$, 616.0771; found: 616.0775.

2.5 Synthesis of the tryptophan-conjugated Pt(II) complex

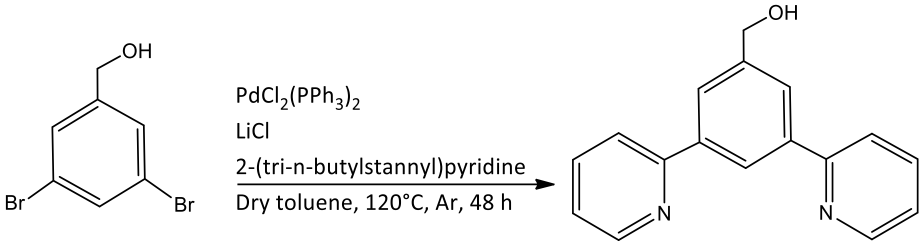

27

27. 3,5-dibromobenzyl alcohol (1.14 g, 4.3 mmol), 2-(tri-*n*-butylstannyl)pyridine (3.79 g, 10.3 mmol), $PdCl_2(PPh_3)_2$ (0.18 g, 0.3 mmol), and LiCl (3.29 g, 77.5 mmol) were placed in a two neck round-bottomed flask under argon. Then, 10.9 mL of anhydrous toluene were added and the mixture was deaerated bubbling argon inside the solution for 30 min. The vessel was finally sealed and heated under reflux at 120°C for 48 hours. The mixture was then let cool to room temperature and a saturated solution of KF (2 mL) was added. The suspension was stirred for an hour and then filtered on a pad of celite. Finally, the mixture was extracted with ethyl acetate (3 x 30 mL). The collected fractions were dried over $MgSO_4$, filtered and evaporated *in vacuo*.

The crude product was purified through silica gel flash chromatography, using a mixture of cyclohexane:AcOEt, 9:1 to 1:1, (v/v,) as the eluent. The desired compound was obtained as a colourless oil (641 mg). **Yield:** 65%. **^{1}H-NMR** (300 MHz, $CDCl_3$, δ): 8.69 (m, 2H), 8.47 (t, *J* = 1.6 Hz, 1H), 7.99 (d, *J* = 1.6 Hz, 2H), 7.71-7.82 (m, 4H), 7.21-7.29 (m, 2H), 4.81 (s, 2H), 2.05 (s, 1H). **^{13}C-NMR** (75.48 MHz, $CDCl_3$, δ): 157.1, 149.7, 142.2, 140.3, 136.9, 126.0, 124.8, 122.4, 120.9, 65.3. **HRMS (ESI+):** $(M+Na)^+$ calcd for $C_{17}H_{14}N_2ONa$, 285.0998; found: 285.1001.

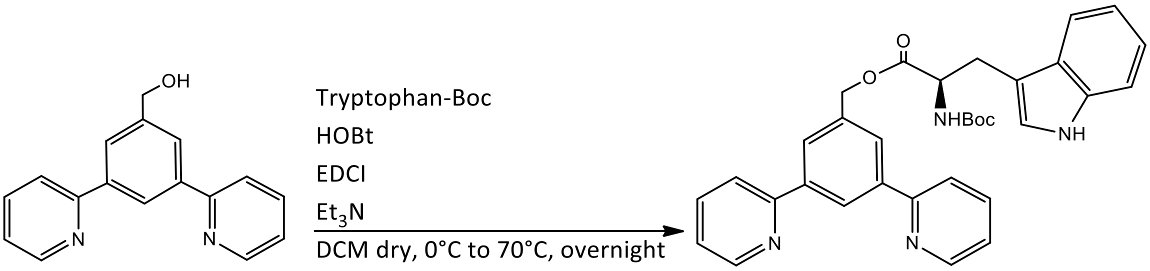

27 **28**

28. In a Sclenk tube under inert atmosphere, Boc protected tryptophan (0.10 g, 0.3 mmol), HOBt (0.05 g, 0.4 mmol) and EDCI (0.08 g, 0.4 mmol) were dissolved in 4 mL of dry DCM at 0°C. Then, Et_3N (55 µL, 0.4 mmol) was added and the mixture was let stirring for one hour, before the ligand (0.10 g, 0.4 mmol) was dissolved in the mixture as well. The vessel was finally sealed and heated at 70°C for 72h. Upon cooling to room temperature, the solvent was evaporated *in vacuo.*

The crude product was purified through silica gel flash chromatography, using a mixture of cyclohexane:AcOEt, 8:2 (v/v) as the eluent. The desired compound was obtained as a colourless oil (55.2 mg). **Yield:** 30%. **^{1}H-NMR** (300 MHz, $CDCl_3$, δ): 8.78 (d, *J* = 4.7 Hz, 2H), 8.59 (s, 1H), 7.97 (s, 2H), 7.78-7.87 (m, 4H), 7.58 (d, *J* = 6.9 Hz, 1H), 7.30-7.39 (m, 2H), 7.20 (d, *J* = 6.7 Hz, 1H), 7.05-7.16 (m, 2H), 6.67 (s, 1H), 5.10-5.35 (m, 3H), 4.68-4.78 (m, 1H), 3.20-3.34 (m, 2H), 1.44 (s, 9H). **^{13}C-NMR** (75.48 MHz, $CDCl_3$, δ): 172.3, 156.9, 149.6, 140.5, 136.9, 136.4, 136.2, 128.4, 126.3, 123.4, 122.8, 121.9, 121.4, 121.1, 119.4, 118.7, 111.1, 109.7, 66.8, 54.6, 28.5. **HRMS (ESI+):** $(M+Na)^+$ calcd for $C_{36}H_{33}N_6O_4Na$, 635.2377; found: 635.2384.

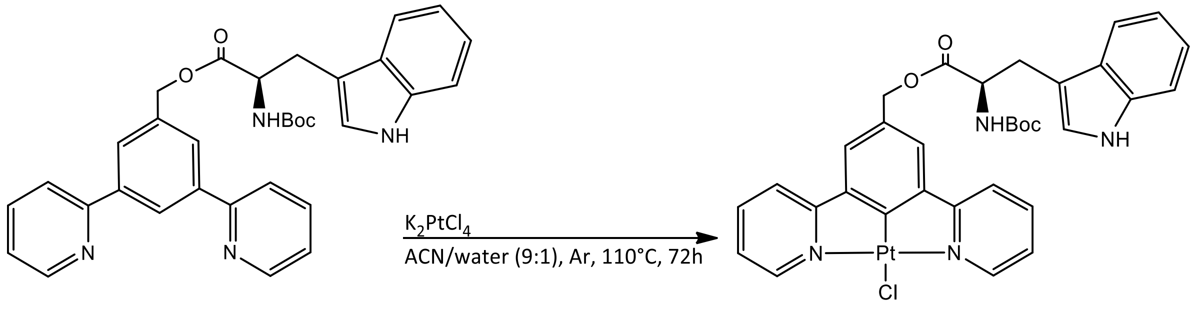

28

Pt-10

Pt-10. A Schlenk tube was charged with **28** (55.2 mg, 0.09 mmol) dissolved in 9 mL of acetonitrile and with K_2PtCl_4 (40.6 mg, 0.1 mmol) solubilized in 1 mL of water. The reaction vessel was then filled with argon and a needle was inserted in the solvent in order to directly bubble Ar in the reaction mixture. After 40 min, the vessel was sealed and heated at reflux at 110°C for 72h. In the end, the reaction mixture was let cool. Afterwards, the brown solid was isolated after filtration through a nylon membrane filter and washed with water, MeOH and diethyl ether. The brown solid was then collected and dried (43 mg). **Yield:** 55%. Due to severe solubility issues in any solvent, it was not possible to obtain a clear NMR spectrum and to attribute the peaks.

2.6 Synthesis of a Pt complex for bioconjugation through modification of the N^C^N pincer

Bioconjugation provides an efficient way to selectively direct therapeutic agents inside specific organelles, a crucial feature for compounds used as emitters in the biological environment. Given these premises, a Pt(II) cyclometalated complex bearing an hydroxyl group on the backbone was designed and synthesized with the purpose to further functionalize it with a biologically relevant substrate.

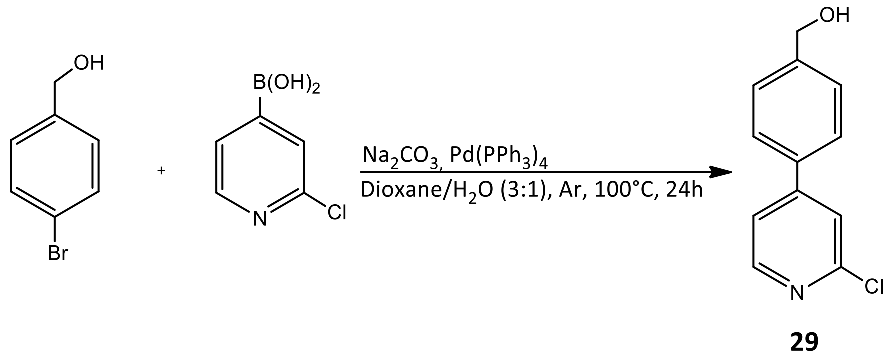

29

29. 2-chloro-pyridine-4-boronic acid (1.18 g, 7.5 mmol), p-Bromobenzylalcohol (1.00 g, 5.3 mmol), $Pd(PPh_3)_4$ (0.31 g, 0.3 mmol), Na_2CO_3 (1.70 g, 16.0 mmol) were placed in a Schlenk tube and solubilized in a mixture made of 8 mL of distilled water and 24 mL of 1,4-dioxane. The air was completely removed from the reaction vessel by vigorously bubbling argon for 10 min and it was finally sealed. The reaction mixture was then stirred and heated to reflux at 100°C overnight. The vessel was thus let cool to ambient temperature. The mixture was then acidified with HCl_{aq} and exctracted three times with 50 mL of ethyl acetate. The organic layer was separated and washed three times with 50 mL of water and 20 mL of brine. The solvent was finally dried over anhydrous $MgSO_4$ and evaporated under reduced pressure.

The crude was purified using silica gel chromatography (cyclohexane:AcOEt, 4:1, v/v) to obtain a colourless oil (287 mg). **Yield:** 24%. **^{1}H-NMR** (300 MHz, $CDCl_3$, δ): 8.44 (d, *J* = 5.2 Hz, 1H), 7.64 (d, *J* = 8.2 Hz, 2H), 7.48-7.59 (m, 3H), 7.45 (d, *J* = 5.2 Hz, 1H), 4.80 (d, *J* = 4.1 Hz, 2H), 1.64 (s, 1H). **^{13}C-NMR** (75.48 MHz, $CDCl_3$, δ): 152.2, 151.3, 150.1, 142.8, 136.2, 127.7, 127.2, 122.1, 120.4, 64.9. **HRMS (ASAP):** $(M+H)^+$ calcd for $C_{12}H_{11}NO^{35}Cl$, 220.0524; found: 220.0523.

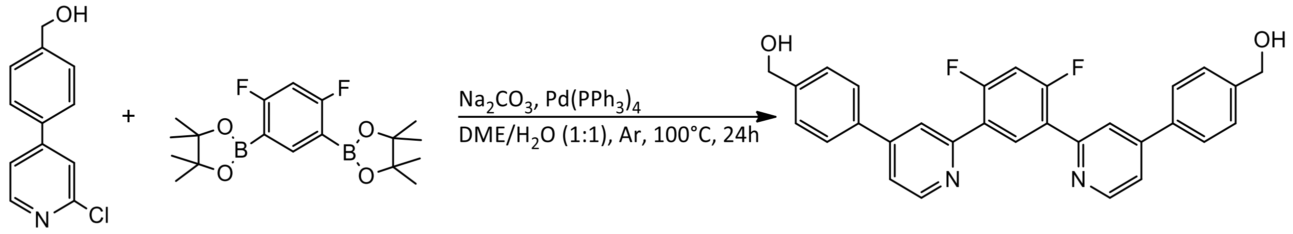

29

30

30. To a two neck round bottom flask, **29** (0.27 mg, 1.3 mmol), the pinacol ester of benzene-1,3-difluoro-4,6-diboronic acid (0.20 g, 0.6 mmol), an aqueous Na_2CO_3 solution (1M, 8 mL), $Pd(PPh_3)_4$ (0.11 g, 0.09 mmol) and 8 mL of DME, were added under an argon atmosphere. The air was fully removed by bubbling Ar for 20 min. The vessel was then sealed and heated to reflux at 100°C overnight. Upon cooling to ambient temperature, the reaction mixture was finally evaporated under reduced pressure and dissolved in a mixture of dichloromethane (30 mL) and water (20 mL). The organic phase was collected, dried over anhydrous $MgSO_4$, filtered and concentrated *in vacuo*. The crude was purified using silica gel chromatography (cyclohexane:AcOEt, 7:3, v/v) to obtain a colourless oil (53 mg). **Yield:** 19%. **^{1}H-NMR** (400 MHz, $CDCl_3$, δ): 8.77 (d, *J* = 5.1 Hz, 1H), 8.06 (dd, *J* = 15.5, 8.8 Hz, 1H), 7.98 (s, 1H), 7.71 (d, *J* = 8.1 Hz, 2H), 7.46-7.56 (m, 4H), 6.92-7.08 (m, 2H), 4.81 (s, 2H). **HRMS (ASAP):** $(M+H)^+$ calcd for $C_{18}H_{14}NOF_2$, 298.1038; found: 298.1043.

The NMR spectrum and the mass analysis highlighted the isolation of a deborylated species (**Figure 109**) as the major product of the coupling reaction. The procedure was attempted multiple times, leading to the formation of the aforementioned monosubstituted deborylated species.

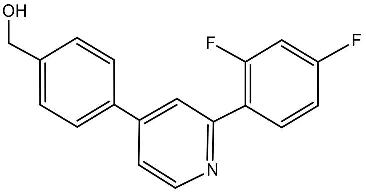

Figure 109. Molecular structure of the deborylated species.

2.7 Synthesis of the glucose conjugated Pt(II) complex

The synthetic route followed to achieve the synthesis of **Pt-11** relies on the procedures reported in literature. Specifically, the ligand's backbone assembly was performed through a Stille coupling, combining 3,5-dibromobenzyl alchol and 2-(tri-*n*-butylstannyl)pyridine.[106] The glucose moiety was prepared modifying 1,2-*O*-isopropylidene-α-D-glucofuranose to properly protect the sugar for the subsequent bioconjugation.[108]

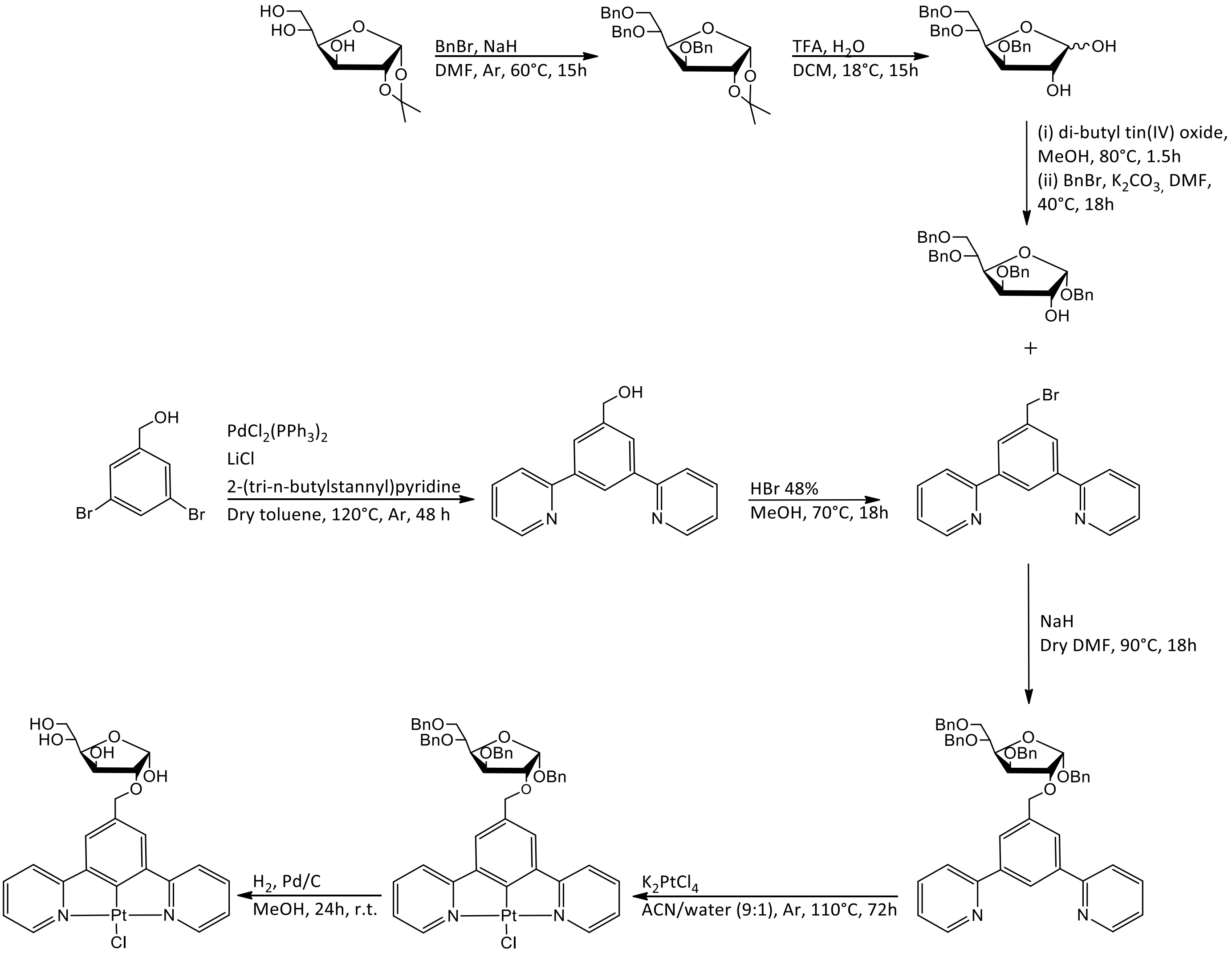

Pt-11

Scheme 6. Schematic illustration of the synthetic pathway followed to achieve the synthesis of the glucose-conjugated Pt(II) complex Pt-11.

2.7.1 Preparation of the glucose moiety

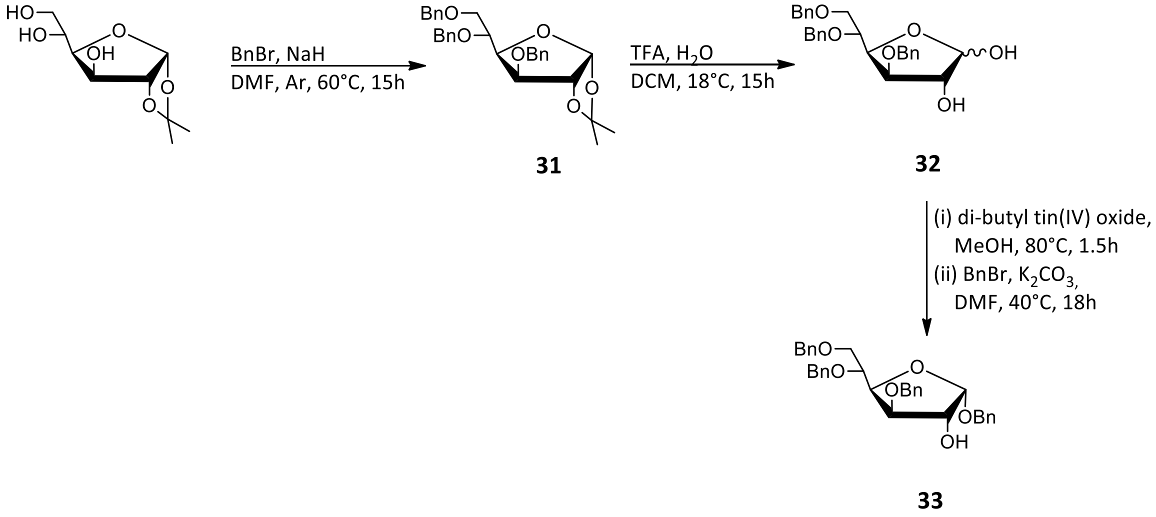

Scheme 7. General synthetic route for the glucose moiety preparation.

31. To a round bottom flask, under an argon atmosphere, 1,2-*O*-isopropylidene-α-D-glucofuranose (5.0 g, 22.7 mmol) was dissolved in 20 mL of anhydrous DMF and immersed in a water bath at room temperature. Then, small portions of NaH (2.75 g, 0.11 mol) were gradually added in the flask and let stir for 30 min. Once the evolution of H_2 was over, benzyl bromide (BnBr) (11.9 mL, 0.10 mol) was slowly injected and the reaction mixture was heated at 60°C overnight. Finally, the reaction was quenched adding ice-cold water and EtOAc (200 mL) was added. The solution was thus washed with water (6 x 100 mL) and brine (25 mL) and the organic phase separated, dehydrated over anhydrous Na_2SO_4, filtered and concentrated under reduced pressure.

The purification of the crude product was performed using a flash column chromatography packed with silica gel. The elution was carried out using a mixture of hexane:EtOAc, 9:1 to 7:3, v/v, to obtain a yellow oil (7.56 g). **Yield:** 67%. **^{1}H-NMR** (300 MHz, $CDCl_3$, δ): 7.19-7.44 (m, 15H), 5.93 (d, *J* = 3.8 Hz, 1H), 4.85 (d, *J* = 11.4 Hz, 1H), 4.58-4,71 (m, 4H), 4.52 (d, *J* = 11.2 Hz, 2H), 4.33 (dd, *J* = 9.3, 3.0 Hz, 1H), 4.04-4.17 (m, 2H), 3.94 (dd, *J* = 10.6, 1.9 Hz, 1H), 3.71-3.75 (m, 1H), 1.51 (s, 3H), 1.34 (s, 3H).

32. In a one neck round bottom flask, **31** (7.56 g, 15.4 mmol) was dissolved in 90 mL of dichloromethane and cooled down to 0°C in an ice-bath. Under stirring, 23.1 mL of trifluoroacetic acid were added in a dropwise manner and finally 1.9 mL of water were placed in the solution. The mixture was let react overnight at room temperature. Thus, the solution was concentrated under reduced pressure and the residue diluted in 100 mL of AcOEt. The organic phase was then neutralized with a saturated solution of $NaHCO_3$, washed twice with water (100 mL) and brine (50 mL), dehydrated over anhydrous $MgSO_4$, filtered and finally evaporated using a rotary evaporator. The purification was carried out using a silica gel flash column chromatography and a mixture of hexane:EtOAc, 2:1 to 1:3, v/v, as the eluent to obtain a colorless oil (3.75 g). **Yield:** 55%. **^{1}H-NMR** (300 MHz, $CDCl_3$, δ): 7.20-7.47 (m, 15H), 5.48 and 5.14 (d, *J* = 3.8 Hz, 1H), 4.74-4.89 (m, 1H), 4.33-4.69 (m, 6H), 3.86-4.24 (m, 6H), 3.67-3.83 (m, 1H).

33. In a two neck round bottom flask fitted with a magnetic stirrer, **32** (2.51 g, 5.6 mmol) dissolved in 60 mL of methanol and dibutyl-tin(IV) oxide (1.65 g, 6.6 mmol) were heated at 80°C for 1.5 h. Then, the clear solution was concentrated *in vacuo*. The residue was solubilized in 8 mL of dimethylformamide and K_2CO_3 (2.31 g, 16.7 mmol) and benzyl bromide (1.6 mL, 13.9 mmol) were added. The reaction mixture was heated at 40°C overnight. The white suspension was filtered through a filter paper under vacuum, a solid was isolated and washed with 2 mL of dichloromethane. The liquid phase was then filtered through a pad of celite to remove the finest impurities. Finally, the solvent was evaporated under reduced pressure. The crude product was purified through silica gel flash column chromatography eluting with hexane:EtOAc, 5:1 to 4:1, v/v, to obtain a colourless oil (2.14 g). **Yield:** 71%. **^{1}H-NMR** (300 MHz, $CDCl_3$): δ (ppm) 7.26-7.43 (m, 20H), 5.26 (d, *J* = 4,6 Hz, 1H), 4.67-4.90 (m, 4H), 4.49-4.66 (m, 5H), 4.34-4.44 (m, 1H), 4.23-4.33 (m, 1H), 4.01-4.14 (m, 2H), 3.87 (dd, *J* = 10.6, 2.0 Hz, 1H) 3.66-3.77 (m, 1H).

2.7.2 Synthesis of the cyclometalated Pt(II) pincer

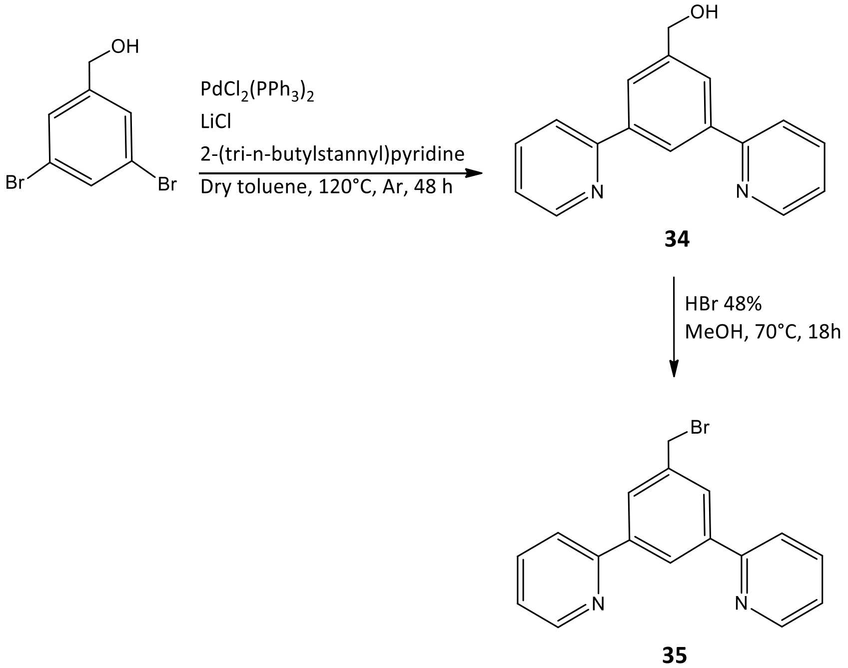

Scheme 8. General scheme for the preparation of the Pt pincer.

34. 3,5-dibromobenzyl alcohol (1.14 g, 4.3 mmol), 2-(tri-*n*-butylstannyl)pyridine (3.79 g, 10.3 mmol), $PdCl_2(PPh_3)_2$ (0.18 g, 0.3 mmol), and LiCl (3.29 g, 77.5 mmol) were placed in a two neck round-bottomed flask under argon. Then, 10.9 mL of anhydrous toluene were added and the mixture was deaerated bubbling argon inside the solution for 30 min. The vessel was finally sealed and heated under reflux at 120°C for 48 hours. The mixture was then let cool to room temperature and a saturated solution of KF (2 mL) was added. The suspension was stirred for an hour and then filtered on a pad of celite. Finally, the mixture was extracted with ethyl acetate (3 x 30 mL). The collected fractions were dried over $MgSO_4$, filtered and evaporated *in vacuo*.

The crude product was purified through silica gel flash chromatography, using a mixture of cyclohexane:AcOEt, 9:1 to 1:1, (v/v,) as the eluent. The desired compound was obtained as a colourless oil (641 mg). **Yield:** 65%. **^{1}H-NMR** (300 MHz, $CDCl_3$, δ): 8.69 (m, 2H), 8.47 (t, *J* = 1.6 Hz, 1H), 7.99 (d, *J* = 1.6 Hz, 2H), 7.71-7.82 (m, 4H), 7.21-7.29 (m, 2H), 4.81 (s, 2H), 2.05 (s, 1H). **^{13}C-NMR** (75.48 MHz, $CDCl_3$, δ): 157.1, 149.7, 142.2, 140.3, 136.9, 126.0, 124.8, 122.4, 120.9, 65.3. **HRMS (ESI+):** $(M+Na)^+$ calcd for $C_{17}H_{14}N_2ONa$, 285.0998; found: 285.1001.

35. In a Schlenk tube, **34** (70 mg, 0.27 mmol) was dissolved in 2 mL of MeOH. Then, 2.1 mL of a 48% HBr solution in water was added and the solution was let stir at 70°C for 18 hours. The mixture was then concentrated *in vacuo*. The residue was thus taken up in DCM and the precipitation of a white solid was assessed. The suspension was sonicated, filtered and the procedure was then repeated in order to remove the impurities from the white solid. The white solid was finally collected, dried under vacuum and used without any further purification (81 mg). **Yield:** 94%. **^{1}H-NMR** (300 MHz, $CDCl_3$, δ): 8.87 (m,2H), 8.57-8.72 (m, 1H), 8.20-8.49 (m, 6H), 7.56-7.86 (m, 2H), 4.74 (s, 2H).

2.7.3 Glucose appendage

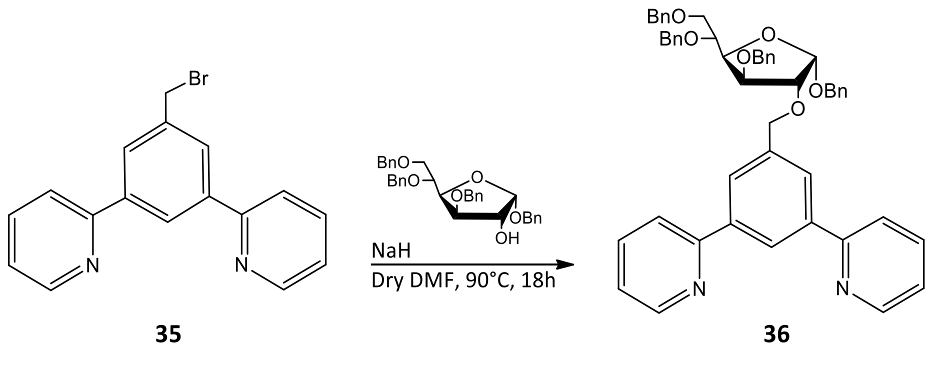

35 **36**

36. In a Schlenk tube filled with Ar, **33** (0.26 g, 0.47 mmol) was dissolved in 6 mL of dry DMF. Then, NaH (28.5 mg, 1.19 mmol), was added and the reaction mixture was let stir for 30 min. In the end, **35** (96.1 mg, 0.3 mmol) was solubilized in the deaerated solution and it was heated at 90°C for 18h. Upon cooling to room temperature, the solvent was evaporated *in vacuo*. The residue was taken up in DCM (20 mL) and washed three times with 15 mL of brine. The collected organic fraction was dried over anhydrous $MgSO_4$, filtered and concentrated under reduced pressure.

The crude product was purified through silica gel chromatography, using a mixture of cyclohexane:AcOEt, 8:2, v/v, as the eluent to obtain a colourless oil (161 mg). **Yield:** 69%. **^{1}H-NMR** (300 MHz, $CDCl_3$, δ): 8.73 (d, *J* = 4.6 Hz, 2H), 8.61 (s, 1H), 8.08 (s, 2H), 7.69-7.86 (m, 26H), 5.17 (d, *J* = 4.2 Hz, 1H), 4.74-4.86 (m, 3H), 4.62-4.72 (m, 2H), 4.51-4.62 (m, 5H), 4.41-4.50 (m, 1H), 4.33-4.40 (m, 1H), 4.01-4.12 (m, 2H), 3.86 (dd, *J* = 10.5, 1.7 Hz, 1H) 3.66-3-76 (m, 1H). **^{13}C-NMR** (75.48 MHz, $CDCl_3$, δ): 156.9, 149.6, 140.1, 139.0, 138.7, 138.0, 137.7, 136.7, 128.3, 128.2, 128.2, 128.2, 128.0, 127.6, 127.6, 127.5, 127.5, 127.5, 127.3, 127.3, 126.9, 125.0, 122.3, 120.8, 99.4, 84.0, 82.2, 73.4, 72.5, 72.4, 72.2, 71.4, 69.5, 31.7, 30.0, 29.7.

2.7.4 Synthesis of the Pt(II) complex

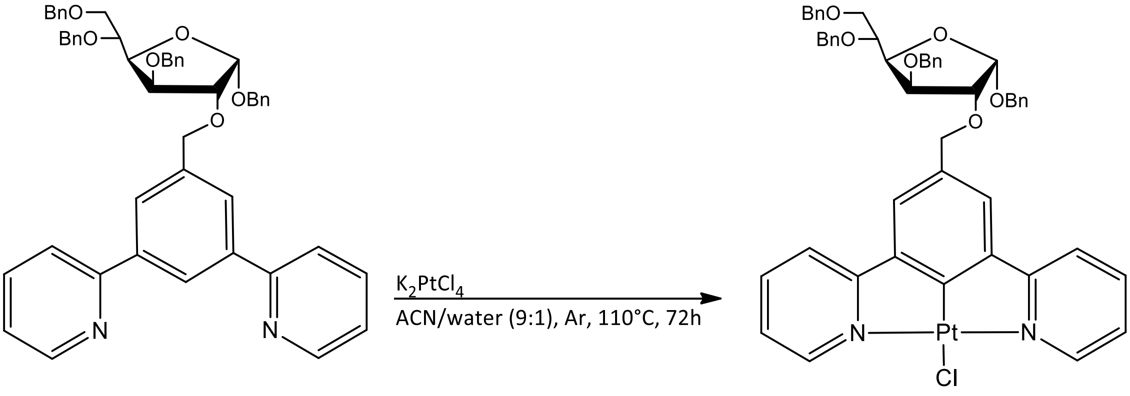

36 **37**

37. A Schlenk tube was charged with **36** (55.2 mg, 0.07 mmol) dissolved in 9 mL of acetonitrile and with K_2PtCl_4 (58.4 mg, 0.1 mmol) solubilized in 1 mL of water. The reaction vessel was then filled with argon and a needle was inserted in the solvent in order to directly bubble Ar in the reaction mixture. After 40 min, the vessel was sealed and heated at reflux at 110°C for 72h. In the end, the reaction mixture was let cool to room temperature and evaporated under reduced pressure. Afterwards, the thus obtained red residue was taken up with DCM and a colourless solid precipitated. The solid was thus filtered off and the solvent concentrated *in vacuo*. ^{1}H-NMR spectrum highlighted the formation of the desired Pt(II) complex, despite the presence of impurities. Various techniques to remove the impurities were attempted, but **37** couldn't be isolated as a pure compound.

Given the difficulties encountered in the context of purification of **37** and in the benzyl removal step, the synthesis of **Pt-11** couldn't be achieved.

3. X- Ray analysis

3.1 X-ray analysis of Pt-1

The crystallization **of Pt-1** (**Figure 110**) was achieved dissolving the powdery complex into diethyl ether and allowing the crystals to form through controlled slow evaporation of the solvent. The structure's parameters were determined performing the X-ray analysis on a yellow needle shaped crystal of dimensions 0.48 mm x 0.30 mm x 0.15 mm using a D8 VENTURE Bruker AXS diffractometer, Mo-Kα radiation ($\lambda = 0.71073$ Å), T = 150 K.

The structure was solved employing the SHELTS program[154] and subsequently refining with full-matrix least-squares methods based on F^2 (SHELXL).[155]

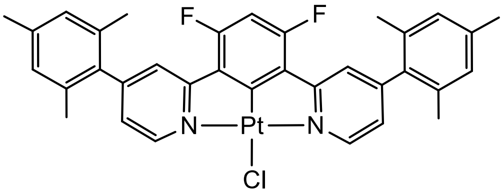

Pt-1

Figure 110. Molecular structure of Pt-1.

The collected data for ($C_{34}H_{29}ClF_2N_2Pt \bullet 2(CH_2Cl_2)$), M: 903.98 g/mol, are reported: orthorhombic, P b c a, where a = 32.569(3) Å, b = 6.6720(6) Å, c = 33.849(3) Å, α = 90°, β = 90°, γ = 90°, V = 7355.2(12) Å^3.

Z = 8, d = 1.633 g·cm^{-3}, $\mu = 4.217$ mm^{-1}. Anisotropic atomic displacement parameters were used to refine non-hydrogen atoms. H atoms were then included on the basis of their calculated positions. A final refinement on F^2 with 8431 unique intensities and 421 parameters converged at $\omega R(F^2) = 0.0684$ ($R(F) = 0.0323$) for 7255 observed reflections with $I > 2\sigma(I)$.

The supplementary crystallographic data are reported free of charge by The Cambridge Crystallographic Data Centre (**CCDC number:** 2087750).

The X-ray analysis highlighted the twisted configuration of the sterically hindered mesityl groups with respect to the molecular plane. Specifically, a torsion angle of 61.7° was measured. The crystalline structure of **Pt-1** is depicted in **Figure 111.**

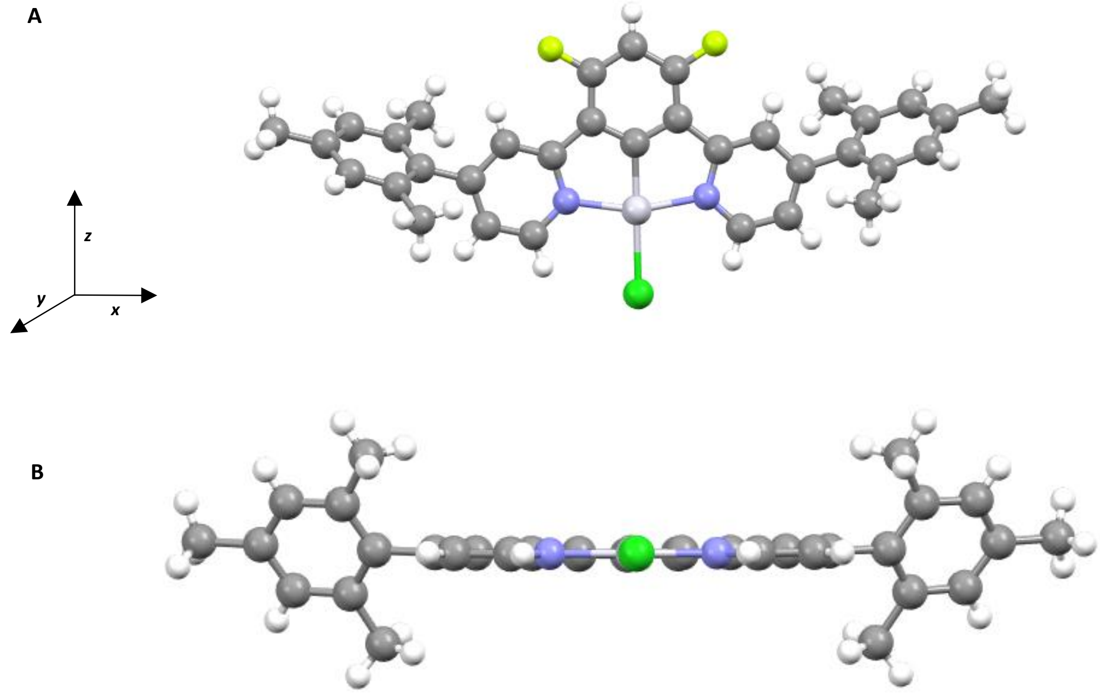

Figure 111. A) X-ray structure of Pt-1 embedded in needle crystals. B) Frontal view of Pt-1. Pt-1 with the molecular plane lying on the xy plane to highlight the orientation of the mesityl groups.

The summarized crystal data collected are reported in **Table 4**.

Table 4. Crystallographic data collected for Pt-1.

CCDC number: 2087750	
Empirical formula	$C_{34}H_{29}ClF_2N_2Pt\cdot 2(CH_2Cl_2)$
Formula weight	903.98 g/mol
Temperature	150 K
Wavelength	0.71073 Å
Crystal system, space group	Orthorhombic, P b c a
Unit cell dimensions	a = 32.569(3) Å, α = 90
	b = 6.6720(6) Å, β = 90

	c = 33.849(3) Å, γ = 90
Volume	7355.2(12) Å^3
Z	8
Calculated density	1.633 g.cm^{-3}
Absorption coefficient	4.217 mm^{-1}
F(000)	3552
Crystal size	0.480 x 0.300 x 0.15 mm
Theta range for data collection	2.501 to 27.508
Limiting indices	$-42 \leq h \leq 42$, $-8 \leq k \leq 8$, $-43 \leq l \leq 39$
Reflections collected / unique	55960 / 8431 [R(int)[a] = 0.0394]
Reflections [I>2σ]	7255
Completeness to theta max	0.996
Absorption correction	Multi-scan
Max. and min. transmission	0.531, 0.278
Refinement method	Full-matrix least-squares on F^2
Data / restraints / parameters	8431 / 0 / 421
Goodness-of-fit on F^2	1.103
Final R indices [I>2σ]	R1[c] = 0.0323, wR2[d] = 0.0684
R indices (all data)	R1[c] = 0.0417, wR2[d] = 0.0723
Largest diff. peak and hole	1.517 and -1.306 e$^-$.Å^{-3}

Bond lengths [Å], bond and torsion angle [°] measurements are provided in **Table 5**.

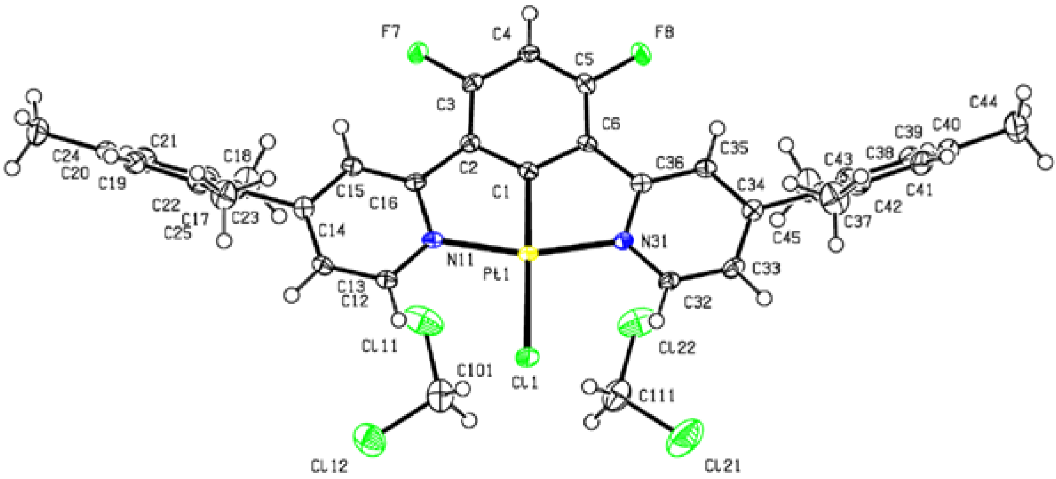

Table 5. Bond lengths [Å], bond and torsion angle [°] of Pt-1.

Bond distance [Å]		Bond angle [°]	
Pt(1)-C(1)	1.918(3)	N(11)-Pt(1)-N(31)	161.92(12)
Pt(1)-N(11)	2.024(3)	C(1)-Pt(1)-Cl(1)	179.56(11)
Pt(1)-N(31)	2.027(3)	C(1)-Pt(1)-N(11)	80.72(13)
Pt(1)-Cl(1)	2.391(9)	C(1)-Pt(1)-N(31)	81.20(13)
		N(11)- Pt(1)- Cl(1)	99.03(9)
		N(31)- Pt(1)- Cl(1)	99.05(9)
		C(15)-C(14)-C(17)-C(18)	61.7(5)
		C(35)-C(34)-C(37)-C(38)	-60.8(5)

4. Thin film preparation

4.1 Pt-1

The unique photoluminescent properties displayed by **Pt-1** (**Figure 112**) prompted us to perform further investigations concerning the emission in the solid state. In particular, the complex was embedded in a thin poly(methylmethacrylate) (PMMA) matrix and deposited on a slide of glass through the spin-coating process.

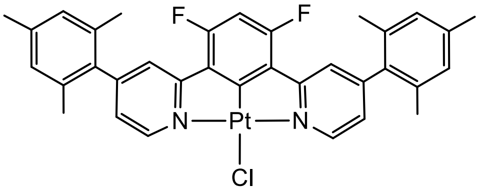

Pt-1

Figure 112. Molecular structure of Pt-1.

Spin-coating provides a useful technique for the formation of thin and homogeneous layers. Spin-coating involves the spreading of the enriched-matrix exploiting the centrifugal force arising from high-speed rotation, with a concomitant evaporation of the volatile solvent chosen for the preparation of the polymeric solution. The representation of the technique steps are depicted in **Figure 113.**

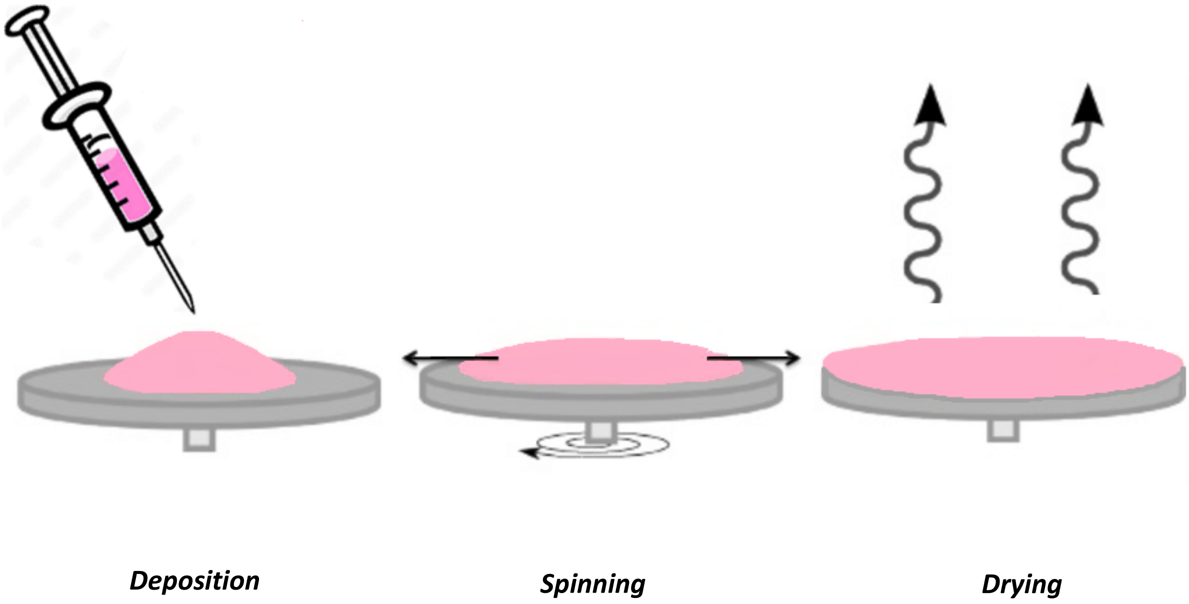

Figure 113. Schematic illustration of spin coating technique steps.

Photophysical analysis performed on this typology of matrixes indeed require high uniformity in the context of thickness and surface roughness. In addition, PMMA offers a suitable polymer for the purpose conferring thermal and photostability to the embedded emitter.[156]

Overall, the combination of the spin-coating technique with the PMMA matrix allows to perform repeatable measurements.

The preparation of the thin film was carried out dissolving PMMA and **Pt-1** (w/w 1% with respect to the polymeric matrix) in dichloromethane. **Pt-1** displayed a limited solubility, thus it was not possible to further increase the concentration of the emitter in the layer. The parameters set for the spin-coating are listed below:

- RPM1 = 800; ramp1 = 1 s; time1 = 5 s;
- RPM2 = 2000; ramp2 =1 s; time2 = 60 s.

The thus obtained film was characterized by profilometry using an α-step stylus profilometer Bruker DektakXT. The thickness resulted to be equal to 2.49 ± 0.15 µm.

The photophysical data were collected irradiating at different wavelengths comprised in the range of 280-437 nm (**Figure 114**). Electronic absorption spectra were recorded using a Shimadzu UV3600 spectrophotometer. Steady state emission, excitation spectra and photoluminescence lifetimes were obtained with a FLS 980 spectrofluorometer (Edinburg Instrument Ltd.).

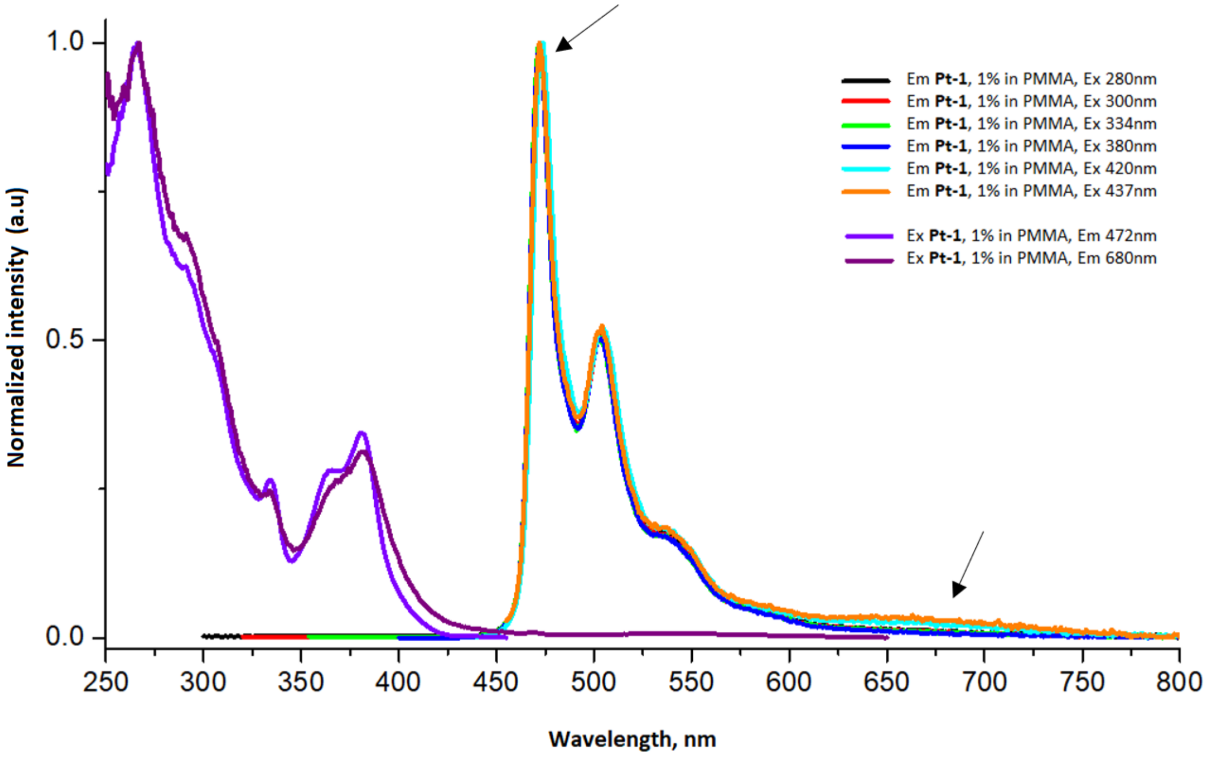

Figure 114. UV-Vis absorption and emission spectra collected for Pt-1 embedded in the PMMA matrix.

The emission spectra highlights that the peaks arising from the excitation of the fluorophore in a wide range of wavelengths are substantially overlapping, except for the broad band observed around 600-750 nm, which visibly increases along with the wavelength of excitation. Specifically, the intense sharp peak observed at λ = 472 nm results as a consequence of the radiative decay of the monomers, whilst the broad signal at longer wavelengths can be attributed to the excimer emission.

Indeed, the excitation of the emitter induced irradiating at 420 and 437 nm provokes the direct excitation of the dimer (M_1M_2) to $^3(M_1M_2)^*$. Nevertheless, the dimer could even be obtained as a consequence of the energy transfer initiated from the excited monomer (M_1) following the scheme reported below:

$$h\nu_{\text{exc}} + \mathrm{M}_1 \rightarrow {}^1\mathrm{M}_1^* \rightarrow {}^3\mathrm{M}_1^*$$

$$\downarrow$$

$${}^3\mathrm{M}_1^* + (\mathrm{M}_1\mathrm{M}_2) \rightarrow {}^3(\mathrm{M}_1\mathrm{M}_2)^*$$

Relying on the calculated energy of the singlet and triplet transitions and on the data collected through X-ray analysis of the monomeric complex, the theoretical structure of the dimer was hypothesized (**Figure 115**).

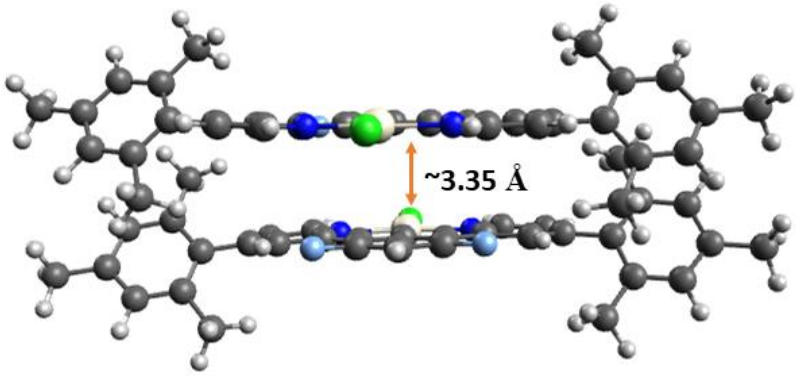

Figure 115. Dimer theoretical structure.

Remarkably, the emitter embedded in the PMMA layer displays an optimal quantum yield (Φ_{lum}: 95.4%), measured with a C11347 Quantaurus Hamamatsu Photonics K.K.

The collected data concerning the life-time of the excited state was also investigated at various wavelength of excitation (Ex) and wavelength of emission (Em) (**Table 6**).

Table 6. Life-time of the excited state measured for Pt-1 embedded in the PMMA matrix.

Wavelength Ex (nm)	**Wavelenght Em (nm)**	τ (μs)
374	472	3.52
374	680	2.50
437	680	1.78

The spin-coating was also performed on a quartz plate, depositing an enriched 50 ± 3 nm layer of PMMA.

The photoluminescent properties were assessed, recording the absorption and emission spectra, where a significant difference is evident: the emission is centred at λ = 671 nm, represented by a single broad structureless peak as displayed in **Figure 116.**

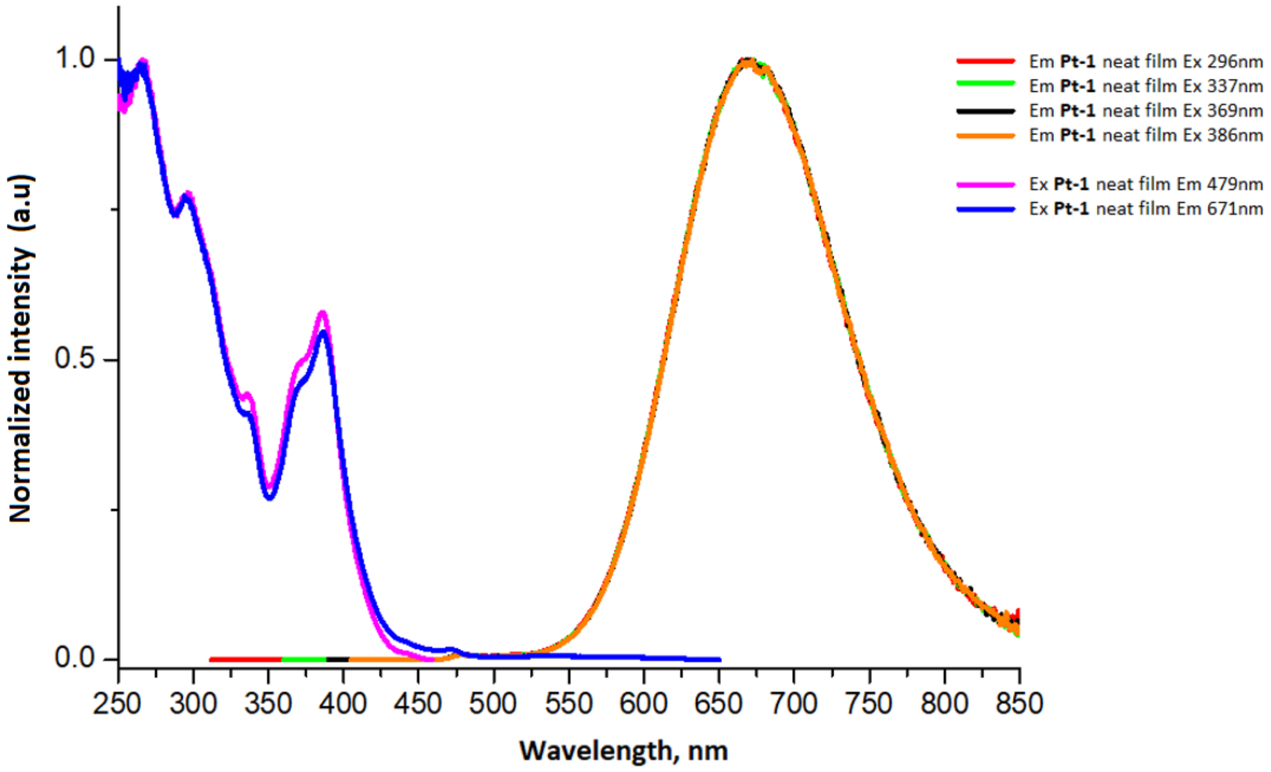

Figure 116. UV-Vis absorption and emission spectra collected for Pt-1 embedded in the neat film.

Indeed, the decreased thickness of the layer promotes the formation of dimers thus, the intense emission observed is related to their direct excitation and consequent radiative decay. On the other hand, the emission of the monomer which was centred at λ = 472 nm in the thin layer deposition is not visible anymore.

Furthermore, the value of the quantum yield appears to be decreased (Φ_{lum}: 72.4%) with respect to the previously investigated layer. Concerning the lifetime of the excited state, the value measured at the maximum of the emission (λ = 671 nm) induced irradiating at λ = 374 nm is equal to τ = 1473.30 ns.

4.2 Pt-5

A thin film with **Pt-5** in a PMMA matrix on a quartz substrate was prepared to fully characterize the photophysical properties of the highly hindered Pt(II) based emitter. Specifically, **Pt-5** (w/w 0.5 % with respect to the polymeric matrix) and PMMA were dissolved in dichloromethane, in order to perform spin coating setting the aforementioned parameters listed in paragraph 4.1.

Due to **Pt-5** limited solubility, higher concentrations of the phosphor couldn't be embedded in the matrix. The thus prepared thin film was measured through profilometry using an α-step stylus profilometer Bruker DektakXT. The thickness resulted to be equal to 1.97 ± 0.12 µm.

Photophysical analysis were performed upon excitation in the 300-480 nm range. The gradual increase of the wavelength of excitation provokes a slight red shift in the wavelength of emission, with the concomitant formation of a broad structureless band arising at λ = 700 nm (**Figure 117**). The latter is attributable to the direct excitation of bimolecular species, whereas the observed shift is caused by the presence of aggregates.

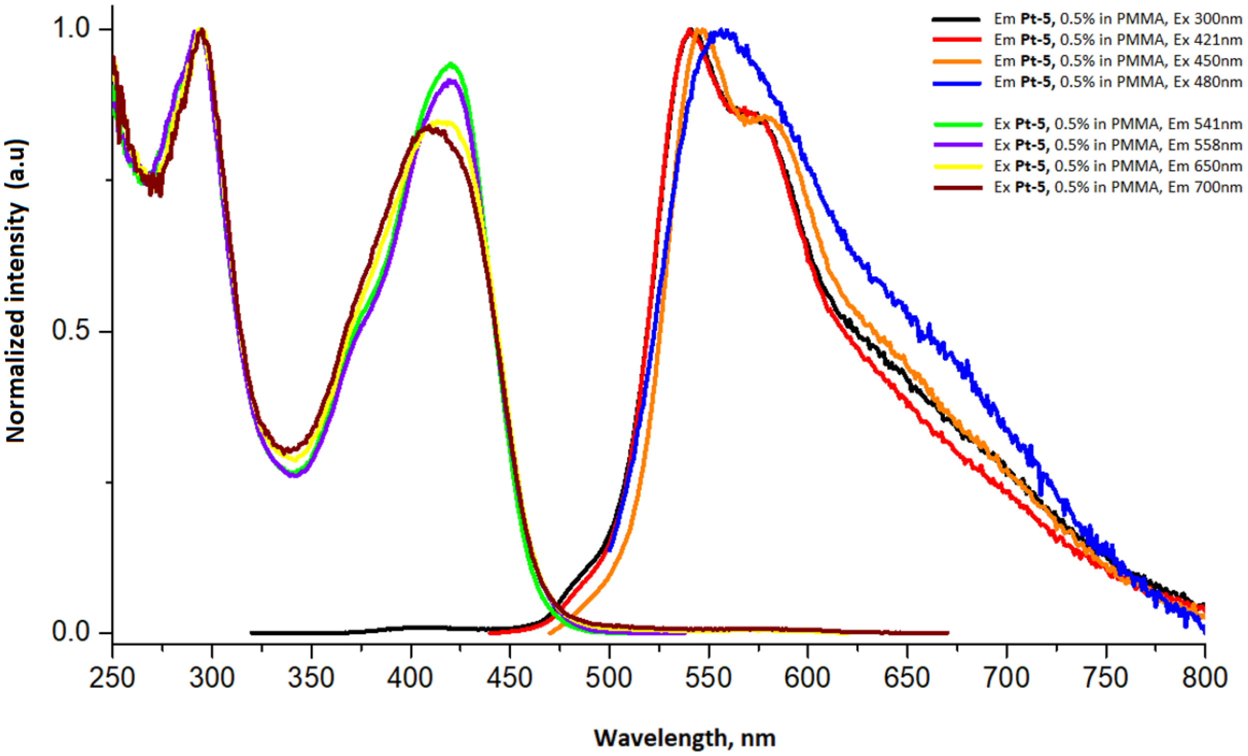

Figure 117. UV-Vis absorption and emission spectra collected for Pt-5 embedded in the PMMA matrix.

The quantum yield associated to the radiative decay is Φ_{lum}: 55.6%. Additionally, the investigation concerning the life-time of the excited state at different wavelengths of emission was carried out (**Table 7**).

Table 7. Life-time of the excited state measured for Pt-5 embedded in the PMMA matrix.

Wavelength Ex (nm)	Wavelenght Em (nm)	τ (μs)
422	541	34.9
422	700	20.8

Pt-5 was further investigated embedding the emitter in a neat film deposited on a quartz substrate through physical vapour deposition (PVD). The profilometry measurement performed on the film evidenced a thickness of 50 ± 3 nm.

Upon irradiation with various wavelengths, the recorded emission spectra highlighted the presence of an intense peak at λ = 700 nm, attributable to the aggregates radiative decay (**Figure 118**). In contrast to the previously discussed data collected for the thicker layer, the monomeric emission could not be observed. This evidence could be explained considering the limited width of the layer, which forces the Pt(II) emitters to be packed in a closer configuration, promoting bimolecular species formation and a consequent a decrease in the life-time of the excited state (τ = 313.81 ns).

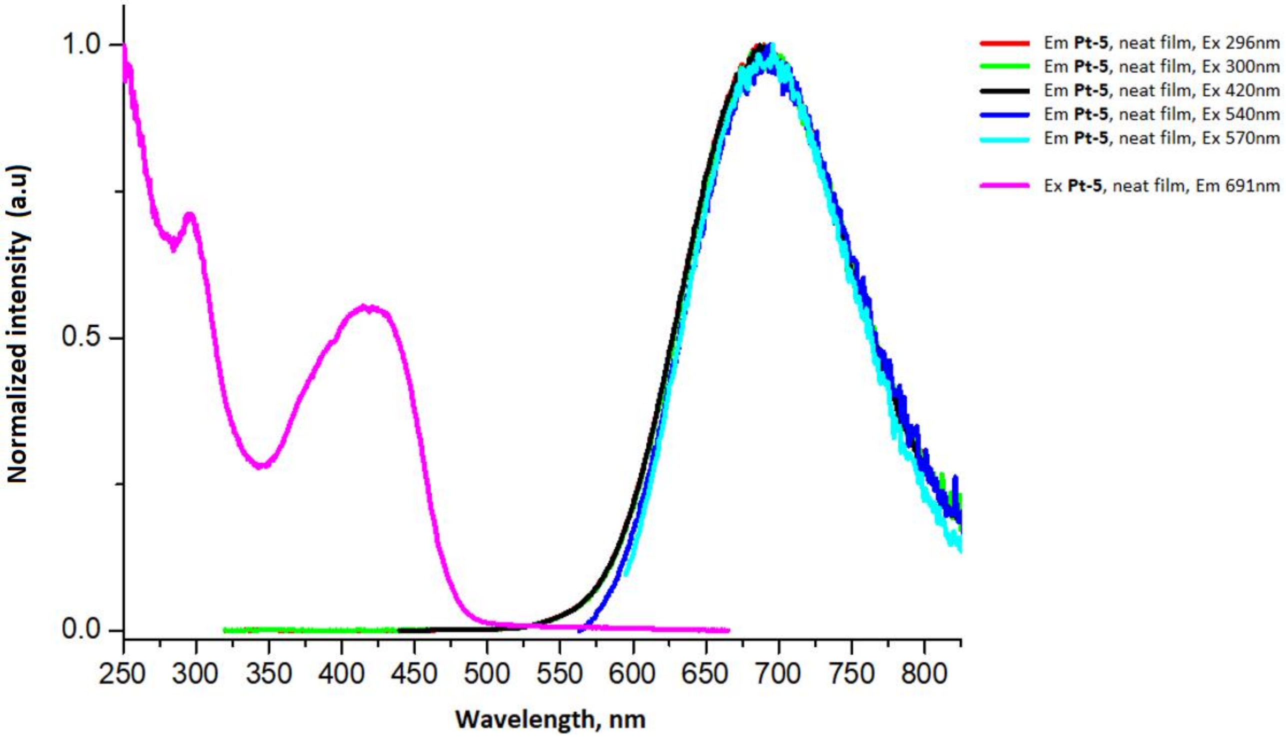

Figure 118. UV-Vis absorption and emission spectra collected for Pt-5 embedded in the neat film.

Chapter IV – Conclusion

The project I carried out during my PhD focused on the design, synthesis and photophysical characterization of Pt and Ir based emitters for life science and OLEDs application.

The remarkable photophysical properties displayed by cyclometalated Pt(II) and Ir(III) complexes encouraged the development of innovative variously functionalized luminophores.

Specifically, a series of sterically hindered Pt(II) emitters bearing the 1,3-di-(2-pyridyl)benzene pincer were synthesized, aiming to enhance the efficiency of the related previously investigated compounds.

For the purpose, bulky aryl substituents were introduced on the 4-position of the pyridyl rings in order to prevent aggregation between neighbouring chromophore, which is usually responsible for excitation energy loss. The photophysical analysis performed in solution highlighted outstanding results. In particular, quantum yields ranging from 130% to 200% were assessed. In literature, similar results have never been reported for N^C^N complexes. Given the collected data, **Pt-1** and **Pt-5** were embedded in the emissive layer of OLEDs devices, with the purpose to evaluate their structural features influence on electroluminescent phenomena. Overall, the fabricated devices displayed a promising response to the applied bias, resulting in efficient and versatile devices. Indeed, the color of emission can be easily tuned both through the modification of the emitters scaffold and through the doping level variation. In this context, the development of a WOLED device was achieved with **Pt-1**, exploiting the combined monomer and excimer emission.

Given the remarkable results, the photophysical properties of the complexes will be evaluated in the biological environment with the purpose to assess their efficiency as luminescent labels for bioimaging and as photosensitizers for photodynamic therapy. Specifically, the assays will be carried out in brain cells.

In the context of life science applications, a crucial feature besides the excellent photophysical properties, is represented by the possibility to selectively address the emitter inside specific cells or cellular components.

Thus, the appendage of biologically relevant substrate onto the organic backbone of the luminophore provides a great strategy to achieve this goal. For the purpose, the overexpression of GLUT1 and LAT1 transporters in tumorigenesis was exploited, thus glucose and tryptophan conjugated Pt and Ir based complexes were synthesized.

A series of tryptophan conjugated Ir(III) emitters bearing various cyclometalated ligands in the coordination sphere were synthesized and extensively characterized. Among the evaluated luminophores, **Ir-3** displayed the most promising photophysical properties in dichloromethane solution, with a quantum yield close to unity. Biological assays in brain cells are still in progress.

Finally, a Pt(II) and an Ir(III) complex purposely designed for further functionalization with a targeting vector were synthesized. In this context, the hydroxymethyl moiety was introduced in the backbone as an anchoring group. Specifically, for the Pt complex the key feature was inserted on the ancillary ligand through exchange of the chlorine atom previously completing the coordination sphere. The extensive photophysical investigations in solution and in the biological environment are still in progress.

In conclusion, the versatile nature of the cyclometalated Pt(II) and Ir(III) luminophores has been confirmed in the developed project. Furthermore, new frontiers have been opened up concerning the ability of sterically hindered Pt based emitters to exceed the quantum yield theoretical limit of 100%.

Chapter V – Bibliography

[1] Vander Heiden, M. G. *Nat. Rev. Drug Discov.*, 2011, **10**, 671-684.

[2] Warburg, O.; Wind, F.; Negelein, E. *J. Gen. Physiol*., 1927, **8**, 519-530.

[3] Liu, P.; Lu, Y.; Gao, X.; Liu, R.; Zhang-Negrerie, D.; Shi, Y.; Wang, Y.; Wang, S.; Gao, Q. *Chem. Commun.,* 2013, **49**, 2421-2423.

[4] Wolf, H. *Scand. J. Clin. Lab. Invest. Suppl.*, 1974, **136**, 1-186.

[5] Hiraoka, N.; Toue, S.; Okamoto, C.; Kikuchi, S.; Ino, Y.; Yamazaki-Itoh, R.; Esaki, M.; Nara, S.; Kishi, Y.; Imaizumi, A.; Ono, N.; Shimada, K. *Sci Rep.*, 2019, **9**, 9816-9829.

[6] Pawlicki, M.; Collins, H. A.; Denning, R. G.; Anderson, H. L. *Angew. Chem. Int. Ed.,* 2009, **48**, 3244-3266.

[7] Murphy, L.; Brulatti, P.; Fattori, V.; Cocchi M.; Williams, J. A. G. *Chem. Commun.*, 2012, **48**, 5817-5819.

[8] Atkins, P. W.; Friedman, R. S. Molecular Quantum Mechanics, *Oxford University Press*, 1999.

[9] Woolley, R.G.; Sutcliffe, B.T. Chem. Phys. Lett., 1977, **45**, 393-398.

[10] Schulman, S. G. Fluorescence and phosphorescence spectroscopy: physicochemical principles and practice, *Elsevier*, 2017.

[11] Vitha, M. F. Spectroscopy: Principles and Instrumentation, *John Wiley & Sons*, 2018.

[12] Omary, M. A.; Patterson, H. H. *Encyclopedia of Spectroscopy and Spectrometry (Third Edition)*, 2017, 636-653.

[13] Yersin, H.; Rausch, A. F.; Czerwieniec, R.; Hofbeck, T.; Fischer, T. *Coord. Chem. Rev.*, 2011, **255**, 2622-2652.

[14] Zhao, Q.; Huang, C; Li, F. *Chem. Soc. Rev.*, 2011, **40**, 2508-2524.

[15] Garbe, S.; Krause, M.; Klimpel, A.; Neundorf, I.; Lippmann, P.; Ott, I.; Brünink, D.; Strassert, C. A.; Doltsinis, N. L.; Klein, A. *Organometallics*, 2020, **39**, 746-756.

[16] Malicka, J. M.; Fattori, V.; Cocchi, M.; Colombo, A.; Dragonetti, C.; Murphy, L.; Williams, J. A. G. *Fotonica AEIT Italian Conference on Photonics Technologies*, 2014, 1-3.

[17] Williams, J. A. G. *Top. Curr. Chem*., 2007, **281**, 205-268.

[18] Li, K.; Tong, G. S. M.; Wan, Q.; Cheng, G.; Tong, W. Y.; Ang, W. H.; Kwong, W. L.; Che, C. M. *Chem. Sci.*, 2016, **7**, 1653-1673.

[19] Tong, G. S. M.; Che, C. M. *Chem. Eur. J.*, 2009, **15**, 7225-7237.

[20] Mauro, M.; Aliprandi, A.; Septiadi, D.; Kehra, N. S.; De Cola, L. *Chem. Soc. Rev.*, 2014, **43**, 4144-4166.

[21] Huo, S.; Carroll, J.; Vezzu, D. A. *Asian J. Org. Chem.*, 2015, **4**, 1210-1245.

[22] Wilson, M. H.; Ledwaba, L. P.; Field, J. S.; McMillin, D. R. *Dalton Trans*., 2005, **16**, 2754-2759.

[23] Connick, W. B.; Marsh, R. E.; Schaefer, W. P.; Gray, H. B. *Inorg. Chem.,* 1997, **36**, 913-922.

[24] Botchway, S. W.; Charnley, M.; Haycock, J. W.; Parker, A. W.; Rochester, D. L.; Weinstein, J. A.; Williams, J. A. G. *PNAS*, 2008, **105**, 16071-16076.

[25] Cocchi, M.; Virgili, D.; Fattori, V.; Rochester, D. L.; Williams, J. A. G. *Adv. Funct. Mater.*, 2007, **17**, 285–289.

[26] Càrdenas, D. J.; Echavarren, A. M.; Ramìrez de Arellano, M. C. *Organometallics*, 1999, **18**, 3337-3341.

[27] Rausch, A. F.; Murphy, L.; Williams, J. A. G.; Yersin, H. *Inorg. Chem.*, 2009, **48**, 11407-11414.

[28] Rossi, E.; Colombo, A.; Dragonetti, C.; Righetto, S.; Roberto, D.; Ugo, R.; Valore, A.; Williams, J. A. G.; Lobello, M. G.; De Angelis, F.; Fantacci, S.; Ledoux-Rak, I.; Singh, A.; Zyss, J. *Chem. Eur. J.*, 2013, **19**, 9875-9883.

[29] Colombo, A.; Fiorini, F.; Septiadi, D.; Dragonetti, C.; Nisic, F.; Valore, A.; Roberto, D.; Mauro, M.; De Cola, L. *Dalton Trans.*, 2015, **44**, 8478-8487.

[30] Lamansky, S.; Djurovich, P.; Murphy, D.; Abdel-Razzaq, F.; Kwong, R.; Tsyba, I.; Bortz, M.; Mui, B.; Bau, R.; Thompson, M. E. *Inorg. Chem.*, 2001, **40**, 1704-1711.

[31] Ohsawa, Y.; Sprouse, S.; King, K. A.; DeArmond, M. K.; Hanck, K. W.; Watts, R. J. *J. Phys. Chem.*, 1987, **91**, 1047-1054.

[32] Baggaley, E.; Weinstein, J. A.; Williams, J. A. G. *Coord. Chem. Rev.*, 2012, **256**, 1762-1785.

[33] Ladouceur, S.; Fortin, D.; Zysman-Colman E. *Inorg. Chem.*, 2010, **49**, 5625–5641.

[34] Ladouceur, S.; Zysman-Colman, E. *Eur. J. Inorg. Chem.*, 2013, **17**, 2985-3007.

[35] Zhao, Q.; Liu, S.; Shi, M.; Wang, C.; Yu, M.; Li, L.; Li, F.; Yi, T.; Huang, C. *Inorg. Chem*., 2006, **45**, 6152-6160.

[36] Colombo, M. G.; Hauser, A.; Güdel, H. U. *Inorg. Chem*., 1993, **32**, 3088-3092.

[37] Costa, R. D.; Ort, E.; Bolink, H. J.; Monti, F.; Accorsi, G.; Armaroli, N. *Angew. Chem. Int. Ed.*, 2012, **51**, 8178-8211.

[38] Mandal, S.; Poria, D. K.; Ghosh, R.; Ray, P. S.; Gupta, P. *Dalton Trans.*, 2014, **43**, 17463-17474.

[39] Lamansky, S.; Djurovich, P.; Murphy, D.; Abdel-Razzaq, F.; Kwong, R.; Tsyba, I.; Bortz, M.; Mui, B.; Bau, R.; Thompson, M. E. *Inorg. Chem.*, 2001, **40**, 1704-1711.

[40] You, Y.; Cho, S.; Nam, W. *Inorg. Chem.,* 2014, **53**, 1804-1815.

[41] Sun, J.; Zhao, J.; Guo, H.; Wu, W. *Chem. Commun.*, 2012, **48**, 4169-4171.

[42] Monti, F.; Pavoni, E.; Armaroli, N. *NATO Science for Peace and Security Series B: Physics and Biophysics,* 2015, **68**, 373-414

[43] Steunenberg, P.; Ruggi, A.; Van den Berg, N. S.; Buckle, T.; Kuil, J.; Van Leeuwen, F. W. B.; Velders, A. H. *Inorg. Chem.*, 2012, **51**, 2105-2114.

[44] Lakowicz, J. R. *Fluorescence Sensing. In: Principles of Fluorescence Spectroscopy*, 2006, **19**, 623-673.

[45] Beeby, A.; Botchway, S.W.; Clarkson, I. M.; Faulkner, S.; Parker, A. W.; Parker, D.; Williams, J. A. G. *J. Photochem. Photobiol.*, 2000, **57**, 83-89.

[46] Lowry, M. S.; Hudson, W. R.; Pascal, R. A.; Bernhard, S. *J. Am. Chem. Soc.*, 2004, **126**, 14129-14135.

[47] Murphy, L.; Brulatti, P.; Fattori, V.; Cocchi M.; Williams, J. A. G. *Chem. Commun.*, 2012, **48**, 5817-5819.

[48] Williams, J. A. G.; Beeby, A.; Davies, E. S.; Weinstein, J. A.; Wilson, C. *Inorg. Chem.*, 2003, **42**, 8609-8611.

[49] Cocchi, M.; Kalinowski, J.; Murphy, L.; Williams, J. A. G.; Fattori, V. *Org. Electron*., 2010, **11**, 388-396.

[50] Farley, S. J.; Rochester, D. L.; Thompson, A. L.; Howard, J. A. K.; Williams, J. A. G. *Inorg. Chem*., 2005, **44**, 9690-9703.

[51] Henwood, F.; Bansal, A. K.; Cordes, D. B.; Slawin, A. M. Z.; Samuel, I. D. W.; Zysman-Colman, E. *J. Mater. Chem. C,* 2016, **4**, 3726-3737.

[52] Abhervé, A.; Martin, K.; Hauser, A.; Avarvari, N. *Eur. J. Inorg. Chem*., 2019, **45**, 4807-4814.

[53] Sotoyama, W.; Satoh, T.; Sato, H.; Matsuura, A.; Sawatari, N. *J. Phys. Chem. A*, 2005, **109**, 9760-9766.

[54] Singh, S.; Jones, W. J.; Siebrand, W.; Stoicheff, B. P.; Schneider, W. G. *J. Chem. Phys*., 1965, **42**, 330-342.

[55] Small, D. W.; Head-Gordon, M. *Phys. Chem. Chem. Phys*., 2011, **13**, 19285-19297.

[56] Dexter, D. L. *J. Chem. Phys.,* 1953, **21**, 836-850.

[57] Basel, B. S.; Zirzlmeier, J.; Hetzer, C.; Phelan, B. T.; Krzyaniak, M. D.; Reddy, S. R.; Coto, P. B.; Horwitz, N. E.; Young, R. M.; White, F. J.; Hampel, F.; Clark, T.; Thoss, M.; Tykwinski, R. R.; Wasielewski, M. R.; Guldi, D. M. *Nat. Commun*., 2017, **8**, 15171-15178.

[58] Smith, M. B.; Michl, J. *Chem. Rev.*, 2010, **110**, 6891-6936.

[59] Paddon-Row, M. N. *Adv. Phys. Org. Chem*., 2003, **38**, 1-85.

[60] Ullrich, T.; Munz, D.; Guldi, D. M. *Chem. Soc. Rev*., 2021, **50**, 3485-3518.

[61] Král, K. *Czech J. Phys. B*, 1972, **22**, 566-571.

[62] Greyson, E. C.; Vura-Weis, J.; Michl, J.; Ratner, M. A. *J. Phys. Chem. B,* 2010, **114**, 14168-14177.

[63] Lima, C. G. S.; Lima, T. M.; Duarte, M.; Jurberg, I. D.; Paixão, M. W. *ACS Catal*., 2016, **6**, 1389-1407.

[64] Schwerin, A. F.; Johnson, J. C.; Smith, M. B.; Sreearunothai P.; Popovic´, D.; Černy´, J.; Havlas, Z.; Paci, I.; Akdag, A.; MacLeod, M. K.; Chen, X.; David, D. E.; Ratner, M.; Miller, J. R.; Nozik, A. J.; Michl, J. *J. Phys. Chem. A*, 2010, **114**, 1457-1473.

[65] Herkstroeter, W. G.; Merkel, P. B. *J. Photochem,* 1981, **16**, 331-341.

[66] Ziebig, R.; Pragst, F. Z. *Z. Phys. Chem*., 1979, **260**, 795-803.

[67] Howard, J. A.; Mendenhall, G. D. *Can. J. Chem*., 1975, **53**, 2199-2201.

[68] Johnson, J. C.; Michl, J. *Curr. Chem*., 2017, **375**, 1-29.

[69] Johnson, J. C.; Nozik, A. J.; Michl, J. *J. Am. Chem. Soc*., 2010, **132**, 16302-16303.

[70] King, K. A.; Watts, R. J. *J. Am. Chem. Soc*., 1987, **109**, 1589-1590.

[71] Takizawa, S.; Aboshi, R.; Murata, S. *Photochem. Photobiol. Sci*., 2011, **10**, 895-903.

[72] Lo, K. K. W.; Chan, J. S. W.; Lui, L. H.; Chung, C. K. *Organometallics*, 2004, **23**, 3108-3116.

[73] Lo, K. K. W.; Lee, P. K.; Lau, J. S. Y. *Organometallics*, 2008, **27**, 2998-3006.

[74] Li, S. P. Y.; Liu, H. W.; Zhang, K. Y.; Lo, K. K. W. *Chem. Eur. J.*, 2010, **16**, 8329-8339.

[75] Steunenberg, P.; Ruggi, A.; Van den Berg, N. S.; Buckle, T.; Kuil, J.; Van Leeuwen, F. W. B.; Velders, A. H. *Inorg. Chem.,* 2012, **51**, 2105-2114.

[76] Pavlova, N. N.; Thompson, C. B. *Cell Metab.*, 2016, **23**, 27-47.

[77] Warburg, O.; Wind, F.; Negelein, E. *J. Gen. Physiol.*, 1927, **8**, 519-530.

[78] Eagle, H. *Science*, 1955, **122**, 501-514.

[79] Nicklin, P.; Bergman, P.; Zhang, B.; Triantafellow, E.; Wang, H.; Nyfeler, B.: Yang, H.; Hild, M.; Kung, C.; Wilson, C., Myer, V. E.; MacKeigan, J. P.; Porter, J. A.; Wang, K.; Cantley, L. C.; Finan, P. M.; Murphy, L. O. *Cell*, 2009, **136**, 521-534.

[80] Zhao, Y.; Wang, L.; Pan, J. *Intractable Rare Dis. Res.*, 2015, **4**, 165-169.

[81] Fotiadis, D.; Kanai, Y.; Palacín, M. *Mol. Aspects Med.*, 2013, **34**, 139-158.

[82] Hiraoka, N.; Toue, S.; Okamoto, C.; Kikuchi, S.; Ino, Y.; Yamazaki-Itoh, R.; Esaki, M.; Nara, S.; Kishi, Y.; Imaizumi, A.; Ono, N.; Shimada, K. *Sci Rep.*, 2019, **9**, 9816-9829.

[83] Verrey, F.; Closs, E.; Wagner, C. A.; Palacin, M.; Endou, H.; Kanai, Y. *Pflugers Arch.*, 2004, **447**, 532-542.

[84] Hayashi, K.; Anzai, N.; *World J. Gastrointest. Oncol.,* 2017, **9**, 21-29.

[85] Morimoto, E.; Kanai, Y.; Kim, D. K.; Chairoungdua, A.; Choi, H. W.; Wempe, M. F.; Anzai, N.; Endou, H. *J. Pharmacol. Sci.,* 2008, **108**, 505-516.

[86] Nakada, N.; Mikami, T.; Hana, K.; Ichinoe, M.; Yanagisawa, N.; Yoshida, T.; Endou, H.; Okayasu, I. *Histol. Histopathol.,* 2014, **29**, 217-227.

[87] Wolf, H. *Scand. J. Clin. Lab. Invest. Suppl.*, 1974, **136**, 1-186.

[88] Vécsei, L.; Szalárdy, L.; Fülöp, F.; Toldi, J. *Nat. Rev. Drug Discov.*, 2013, **12**, 64-82.

[89] Dounay, A. B.; Tuttle, J. B.; Verhoest, P. R. *J. Med. Chem.*, 2015, **58**, 8762-8782.

[90] Pardridge, W. M. *Neurochem. Res.*, 1998, **23**, 635-644.

[91] Li, S. P. Y.; Liu, H. W.; Zhang, K. Y.; Lo, K. K. W. *Chem. Eur. J.*, 2010, **16**, 8329-8339.

[92] Lo, K. K. W.; Lee, P. K.; Lau, J. S. Y. *Organometallics*, 2008, **27**, 2998-3006.

[93] Ma, X.; Jia, J.; Cao, R.; Wang, X.; Fei, H. *J. Am. Chem. Soc.*, 2014, **136**, 17734-17737.

[94] Mandal, S.; Poria, D. K.; Ghosh, R.; Ray, P. S.; Gupta, P. *Dalton Trans.*, 2014, **43**, 17463-17474.

[95] Liu, J.; Jin, C.; Yuan, B.; Chen, Y.; Liu, X.; Ji, L.; Chao, H. *Chem. Commun.*, 2017, **53**, 9878-9881.

[96] Lamansky, S.; Djurovich, P.; Murphy, D.; Abdel-Razzaq, F.; Lee, H. E.; Adachi, C.; Burrows, P. E.; Forrest, S. R.; Thompson, M. E. *J. Am. Chem. Soc.*, 2001, **123**, 4304-4312.

[97] Yang, Z.; Zhao, Y.; Wang, C.; Song, Q.; Pang, Q.; *Talanta*, 2017, **166**, 169-175.

[98] Fernie, A. R.; Carrari, F.; Sweetlove, L. J., *Curr. Opin. Plant. Biol.*, 2004, **7**, 254-261.

[99] Devin, A.; Rigoulet, M. *Am. J. Physiol. Cell Physiol*. 2007, **292**, C52-C58.

[100] Anderson, N. M.; Mucka, P.; Kern, J. G.; Feng, H. *Protein Cell*, 2018, **9**, 216-237.

[101] Liberti, M. V.; Locasale, J. W. *Trends Biochem. Sci*., 2016, **41**, 211-218.

[102] Stepien, K.; Ostrowski, R. P.; Matyja, E. *Med. Oncol*., 2016, **33**, 101-109.

[103] Nishioka, T.; Oda, Y.; Seino, Y.; Yamamoto, T.; Inagaki, N.; Yano, H.; Imura, H.; Shigemoto, R.; Kikuchi, H. *Cancer Res*., 1992, **52**, 3972-3979.

[104] Brown, R. S.; Wahl, R. L. *Cancer*, 1993, **72**, 2979-2985.

[105] Nagase, Y.; Takata, K.; Moriyama, N.; Aso, Y.; Murakami, T.; Hirano, H. *J. Urol*., 1995, **153**, 798-801.

[106] Williams, J. A. G.; *Chem. Soc. Rev*., 2009, **38**, 1783-1801.

[107] Wang, X.; Li, X.; Li, J.; Hou, J.; Qu, Y.; Yu, C.; He, F.; Xu, W.; Wu, J. *Chem. Biol. Drug Des*., 2017; **89**, 38-46.

[108] Patra, M.; Awuah, S. G.; Lippard, S. J. *J. Am. Chem. Soc*., 2016, **138**, 12541-12551.

[109] Rausch, A. F.; Murphy, L.; Williams, J. A. G.; Yersin, H. *Inorg. Chem*., 2012, **51**, 312-319.

[110] Lanoë, P. H.; Fillaut, J. L.; Toupet, L.; Williams, J. A. G.; Le Bozec, H.; Guerchais, V.; *Chem. Commun*., 2008, **36**, 4333-4335.

[111] Tamayo, A. B.; Alleyne, B. D.; Djurovich, P. I.; Lamansky, S.; Tsyba, I.; Ho, N. N.; Bau, R.; Thompson, M. E. *J. Am. Chem. Soc.,* 2003, **125**, 24, 7377-7387.

[112] Cai, Z. B.; Liu, L. F.; Hong, Y. Q.; Zhou, M. *J. Coord. Chem*., 2013, **66**, 2388-2397.

[113] Lee, L. C. C.; Tsang, A. W. Y.; Liu, H. W.; Lo, K. K. W. *Inorg. Chem*., 2020, **59**, 14796-14806.

[114] Sun, J.; Wu, W.; Guo, H.; Zhao, J. *Eur. J. Inorg. Chem*., 2011, **21**, 3165-3173.

[115] Yin, R.; Dai, T.; Avci, P.; Jorge, A. E. S.; De Melo, W. C. M. A.; Vecchio, D.; Huang, Y. Y.; Gupta, A.; Hamblin, M. R. *Curr. Op. Pharm.,* 2013, **13**, 1-32.

[116] Moan, J.; Berg, K. *Photochem. Photobiol.*, 1991, **53**, 549-553.

[117] Dougherty, T. J.; Gomer, C. J.; Henderson, B. W.; Jori, G.; Kessel, D.; Korbelik, M.; Moan, J.; Peng, Q. *J. Natl. Cancer Inst*., 1998, **90**, 889-905.

[118] Mroz, P.; Yaroslavsky, A.; Kharkwal, G. B.; Hamblin, M. R. *Cancers*, 2011, **3**, 2516-2539.

[119] Juarranz, Á.; Jaén, P.; Sanz-Rodríguez, F.; Cuevas, J.; González, S. *Clin. Transl. Oncol*., 2008, **10**, 148-154.

[120] Johnstone, T. C.; Suntharalingam, K.; Lippard, S. J. *Philos. Trans. R. Soc.*, 2015, **373**, 20140185-20140197.

[121] Dam, T. K.; Brewer, C. F. *Glycobiology,* 2010, **20**, 270-279.

[122] Shaw, R. J. *Curr. Opin. Cell Biol*., 2006, **18**, 598-608.

[123] Vander Heiden, M. G.; Cantley, L. C.; Thompson, C. B. *Science*, 2009, **324**, 1029-1033.

[124] Liu, P.; Lu, Y.; Gao, X.; Liu, R.; Zhang-Negrerie, D.; Shi, Y.; Wang, Y.; Wang, S.; Gao, Q. *Chem. Commun.,* 2013, **49**, 2421-2423.

[125] Patra, M.; Johnstone, T. C.; Suntharalingam, K.; Lippard, S. J. *Angew. Chem.*, 2016, **55**, 2550-2554.

[126] Sudimack, J.; Lee, R. J. *Adv. Drug Delivery Rev.*, 2000, **41**, 147-162.

[127] Weitman, S. D.; Lark, R. H.; Coney, L. R.; Fort, D. W.; Frasca, V.; Zurawski, V. R.; Kamen, B. A. *Cancer Res*., 1992, **52**, 3396-3401.

[128] Gabano, E.; Ravera, M.; Cassino, C.; Bonetti, S.; Palmisano, G.; Osella, D. *Inorg. Chim. Acta*, 2008, **361**, 1447-1455.

[129] Jiang, X.; Zhu, N.; Zhao, D.; Ma, Y. *Sci. China Chem*., 2016, **59**, 40-52.

[130] Garbe, S.; Krause, M.; Klimpel, A.; Neundorf, I.; Lippmann, P.; Ott, I.; Brünink, D.; Strassert, C. A.; Doltsinis, N. L.; Klein, A. *Organometallics*, 2020, **39**, 746-756.

[131] Ramu, V.; Gautam, S.; Garai, A.; Kondaiah, P.; Chakravarty, A. R. *Inorg. Chem*., 2018, **57**, 1717-1726.

[132] Deng, D.; Sun, P.; Yan, C.; Ke, M.; Jiang, X.; Xiong, L.; Ren, W.; Hirata, K.; Yamamoto, M.; Fan, S.; Yan, N. *Nature*, 2015, **526**, 391-396.

[133] Deng, D.; Xu, C.; Sun, P.; Wu, J.; Yan, C.; Hu, M.; Yan, N. *Nature*, 2014, **510**, 121-125.

[134] Gao, R.; Ho, D. G.; Hernandez, B.; Selke, M.; Murphy, D.; Djurovich, P. I.; Thompson, M. E. *J. Am. Chem. Soc.,* 2002, **124**, 14828-14829.

[135] Takizawa, S.; Aboshi, R.; Murata, S. *Photochem. Photobiol. Sci*., 2011, **10**, 895-903.

[136] Takizawa, S.; Nishida, J.; Tsuzuki, T.; Tokito, S.; Yamashita, Y. *Inorg. Chem.*, 2007, **46**, 4308‑4319.

[137] Kane R.; Sell, H. Revolution in Lamps: A Chronicle of 50 Years of Progress, The Fairmont Press, Inc., 2nd edn, 2001.

[138] Kallman, H.; Pope, M. *Nature*, 1960, **186**, 31-33.

[139] Pope, M.; Kallman, H.; Magnate, P. *J. Chem. Phys*., 1963, **38**, 2042-2043.

[140] Tang, C.; VanSlyke, S.; *Appl. Phys. Lett.*, 1987, **51**, 913-915.

[141] Burroughes, J.; Bradley, D.; Brown, A.; Marks, R.; MacKay, K.; Friend, R.; Burns, P.; Holmes, A. *Nature*, 1990, **347**, 539-541.

[142] Minaev, B.; Baryshnikov G.; Agren, H.; *Phys. Chem. Chem. Phys.,* 2014, **16**, 1719-1758.

[143] Swayamprabha, S. S.; Dubey, D. K.; Shahnawaz, R. A. K.; Yadav, Nagar, M. R.; Sharma, A.; Tung, F. C.; Jou, J. H. *Adv. Sci.,* 2021, **8**, 2002254-2002283.

[144] Hong, G.; Gan, X.; Leonhardt, C.; Zhang, Z.; Seibert, J.; Busch, J. M.; Bräse, S. *Adv. Mater.*, 2021, **33**, 2005630-2005654.

[145] Baldo, M. A.; Lamansky, S.; Burrows, P. E.; Thompson, M. E.; Forrest, S. R. *Appl. Phys. Lett.,* 1999, **75**, 4-6.

[146] Kwong, R. C.; Lamansky, S.; Thompson, M. E. *Adv. Mater.,* 2000, **12**, 1134-1138.

[147] Holder, E.; Langeveld, B. M. W.; Schubert, U. S. *Adv. Mater.,* 2005, **17**, 1109-1121.

[148] Lai, S. W.; Chan, M. C. W.; Cheung, T. C.; Peng, S. M.; Che, C. M. *Inorg. Chem.* 1999, **38**, 4046-4055.

[149] Lu, W.; Mi, B. X.; Chan, M. C. W.; Hui, Z.; Che, C. M.; Zhu, N. Y.; Lee, S. T. *J. Am. Chem. Soc.,* 2004, **126**, 4958-4971.

[150] Caubet, A.; Lopez, C.; Solans, X.; Font-Bardia, M. *J. Organomet. Chem.,* 2003, 669, 164-171.

[151] Rochester, D. L.; Develay, S.; Zàlis, S.; Williams, J. A. G. *Dalton Trans*., 2009, 1728-1741

[152] Brooks, J.; Babayan, Y.; Lamansky, S.; Djurovich, P. I.; Tsyba, I.; Bau, R.; Thompson, M. E. *Inorg. Chem.*, 2002**, 41**, 3055-3066.

[153] Chow, P. K.; Cheng, G.; Tong, G. S. M.; To, W. P.; Kwong, W. L.; Low, K. H.; Kwok, C. C.; Ma, C.; Che, C. M.; *Angew. Chem.,* 2015, **54**, 2084 -2089.

[154] Sheldrick, G. M. *Acta Cryst.*, 2015, **A71**, 3.

[155] Sheldrick, G. M. *Acta Cryst*., 2015, **C71**, 3.

[156] Martínez, V. M.; Arbeloa, F. L.; Prieto, J. B.; Arbeloa, I. L. *J. Phys. Chem. B*, 2005, **109**, 7443-7450.